Citation: Ananthapuvirajah, A. (2019). Free vibration and flutter behaviour of metallic and composite aircraft using DSM and developments of dynamic stiffness matrices for structural elements with applications. (Unpublished Doctoral thesis, City, University of London)

Free Vibration and Flutter Behaviour of Metallic and Composite Aircraft Using DSM and Developments of Dynamic Stiffness Matrices for Structural Elements with Applications

Thesis submitted as part of the requirement
for the fulfilment of a degree of
Doctor of Philosophy
by
Ajandan Ananthapuvirajah

School of Mathematics, Computer Science & Engineering
City, University of London
January 2019

Contents

List of Figures

List of Tables

Acknowledgments

First, I would like to acknowledge the almighty God without whom it will not be possible for my existence, It is my belief that without God nothing will happen and God will carry us when we are unable to move on our own. Secondly, I would like to acknowledge Prof Ranjan Banerjee, my supervisor who shaped me during my PhD period both academically and at personal level. He was there for me always whenever I need his help and I am lucky to have a good teacher who wants his student to succeed him and propel me whenever I feel demotivated. All he expected from me is to do well in my life and studies, hopefully with God's grace I will aim to make him proud of me with my achievements. I would also like to acknowledge Prof Abdulnaser Sayma for agreeing to be my supervisor when Prof Ranjan Banerjee retired. His timely help in adhering to University policy makes me very grateful to him. I also like to thank Dr Chak Cheung for his stimulating encouragements during my PhD. Thirdly, I would like to acknowledge my family. My parents and my wife who believed in me when I don't even believe in myself, also my daughter who gives me the motivation to focus on my work.

Lastly, I would like to acknowledge my University lecturer's, colleagues, my relatives and especially my friends who spend their time hearing my ramblings and supported me whenever I began to doubt myself. I understand it will be harder to mention everyone who have helped me while I was doing my PhD, still I would like to name few of my friends. I would specially like to mention Hassan Kasseem and Xiang Liu for their support during the start of my PhD especially Hassan who always welcomed me with open heart and gave advice. It is rare to get a friend like Hassan who will reply to your email always whenever you ask questions whether it seems important or not. Also Hao Li and Siti who challenges my way of doing research and made me think before I act. I would also like to thank Muthukumar for encouraging me to use Latex to write my thesis as well as Sunny and Dhamotharan for their assistance in using Latex.

Declaration

I declare that the work I have produced in this thesis is without the prohibited assistance of third parties and without making use of aids other than those specified, notions taken over directly or indirectly from other sources have been identified as such by appropriate references, and that this work has not been submitted for any other degree or professional qualification. Some parts of this work have been published in papers and are given under list of publications. I also grant powers of discretion to the University librarian to allow the thesis to be copied in whole or in part. This permission covers only single copies made for study purposes, subject to normal conditions of acknowledgement.

List of publications

1] Banerjee, JR and A Ananthapuvirajah (2018). “Free vibration of functionally graded beams and frameworks using the dynamic stiffness method”. In: *Journal of Sound and Vibration* 422.26, pp. 37-47.

2] Banerjee, JR and A Ananthapuvirajah (2019). “An exact dynamic stiffness matrix for a beam incorporating Rayleigh–Love and Timoshenko theories”. In: *International Journal of Mechanical Sciences* 150.1, pp. 337-347.

3] Banerjee, JR and A Ananthapuvirajah (2019). “Coupled axial-bending dynamic stiffness matrix for beam elements”. In: *Computers & Structures* 215.15, pp. 1-9.

4] Banerjee, JR and A Ananthapuvirajah (In press). “Discussion on ‘Free vibration of functionally graded beams and frameworks using the dynamic stiffness method’”. In: *Journal of Sound and Vibration*.

5] Ananthapuvirajah, A and JR Banerjee (Submitted: under review). “On the dynamical behaviour of a range of high aspect ratio aircraft wings”. In: *The Aeronautical Journal*.

Abstract

This thesis focuses on two types of original research, of which the first one (Section A) can be categorised as applied or engineering research concerning the free vibration and flutter behaviour of metallic and composite aircraft whereas the second one (Section B) is focused on fundamental research, on the developments of the dynamic stiffness matrices and application for a range of structural elements of varying degrees of complexities.

The main focus of the first part of the research is to use analytical methods through the application of in-house computer programs to determine stiffness properties (*EI*, *GJ* and *K*) and then to carry out free vibration analysis and flutter analysis. Stiffness analysis using both single and double cell idealisation of the wing is first carried out and then free vibration and flutter analysis behaviour is subsequently investigated in details. Both low-fidelity model using bending-torsion coupled beam representation of the aircraft and high-fidelity model using FEMAP/NASTRAN in which the aircraft is idealised in detail using beam, plate and shell elements have been used. In the low fidelity model, of particular significance is the inclusion of the bending-torsion coupling stiffness which exists in composite wings. The scope of the investigation is broadened by carrying out wing-only as well as whole aircraft configurations. In this endeavour a detail parametric study is undertaken by changing significant aircraft parameters such as bending and torsion stiffnesses, fuselage mass and inertia, engine mass and its location. Three categories of aircraft namely sailplane, light aircraft trainer and transport airliners are analysed with significant conclusion drawn.

Alongside the above investigation, fundamental research on the dynamic stiffness formulation for a range of structural elements is also carried out. This includes functionally graded beams, cracked beams, Rayleigh-Love bars, Timoshenko beams and axial-bending coupled beams. In each case, the governing differential equations and associated natural boundary conditions are derived using Hamilton's principle. The equations are solved in closed analytical form and explicit expressions for the dynamic stiffness coefficients were obtained using symbolic computations wherever possible. Finally, the dynamic stiffness matrices are developed by relating the amplitudes of the forces to those of the displacements. The Wittrick-Williams algorithm is used to yield the natural frequencies and mode shapes. The results obtained are validated using published results.

Structure of the thesis

This thesis consists of two sections, namely Section A and Section B. Section A deals with stiffness, free vibration and flutter behaviour of metallic and composite aircraft which is basically an engineering or applied science research whereas Section B deals with fundamental research wherein dynamic stiffness theory for a wide range of structural elements is developed. Section A involves Chapters 1 through Chapter 5 constituting the subject matter of applied research while Section B involves Chapters 6 through Chapter 9 constituting the subject matter of fundamental research.

Section A

An overview and layout of Section A

A satisfactory design of aircraft has to meet specific requirements in compliance with airworthiness, for example to improve environmental impact and cost efficiency. Airworthiness requirements specify that when designing an aircraft, undesirable aeroelastic phenomena such as flutter and divergence must be avoided. Since divergence generally occurs at a relatively higher speed than flutter, the research in this thesis is principally focused on flutter. Although a range of isotropic materials have been traditionally used for aircraft structures, composite materials are making their headways because they offer much greater specific strength and their stiffness properties can be engineered and optimized to achieve much lighter aircraft. However, the use of laminated composites because of their fibrous nature presents significant challenges, particularly from an aeroelastic standpoint. Within this pretext, a major investigation on the stiffness, free vibration and flutter behaviour of metallic and composite aircraft is undertaken in this thesis. The diverse nature of this research demanded that altogether eight aircraft of three different categories namely, sailplanes, light aircraft trainers and transport airliner were to be investigated. One of the aims of this thesis is to provide an improved understanding of the free vibration and flutter behaviour of both metallic and composite aircraft from an engineering perspective. The structure of Section A with its constituent chapters is as follows. Chapter 1 describes the background of flutter analysis and the theories for high aspect ratio aircraft. This is followed by Chapter 2 which consists of stiffness, free vibration and flutter analysis of metallic and composite aircraft structure. For composite aircraft, particular emphasis is given on stiffness evaluation of single cell and double cell wing sections prior to free vibration and flutter analysis. Next, Chapter 3 focuses on detailed stiffness analysis of the entire composite wing and provides some preliminary results as well as some case studies based on the geometrical considerations carried out. In Chapter 4, results for three different, but wide ranging categories of high aspect ratio aircraft wings are presented. Furthermore, some results using a parametric study are also given which include stiffness properties variation, engine mass and its position variation. Chapter 5 which is the final chapter of Section A consists of two parts. In the first part, the fuselage, tail plane, fin and rudder masses and inertias were lumped together and deposited at the wing-fuselage centreline intersection and thus allowing the aircraft to have a free motion resulting in rigid body freedoms in heave and pitch. A parametric study by varying the lumped fuselage mass and inertia was also performed. The second part of Chapter 5 involves idealising the whole aircraft configuration by using stick model comprising bending-torsion coupled beams for the wing, fuselage, tail and rudder. The analysis is carried out by using only one symmetric half of the aircraft and imposing the appropriate boundary conditions on the enforced plane of symmetry such that both symmetric and antisymmetric flutter analyses were covered in the analysis.

Chapter 1

Introduction to the flutter and the theories involved

1.1 Introduction to free vibration and flutter analysis

Aeroelasticity is defined as the science of studying the mutual interaction between aerodynamic, elastic and inertia forces and particularly, the influence of this interaction on aircraft. Aeroelastic problems would not exist if aircraft structures were perfectly rigid. For rigid bodies it is assumed that the deformation due to external forces is very small which is not true for high aspect ratio aircraft wing. Modern aircraft structures are indeed very flexible and this flexibility is fundamentally responsible for the various types of aeroelastic phenomena that are encountered in practise. At lower speeds of flight, the effect of elastic deformation is relatively small. However, at higher speeds, the effect of elastic deformations can become a serious problem causing aeroelastic instabilities such as flutter, divergence and control reversal, amongst others. The consequence of these instabilities may result in catastrophic effect including loss of the aircraft.

Aeroelasticity can be generally classified into two major branches- static and dynamic [1, 2]. Static aeroelastic phenomena involve interactions between aerodynamic and elastic forces. By contrast, dynamic aeroelastic phenomena involve interaction amongst inertial, aerodynamic and elastic forces. When small disturbances of an incidental nature induce violent and self-excited sustained oscillations, they fall under the category of dynamic aeroelastic instability. Also there exists other types of aeroelastic phenomena that can occur due to externally applied forces such as an input to the control surfaces of an aircraft, or by disturbances arising from gusts, turbulence in the flow as well as impact during landing.

1.1.1 A brief description of flutter

Consider a cantilever wing mounted in a wind tunnel at a small angle of attack and with a rigid support at the root. There is no flow in the wind tunnel and if the model is disturbed, oscillation sets in, which is gradually damped. If the speed of air flow in the wind tunnel is gradually increased, the rate of damping of the oscillation of the disturbed aerofoil increases. With further increase of the speed of the flow, a point is reached, where an oscillation can just maintain itself with steady amplitude. The speed at this point is called critical flutter speed. At speeds of flow somewhat above the critical, a small accidental disturbance of the aerofoil can serve as a trigger to initiate a violent oscillation. In such circumstances the aerofoil suffers from oscillatory instability, called ‘flutter’. The elasticity of the structure plays an essential part in this instability. Experiments on wing flutter show that the oscillation is self-sustained, i.e. no external oscillator or forcing agency is required. The motion can maintain itself or grow for a range of airspeeds based on the design of the wing and the conditions of the test. For a simple cantilever wing, flutter occurs at an airspeed above the critical [1].

1.2 Dynamic stiffness method (DSM) for free vibration analysis

One of the motivations for modal analysis of aircraft wings originates from the fact that it is a fundamental prerequisite to carry out an aeroelastic or response analysis, when using the normal mode method. There are some published literature which elucidates the importance of this research [3–5]. In general, the finite element method (FEM) is widely used to investigate the modal behaviour of aircraft wings. However, the FEM is an approximate method based on assumed shaped functions from which the stiffness and mass properties of all individual elements are derived and assembled to form the overall stiffness matrix **[K]** and mass matrix **[M]** of the final structure. Then the modal analysis is carried out by imposing the boundary conditions which leads to an eigenvalue problem of the type $[[\mathbf{K}] - \lambda[\mathbf{M}]]\{\mathbf{\Delta}\} = \mathbf{0}$ where $\{\mathbf{\Delta}\}$ is the nodal displacement vector and the square root of λ gives the natural frequencies of the structure. Against the above background, it should be noted that there is an elegant and powerful alternative to the FEM for modal analysis of structures including aircraft wings, which is not as widely used as the FEM. The alternative is that of the dynamic stiffness method (DSM).

Dynamic stiffness method (DSM) is used for aeroelastic analysis in this part of the research. In brief, DSM relies on the frequency dependent exact shape function of the structural element derived from its differential equation in free vibration. For the exactness of the shape function, the results obtained from the DSM are often called exact. In the DSM, separate mass and stiffness matrices are not derived, instead a single frequency dependent element stiffness matrix which contains both the mass and stiffness properties of the element are utilised. Also, the results obtained from the DSM are independent of the number of elements used in the analysis. The dynamic stiffness method (DSM) was pioneered by Kolousek in the early 1940s [6, 7] when he introduced for the first time the frequency dependent dynamic stiffness coefficients known as Kolousek functions for a Bernoulli-Euler beam derived from its free vibrational response. The DSM is also known as continuous element method (CEM) and spectral element method (SEM). The basic concept put forward by Kolousek made it possible to relate the amplitudes of forces to the displacements at the nodes of a structural element through its dynamic stiffness matrix which is essentially the basic building block of the DSM.

First of all, the shape functions in the DSM are obtained from the solution of the governing differential equations of motion of the element when it is undergoing free vibration. As a consequence, the shape functions in the DSM are frequency dependent and from an analytical justification point of view, they can be regarded as exact because there are no assumptions made to describe the displacement field. If there are at all any assumptions, they are within the limits of the governing differential equations of motion. Using these so-called exact shape functions which are essentially solutions of the free vibratory motion of the element, the dynamic stiffness matrix is developed by applying the boundary conditions of the harmonically varying forces to the displacements at the nodes of the elements in an algebraic form. During this process, a single frequency dependent element matrix is generated relating the amplitudes of the nodal forces and displacements. Thus derived, this so-called dynamic stiffness matrix contains both the mass and stiffness properties of the element as functions of the structural parameters as well as the frequency.

The dynamic stiffness matrix of a structural element essentially relates the amplitudes of the forces to those of the corresponding displacements at the nodes of the harmonically vibrating structural element. A general procedure to formulate the dynamic stiffness matrix of a structural element is briefly described in following steps:

(i) Derive the governing differential equation of motion in free vibration of the structural element for which the dynamic stiffness matrix is to be developed. This can be achieved by applying Newton's second law or Lagrange's equation or Hamilton's principle. However, Hamilton's principle is preferred because unlike Newton's second law and Lagrange's equation, the variationally based Hamilton's principle provides natural boundary conditions, giving the expressions for forces and moments which are required in the dynamic stiffness formulation.

(ii) For harmonic oscillation, seek a closed form analytical solution of the governing differential equation derived in (i) above, in terms of the arbitrary integration constants. The number of constants in the general solution will, of course, depend on the order of the

differential equation.
(iii) Apply the boundary conditions in algebraic form. The number of boundary conditions is generally equal to twice the number of integration constants. The boundary conditions are typically the nodal displacements and forces.
(iv) Eliminate the constants by relating the harmonically varying amplitudes of nodal forces to the corresponding displacements at the nodes of the element. This will generate the frequency dependent dynamic stiffness matrix connecting dynamically the amplitudes of the nodal forces to those of the nodal displacements.
The assembly procedure in the DSM involves a single dynamic stiffness element matrix for each structural component to form the overall frequency-dependent dynamic stiffness matrix $\mathbf{K_D}$ of the final structure. The eigenvalue problem is formulated as $[\mathbf{K_D}]\{\mathbf{\Delta}\}=0$ where $\{\mathbf{\Delta}\}$ is the nodal displacement vector comprising amplitudes of the nodal displacements. The next step is to extract the eigenvalues of the structure. The formulation $[\mathbf{K_D}]\{\mathbf{\Delta}\}=0$ leads to a transcendental (non-linear) eigenvalue problem. The best available solution technique to extract the eigenvalues in the DSM is to apply the algorithm of Wittrick and Williams, known as the Wittrick-Williams algorithm in the literature which has featured in literally hundreds of papers. The algorithm which monitors the Sturm sequence property of the dynamic stiffness matrix is robust ensuring that no natural frequency of the structure is missed. The Wittrick-Williams algorithm has become an indispensable tool for free vibration analysis of structures using the DSM. Subsequent to the pioneering contributions of Kolousek [6, 8], followed by the work of Williams and Wittrick [7] and of course, very importantly, the development of the Wittrick-Williams algorithm [9, 10] the DSM has continued to enjoy a sustained period of developments for more than half a century and undoubtedly, it has reached a high degree of maturity to date.

1.2.1 Development of dynamic stiffness method for a bending-torsion coupled beam

The procedure to develop the dynamic stiffness matrix of a structural element is systematic and rather simple [11]. In essence, there are four main steps to accomplish this task. First, the governing differential equation of motion of the structural element in free vibration is to be derived using either Newton's law or Lagrange's equation or Hamilton's principle. (Hamilton's principle is preferred because it gives natural boundary conditions which are essential in dynamic stiffness formulation.). In the second step, the differential equation needs to be solved in an exact sense in terms of some arbitrary constants. In this step, it is necessary to obtain all expressions for displacements and forces in an explicit algebraic form in terms of the integration constants by using the exact solution of the governing differential equation. In the third step, boundary conditions for displacements and forces at the nodes of the element are applied algebraically. (Note that the nodes can be point nodes or line nodes depending on the type of the element to be developed in the analysis.). Thus, if $\{\delta\}$ is the displacement vector comprising the amplitudes of nodal displacements and $\{\mathbf{f}\}$ is the force vector comprising the amplitudes of the nodal forces of the element, then the applications of the boundary conditions for displacements and forces will give the matrix relationships $\{\delta\} = [A]\{C\}$ and $\{\mathbf{f}\} = [B]\{C\}$, respectively where $\{\mathbf{C}\}$ is the unknown constant vector and matrices **[A]** and **[B]** are frequency- dependent square matrices already known from the element mass and stiffness properties and other structural parameters of the element. In the fourth and final step, the constant vector {C} is eliminated from the two matrix relationships shown above to give $\{\mathbf{f}\} = [\mathbf{k_D}]\{\delta\}$ where $[\mathbf{k_D}] = [\mathbf{B}][\mathbf{A}]^{-\mathbf{1}}$ is the required frequency dependent dynamic stiffness matrix. This dynamic stiffness formulation process can be completed efficiently by taking advantage of symbolic computation wherever possible. In essence, upon elimination of the constants from the solution of the governing differential equation of motion of the element undergoing free vibration, the dynamic stiffness matrix $[\mathbf{k_D}]$ of the element is obtained, relating amplitudes of forces and displacements at its nodes.

1.2.1.1 Application of the Wittrick-Williams algorithm

The dynamic stiffness matrix of Equation 1.1 can now be used to compute the natural frequencies and mode shapes of aircraft wings. A non-uniform and/or swept wing can be analysed for its natural frequencies and mode shapes by idealising it as an assemblage of many uniform dynamic stiffness elements of bending-torsion coupled beams. The natural frequency calculation is accomplished by applying the Wittrick-Williams algorithm [9] which has received extensive coverage in the literature. Before applying the algorithm the dynamic stiffness matrices of all individual elements need to be assembled to form the overall dynamic stiffness matrix $\mathbf{K_f}$ of the complete wing. The algorithm monitors the Sturm sequence condition of $\mathbf{K_f}$ in such a way that there is no possibility of missing any natural frequency of the wing. The application procedure of the algorithm is briefly summarised as follows.

Suppose that ω denotes the circular (or angular) frequency of the vibrating wing. Then according to the Wittrick-Williams algorithm [9], j, the number of natural frequencies passed as ω is increased from zero to ω^*, is given by

$$j = j_0 + s\{\mathbf{K_f}\} \tag{1.1}$$

where $\mathbf{K_f}$,the overall dynamic stiffness matrix of the wing whose elements depend on ω is evaluated at $\omega = \omega^*$; $\mathbf{s}\{\mathbf{K_f}\}$ is the number of negative elements on the leading diagonal of $\mathbf{K_f^\Delta}$, $\mathbf{K_f^\Delta}$ is the upper triangular matrix obtained by applying the usual form of Gauss elimination to $\mathbf{K_f}$, and j_0 is the number of natural frequencies of the wing still lying between $\omega = 0$ and $\omega = \omega^*$ when the displacement components to which $\mathbf{K_f}$ corresponds are all zeros. (Note that the structure can still have natural frequencies when all its nodes are clamped, because exact member equations allow each individual member to displace between nodes with an infinite number of degrees of freedom, and hence infinite number of natural frequencies between nodes.) Thus

$$j_0 = \Sigma\, j_m \tag{1.2}$$

where j_m is the number of natural frequencies between $\omega = 0$ and $\omega = \omega^*$ for an individual component member with its ends fully clamped, while the summation extends over all members of the structure. Thus, with the knowledge of Equations 1.1 and 1.2, it is possible to ascertain how many natural frequencies of the wing lie below an arbitrarily chosen trial frequency ω^*. This simple feature of the algorithm can be used to converge upon any required natural frequency to any desired accuracy. As successive trial frequencies can be chosen, computer implementation of the algorithm is very simple. However, for a detailed understanding, readers are referred to the original work of Wittrick and Williams [9].

1.2.2 Methodology

The methodology used in this section relies on the use of normal mode method through the application of two-dimensional unsteady aerodynamics of Theodorsen type [1, 2] when establishing the flutter speed and flutter frequency of an idealised stick-model based high aspect ratio aircraft wing. For structural idealisation, the dynamic stiffness method is used to compute the normal modes accurately. However, for aerodynamic idealisation, as the wings analysed have all high aspect ratios, it was decided to use two-dimensional unsteady aerodynamics of Theodorsen type. Some details pertaining to these idealisations and computer implementation are embedded within the aeroelastic package CALFUN which will be discussed later in this chapter. Also various programs are used throughout Section A in performing stiffness, free vibration and flutter analysis and their example data files are given in Appendix A.

1.2.3 Structural idealisation of high aspect ratio aircraft wings using the dynamic stiffness method

An aircraft wing such as the one shown in Figure 1.1 is a classic example of a bending-torsion coupled beam. Such a representation is particularly relevant to analyse a high aspect ratio wing.

In essence, the coupling between the bending and the torsional motions arises due to non-coincident mass and elastic axes which are respectively the loci of the centroid and shear

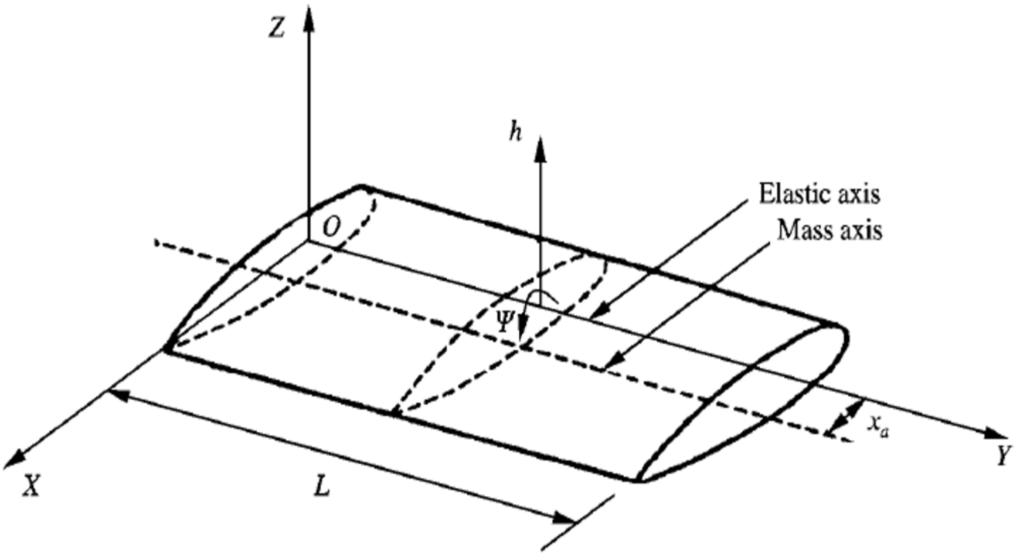

Figure 1.1: An aircraft wing idealised as a bending-torsion coupled beam.

centres of the beam cross-section. Thus for an aircraft wing it is not generally possible to realize a torsion-free bending displacement or a bending-free torsional rotation during its dynamic motion unless the load or the torque is applied through or about the shear centre. Given this perspective, a high aspect ratio non-uniform aircraft wing can be accordingly modelled as an assemblage of bending-torsion couple beams of the type shown in Figure 1.1. In essence, dynamic stiffness approach is used to develop the dynamic stiffness matrix of a uniform bending-torsion coupled beam and then extends it to model a non-uniform wing [11].

The governing partial differential equations of motion of the bending-torsion coupled beam (wing) shown in Figure 1.1 are given by [12, 13]

$$EIh'''' + m\ddot{h} - mx_\alpha\ddot{\psi} = 0 \tag{1.3}$$

$$GJ\psi'' + mx_\alpha\ddot{h} - I_\alpha\overset{...}{\ddot{\psi}} = 0 \tag{1.4}$$

where EI and GJ are the bending and torsional stiffnesses of the beam, m is the mass per unit length, I_α is the polar mass moment of inertia per length about the Y-axis, and the primes and over dots denotes partial differentiation with respect to position y and time t, respectively.

For harmonic oscillation, sinusoidal variation in h and ψ with circular frequency ω may be assumed to give

$$h(y,t) = H(y)\,sin\omega t, \qquad \psi(y,t) = \Psi(y)\,sin\omega t \tag{1.5}$$

where $H(y)$ and $\Psi(y)$ denotes the amplitude of the bending displacement and torsional

rotation.
Substituting Equation 1.5 into Equations 1.3 and 1.4 eliminates the time component and gives the following ordinary differential equations

$$EIH'''' - m\omega^2 H + mx_\alpha \omega^2 \Psi = 0 \tag{1.6}$$

$$GJ\Psi'' + I_\alpha \omega^2 \Psi + \omega^2 mx_\alpha H = 0 \tag{1.7}$$

where prime now denotes full differentiation with respect to y.
Equations 1.6 and 1.7 can be combined into a sixth order ordinary differential equation by eliminating either H or Ψ to give

$$W'''''' + \left(\frac{I_\alpha \omega^2}{GJ}\right) W'''' - \left(\frac{m\omega^2}{EI}\right) W'' - \left(\frac{m\omega^2}{EI}\right)\left(\frac{I_\alpha \omega^2}{GJ}\right)\left(\frac{I_\alpha - mx_\alpha^2}{I_\alpha}\right) W = 0 \tag{1.8}$$

where

$$W = H \; or \; \Psi \tag{1.9}$$

Equation 1.8 can be non-dimensionalised by using the non-dimensionalised length ξ where

$$\xi = \frac{y}{L} \tag{1.10}$$

Thus, with the help of Equation 1.10, the non-dimensional form of Equation 1.8 becomes

$$(D^6 + aD^4 - bD^2 - abc)W = 0 \tag{1.11}$$

where a, b and c are non-dimensional parameters given by

$$a = \left(\frac{I_\alpha \omega^2 L^2}{GJ}\right), \quad b = \left(\frac{m\omega^2 L^4}{EI}\right), \quad c = \left(\frac{I_\alpha - mx_\alpha^2}{I_\alpha}\right) \tag{1.12}$$

and D is the following differential operator

$$D = \frac{d}{d\xi} \tag{1.13}$$

The differential equation given by Equation 1.11 can be solved using standard procedure [12, 13] to give

$$W(\xi) = C_1 cosh\alpha\xi + C_2 sinh\alpha\xi + C_3 cos\beta\xi + C_4 sin\beta\xi + C_5 cos\gamma\xi + C_6 sin\gamma\xi \tag{1.14}$$

where

$$\alpha = \left[2\left(\frac{q}{3}\right)^{\frac{1}{2}} \cos\left(\frac{\phi}{3}\right) - \frac{a}{3}\right]^{\frac{1}{2}}, \beta = \left[2\left(\frac{q}{3}\right)^{\frac{1}{2}} \cos\left(\frac{(\pi - \phi)}{3}\right) + \frac{a}{3}\right]^{\frac{1}{2}}, \gamma = \left[2\left(\frac{q}{3}\right)^{\frac{1}{2}} \cos\left(\frac{(\pi + \phi)}{3}\right) + \frac{a}{3}\right]^{\frac{1}{2}} \tag{1.15}$$

with

$$q = b + \frac{a^2}{3} \tag{1.16}$$

and

$$\phi = cos^{-1}\left[\frac{27abc - 9ab - 2a^3}{\left\{2(a^2 + 3b)^{\frac{3}{2}}\right\}}\right] \tag{1.17}$$

In Equation 1.14, $C_1 - C_6$ are the integration constants resulting from the solution of the governing differential equation i.e. Equation 1.11

$W(\xi)$ of Equation 1.14 is the solution for both the bending displacement H and the torsional rotation Ψ, but with two different sets of constants. Thus,

$$H(\xi) = A_1 cosh\alpha\xi + A_2 sinh\alpha\xi + A_3 cos\beta\xi + A_4 sin\beta\xi + A_5 cos\gamma\xi + A_6 sin\gamma\xi \tag{1.18}$$

and

$$\Psi(\xi) = B_1 cosh\alpha\xi + B_2 sinh\alpha\xi + B_3 cos\beta\xi + B_4 sin\beta\xi + B_5 cos\gamma\xi + B_6 sin\gamma\xi \tag{1.19}$$

The two different sets of constants $A_1 - A_6$ and $B_1 - B_6$ in Equations 1.18 and 1.19 can be related with the help of either Equation 1.6 or Equation 1.7 to give

$$B_1 = k_\alpha A_1, \quad B_2 = k_\alpha A_2, \quad B_3 = k_\beta A_3, \quad B_4 = k_\beta A_4, \quad B_5 = k_\gamma A_5, \quad B_6 = k_\gamma A_6 \tag{1.20}$$

where

$$k_\alpha = \frac{b - \alpha^4}{bx_\alpha}, \quad k_\beta = \frac{b - \beta^4}{bx_\alpha}, \quad k_\gamma = \frac{b - \gamma^4}{bx_\alpha} \tag{1.21}$$

The expressions for bending rotation $\Theta(\xi)$, bending moment $M(\xi)$, shear force $S(\xi)$ and torque $T(\xi)$ are given by

$$\theta(\xi) = H'\left(\frac{\xi}{L}\right) = \left(\frac{1}{L}\right)\{A_1\alpha sinh\alpha\xi + A_2\alpha cosh\alpha\xi - A_3\beta sin\beta\xi + A_4\beta cos\beta\xi - A_5\gamma sin\gamma\xi + A_6\gamma cos\gamma\xi\} \tag{1.22}$$

$$M(\xi) = -\left(\frac{EI}{L^2}\right)H''(\xi) = -\left(\frac{EI}{L^2}\right)\left\{A_1\alpha^2 cosh\alpha\xi + A_2\alpha^2 sinh\alpha\xi - A_3\beta^2 cos\beta\xi - A_4\beta^2 sin\beta\xi - A_5\gamma^2 cos\gamma\xi - A_6\gamma^2 sin\gamma\xi\right\} \tag{1.23}$$

$$S(\xi) = \left(\frac{EI}{L^3}\right)\left\{A_1\alpha^3 sinh\alpha\xi + A_2\alpha^3 cosh\alpha\xi + A_3\beta^3 sin\beta\xi - A_4\beta^3 cos\beta\xi + A_5\gamma^3 sin\gamma\xi - A_6\gamma^3 cos\gamma\xi\right\} \tag{1.24}$$

$$T(\xi) = \left(\frac{GJ}{L}\right)\Psi'(\xi) = \left(\frac{GJ}{L}\right)\{B_1\alpha sinh\alpha\xi + B_2\alpha cosh\alpha\xi - B_3\beta sin\beta\xi + B_4\beta cos\beta\xi - B_5\gamma sin\gamma\xi + B_6\gamma cos\gamma\xi\} \tag{1.25}$$

With the help of Equations 1.18 to 1.25, the dynamic stiffness matrix of the coupled bending-torsion beam element which is essentially an aircraft wing element can be developed by applying the boundary conditions algebraically for displacements and forces at the ends of the elements.

Referring to Figure 1.2, the boundary conditions for displacements are

$$\begin{aligned} &At\;\; y = 0 \;\; (\xi = 0) : H = H_1, \quad \theta = \theta_1 \quad \Psi = \Psi_1 \\ &At\;\; y = L \;\; (\xi = 1) : H = H_2, \quad \theta = \theta_2 \quad \Psi = \Psi_2 \end{aligned} \tag{1.26}$$

Similarly, referring to Figure 1.3, the boundary conditions for the forces are

$$\begin{aligned} &At\;\; y = 0 \;\; (\xi = 0) : S = S_1, \quad M = M_1 \quad T = -T_1 \\ &At\;\; y = L \;\; (\xi = 1) : H = -S_2, \quad M = -M_2 \quad T = T_2 \end{aligned} \tag{1.27}$$

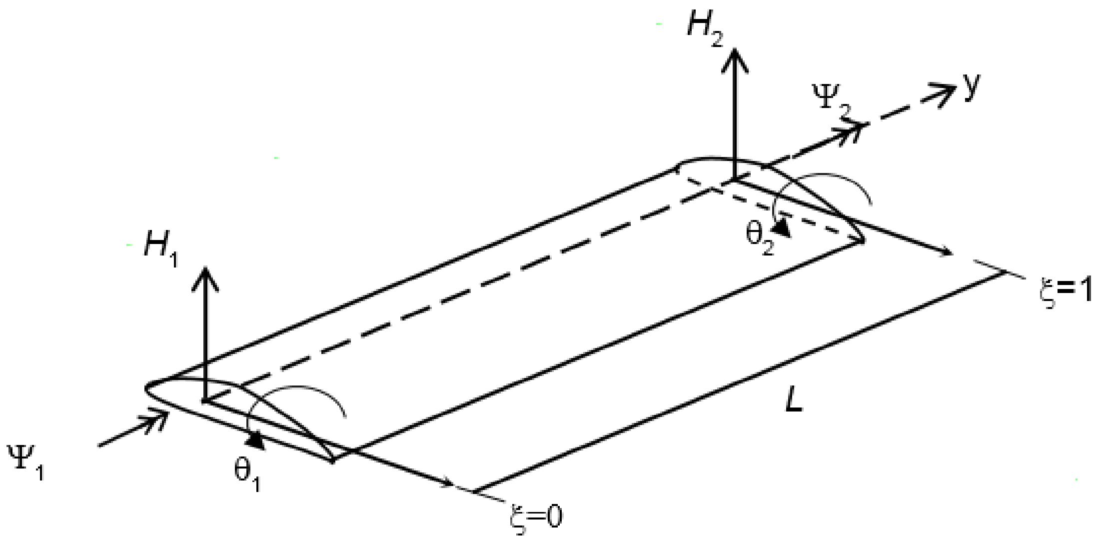

Figure 1.2: Boundary conditions for displacements of an aircraft wing element.

Substituting the boundary conditions for displacements given by Equation 1.26 into Equations 1.18, 1.19 and 1.22, one obtains the following matrix relationship

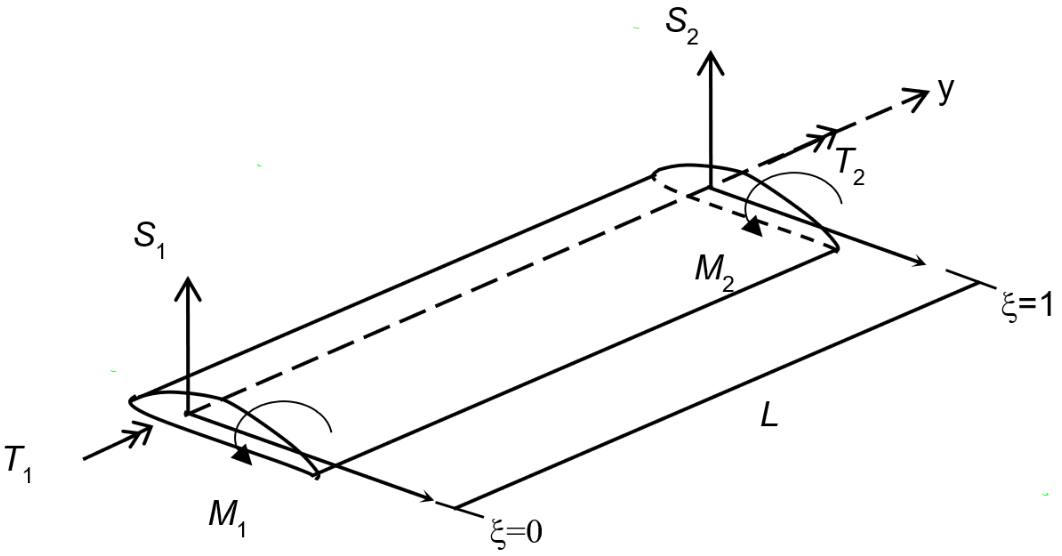

Figure 1.3: Boundary conditions for forces of an aircraft wing element.

$$\begin{bmatrix} H_1 \\ \theta_1 \\ \Psi_1 \\ H_2 \\ \theta_2 \\ \Psi_2 \end{bmatrix} = \begin{bmatrix} 1 & 0 & 1 & 0 & 1 & 0 \\ 0 & \alpha/L & 0 & \beta/L & 0 & \gamma/L \\ k_\alpha & 0 & k_\beta & 0 & k_\gamma & 0 \\ C_{h_\alpha} & S_{h_\alpha} & C_\beta & S_\beta & C_\gamma & S_\gamma \\ \alpha S_{h_\alpha}/L & \alpha C_{h_\alpha}/L & -\beta S_\beta/L & \beta C_\beta/L & -\gamma S_\gamma/L & \gamma C_\gamma/L \\ k_\alpha C_{h_\alpha} & k_\alpha S_{h_\alpha} & k_\beta C_\beta & k_\beta S_\beta & k_\gamma C_\gamma & k_\gamma S_\gamma \end{bmatrix} \begin{bmatrix} A_1 \\ A_2 \\ A_3 \\ A_4 \\ A_5 \\ A_6 \end{bmatrix} \tag{1.28}$$

or

$$\mathbf{\Delta} = \mathbf{BA} \tag{1.29}$$

where **A** is the contact vector comprising the constants $A_1 - A_6$ and

$$C_{h\alpha} = \cosh\alpha \ ; \quad S_{h\alpha} = \sinh\alpha; \ C_\beta = \cos\beta; \ S_\beta = \sin\beta; \ C_\gamma = \cos\gamma; \ S_\gamma = \sin\gamma \tag{1.30}$$

Substituting the boundary conditions for forces given by Equation 1.27 into Equations 1.23, 1.24 and 1.25, one obtains the following matrix relationship

$$\begin{bmatrix} S_1 \\ M_1 \\ T_1 \\ S_2 \\ M_2 \\ T_2 \end{bmatrix} = \begin{bmatrix} 0 & W_3\alpha^3 & 0 & -W_3\beta^3 & 0 & -W_3\gamma^3 \\ -W_2\alpha^2 & 0 & W_2\beta^2 & 0 & W_2\gamma^2 & 0 \\ 0 & -W_1k_\alpha\alpha & 0 & -W_1k_\beta\beta & 0 & -W_1k_\gamma\gamma \\ -W_3\alpha^3S_{h_\alpha} & -W_3\alpha^3C_{h_\alpha} & -W_3\beta^3S_\beta & W_3\beta^3C_\beta & -W_3\gamma^3S_\gamma & W_3\gamma^3C_\gamma \\ W_2\alpha^2C_{h_\alpha} & W_2\alpha^2S_{h_\alpha} & -W_2\beta^2C_\beta & -W_2\beta^2S_\beta & -W_2\gamma^2C_\gamma & -W_2\gamma^2S_\gamma \\ W_1k_\alpha\alpha S_{h_\alpha} & W_1k_\alpha\alpha C_{h_\alpha} & -W_1k_\beta\beta S_\beta & W_1k_\beta\beta C_\beta & -W_1k_\gamma\gamma S_\gamma & W_1k_\gamma\gamma C_\gamma \end{bmatrix} \begin{bmatrix} A_1 \\ A_2 \\ A_3 \\ A_4 \\ A_5 \\ A_6 \end{bmatrix} \tag{1.31}$$

or

$$\mathbf{F} = \mathbf{DA} \tag{1.32}$$

where

$$W_1 = \frac{GJ}{L}; \quad W_2 = \frac{EI}{L^2}; \quad W_3 = \frac{EI}{L^3} \tag{1.33}$$

The constant vector **A** can now be eliminated from Equations 1.29 and 1.32 to give the following force-displacement relationship

$$\mathbf{F} = \mathbf{K\Delta} \tag{1.34}$$

where **K** is the 6 × 6 frequency dependent dynamic stiffness matrix given by

$$\mathbf{K} = \mathbf{DB}^{-1} \tag{1.35}$$

The dynamic stiffness matrix of Equation 1.35 representing a bending-torsion coupled beam such as an aircraft wing can now be used to model an aircraft wing. A non-uniform aircraft wing can be modelled as an assembly of many uniform dynamic stiffness elements. For instance, the unswept cantilever wing of Figure 1.4 can be modelled as a stepped cantilever beam (wing) as shown in Figure 1.5 where the non-uniform wing is split into 10 uniform dynamic stiffness elements. The dynamic stiffness elements of each of the 10 elements can be assembled to form the overall dynamic stiffness matrix of the complete wing. The illustrative wing and its idealisation are shown in Figures 1.4 and 1.5.

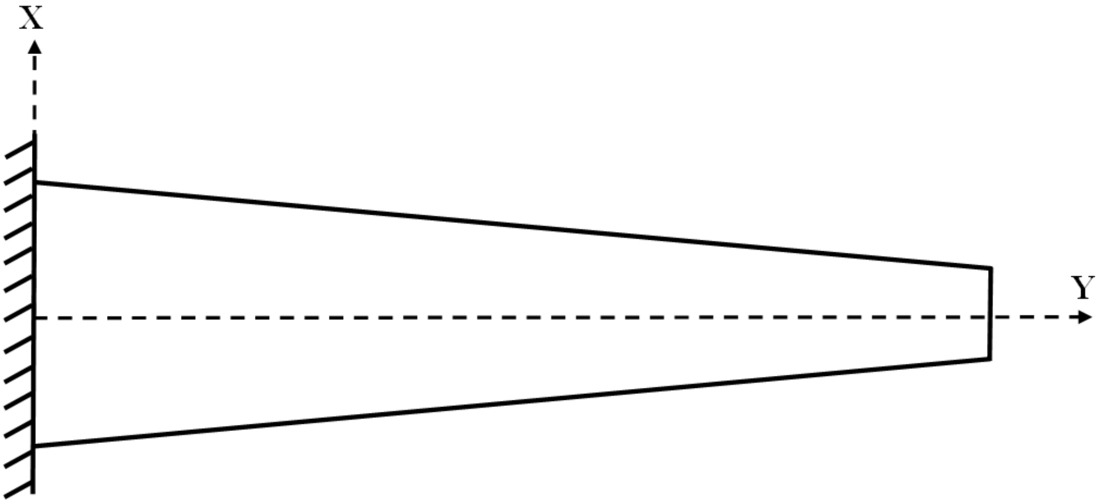

Figure 1.4: A representation of non-uniform cantilever wing.

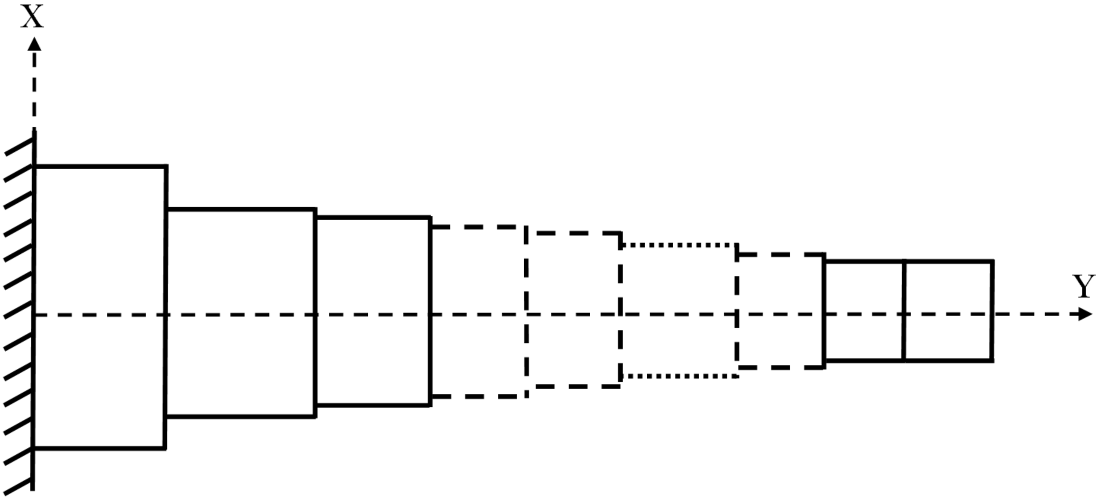

Figure 1.5: A non-uniform cantilever wing idealised as a stepped beam.

Note that the conventional mass [**M**] and stiffness [**K**] matrices that are traditionally used in the Finite element method [**FEM**] can be extracted from the dynamic stiffness matrix [$\mathbf{K_D}$] by using two small values of the frequency, say $\omega = 10^{-6}$ rad/s and $\omega = 10^{-5}$ rad/s and solving the two simultaneous equations given by $[\mathbf{K}] - \omega^2[\mathbf{M}] = [\mathbf{K_D}]$.
The solution procedure to extract the natural frequencies and mode shapes from the overall dynamic stiffness matrix of the wing is based on the application of the Wittrick-Williams algorithm [9]. The algorithm is particularly suitable in solving free vibration problem using the dynamic stiffness method. The working principle of the algorithm is briefly summarised in the next section.

1.2.4 Flutter analysis using generalised coordinates, normal modes and Theodorsen theory of unsteady aerodynamics

The normal mode method of flutter analysis is well known [3, 4], particularly in the context of high aspect ratio wings for which the computer program CALFUN [14, 15] is well suited and it also has the composite capability. CALFUN idealises the aircraft wing both structurally and aerodynamically. In the structural idealisation, bending-torsion couple beam theory (DSM method) is used to represent the wing [16, 17] whereas the aerodynamic idealisation includes strip theory based on Theodorsen type unsteady aerodynamics [1, 18]. The methodology is briefly summarised as follows [9].

1.2.4.1 Formulation of generalised mass, stiffness and aerodynamic matrices

The mass and stiffness matrices of the wing are first obtained from the overall dynamic stiffness matrix as explained underneath Equation 1.35 and then they are reduced to diagonal form to give generalised mass and stiffness matrices. This is achieved by using the normal modes obtained from dynamic stiffness method. The procedure is briefly explained as follows.

If $[\mathbf{\Phi}]$ is the modal matrix formed by selected normal mode shapes such that each column of $[\mathbf{\Phi}]$ represents a normal mode shape $\mathbf{\Phi_i}$, then the generalised mass and stiffness matrices are respectively obtained by post multiplying the mass and stiffness matrices by the modal matrix $[\mathbf{\Phi}]$, and premultiplying the resultant matrix by the transpose of the modal matrix (i.e $[\mathbf{\Phi}]^{\mathbf{T}}$). In matrix notation

$$[M_G] = [\varphi]^T [M] [\varphi] \tag{1.36}$$

$$[K_G] = [\varphi]^T [K] [\varphi] \tag{1.37}$$

where $[\mathbf{M_G}]$ and $[\mathbf{K_G}]$ are respectively, the generalised mass and stiffness matrices of the wing. Clearly if the number of modes chosen in the analysis is n, the order of $[\mathbf{M_G}]$ and $[\mathbf{K_G}]$ will each be n × n.

1.2.4.2 Formulation of generalised aerodynamic matrix

The generalised aerodynamic matrix is formed by applying the principle of virtual work. The aerodynamic strip theory is based on Theodorsen expression for unsteady lift and moment [1, 18] and the normal modes obtained from the dynamic stiffness method [16, 17] are used when applying the principle of virtual work. The displacements considered are the vertical deflection (bending) $h(y)$, and the pitching rotation (torsion) $\alpha(y)$ of the elastic axis of the wing at a spanwise distance y from the root. Thus the displacement components of the i^{th} mode $\mathbf{\Phi_i}$ are respectively, $h_i(y)$ and $\alpha_i(y)$. If $q_i(t)$ (1=1,2,3....n) are the generalised coordinates, $h(y)$ and $\alpha(y)$ can be expressed as

$$\mathrm{h}\,(\mathrm{y}) = \sum_{\mathrm{i}=1}^{\mathrm{n}} \mathrm{h_i}\,(\mathrm{y})\,\mathrm{q_i}\,(\mathrm{t}) \tag{1.38}$$

$$\alpha\,(\mathrm{y}) = \sum_{\mathrm{i}=1}^{\mathrm{n}} \alpha_{\mathrm{i}}\,(\mathrm{y})\,\mathrm{q_i}\,(\mathrm{t}) \tag{1.39}$$

The equation above i.e., $h(y)$, Equation 1.38 and $\alpha(y)$, Equation 1.39 can be written in matrix form as

$$\begin{bmatrix} h\,(y) \\ \alpha\,(y) \end{bmatrix} = \begin{bmatrix} \mathrm{h_1}\,(\mathrm{y}) & \mathrm{h_2}\,(\mathrm{y}) & \cdots\cdots\cdots & \mathrm{h_n}\,(\mathrm{y}) \\ \alpha_1\,(\mathrm{y}) & \alpha_2\,(\mathrm{y}) & \cdots\cdots\cdots & \alpha_{\mathrm{n}}\,(\mathrm{y}) \end{bmatrix} \begin{bmatrix} q_1 \\ q_2 \end{bmatrix} \tag{1.40}$$

If $L(y)$ and $M(y)$ are respectively the unsteady lift and moment at a spanwise distance y from the root, the virtual work done ($\delta\mathbf{W}$) by the aerodynamic forces is given by

$$\delta\mathrm{W} = \sum_{\mathrm{i}=1}^{\mathrm{n}} \delta\mathrm{q_i} \int_0^{\mathrm{s}} \mathrm{L}\,(\mathrm{y})\,\mathrm{h_i}\,(\mathrm{y}) + \mathrm{M}\,(\mathrm{y})\,\alpha_{\mathrm{i}}\,(\mathrm{y})\ \mathrm{dy} \tag{1.41}$$

where s is the semi-span of the wing and n is the number of normal modes considered in the analysis.

Equation 1.41 can be written in matrix form as

$$\begin{bmatrix} \frac{\delta W_1}{\delta q_1} \\ \frac{\delta W_2}{\delta q_2} \\ \vdots \\ \vdots \\ \frac{\delta W_n}{\delta q_n} \end{bmatrix} = \int_0^s \begin{bmatrix} h_1 & \alpha_1 \\ h_2 & \alpha_2 \\ \vdots & \vdots \\ \vdots & \vdots \\ h_n & \alpha_n \end{bmatrix} \begin{bmatrix} L\,(y) \\ M\,(y) \end{bmatrix} \tag{1.42}$$

The unsteady lift $L(y)$ and moment $M(y)$ in two dimensional flow given by Theodorsen [1, 18] can be expressed as

$$\begin{bmatrix} L\,(y) \\ M\,(y) \end{bmatrix} = \begin{bmatrix} A_{11} & A_{12} \\ A_{21} & A_{22} \end{bmatrix} \begin{bmatrix} h\,(y) \\ \alpha\,(y) \end{bmatrix} \tag{1.43}$$

where

$$\begin{aligned} A_{11} &= -\pi\rho U^2 \left\{-k^2 + 2C\,(k)\,iK\right\} \\ A_{12} &= -\pi\rho U^2 b \left[\left(a_h k^2 + ik\right) + 2C\,(k) \left\{1 + ik\left(\frac{1}{2} - a_h\right)\right\}\right] \\ A_{21} &= -\pi\rho U^2 b \left\{2C\,(k)\,ik\left(\frac{1}{2} + a_h\right) - K^2 a_h\right\} \\ A_{22} &= -\pi\rho U^2 b \left\{2\left(\frac{1}{2} + a_h\right) C\,(k) \left\{1 + ik\left(\frac{1}{2} - a_h\right)\right\} + \frac{k^2}{8} + k^2 a_h^2 + \left(a_h - \frac{1}{2}\right) ik\right\} \end{aligned} \tag{1.44}$$

In the above equation, U, b, ρ, k, $C(k)$ and a_h are in the usual notation: the airspeed, semi-chord, density of air, reduced frequency parameter, Theodorsen function and elastic axis location from mid-chord, respectively.
On substituting Equation 1.43 into Equation 1.42 and then using Equation 1.40

$$\begin{bmatrix} \frac{\delta W_1}{\delta q_1} \\ \frac{\delta W_2}{\delta q_2} \\ \vdots \\ \vdots \\ \frac{\delta W_n}{\delta q_n} \end{bmatrix} = \int_0^s \begin{bmatrix} h_1 & \alpha_1 \\ h_2 & \alpha_2 \\ \vdots & \vdots \\ \vdots & \vdots \\ h_n & \alpha_n \end{bmatrix} \begin{bmatrix} A_{11} & A_{12} \\ A_{21} & A_{22} \end{bmatrix} \begin{bmatrix} \mathrm{h}_1 & \mathrm{h}_2 & \ldots & \mathrm{h}_\mathrm{n} \\ \alpha_1 & \alpha_2 & \ldots & \alpha_\mathrm{n} \end{bmatrix} \begin{bmatrix} q_1 \\ q_2 \\ \vdots \\ q_n \end{bmatrix} dy$$

$$= \begin{bmatrix} \mathrm{QF}_{11} & \mathrm{QF}_{12} & \ldots & \mathrm{QF}_{1\mathrm{n}} \\ \mathrm{QF}_{21} & \mathrm{QF}_{22} & \ldots & \mathrm{QF}_{2\mathrm{n}} \\ \ldots & \ldots & \ldots & \ldots \\ \mathrm{QF}_{\mathrm{n}1} & \mathrm{QF}_{\mathrm{n}2} & \ldots & \mathrm{QF}_{\mathrm{nn}} \end{bmatrix} \tag{1.45}$$

where [**QF**] is the generalised aerodynamics matrix with

$$\mathrm{QF}_{\mathrm{ij}} = \int_0^{\mathrm{s}} \left(\mathrm{A}_{11}\mathrm{h}_\mathrm{i}\mathrm{h}_\mathrm{j} + \mathrm{A}_{12}\mathrm{h}_\mathrm{j}\propto_\mathrm{i} + \mathrm{A}_{21}\mathrm{h}_\mathrm{i}\propto_\mathrm{j} + \mathrm{A}_{22}\propto_\mathrm{i}\propto_\mathrm{j} \right) \mathrm{dy} \tag{1.46}$$

The generalised aerodynamic matrix [**QF**] is usually a complex matrix with each element having a real part and an imaginary part. This is as a consequence of the term A11, A12, … etc in Equation 1.40 being complex (see Equation 1.38). In contrast, the generalised mass and stiffness matrices are both real (and diagonal matrices).

1.2.4.3 Formation and solution of the flutter determinant as a double Eigen-value problem

The flutter determinant is the determinant formed from the flutter matrix, and the flutter matrix is formed by algebraically summing the generalised mass, stiffness and aerodynamic matrices. Thus for a system without structural damping (structural damping has generally a small effect on the oscillatory motion and is not considered here) the flutter matrix [**QA**] can be formed as

$$[QA]\{q\} = \left[-\omega^2 [M_G] + [K_G] - [QF] \right] \{q\} \tag{1.47}$$

where ω is the circular frequency in rad/s of the oscillatory harmonic motion.
For flutter condition to occur, the determinant of the complex flutter matrix must be zero so that from Equation 1.47,

$$\left| -\omega^2 [M_G] + [K_G] - [QF] \right| = 0 \tag{1.48}$$

The solution of the above flutter determinant is a complex eigenvalue problem because the determinant is primarily a complex function of two unknown variables, the airspeed (**U**) and the frequency (ω). The method used in CALFUN [14, 15] selects an airspeed and evaluates the real and imaginary parts of flutter determinant for a range of airspeeds until both the real and imaginary part of the flutter determinant (and hence the whole flutter determinant) vanish completely.

1.2.4.4 Application of the aeroelastic package CALFUN

The program used for flutter analysis is based on CALFUN. CALFUN (Calculations of Flutter Speed Using Normal Modes) is a FORTRAN program which finds the flutter speed of high aspect ratio, slender wing aircraft with the option of finding flutter modes [14]. CALFUN uses normal modes and generalized coordinates as described in the previous sections to compute the flutter speed of a wing from its basic aerodynamic and structural data. It calculates the natural frequencies and normal modes of an aircraft wing and uses them to generate dynamic stiffness and aerodynamic matrices. It uses strip theory based on Theodorsen-type unsteady aerodynamics. In the data, the aircraft is idealised both structurally and aerodynamically. The structural idealisation includes beam and lumped mass representation of the aircraft while strip theory based on Theodorsen expressions for unsteady lift and moment are used on the aerodynamic idealisation. From the structural point of view, the aircraft is idealised as a collection of beam members joined together with the allowance for independent mass, inertia or spring stiffness at any particular node (joint). From the aerodynamic point of view, the program assumes the validity of strip theory and required in the data, the chord lengths and relative positions of the mass and shear centres at spanwise stations on the wing. It assumes that all aerodynamic forces and moments are generated entirely by the wings. However provisions have been made to include the body freedoms of the aircraft in calculating the flutter speed.

The use of generalised co-ordinates in flutter analysis is fundamental to the development of the program. Implementing this well-established method [3, 18, 19] the mass, stiffness and aerodynamic matrices of the aircraft are expressed in terms of the generalized coordinates. The finite element method is used to obtain the mass, stiffness matrix and the normal modes, whereas strip theory based on Theodorsen expressions for unsteady aerofoil motion is employed to form the aerodynamic matrix. The flutter matrix is formed by algebraically summing the generalized mass, stiffness, and aerodynamic matrices.

The solution for flutter determinant is a complex eigenvalue problem because the determinant is primarily a complex function of two unknown variables, the airspeed and the frequency. The method used is to select an airspeed and evaluate the real and imaginary parts of the flutter determinant for a range of frequencies. The process is repeated for a range of airspeeds until both the real and imaginary part of the flutter determinant vanish

completely [14]. Once the flutter speed and frequency are established the corresponding vector i.e., flutter mode is found in the classical way by deleting one row of say, the n-th order determinant and solving for (n-1) of the co-ordinate in terms of the n-th.
Also, strip theory is revalidated as an aerodynamic tool for flutter analysis of high aspect ratio wings at low speeds. The investigation has shown that the bottom limit of the aspect ratio for good flutter prediction is about 6. However, on occasions with suitable combination of other parameters, this limit can be lowered to as low as 4 and an acceptable engineering accuracy can still be achieved. Care must be exercised when considering taper and sweep effects particularly for wings at the lower end of the aspect ratio. If the air speed predicted by CALFUN required for flutter is supersonic, the strip theory aerodynamics employed by CALFUN are no longer valid. CALFUN is accurate at predicting flutter at subsonic airspeeds.

1.3 Conclusions

In this chapter the discussion has been carried in detail about flutter, steps to be followed to formulate the dynamic stiffness matrix, the methods involved in the development of dynamic stiffness method for an aircraft wing idealised as a bending-torsion coupled beam, the procedure behind Wittrick-Williams algorithm, the formulation involved in the development of free vibration and flutter analysis and the theories resulted in the development of programs particularly CALFUN which were used in Section A.

Chapter 2

Metallic and composite wing boxes

2.1 Introduction to metallic and composite structures used in aircraft design

In the past, aluminium alloys were mainly used in the design of aircraft wings but nowadays with modern technological developments in material science, aircraft wings are increasingly being made up of composites. There are various aircraft both military and transport that are made up of composites. For instance the Boing787 and Airbus350 are predominantly made up of composite materials. If composites are used as an alternative for metal say aluminium then their usage must be carefully examined so that there are no adverse aeroelastic phenomena to prevent the realisation of the benefits of using composites. For aircraft whose wings are made up of composite standard formulae will not be used when carrying out stiffness analysis.

Estimation of stiffness properties for metallic wings is well established and there are standard texts available [20–22] which provide details to compute the bending and torsional stiffness of single cell and multi-cell wings. However for laminated composite wings, the estimation of stiffness properties is quite difficult, mainly due to the anisotropic nature of fibrous composites. It should be noted, the coupling between bending and torsional deformation arises due to the non-coincident centroid and shear center of the wing cross-sections or in other words it is due to the separation of mass axis and elastic axis of the wing. In this respect for a metallic wing, the coupling is essentially inertial in nature and can be termed as geometrical because the centroid and shear center for a metallic wing cross section are properties of the geometry of the cross-section. By contrast, for a composite wing, there is an additional coupling term which arises due to the material properties and ply orientation which causes material coupling in addition to the geometric coupling mentioned above [23]. Researchers have expended considerable efforts in modelling composite wings [24–26]. In this thesis, the procedure used by Armonios and

Badir [27, 28] has been adopted to compute the bending, torsional and bending-torsional coupling stiffness properties of composite wings.

Composite materials have properties such as low weight, high specific strength(i.e., strength to weight ratio is exceptionally high), corrosion-free and high durability which leads to lower fuel consumption (due to low weight), longer lifespan of aircraft and maintenance costs reduction. Composites are also used for their anisotropic properties which is responsible for the manipulation of structural response. Because of anisotropic properties, out-of-plane warping and shear deformation significantly influence the response of composite structures. Composites have in general two constituents– the fibre and the raisin. There are various kinds of composites such as carbon fibre reinforced plastic (CFRP), glass fibre (heavy but not much strong) and boron fibre (expensive), etc. The fibre orientation in composites can be controlled based on the desirable properties which results in various modes of deformation. Laminated composites are made by stacking plies of different ply orientation and the plies are arranged sequentially from bottom to top in this thesis. Ply Orientation of composites plays major role in varying the material properties, they can be classified as specially orthotropic ply (zero ply orientation) and generally orthotropic ply (angled ply orientation).

As discussed in the previous chapter, stiffness matrices and mass matrices are generally required to perform free vibration and flutter analysis. Estimating the mass of an aircraft is relatively simple and easier than determining its stiffness properties. Hence this chapter is focused on performing stiffness analysis. Stiffness analysis for composite wings has been performed by using both single cell and double cell theories. Stiffness analysis for metallic wing can be performed by using standard techniques. The FORTRAN programs developed for composite wing stiffness analysis are called BOXMXES and BOXMXESDC for analysing single cell and double cell wing boxes, respectively. Once stiffness analysis is carried out then free vibrational analysis and flutter analysis can be carried out for both metallic and composite wings using CALFUN which has versions CALFUNB and COMPCAL to analyse metallic and composite wings, respectively. For metallic wings the bending torsion material coupling stiffness (K) is zero and hence CALFUNB is used. However, for composite wings, the bending torsion material coupling stiffness K is an important parameter which must be taken into account in the modal and subsequent flutter analysis. To this end, the COMPCAL version of CALFUN is used. It should be noted that if COMPCAL is applied to analyse a metallic wing, a small value of (K), not zero but typically of the order of 10^{-6} must be used to avoid numerical ill-conditioning and/or numerical overflow or underflow. In this Chapter, attention is confined to wing only analysis so that the built-in boundary condition at the root of the wing is strictly adhered to. (Chapter 5 deals with the whole aircraft configuration wherein the complete aircraft including wing, fuselage, tailplane, fin and rudder is idealised using stick model and thus allowing for the rigid body motions to take place.)

2.1.1 Single and double cell wing box modelling

This chapter is principally concerned with the stiffness estimation of single and double cell composite wing boxes, but some results have also been given for metallic wing boxes for comparison. Clearly, composite wing modelling poses more challenges than that of the metallic one because of the complexities arise in the former due to the anisotropic nature of fibrous composites. Thus, advanced methodologies are required to deal with composite wing box modelling as explained in the subsequent sections. The relative simple case of the single cell wing box modelling is treated first before proceeding to more complex double cell wing box modelling. In particular, the bending (EI), torsional (GJ) and bending-torsional coupling (K) stiffnesses are derived for a composite wing box and numerical results are given together with some comparative results of metallic wing boxes wherever applicable. Also, the following assumptions are made in the thin-walled section theory

(i) Shear stresses normal to the skin surface are neglected,

(ii) Normal stress and shear stresses are constant across the thickness of the cross section,

(iii) The cross section is uniform along the length so that the thickness remains constant along the length direction but it may vary from point to point round the cross-section,

(iv) The three dimensional effect is not taken into account.

2.1.1.1 Theory for modelling a single cell composite wing box

The theoretical development given in this section is based on the paper published by Armanios and Badir [27]. Some salient features of the theory are reproduced here in order to make the thesis self-contained and also to lead the reader smoothly to later Chapters. Consider the slender thin–walled elastic cylindrical shell shown in the Figure 2.1. The length of the shell is denoted by L, its thickness by h, the radius of curvature of the middle surface by R, and d represents a characteristic cross-sectional dimension.

It is assumed that

$$d << L, h << d \ \ and \ \ h << R \tag{2.1}$$

It is also assumed that the variation of the material properties over distances in the axial direction is small. The material is anisotropic hence the properties vary both circumferentially and also in the direction normal to the middle surface.

The shell thickness varies along the circumferential direction. Equations y = y(s) and z = z(s) define the closed contour in the y, z plane associated with the Cartesian coordinate system x, y and z. The circumferential coordinate s is measured along the tangent to the

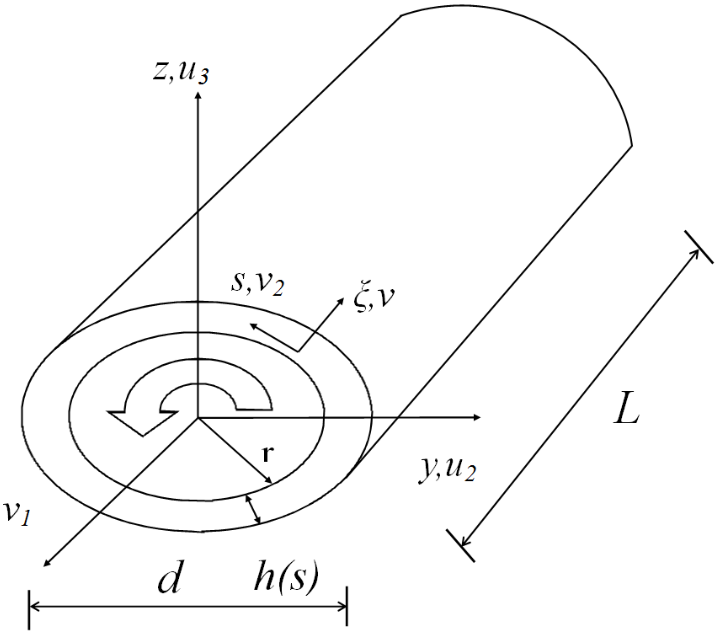

Figure 2.1: Coordinate systems and kinematic variables for a cylindrical shell.

middle surface in a counter clockwise direction.
The displacement field is defined as

$$u_1\,(x,s) = U_1(x) - y(s)U'_2(x) - z(s)U'_3(x) + g(s,x), \tag{2.2}$$

$$u_2(x,s) = U_2(x) - z(s)\varphi(x), \tag{2.3}$$

$$u_3(x,s) = U_3(x) + y(s)\varphi(x) \tag{2.4}$$

where $U_i(x)$ (i=1,2,3) represents average displacements along the coordinates and φ is the twist angle. The function g(s,x) added to the classical displacement field of extension, torsion and bending represents the out of plane warping of the cross section and is determined from continuity of the displacement field.
The relationship between shear flow N_{12} and strain γ_{12} is given as

$$\frac{\partial g}{\partial s} + \frac{2B(s)}{C(s)} g'(x,s) = -r_n(s)\varphi' - \frac{2B(s)}{C(s)}\left[U'_1 - y(s)U''_2 - z(s)U'''_3\right] + \frac{4N_{12}}{C(s)} \tag{2.5}$$

where r_n is the projection of the position vector r in the normal direction.
For a thin walled slender beam whose dimensions satisfies $d << L,\ h << d\ and\ h << R$, the rate of change of the displacement along the axial direction is much smaller than its rate of change along the circumferential direction. The coefficient of g' represents the ratio of in-plane extension shear coupling stiffness B(s) to the shear stiffness C(s).
The shear flow N_{12} is determined from the condition that the warping function g(s,x) should be a single valued continuous function, i.e.,

$$\overline{\left(\frac{\partial g}{\partial s}\right)} = \frac{1}{l}\oint \frac{\partial g}{\partial s} ds = 0 \tag{2.6}$$

On integrating Equation 2.5 and substituting in Equation 2.6, warping function is obtained as follows

$$g(s,x) = G(s)\varphi'(x) + g_1(s)U'{}_1(s) + g_2(s)U''{}_2(s) + g_3(s)U''{}_3(s) \tag{2.7}$$

The first term in the Equation 2.6 is similar to classical torsional related warping, whereas the remaining three terms represent the out of plane warping due to uniform axial extension ($g_1(s)U'{}_1(x)$), due to bending about the z axis ($g_2(s)U''{}_2(x)$) and due to bending about the y axis ($g_3(s)U'''{}_3(x)$). These three terms are significantly influenced by the material anisotropy and cross–sectional geometry. They vanish for materials that are either orthotropic or whose properties are anti-symmetric relative to the shell middle surface.
If the beam has a box cross section, the coupling stiffness in the opposite member is of opposite sign. For a cantilevered beam (an aircraft wing) of length L, the characteristic equation can be expressed as a cubic equation

$$\alpha y^3 + \beta y^2 + \gamma y + \delta = 0 \tag{2.8}$$

where
$y = \lambda^2$, $\alpha = \left(C_{22}C_{33} - {C_{23}}^2\right)$, $\beta = C_{33}I\omega^2$, $\gamma = -C_{22}\omega^2 m_c$ and $\delta = -\omega^4 I m_c$
λ represents the space domain eigenvalue.
If T, M_x, M_y, and M_z are the axial force, twisting moment, bending moment about the y and z axes, respectively, then they are related to kinematic variables by

$$\begin{Bmatrix} T \\ M_x \\ M_y \\ M_z \end{Bmatrix} = \begin{bmatrix} C_{11} & C_{12} & C_{13} & C_{14} \\ C_{12} & C_{22} & C_{23} & C_{24} \\ C_{13} & C_{23} & C_{33} & C_{34} \\ C_{14} & C_{24} & C_{34} & C_{44} \end{bmatrix} \begin{Bmatrix} {U_1}' \\ \varphi' \\ {U_3}'' \\ {U_2}'' \end{Bmatrix} \tag{2.9}$$

When analysis is carried out for an aircraft wing, generally in order to determine stiffness analysis, wing can be split into single cell and double cell for composite wing.
Wing is split along spanwise direction as shown in Figure 2.2 and each part is considered as a rectangular box, such that each rectangular box is considered as single cell. Generally wing regions from tip to kink is considered as single cell members. In this case, for single cell member the distance between front spar and rear spar is considered (front spar is usually located at 15% of chord and rear spar is located at 65% of chord.)

To analyse, a composite box having four laminate parts is used with first laminate having all positive plies, second laminate having two positive and two negative plies while the third and fourth laminate have mirror plies and a total of four plies are used in each laminate for single cell analysis. At each of these sections the ply orientation of composite is generally varied between 0 to 90 degrees and for each of these ply angle the bending (EI), torsional (GJ) and coupling (K) stiffnesses are computed.

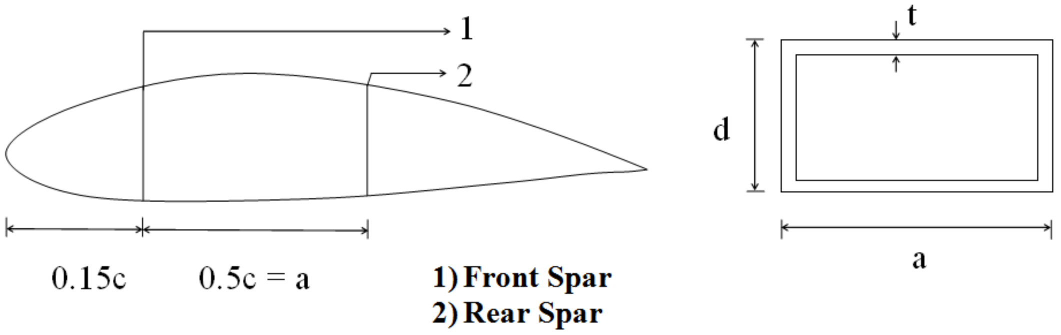

Figure 2.2: Representation of single cell member from an aerofoil.

Some details of the composite wing for which the stiffness properties *EI*, *GJ* and *K* are computed along the span are given in Table 2.1. The wing is assumed to have a sweep angle of 25 degrees, thickness to chord ratio 0.15 and taper ratio 0.25. It is a reasonable assumption that the stiffness contributions come mainly from the torsion box confined between the location of front and rear spars as shown in Figure 2.2.

Table 2.1: General characteristics of aircraft data.

Description	Value
Right side wing span, s (m)	15
Root chord, C_r (m)	6
Root depth, d_r (m)	0.9
Root thickness, t_r (m)	0.01
Composite density (kg/m^3)	2720

During the idealisation, the wing was split into 5 segments of equal parts as shown in Figure 2.3, thus we obtained a total of 6 sections. Root chord is assumed to be of 6m length which gives the tip chord of wing to be 1.5m.

Then each part is considered as a rectangular box (distance between front spar and rear spar, front spar is usually located at 15% of chord and rear spar is located at 65% of chord) and its corresponding dimensions such as length, breadth, thickness, area, second moment of area are calculated using the formulae.

$$c\,(y) = c_r\left(1 - 0.75 \times \left(\frac{y}{s}\right)\right) \tag{2.10}$$

$$t\,(y) = t_r\left(1 - 0.75 \times \left(\frac{y}{s}\right)\right) \tag{2.11}$$

$$d\,(y) = d_r\left(1 - 0.75 \times \left(\frac{y}{s}\right)\right) \tag{2.12}$$

$$A = 2 \times (a + d)\,t \tag{2.13}$$

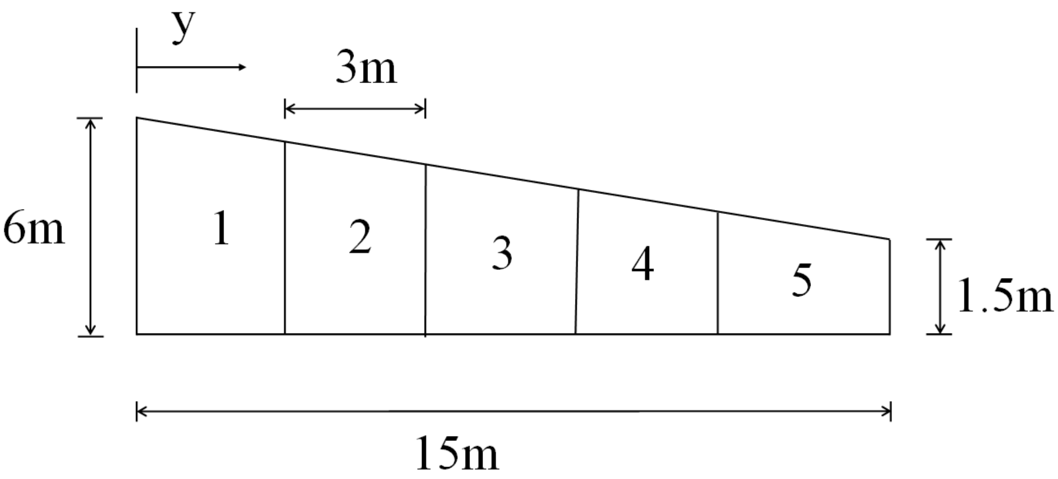

Figure 2.3: Idealisation of wing into five equal parts.

$$I = \left(2 \times \frac{td^3}{12}\right) + \left(2at \times \left(\frac{d}{2}\right)^2\right) \tag{2.14}$$

where *c(y)*, *d(y)* and *t(y)* are chord, depth and thickness at a distance of y respectively, where y is the wing span distance from each section.

2.1.1.2 Theory for modelling a double cell composite wing box

The significant difference between single cell and double cell is in the analysis of torsion which is a statically indeterminate problem. Also the influence of the material's anisotropy on the displacement is too complex to use kinematic assumption similar to classical theory of bending and torsion which was used in single cell analysis. In this analysis the displacement field emerges naturally as a result of the asymptotical analysis of the shell energy. Following the work of Badir [28]
It is assumed that

$$d << L, h << d \;\; and \;\; h << R \tag{2.15}$$

For an applied external loading P_i, the displacement field u_i, determining the deformed state is the stationary point of the energy functional,

$$I = \iint \phi dxds - \iint p_i u_i dxds \tag{2.16}$$

The displacement function corresponding to the zeroth-order approximation is obtained first by minimizing the energy functional while keeping the leading order terms in Equation 2.16 on the basis of inequalities of the assumption used.

The displacement field converges to the following equations

$$\begin{aligned} v_1 &= U_1(x) - y(s)U'_2(x) - z(s)U'_3(x) + G(s)\,\varphi'(x) \\ &+g_1(s)\;U'_1(x) + g_2(s)\,U''_2(x) + g_3(s)\,U'''_3(x) \end{aligned} \tag{2.17}$$

$$v_2 = U_2(x)\frac{dy}{ds} + U_3(x)\frac{dz}{ds} + \varphi(x)r_n, \tag{2.18}$$

$$v = U_2(x)\frac{dz}{ds} - U_3(x)\frac{dy}{ds} - \varphi(x)r_t \tag{2.19}$$

The variables $U_1(x)$, $U_2(x)$ and $U_3(x)$ represent the average cross-sectional translations while $\varphi(x)$ the cross-sectional rotation which is normally referred in beam theory as the torsional rotation. The expressions for the displacements v_2, v and the first 4 terms in v_1 (Equation 2.17) are analogous to the classical theory of extension, bending and torsion of beams and the additional terms represent warping due to axial strain and bending. They are strongly influenced by material's anisotropy, stacking sequence and the cross sectional geometry.

The axial stress resultant N_{11} and the shear flow N_{12} are derived from the energy density and are given by

$$N_{11} = \frac{\partial\phi_1}{\partial\gamma_{11}} = A(s)\,\gamma_{11} + B(s)\,\gamma_{12} \tag{2.20}$$

$$N_{12} = \frac{\partial\phi_1}{\partial(2\gamma_{12})} = \frac{1}{2}\left[B(s)\,\gamma_{11} + C(s)\,\gamma_{12}\right] = constant \tag{2.21}$$

The constitutive relationships can be written in terms of stress resultants and kinematic variables by relating the traction T, torsional moment M_x and bending moments M_y and M_z to the shear flow and axial stress. The result is given as

$$\begin{Bmatrix} T \\ M_x \\ M_y \\ M_z \end{Bmatrix} = \begin{bmatrix} K_{11} & K_{12} & K_{13} & K_{14} \\ K_{12} & K_{22} & K_{23} & K_{24} \\ K_{13} & K_{23} & K_{33} & K_{34} \\ K_{14} & K_{24} & K_{34} & K_{44} \end{bmatrix} \begin{Bmatrix} U_1' \\ \varphi' \\ U_3'' \\ U_2'' \end{Bmatrix} \tag{2.22}$$

For double cell analysis an aerofoil section is considered. Generally an aircraft wing has two spars, first is located at around 15% of chord and the last spar at around 65% of chord. Two cell box analyses are used in those sections. For the initial box distance between 5% of chord and the front spar (15% of chord) is taken and for the second cell distance between front spar and rear spar (65% of chord) are assumed as shown in the Figure 2.4. For spanwise distribution of the stiffnesses *EI*, *GJ* and *K*, the methodology used for single cell and depicted by the schematic diagram in Figure 2.3 is used for the double cell analysis when averaging the properties between two subsequent sections.

To analyse, a composite box having 7 laminate parts is used. At each of these laminates the ply orientation of composite is generally varied between 0 to 90 degrees and for each

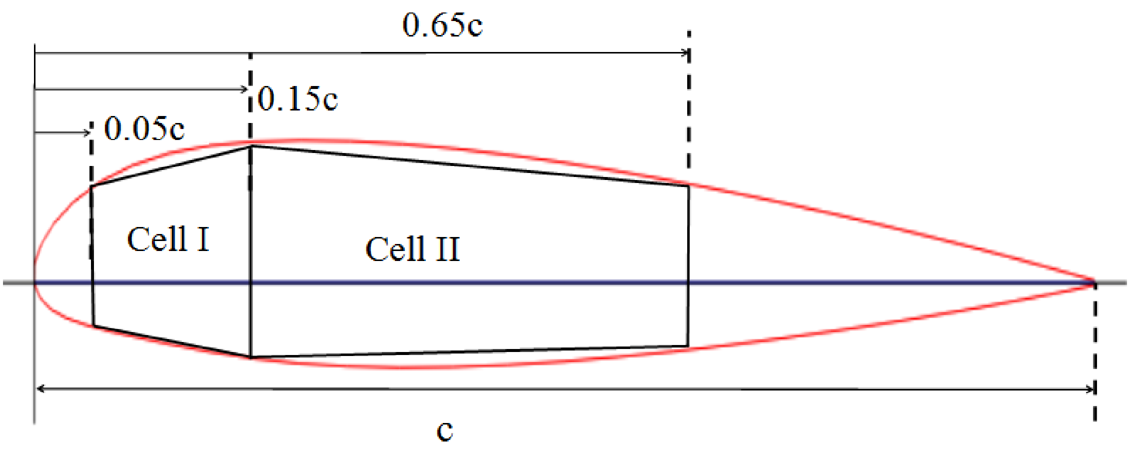

Figure 2.4: Representation of double cell member in an aerofoil.

of these ply angle, the bending (EI), torsional (GJ) and coupling (K) stiffnesses are found. The composite wing laminate is made up of 8 plies, each ply is having a thickness of with 0.125 cm at the root. The wing thickness will vary from root to tip linearly similar to single cell analysis and the double cell box has been split into 7 nodes as shown in Figure 2.5. Several cases have been considered, all having a ply orientation varying from 5 to 90 degrees with an increment of 5 degrees. Among them the following case is found to be the most suitable one to produce desired aeroelastic effect based on its stiffness properties. For the selected case, 3^{rd}, 4^{th}, 5^{th} and 7^{th} laminates have negative ply orientation while the rest of the laminates have positive ply orientations. The elastic constraints used for the composite material are that of carbon-fibre reinforced plastics (CFRP) and are given in Table 2.2.

Table 2.2: Material properties of composite layup.

E_1 (N/m^2)	E_2 (N/m^2)	Poisson's Ratio (ν_{12})	$G_{12} = G_{13} = G_{23}$ (N/m^2)	Density, ρ (kg/m^3)
0.14E12	0.95E10	0.28	0.58E10	1562

Initially wing is split into 6 sections which are of varying thickness similar to that of a single cell analysis. Using an aerofoil, 6 aerofoil shapes at those 6 sections are determined. The coordinates for these aerofoil sections at each of the nodes are calculated using AutoCAD. For these 6 sections, coordinates at 5%, 15% and 65% for lower aerofoil surface and upper aerofoil surface are calculated by having origin from the nose of the aerofoil. Then the origin is moved to the middle of 7^{th} laminate (between nodes 1 and 4), then based on the new centre coordinates the position of the other 6 nodes are calculated. Thus the coordinates at various laminates are calculated for the wing span of 15 m, then stiffness analysis is carried out.

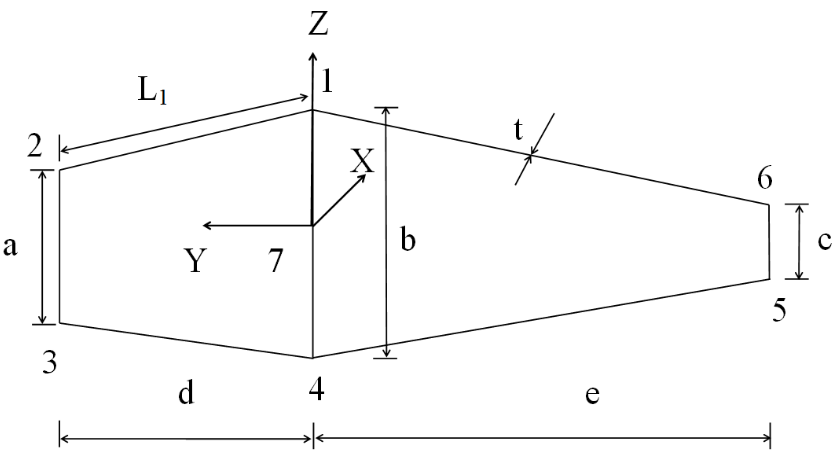

Figure 2.5: Notations used for nodes in double cell member.

Since the thickness is small, thin walled assumptions are used in the analysis and the following formulae is used to generate the results.
Area,

$$Area = t \times \{(a+b+c)+l_1+d+2e\} \tag{2.23}$$

Mass,

$$mass = area \times density = A \times \rho \tag{2.24}$$

Moment of inertia about x- axis,

$$I_{xx} = t \times \left\{ \frac{a^3+b^3+c^3}{12} + 2\left[\left(e \times \left[c+\left(\frac{b-c}{2}\right)\right]^2\right) + \left(d \times \left[a+\left(\frac{b-a}{2}\right)\right]^2\right)\right]\right\} \tag{2.25}$$

Moment of inertia about y- axis,

$$I_{yy} = t \times \left[ad^2+ce^2+\left(\frac{e^3}{1.5}\right)+\left(\frac{d^3+{l_1}^3}{3}\right)\right] \tag{2.26}$$

Moment of Inertia,

$$I = I_{xx} + I_{yy} \tag{2.27}$$

$$I_{alpha}, I_{\alpha} = I \times \rho \tag{2.28}$$

2.1.1.3 Stiffness distribution of metallic wing

For aluminium, the stiffness properties such as the bending (EI) and torsional (GJ) stiffnesses are calculated using the following formulae

$$G = \frac{E}{2.6} \tag{2.29}$$

$$J = \frac{4s^2}{\oint \frac{ds}{t}} = \frac{4{b_{av}}^2{d_{av}}^2 t}{2\left(b_{av}+d_{av}\right)} \tag{2.30}$$

$$I = I_{outer} - I_{Inner} = \frac{\left(\left(b_{outer} {d_{outer}}^3\right) - \left(b_{inner} {d_{inner}}^3\right)\right)}{12} \tag{2.31}$$

$$I_{av} = \frac{b_{av} {d_{av}}^3}{12} \tag{2.32}$$

2.1.2 A precursor to free vibration and flutter analysis of metallic and composite wings

In order to obtain sufficient accuracy of the results for the natural frequency and mode shapes, the idealisation shown in Figure 2.3 for stiffness evaluation was further improved and the wing was split into 10 elements in the spanwise direction as shown in Figure 2.6. (Initially by taking average of 6 sections a total of 11 sections are determined, then on averaging those 11 sections a total of 21 sections are found), the newly found 10 sections are used in the analysis for simplicity and their corresponding stiffness properties such as bending (EI), torsional (GJ) and coupling (K) stiffnesses are calculated as mentioned before.

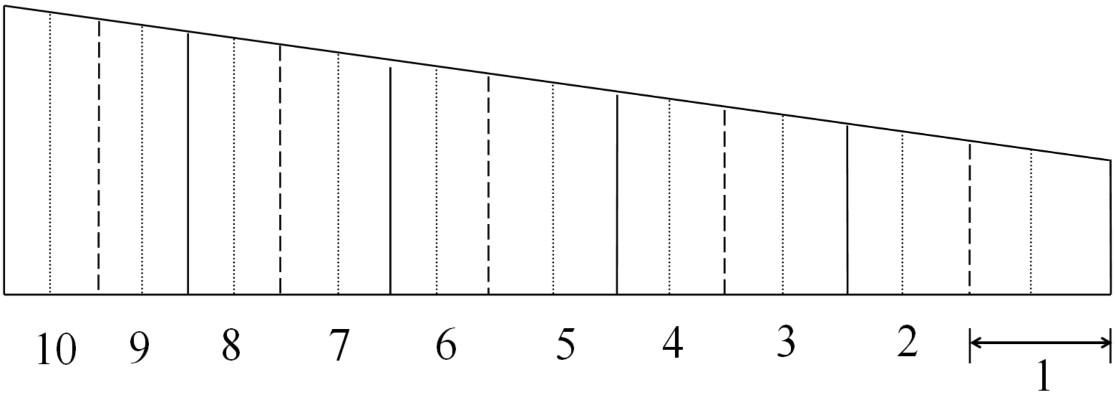

Figure 2.6: A representation of sections obtained for vibrational analysis from an wing.

The flutter behaviour of composite wings can be very different from their metallic counterparts. The analysis for composite wing is significantly influenced by the ply orientation in the laminate. It should be also noted that sweep angle also plays an important role in flutter analysis for both metallic and composite wings. The wing is idealized as a series of composite beams whose bending (EI), torsional (GJ) and coupling (K) stiffnesses have already been established. Using these stiffness properties the natural frequencies and mode shapes of the cantilever wing built-in at the root are computed by applying the method of the dynamic stiffness matrix. First, the free vibrational analysis is carried out for laminated composite wing of rectangular box cross sections with single cell representation having unidirectional ply orientation (θ) for each of the four laminates comprising the wing box. However, for double cell representation which comprises seven laminates, the ply orientations for each of the laminates were different as shown in Table **??**. When obtaining the results, the ply orientations were varied from 5 to 90 degrees in steps of 5 degrees. For presentational purposes and also to avoid the clumsiness of the figures, it was adjudged necessary to show the results for 10 degrees interval of ply orientations.

2.1.3 Selective results and discussions

2.1.3.1 Results using single cell idealisation

Figures 2.7 and 2.8 illustrates the bending (EI) and torsional (GJ) stiffnesses along wing spanwise direction, respectively for various ply orientations when using the single cell theory for the wing described in the previous section. Stiffness distribution for an aluminium wing of same dimensions is also shown in the Figures 2.7 and 2.8 so that a direct comparison of stiffnesses are possible. From Figure 2.7, it can be ascertained that the composite wing has higher bending stiffness than the aluminium one when the ply angle orientation is below 20 degrees. This is to be expected because the effective Young's modulus will be at its maximum at 0 degree or nearer to 0 degree ply orientations, particularly for the wing box configuration under consideration. Clearly, the Figure 2.7 reveals that for ply orientations above 25 degrees aluminium has better bending stiffness properties. This is obvious because with increasing angle of ply orientation, the Young's modulus in the matrix direction which is generally small comes more and more into play in the bending stiffness (EI) formulation. It should be noted that as ply orientation is increased the bending stiffness decreases gradually as expected. From Figure 2.8, it can be seen that aluminium wing always has higher torsional stiffness than the composite wing. This is also to be expected because the torsion constant J, for a closed section such as the rectangular box will have higher values for the aluminium than the composites. Figure 2.9 which is relevant only to composite wing as its shows the variation of the bending-torsional material coupling parameter, K (which is non-existent in isotropic materials such as aluminium) along the span. It is significant to note that the parameter K can be manipulated to advantage in wings of composite construction which, of course, is impossible in aluminium wings. It is observed in Figure 2.9 that the values of K around 15 and 25 degrees of ply orientation provide the maximum material coupling effect. Based on this two angles of ply orientations, bending (EI), torsion (GJ) and the bending-torsion material coupling (K) stiffnesses are plotted in Figure 2.10. In the next stage of the investigation, the free vibration behaviour of the composite wing is studied in detail for different ply orientations.

Table 2.3 shows the first five natural frequencies computed by varying the ply orientation between 5 and 90 degrees in steps of 5 degrees. The bending, torsion and coupled modes are designated by the letters **B**, **T** and **C** respectively. From Table 2.3, it can be observed

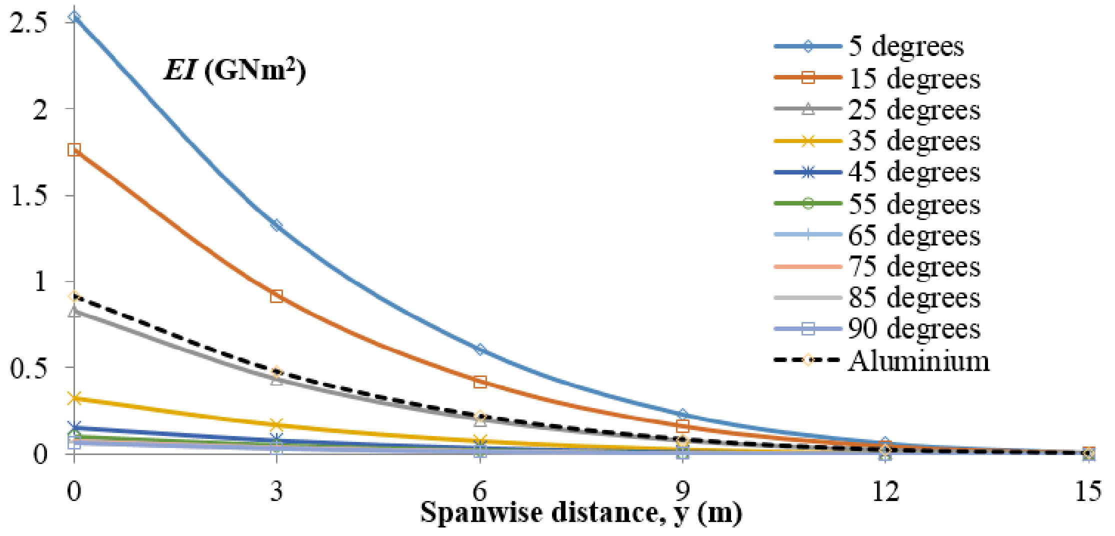

Figure 2.7: Comparison of bending stiffnesses along span wise distribution.

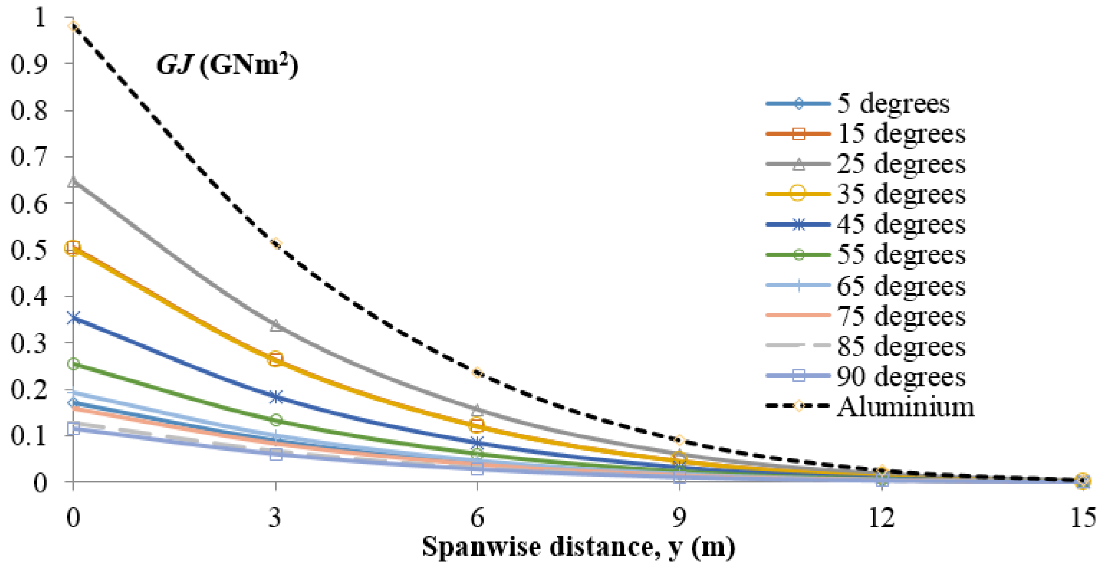

Figure 2.8: Comparison of torsional stiffnesses along span wise distribution.

that the natural frequencies in general decrease with increasing ply angles. An interesting and intriguing features of the results indicate the modal interchanges or flip-overs are possible in composite wings of the same mass and the geometry of constructions. This is certainly not possible for wings with metallic constructions. It can also be noted in Table 2.3, that the fundamental node is always a bending one, whereas the second and third mode can be changed from couple to bending or from torsion to coupled or from coupled to bending depending on the ply orientation. However, the fifth mode is basically a torsional mode for almost all ply orientation.

Figure 2.11 illustrates representative mode shapes corresponding to ply orientations of

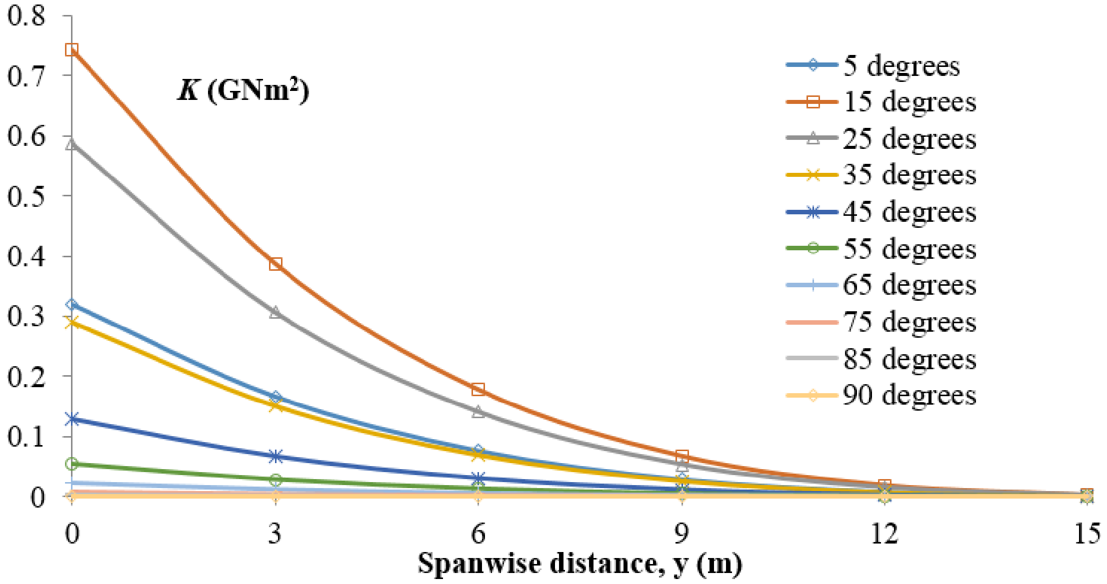

Figure 2.9: Comparison of coupling stiffnesses along span wise distribution.

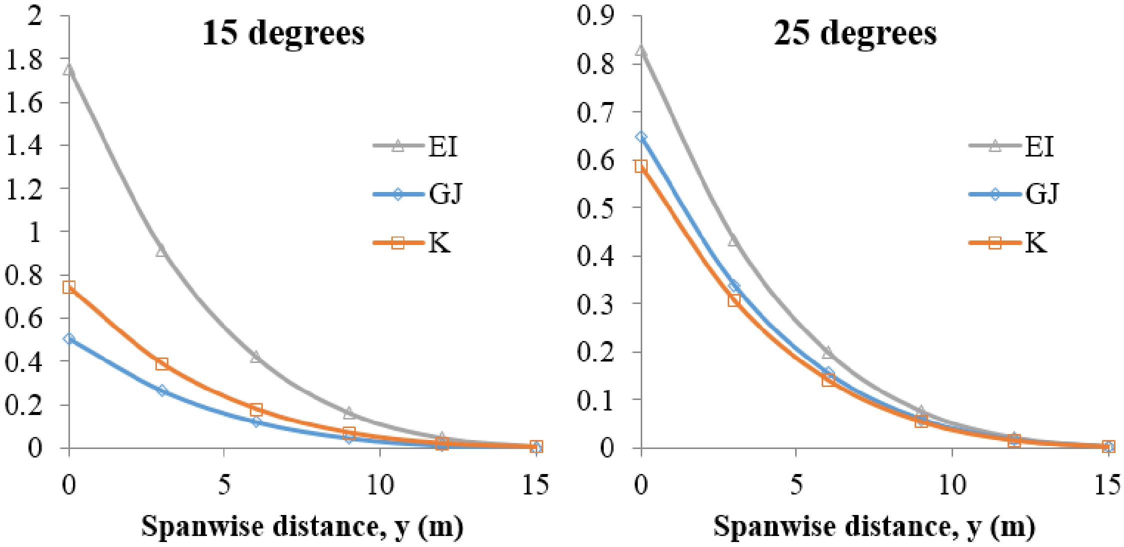

Figure 2.10: Stiffness properties at ply orientation of 15 and 25 degrees for single cell.

15 and 35 degrees with the solid black line showing bending displacements and the red broken lines showing the torsional rotations. An inspection of the mode shapes in Figure 2.11 suggests that for 15 degrees ply angles the fundamental mode is bending, whereas the second and third mode are bending-torsion coupled. For the same ply angle, the fourth mode is a pure torsional mode whereas the fifth one is a coupled mode. Now turning attention to the mode shapes corresponding to 35 degrees, somehow some similar as well as different observations for the five modes can be made. For instance, the first three modes follow more or less the same pattern, but the fourth mode for the 35 degrees case is a

coupled one unlike the 15 degrees case for which it was a pure torsional mode. The fifth mode for the 35 degrees case is pure torsional mode whereas it was a coupled mode for the 15 degrees case.

Using the modes described in Table 2.3 flutter analysis was carried out on the single cell composite wing and the results are shown in Table 2.4, for the entire range of ply orientations. The maximum achievable flutter speed appears to be at the higher end of ply angles. The reason for this can be attributed to the fact that the fundamental bending frequency goes down significantly at high ply angles whereas the reduction in fundamental torsional frequency will not be that much and as a consequence, the separation between the fundamental bending and torsional natural frequencies becomes much wider which predictably increase the flutter speeds.

Table 2.3: Natural frequencies and characterisation of modes for various ply orientation of a single cell composite wing. (B: Bending dominated mode; T: Torsion dominated mode; C:Bending-torsion coupled mode.)

Ply orientation	Natural frequencies (rad/s)				
	Mode 1	Mode 2	Mode 3	Mode 4	Mode 5
5	18.13 (B)	161.8 (C)	227.3 (T)	367.8 (C)	446.7 (T)
10	13.59 (B)	123.5 (C)	298.1 (T)	325.4 (C)	525.3 (T)
15	10.66 (B)	98.40 (C)	259.6 (C)	384.7 (T)	476.1 (C)
20	8.627 (B)	80.37 (C)	216.7 (C)	408.2 (C)	428.9 (T)
25	7.113 (B)	66.62 (C)	181.8 (C)	350.3 (C)	431.2 (T)
30	6.176 (B)	58.04 (C)	155.6 (C)	312.2 (C)	404.0 (T)
35	5.222 (B)	49.18 (C)	135.8 (C)	266.8 (C)	378.8 (T)
40	4.671 (B)	44.05 (B)	122.0 (C)	240.8 (C)	346.5 (T)
45	4.284 (B)	40.42 (B)	112.1 (C)	222.0 (C)	316.8 (T)
50	4.010 (B)	37.86 (B)	105.2 (C)	208.8 (C)	290.8 (T)
55	3.816 (B)	36.04 (B)	100.2 (C)	199.1 (C)	268.8 (T)
60	3.680 (B)	34.77 (B)	96.71 (C)	192.4 (C)	250.3 (T)
65	3.583 (B)	33.85 (B)	94.19 (B)	187.4 (C)	234.9 (T)
70	3.517 (B)	33.23 (B)	92.49 (B)	184.1 (C)	222.1 (T)
75	3.474 (B)	32.83 (B)	91.38 (B)	182.0 (C)	211.3 (T)
80	3.446 (B)	32.56 (B)	90.62 (B)	180.4 (C)	201.2 (T)
85	3.433 (B)	32.44 (B)	90.31 (B)	179.8 (C)	189.6 (T)
90	3.427 (B)	32.38 (B)	90.10 (B)	179.4 (B)	181.5 (T)

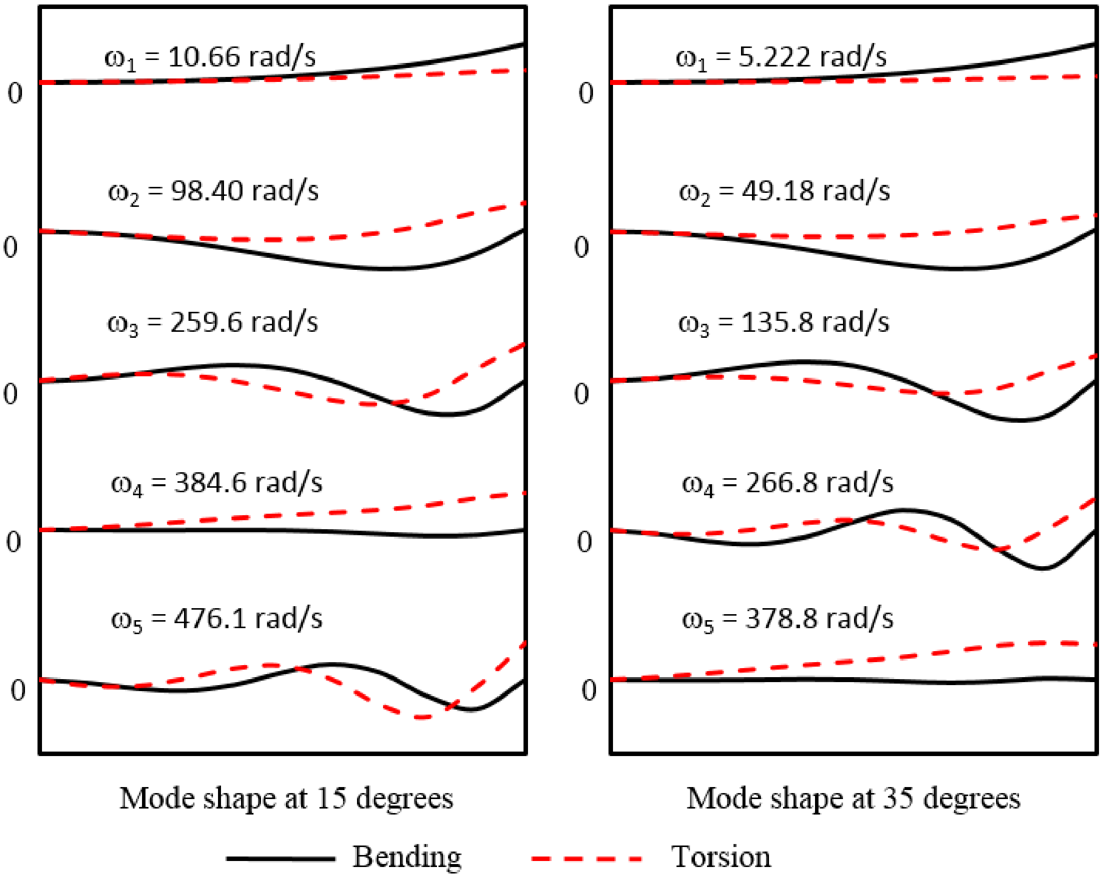

Figure 2.11: Mode shape at 15 degrees and 35 degrees ply orientation.

Table 2.4: Flutter analysis for single cell composite.

Ply angle (Degrees)	Flutter speed (m/s)	Flutter frequency (rad/s)
5	120	27.64
10	190	23.83
15	230	22.50
20	90	15.82
25	120	12.78
30	140	12.50
35	160	11.25
40	170	11.25
45	175	10.63
50	180	10.63
55	195	10.63
60	250	12.50
65	280	13.75
70	310	11.84
75	330	12.21
80	285	11.69
85	330	11.97
90	310	11.40

2.1.3.2 Results using double cell idealisation

For an accurate representation of the stiffness properties of the composite wing, it is often instructive to use double cell representation of the wing cross section (see Figure 2.4) as opposed to a single cell one (see Figure 2.2). Therefore, the results for stiffnesses, natural frequencies, mode shapes, flutter speeds and flutter frequencies in this section are computed based on double cell idealisation. Figures 2.12, 2.13 and 2.14 illustrates the bending (EI), torsional (GJ) and bending-torsional coupling (K) stiffness distributions, respectively along the span of the composite wing for different ply orientations using double cell wing box idealisation. As can be seen in Figure 2.12, lower values of ply orientations yield higher bending stiffness properties (EI) as was the case with single box idealisation. The reason for this is of course due to the enormous strength of the fibres as opposed to the matrix for lower values of ply orientations. Interestingly, Figure 2.13 shows that the torsional (GJ) stiffness is at its highest when the ply orientations is at 25 degrees whereas Figure 2.14 reveals that for both 15 and 25 degree ply orientations the bending and torsional coupling (K) stiffness will reach its maximum value. The above

results led to the presentation of Figure 2.15 which shows the interesting results for *EI*, *GJ* and *K* corresponding to 15 and 25 degrees ply orientations in one graph.
Based on the stiffness properties illustrated in Figures 2.12 to 2.14, the natural frequencies and mode shapes of a double cell composite wing was computed for further flutter analysis.

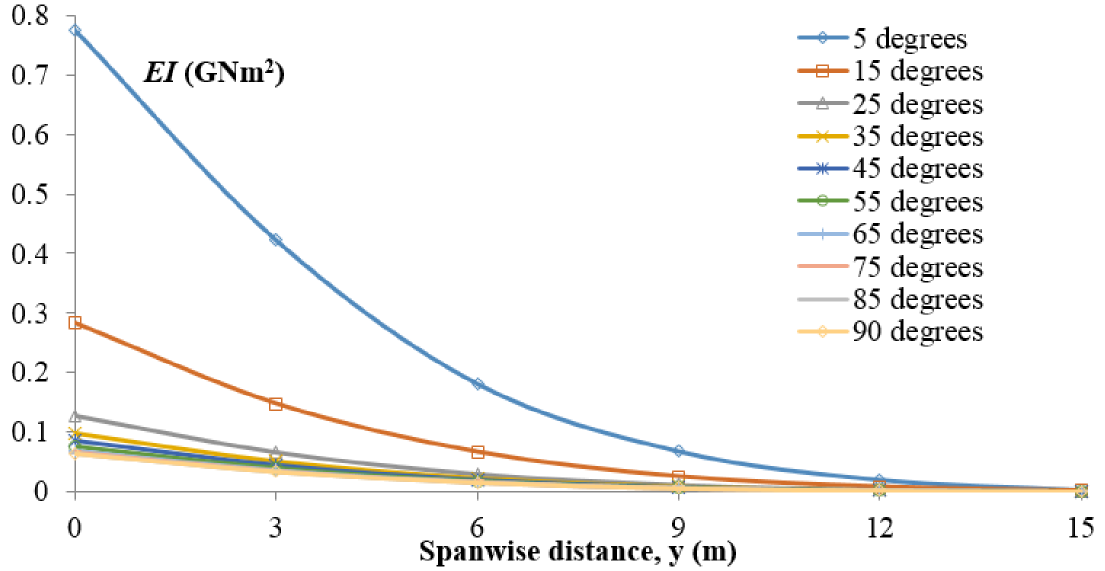

Figure 2.12: Comparison of bending stiffnesses along span wise distribution.

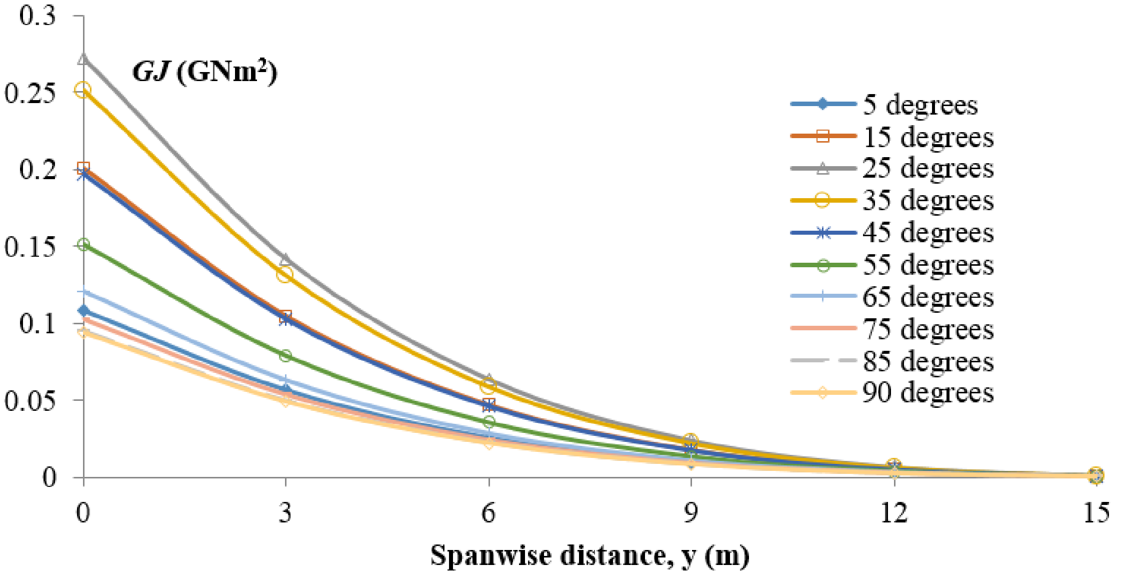

Figure 2.13: Comparison of torsional stiffnesses along span wise distribution.

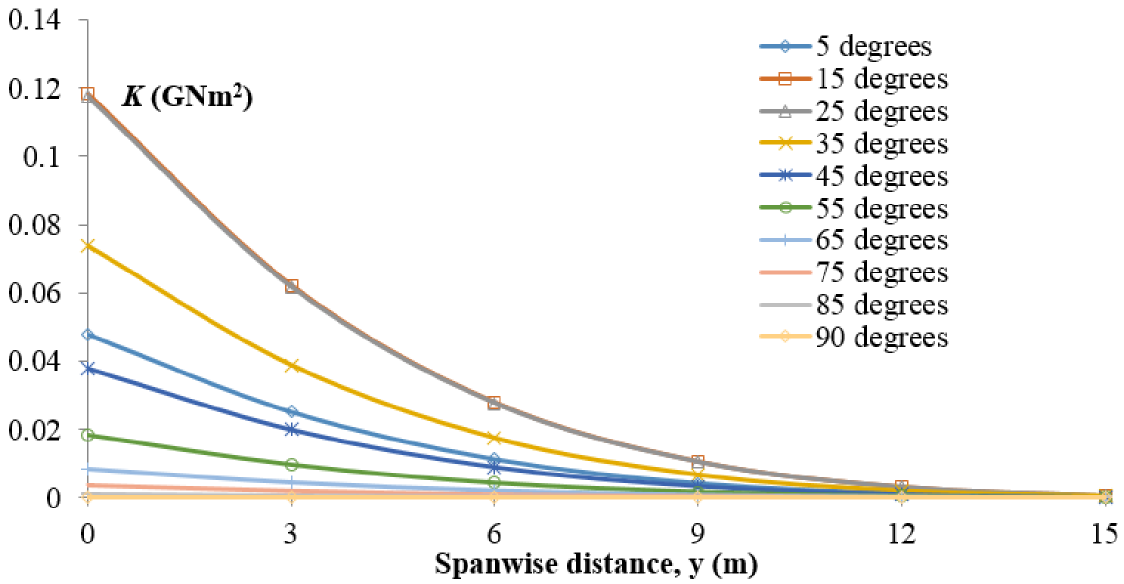

Figure 2.14: Comparison of coupling stiffnesses along span wise distribution.

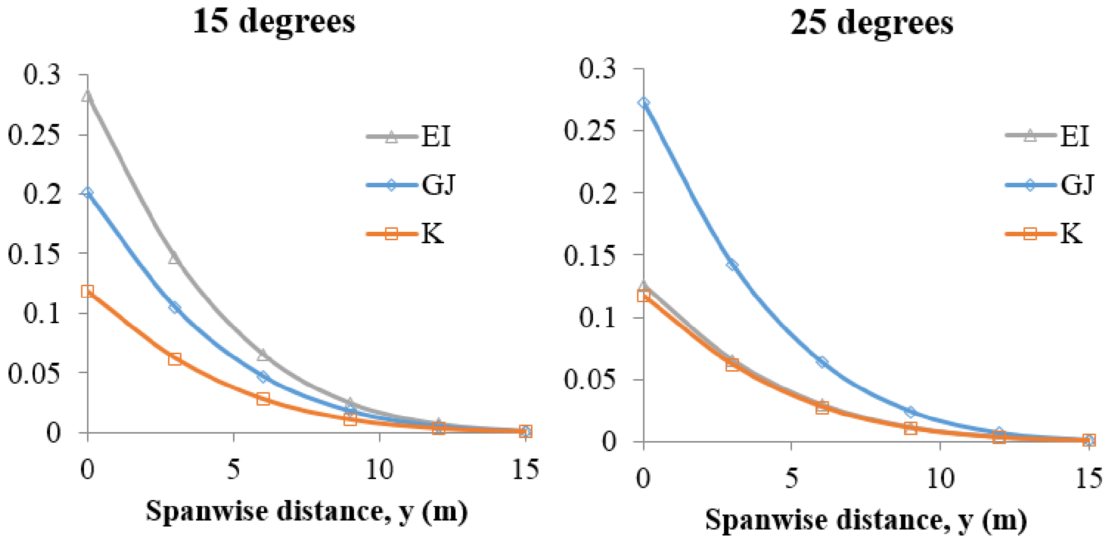

Figure 2.15: Stiffness properties at ply orientation of 15 and 25 degrees for double cell.

Table 2.5 shows the first five natural frequencies computed by varying the ply orientation between 5 and 90 degrees in steps of 5 degrees. The bending, torsion and coupled modes are designated by the letters **B**, **T** and **C** respectively. It is observed that with increase in ply orientations the natural frequencies decrease as was the case with single cell idealisation. However, unlike the single cell idealisation Table 2.5 shows that the first two modes are predominantly bending modes, whereas the third mode can be either predominantly coupled or bending. By contrast, the fourth mode is either torsional or coupled as can be seen. Interestingly, the fifth mode can be either coupled or torsional or bending and no predictable pattern is evident.

Figure 2.16 shows representative mode shapes for ply orientation of 15 and 25 degrees for the double cell composite wing with the solid black line showing bending displacements and the red broken lines showing the torsional rotations. As mentioned before values obtained are not similar to single cell because of the laminate layup chosen but the trends in all the results follow closely with those of single cell member. For Figure 2.16, at ply orientation of 15 degree it is observed that mode 1 is bending, modes 2 and 3 are strongly coupled, mode 4 is torsion dominant, mode 5 is strongly coupled. Now on observing mode shapes corresponding to the ply orientation of 35 degrees it is observed that mode 1 and 2 are bending dominant, mode 3 is strongly coupled, mode 4 is torsion dominant and mode 5 is coupled. It is evident that as ply orientation changes bending and torsion will be varied. Using the modes described in Table 2.5, flutter analysis was carried out on the double cell composite wing and the results are shown in Table 2.6, for the entire range of ply orientations. The maximum achievable flutter speed appears to be at the middle range of ply angles.

Table 2.5: Natural frequencies and characterisation of modes for various ply orientation of a double cell composite wing. (B: Bending dominated mode; T: Torsion dominated mode; C:Bending-torsion coupled mode.)

Ply orientation	Natural frequencies (rad/s)				
	Mode 1	Mode 2	Mode 3	Mode 4	Mode 5
5	8.790 (B)	83.21 (B)	109.9 (T)	193.6 (T)	245.0 (C)
10	8.470 (B)	75.30 (C)	128.6 (T)	199.0 (C)	234.7 (T)
15	5.928 (B)	52.86 (C)	142.1 (C)	151.2 (T)	262.5 (C)
20	4.229 (B)	37.84 (B)	103.3 (C)	166.3 (T)	199.9 (C)
25	3.509 (B)	31.47 (B)	86.34 (C)	168.0 (C)	174.6 (T)
30	3.420 (B)	30.70 (B)	84.50 (C)	165.6 (C)	173.6 (T)
35	3.501 (B)	31.39 (B)	86.45 (C)	166.5 (T)	170.6 (C)
40	3.566 (B)	32.03 (B)	88.52 (C)	157.6 (T)	174.9 (C)
45	3.571 (B)	32.08 (B)	88.74 (C)	147.6 (T)	175.7 (C)
50	3.535 (B)	31.77 (B)	87.97 (C)	138.0 (T)	174.5 (C)
55	3.482 (B)	31.30 (B)	86.71 (B)	129.4 (T)	172.1 (C)
60	3.424 (B)	30.78 (B)	85.33 (B)	121.9 (T)	169.5 (C)
65	3.371 (B)	30.30 (B)	83.98 (B)	115.7 (T)	166.9 (C)
70	3.327 (B)	29.90 (B)	82.90 (B)	110.6 (T)	164.8 (C)
75	3.294 (B)	29.61 (B)	82.10 (B)	106.8 (T)	163.2 (C)
80	3.271 (B)	29.40 (B)	81.52 (B)	104.0 (T)	162.1 (B)
85	3.258 (B)	29.29 (B)	81.23 (B)	102.4 (T)	161.5 (B)
90	3.253 (B)	29.24 (B)	81.10 (B)	101.8 (T)	161.2 (B)

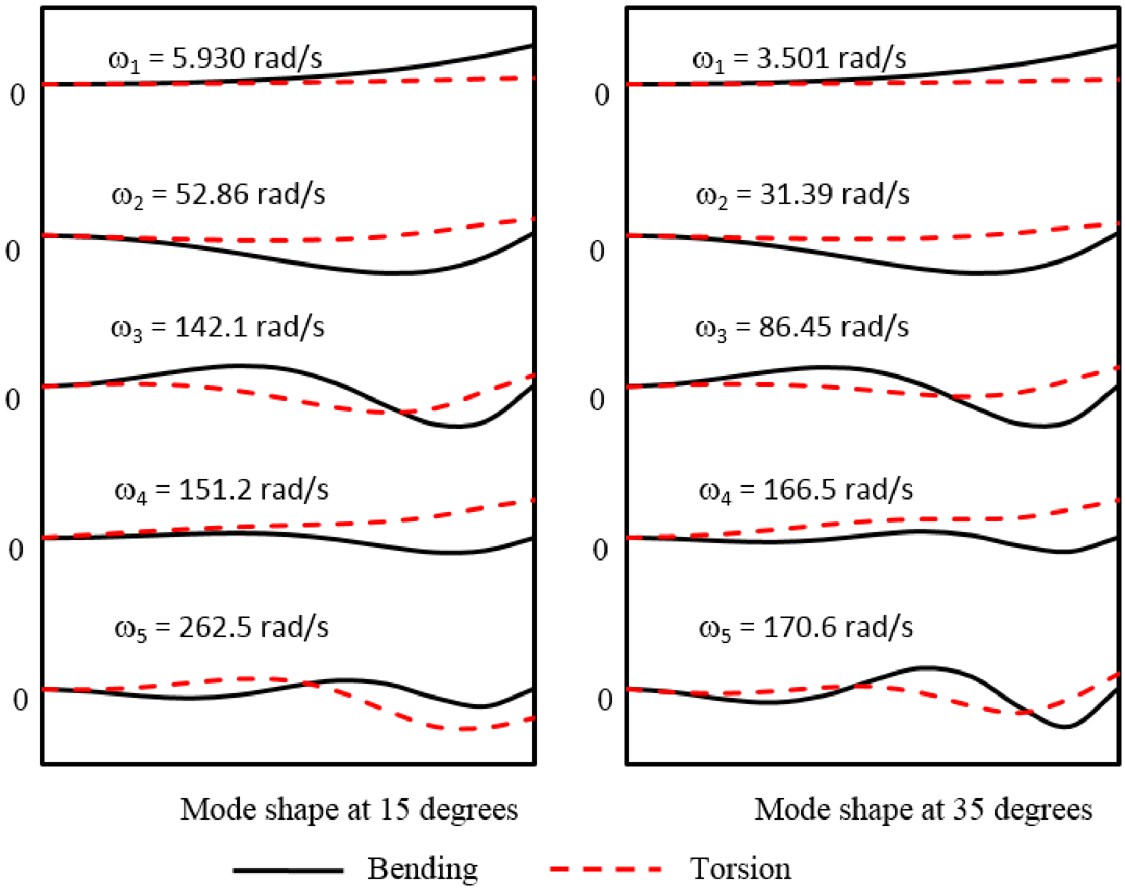

Figure 2.16: Mode shape at 15 degrees and 35 degrees ply orientation.

Table 2.6: Flutter analysis for double cell composite.

Ply angle (Degrees)	Flutter speed (m/s)	Flutter frequency (rad/s)
5	100	15.85
10	110	13.66
15	150	12.50
20	169	11.02
25	220	12.50
30	260	11.66
35	270	11.87
40	260	13.75
45	270	13.75
50	290	12.03
55	270	11.34
60	240	12.50
65	220	11.25
70	210	11.25
75	220	11.25
80	215	11.25
85	217	11.25
90	220	11.25

2.1.3.3 Results for metallic wing

In order to understand the analysis for free vibration and flutter of an metallic wing, an aircraft wing made up of aluminium is used. Geometry of the metallic wing box is similar to those of the wing box used for single and double cell analysis. The mode shapes obtained from the analysis is similar in shape to the composite wing box analysis but the natural frequency values are much higher for the metallic wing.It should be noted that standard formulae described in section 2.1.1.3 are used to perform stiffness analysis. Figure 2.17 gives the mode shape for an aluminium wing with similar dimension used to obtained single cell and double cell results. Table 2.7 shows the flutter speed and flutter frequency obtained for metallic wing. It can be seen that the flutter speed of 510 m/s is obtained for metallic wing.

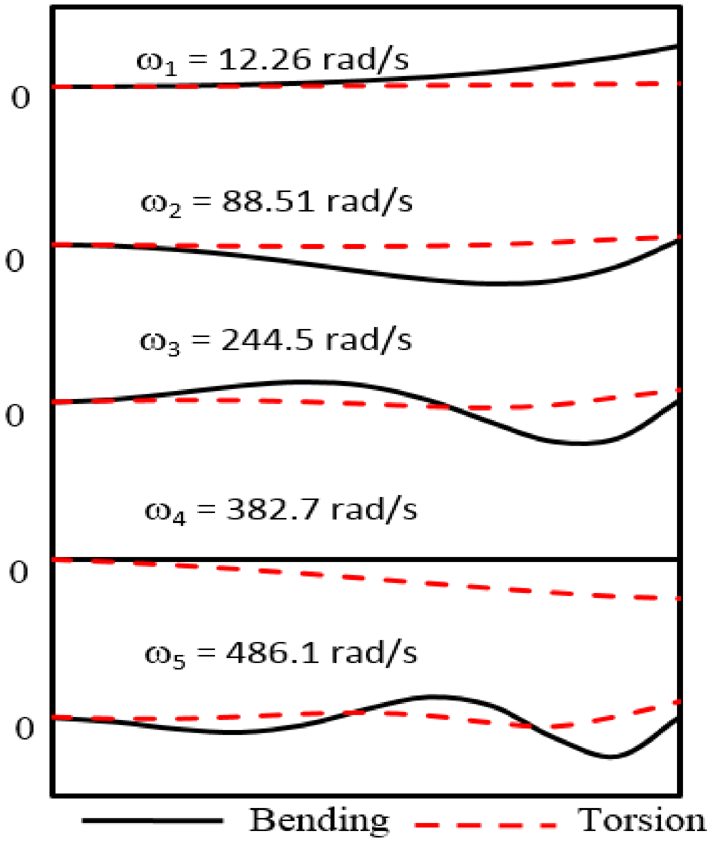

Figure 2.17: Mode shape for aluminium wing.

Table 2.7: Flutter results for aluminium wing.

Aluminium	
Flutter speed (m/s)	510.0
Frequency (rad/s)	28.94

2.2 Conclusions

It can be concluded that by using laminated composite wings, aeroelastic properties can be varied based on the user's criteria. For metallic wing box, since there can be no control in the stiffness properties, its flutter speed cannot be varied while for composites it can be changed using different ply orientation. Thus desired flutter results can be obtained by varying ply orientations and also by using double cells improved results can be achieved than by using single cell. Only geometric coupling is possible in metallic structure while both geometric coupling and material coupling are possible in composites. Bending–torsional coupling, which is not possible in metallic wing, can be varied for the composite wing to achieve desired aeroelastic effect. Also its effect on the flutter analysis was discussed in detail in the next chapter. Since the analysis is carried on the swept wing which gets more aeroelastic effect than that of rectangular wing, this result is also applicable to unswept wings. Also, it should be noted that the thin-walled section theory used in this chapter to perform single cell and double cell analysis which neglects the effect of shear contribution and the assumptions about normal and shear stresses being constant is also not applicable for 3D wing.

Chapter 3

Wing analysis and parametric investigation

3.1 Introduction to wing analysis and parametric investigation

In this chapter an investigation is carried out to establish the stiffness properties of wing sections by means of both two-dimensional cross sectional analysis as well as by applying FEMAP/NASTRAN in an equivalent three-dimensional static model. The FEMAP /NASTRAN model was realised as a consequence of a collaborative effort with an aircraft company. As the stiffness properties forms the basis for accurate computation of modal and flutter behaviour, it was necessary to undertake a parametric study to establish the stiffness properties as accurately as possible. Once the stiffness properties are established with reasonable degree of accuracy, free vibration analysis and flutter analysis are carried out for the wing in a number of case studies.

It has been discussed in Chapter 2 how to perform stiffness analysis of a wing section using single and double cell idealisations. The results obtained from this idealisation needed authentication and in the absence of experimental results it was decided to perform a 3-D static analysis using FEMAP/NASTRAN to extract the required stiffnesses. Thus two types of methods are used for stiffness analysis. The cross section based program BOXMXES is used first to compute the stiffnesses which were later compared with those obtained from the 3-D static analysis using FEMAP/NASTRAN. In essence the principle stiffness properties are those of bending (EI) and torsion (GJ). Because of the intrinsic difficulties in capturing the bending-torsion material coupling stiffness (K) from the FEMAP/NASTRAN model, the parametric study involving this particular stiffness is solely confined to the 2-D wing box model. Free vibration analysis and flutter analysis are then carried out using the dynamic stiffness method on a few selective illustrative exam-

Table 3.1: General specifications of the wing.

Geometric parameter	Value
Aspect ratio	10
Wing area (m^2)	92.25
Wing span (m)	30.42
Root chord (m)	5.30
Tip chord (m)	1.34
Mean aerodynamic chord (m)	3.363

ples by utilising and suitably adopting wherever possible the stiffness data obtained from BOXMXES and FEMAP/NASTRAN.

It should be noted that there were some marked variations in the stiffness properties from the two types of analysis described above and this could be due to the complexities of the wing design, particularly due to the presence of the manholes in the lower skin of the wing. Also, whilst the practical 3D wing model in FEMAP/NASTRAN includes cut-outs, sweep, taper ratio, flexible ribs, the 2D BOXMXES model uses only the cross section of the wing in a 2D plane. This necessitated a further investigation of parametric nature involving the wing box geometry for the stiffness analysis. Therefore, at the end of this chapter, an investigation is undertaken to understand and provide an insight into the parameters affecting the wing box stiffnesses.

3.2 Description of the wing analysed

Figure 3.1 represents the finite element wing model which was used in FEMAP/NASTRAN. The model essentially consists of plate, shell and bar elements and the model accuracy was established by increasing and decreasing the number of elements used in the analysis until a consistency of the results was achieved. The model wing consists of spars, ribs, spar caps, stringers, rib flanges and web stiffeners. The cross sections of the spars and stringers have the same dimensions from root to tip. Shell elements with varying degrees of complexities were used to model the skin covers, spar and rib webs. Furthermore, the top and bottom wing skins were modelled by using composite material in quasi-isotropic layup ($E_x = E_y$). Material with equivalent properties of aluminium alloy was employed for the stiffeners. As for the pylon, isotropic aluminium material was utilised. Some pertinent details of the wing are given in Tables 3.1, 3.2 and 3.3.

Table 3.2: Material properties of composite layup.

Metal	Density, ρ (kg/m^3)	Young's modulus, E (N/m^2)	Shear modulus, G (N/m^2)	Poisson's ratio (ν)
Pylon	N/A	7.0E10	2.69E10	0.3
Spars, Stringers, Ribs and Web Stiffeners	2700	7.0E10	2.69E10	0.3

Table 3.3: Material properties of skin for the wing model.

Composite	Density, ρ (kg/m^3)	E_1 (N/m^2)	E_2 (N/m^2)	G_{12} (N/m^2)	Poisson's ratio (ν_{12})
Skin	1580	1.48E11	1.03E10	5.93E9	0.27

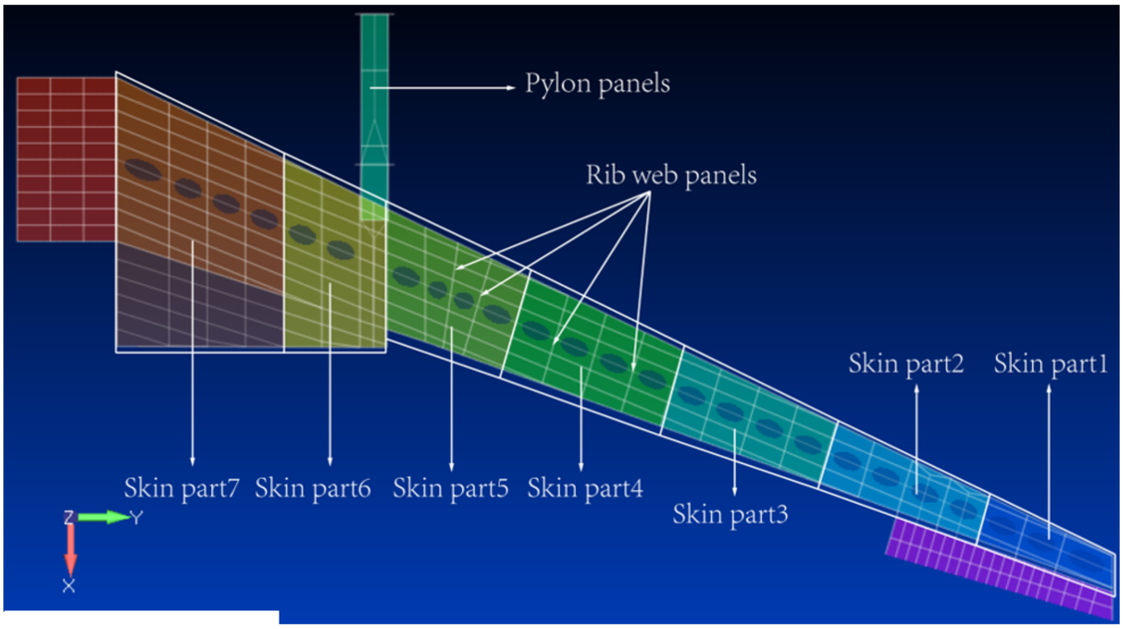

Figure 3.1: Composite wing model with 26 sections represented by 7 skin parts (see Table 3.4). Skin part 1: sections 1-3; Skin part 2: sections 4-7; Skin part 3: sections 8-11; Skin part 4: sections 12-15; Skin part 5: sections 16-19; Skin part 6: sections 20-22; Skin part 7: sections 23-26.

First the composite wing model which has 27 ribs along semi-span is considered and it was divided into 26 sections, numbered from tip to root, with each section chosen between two successive ribs so that they lie across the centre line of each manhole, see Figure 3.1. Note that, section 1 to section 19 (outboard wing) consist of only two spars, front spar and rear spar. They are considered as single cell box sections for the analysis. On the other hand, section 20 to section 26 (inboard wing) consist of three spars, front spar, middle spar and rear spar. They are considered as double cell box sections for the analysis. Section 1 represents the section near the wing tip whereas section 26 represents the section near the wing root. The composite layup orientation and stacking sequence are given in Appendix B. The thickness for each laminate for the top and bottom skin of the wing is taken as 1.83×10^{-4} m. It should be noted that wing model analysed has manhole openings on the lower skin between two successive ribs which complicates the stiffness analysis.

3.3 Theoretical and numerical procedures

For the given wing, BOXMXES program needs the coordinates of each part divided around the circumference of the box section which is difficult to obtain directly from FEMAP/NASTRAN and furthermore, the BOXMXES prefers the wing box section to be roughly symmetrical about the horizontal axis. Therefore, as an acceptable alternative, the dimensions needed for the wing box sections are determined from FEMAP/NASTRAN model by taking proper account of the distances between nodes appearing along upper skin, lower skin, front spar, rear spar (for sections 1-19) and middle spar (for sections 20-26). Upper skin and lower skin were further subdivided between two stringers. AUTOCAD is then used to plot these parts to recreate the cross-sections. By using AUTOCAD, coordinates of each part were identified along the circumference of the wing box sections. Using the cross sectional coordinates, element properties, material properties, laminate layup and stacking sequence, two input data file for BOXMXES program was created, one for the single cell and the other is for the double cell. Then using BOXMXES program bending (EI) and torsional (GJ) stiffnesses are calculated. To facilitate this work, MATLAB is used to determine the preliminary estimates of EI and GJ values which are subsequently refined and improved. It is to be noted that the BOXMXES program does not take into account the contribution of the stringers. So by using the parallel axis theorem, effect of the stringers was taken into account by lumping the appropriate areas. The output from the BOXMXES program gives the stiffness properties, EI, GJ and the effective elastic constants E_x, E_y and G_{xy}. For the sections 1-26 the effective elastic constants E_x, E_y and G_{xy} are given in Table 3.4. The elastic constants E_x, E_y and G_{xy} obtained from BOXMXES program are then fed into FEMAP/NASTRAN to determine the stiffness properties EI and GJ. The bending-torsion coupling (K) was not calculated using the FEMAP/NASTRAN because of the difficulties encountered to adapt the package for this purpose. These stiffness properties, EI and GJ are then used to create the data needed for CALFUNB and COMPCAL programs to compute the free vibrational modes and flutter speed.

Table 3.4: Equivalent values obtained for the sections 1-26.

Skin part 1			
Section 1,2,3	Ex	Ey	Gxy
Upper skin, Lower Skin, Rear Spar	0.510E11	0.636E11	0.219E11
Front spar	0.518E11	0.518E11	0.254E11
Skin part 2			
Section 4,5,6,7	Ex	Ey	Gxy
Upper skin, Front Spar, Rear Spar	0.576E11	0.576E11	0.222E11
Lower Skin	0.569E11	0.569E11	0.213E11
Skin part 3			
Section 8-11	Ex	Ey	Gxy
Upper skin, Lower skin,	0.620E11	0.529E11	0.220E11
Front spar, Rear Spar	0.529E11	0.620E11	0.220E11
Skin part 4			
Section 12-15	Ex	Ey	Gxy
Upper skin,	0.554E11	0.629E11	0.212E11
Front spar,	0.572E11	0.572E11	0.217E11
Lower skin, Rear Spar	0.559E11	0.559E11	0.230E11
Skin part 5			
Section 16-19	Ex	Ey	Gxy
Upper skin, Front spar	0.529E11	0.594E11	0.230E11
Lower Skin, Rear Spar	0.591E11	0.526E11	0.227E11
Skin part 6			
Section 20-22	Ex	Ey	Gxy
Upper skin, Front Spar, Lower skin	0.562E11	0.562E11	0.229E11
Rear Spar, Mid wall	0.621E11	0.502E11	0.229E11
Skin part 7			
Section 23-26	Ex	Ey	Gxy
Upper skin, Lower skin, Rear spar, Mid wall	0.591E11	0.537E11	0.229E11
Front Spar	0.589E11	0.535E11	0.226E11

3.4 Stiffness evaluation using finite element model

To calculate the bending and torsional stiffnesses, each of the box sections is isolated and clamped at the inboard end so as to make it a cantilever. Next bending moment and torque are respectively applied at the outboard (free) end and then displacements and rotations of the free end section were computed. Illustrative examples of forces and boundary condition applied in this analysis are shown in Figure 3.2 below.

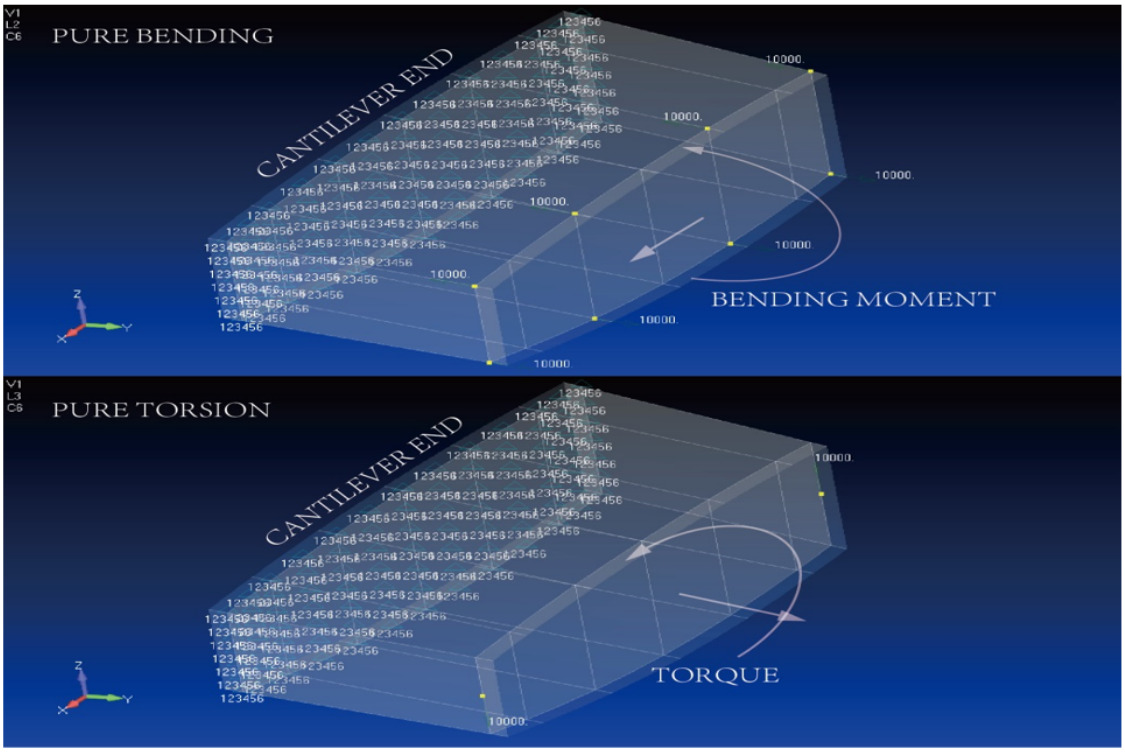

Figure 3.2: Applied bending moment and torque for an cantilevered wing box.

To calculate the wing box bending stiffness, Euler-Bernoulli beam theory is used. Thus the moment-curvature relationship is given by

$$M\left(l\right) = EIk = EIw^{''}\left(y\right) \tag{3.1}$$

where M is the bending moment, EI is the bending stiffness, k is the curvature and w is the vertical displacement of the section and a 'prime' denotes differentiation with respect to the span wise displacement y.

For a bending moment M applied at the tip of a typical representative sectional length L, it can be established that the bending stiffness EI follows the following relationships

$$EI = \frac{ML}{\theta\left(L\right)} \tag{3.2}$$

where $\theta(L)$ is the bending slope in radian at the tip of the section analysed.
In a similar manner, the torsional stiffness GJ is computed by applying a constant torque T at the tip of the outboard section. Using elementary torsion theory the twist $\psi(L)$ at the tip of the section can be related to the torque T and torsional stiffness GJ as follows

$$\psi(L) = \frac{TL}{GJ} \tag{3.3}$$

Equation 3.3 can be rearranged to give the torsional stiffness GJ by the following equation

$$GJ = \frac{TL}{\psi(L)} \tag{3.4}$$

3.4.1 Results for bending stiffnesses

Based on the underlying methodology described above the values of the applied bending moments and the corresponding bending displacements and bending rotations of each of the 26 sections are shown in Table 3.5 which were computed by using FEMAP/NASTRAN.

Table 3.5: Applied bending moment and bending rotation of each section.

Section number	Applied bending moment (Nm)	Resulting bending angle (rad)	Section number	Applied bending moment (Nm)	Resulting bending angle (rad)
1	3826.55	1.14E-03	14	8452.94	1.64E-04
2	4346.56	7.86E-04	15	8853.23	1.46E-04
3	4740.29	7.14E-04	16	9252.46	1.29E-04
4	5129.59	5.71E-04	17	9649.82	8.48E-05
5	5516.98	5.22E-04	18	9924.52	8.01E-05
6	5904.00	4.90E-04	19	10183.29	1.08E-04
7	6288.33	4.17E-04	20	11199.63	4.40E-05
8	6671.89	3.05E-04	21	12404.49	5.88E-05
9	7054.49	2.80E-04	22	14113.15	4.92E-05
10	6829.96	2.34E-04	23	15828.16	4.13E-05
11	7239.64	2.18E-04	24	17551.67	3.74E-05
12	7646.48	1.94E-04	25	19277.49	3.38E-05
13	8051.65	1.81E-04	26	20203.40	3.62E-05

The data given in Table 3.5 which were obtained through the application of FEMAP/NASTRAN are further utilised to estimate the bending stiffness EI of each section by applying Equation 3.2. The results are shown in Table 3.6.

Table 3.6: Bending stiffness, EI of the wing boxes.

Section	Bending Stiffness (Nm^2)	Section	Bending Stiffness (Nm^2)
1	2.59E+06	14	3.04E+07
2	3.24E+06	15	3.57E+07
3	3.90E+06	16	4.23E+07
4	5.27E+06	17	4.67E+07
5	6.20E+06	18	4.81E+07
6	7.07E+06	19	5.10E+07
7	8.85E+06	20	9.58E+07
8	1.28E+07	21	1.14E+08
9	1.48E+07	22	1.57E+08
10	1.71E+07	23	2.10E+08
11	1.94E+07	24	2.59E+08
12	2.32E+07	25	3.18E+08
13	2.61E+07	26	4.02E+08

3.4.2 Results for torsional stiffnesses

Based on the underlying methodology described in section 3.4 the values of the applied torque and the corresponding twist of each of the 26 sections are shown in Table 3.7 which were computed by using FEMAP/NASTRAN.
The data given in Table 3.7 which were obtained through the application of FEMAP /NASTRAN are further utilised to estimate the torsional stiffness GJ of each section by applying Equation 3.4. The results are shown in Table 3.8.

Table 3.7: Applied torque and twist of the wing box sections.

Section	Applied torque (Nm)	Cross section twist angles (rad)	Section	Applied torque (Nm)	Cross section twist angles (rad)
1	4524.72	0.003956	14	12168.61	0.000241
2	4991.11	0.001930	15	12766.88	0.000220
3	5588.99	0.001548	16	13365.16	0.000179
4	6186.92	0.001141	17	13963.47	0.000102
5	6784.92	0.000983	18	14761.07	0.000085
6	7383.78	0.000848	19	15914.49	0.000119
7	7981.13	0.000709	20	19305.14	0.000044
8	8579.26	0.000531	21	21112.71	0.000059
9	9177.42	0.000475	22	23669.77	0.000049
10	9775.63	0.000429	23	26229.54	0.000046
11	10373.85	0.000390	24	28791.83	0.000055
12	10972.09	0.000298	25	31356.53	0.000054
13	11570.34	0.000272	26	33923.45	0.000079

Table 3.8: Torsional stiffness *GJ* of the box sections.

Section	Torsional Stiffness FEMAP/NASTRAN (Nm^2)	Section	Torsional Stiffness FEMAP/NASTRAN (Nm^2)
1	8.87E+05	14	2.96E+07
2	1.52E+06	15	3.41E+07
3	2.12E+06	16	4.38E+07
4	3.18E+06	17	5.57E+07
5	4.04E+06	18	6.63E+07
6	5.10E+06	19	7.68E+07
7	6.60E+06	20	1.79E+08
8	9.48E+06	21	2.04E+08
9	1.13E+07	22	2.75E+08
10	1.33E+07	23	3.29E+08
11	1.56E+07	24	3.02E+08
12	2.16E+07	25	3.33E+08
13	2.49E+07	26	3.36E+08

3.4.3 Free vibration and flutter analysis

Free vibration and flutter analyses are carried out using both CALFUNB and COMPCAL which are the derivatives of the original program CALFUN. These two programs are completely independent in that CALFUNB is developed for metallic wings which does not require the bending-torsion material coupling stiffness (K) in the input data whereas COMPCAL is developed for composite wing requiring the stiffness K. However, in order to verify the CALFUNB results a small values of the bending-torsion coupling parameter K of the order 10^{-4} was used in COMPCAL as a degenerate case.

For ease of computation, the 26 wing box sections are reduced to 13 sections (see Table 3.9) by using the appropriate EI and GJ values obtained from FEMAP/NASTRAN. The input data file for CALFUNB and COMPCAL were then created. The data preparation included determining mass per unit length, polar mass moment of inertia per unit length, distance between mass and element axis, projection of the element length along X and Y axes, semi chord, etc. From the input file thus created, the in-house programs CALFUNB and COMPCAL were activated and the mode shapes and flutter speed were computed.

The first six natural frequencies and mode shapes computed using CALFUNB and COMPCAL are shown in Figure 3.3 in which the solid black line shows bending displacement and the broken red line shows torsional displacement. Predictably the program COMPCAL produced more or less the same natural frequencies and mode shapes as CALFUNB. The modes generated by CALFUNB or COMPCAL needs some discussion. Referring to Figure 3.3, mode 1 of the wing is basically the fundamental bending mode. The second mode is also bending with very little torsion in it, whereas third mode is coupled in bending and torsion. The fourth and fifth modes are also to all intents and purposes couple modes whereas the sixth mode can be regarded as a pure torsional mode. These 6 modes are subsequently used in the flutter analysis and the results are shown in Table 3.10 which shows the flutter speeds and flutter frequencies obtained using CALFUNB and COMPCAL for FEMAP/NASTRAN and BOXMXES.

Table 3.9: Stiffness properties of 13 sections.

Sections	EI (Nm^2)	GJ (Nm^2)
Section 1 (tip)	2.92E+06	1.20E+06
Section 2	4.59E+06	2.65E+06
Section 3	6.64E+06	4.57E+06
Section 4	1.08E+07	8.04E+06
Section 5	1.60E+07	1.23E+07
Section 6	2.13E+07	1.86E+07
Section 7	2.83E+07	2.73E+07
Section 8	3.90E+07	3.90E+07
Section 9	4.74E+07	6.10E+07
Section 10	7.34E+07	1.28E+08
Section 11	1.36E+08	2.40E+08
Section 12	2.35E+08	3.16E+08
Section 13	3.60E+08	3.35E+08

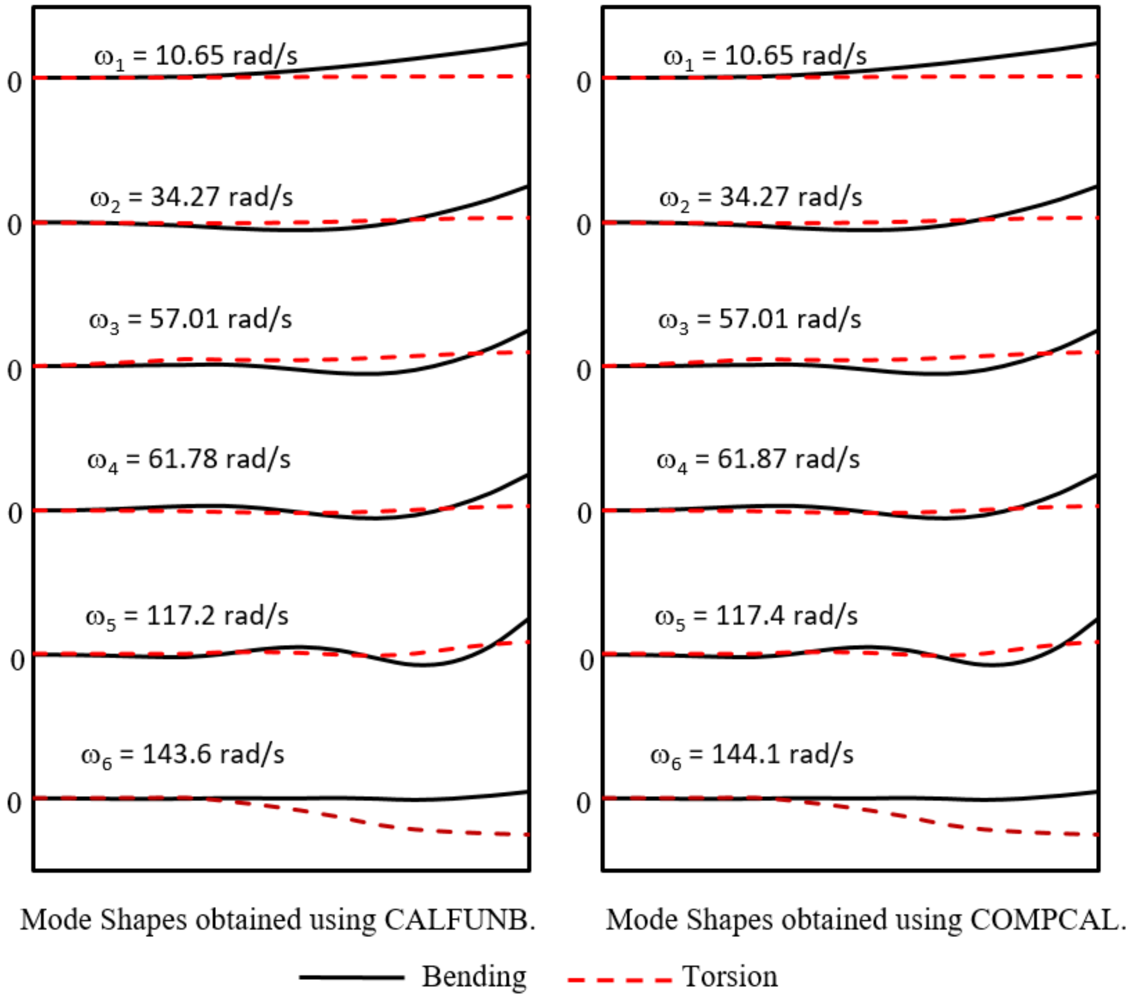

Mode Shapes obtained using CALFUNB.

Mode Shapes obtained using COMPCAL.

Figure 3.3: Mode shapes obtained using CALFUN.

Table 3.10: Flutter results obtained using CALFUN.

Flutter result	Stiffness data used was computed by FEMAP/NASTRAN		Stiffness data used was computed by BOXMXES	
	CALFUNB	COMPCAL	CALFUNB	COMPCAL
Flutter speed (m/s)	381	383	351	354
Flutter frequency (rad/s)	51.22	51.22	59.10	59.04

3.4.4 Comparison of results based on stiffness properties

Although reasonably satisfactory results for flutter speeds and flutter frequencies are obtained from the stiffnesses calculated using FEMAP/NASTRAN, it was felt to be necessary to revisit the estimation of stiffness properties using the BOXMXES and FEMAP /NASTRAN programs. Clearly, there were significant differences in the stiffness properties of the wing computed by the 2-D and 3-D idealisations using these two very different programs. Table 3.11 shows the bending stiffness *EI* computed by the two programs with percentage difference in the stiffnesses for the 26 sections varied from 10% to 35%. The differences are unacceptably large. Similar observations are made for the torsional stiffness (*GJ*) distributions for which the percentage difference was even greater for some cross sections, see Table 3.12. The stiffnesses computed by BOXMXESC were larger than the ones computed by FEMAP/NASTRAN and the reason may be attributed to the fact that the former does not includes the effects of manhole and cut-outs. This prompted a further investigation which includes:

(i) the presence of the manholes (cut-outs for access panels) appearing in the lower skin,

(ii) the rigidity of the ribs to retain the aerofoil shape,

(iii) the taper ratio of the wing planform and the taper ratio of the depth of the wing from root to tip

(iv) the sweep angle of the leading edge.

Table 3.11: Bending stiffness, *EI* of the wing boxes between sections 1-26.

Sections	*EI* from FEMAP/NASTRAN (Nm^2)	*EI* from BOXMXE (Nm^2)	Percentage difference
1	2.59E+06	3.31E+06	21.75
2	3.24E+06	4.03E+06	19.60
3	3.90E+06	4.79E+06	18.58
4	5.27E+06	6.35E+06	17.01
5	6.20E+06	7.49E+06	17.22
6	7.07E+06	8.77E+06	19.38
7	8.85E+06	1.07E+07	17.37
8	1.28E+07	1.50E+07	14.67
9	1.48E+07	1.71E+07	13.45
10	1.71E+07	1.95E+07	12.31
11	1.94E+07	2.21E+07	12.22
12	2.32E+07	2.61E+07	11.11
13	2.61E+07	2.93E+07	10.92
14	3.04E+07	3.39E+07	10.32
15	3.57E+07	3.98E+07	10.30
16	4.23E+07	4.71E+07	10.19
17	4.67E+07	5.13E+07	8.97
18	4.81E+07	5.43E+07	11.42
19	5.10E+07	7.05E+07	27.66
20	9.58E+07	1.10E+08	12.91
21	1.14E+08	1.53E+08	25.49
22	1.57E+08	2.13E+08	26.29
23	2.10E+08	3.05E+08	31.15
24	2.59E+08	3.95E+08	34.43
25	3.18E+08	4.94E+08	35.63
26	4.02E+08	6.33E+08	36.49

Table 3.12: Torsional stiffness, *GJ* of the wing boxes between sections 1-26.

Sections	*GJ* from FEMAP/NASTRAN (Nm^2)	*GJ* from BOXMXE (Nm^2)	Percentage difference
1	8.87E+05	1.26E+06	29.60
2	1.52E+06	1.64E+06	7.32
3	2.12E+06	2.09E+06	-1.44
4	3.18E+06	3.11E+06	-2.25
5	4.04E+06	3.87E+06	-4.39
6	5.10E+06	4.74E+06	-7.59
7	6.60E+06	5.68E+06	-16.20
8	9.48E+06	7.98E+06	-18.80
9	1.13E+07	9.38E+06	-20.47
10	1.33E+07	1.10E+07	-20.91
11	1.56E+07	1.28E+07	-21.88
12	2.16E+07	1.79E+07	-20.67
13	2.49E+07	2.05E+07	-21.46
14	2.96E+07	2.34E+07	-26.50
15	3.41E+07	2.65E+07	-28.68
16	4.38E+07	3.48E+07	-25.86
17	5.57E+07	3.86E+07	-44.30
18	6.63E+07	4.44E+07	-49.32
19	7.68E+07	5.59E+07	-37.39
20	1.79E+08	1.57E+08	-14.01
21	2.04E+08	2.07E+08	1.45
22	2.75E+08	2.63E+08	-4.56
23	3.29E+08	3.88E+08	15.21
24	3.02E+08	4.84E+08	37.60
25	3.33E+08	5.86E+08	43.17
26	3.36E+08	7.21E+08	53.40

3.4.5 Effects of rib-rigidities on the bending and torsional stiffnesses

It is clearly evident from the results shown in Tables 3.11 and 3.12 that there is a small difference in the *EI* but significantly large difference in *GJ* computed from the 3D wing box using FEMAP/NASTRAN and the BOXMXE based on 2D cross-sectional method. This needs further investigation to pin point the real cause. However it should be recognised

Table 3.13: Rib rigidity effect on the bending stiffness of box section 16.

EI (Nm^2) for Section 16 of composite wing			
FEMAP/NASTRAN (Elastic rib)	FEMAP/NASTRAN (Rigid rib)	BOXMXE with cut-out	BOXMXE without cut-out
3.75E+07	4.25E+07	4.30E+07	4.71E+07

that the BOXMXE results do not allow for the cross-sectional warping which essentially means that the ribs have been assumed to be rigid undergoing no in-plane or out of plane displacements. By contrast, the flexibility of the ribs are inherently accounted for in the FEMAP/NASTRAN model. In order to bring parity in the sets of results an investigation is carried out to examine the effect of the rib-rigidity on the bending and torsional stiffnesses for section 16 of the composite wing. This investigation is particularly relevant to the analysis using FEMAP/NASTRAN, but not so for the BOXMXE program because for the latter the question of rib rigidity does not arise as the theory used in BOXMXE inherently assumes that the section does not warp implying that the rib is basically rigid. As explained in the description of the wing analysed in section 3.2, the aircraft wing was split into 26 sections numbered from tip to root. For the analysis, section 16 is considered mainly because it has single cell and the parametric study using single cell box is preferred for simplicity. Also section 16 is a critical section which lies closer to pylon in the kink region. The results of this investigation are shown in Tables 3.13 and 3.14 for the bending and torsional stiffnesses respectively. It is clear that the 3D results for the bending stiffness EI from FEMAP/NASTRAN model using rigid rib are in close agreement with the 2D results with the effect of cut-out computed from BOXMXE. Apparently the flexibility of the rib made a significant difference to the bending stiffness and the probable explanation could be the fact that the length of the box element chosen was quite small and comparable to its width, bearing in mind that the application of load to such a small element is expected to have substantial localized effect. With regard to the torsional stiffness GJ, Table 3.14 shows the result using FEMAP/NASTRAN and BOXMXE. Clearly the comparative results show that the rigid rib assumption from the two programs is producing more differences in torsion stiffness GJ than the observed differences in the bending stiffness EI. This suggests that a thorough but detailed investigation on the estimation of the torsional stiffness GJ is needed to ascertain the suitability using FEMAP/NASTRAN and BOXMXE model when establishing the torsional properties of the composite wing. Therefore, an in-depth investigation to determine the effects of various parameters on the torsional strength of wing sections is carried out in the subsequent section.

Table 3.14: Rib rigidity effect on the torsional stiffness of box section 16.

GJ (Nm^2) for Section 16 of composite wing			
FEMAP/NASTRAN (Elastic rib)	FEMAP/NASTRAN (Rigid rib)	BOXMXE with cut-out	BOXMXE without cut-out
3.53E+07	4.88E+07	2.38E+07	3.48E+07

3.4.6 Parametric study influencing the torsional stiffnesses

The previous section is concerned with the effects of rib rigidity on the bending and torsional stiffnesses of a typical composite wing section and as it turned out, the bending stiffnesses can be computed reasonably accurately using the rigid rib assumptions, but the estimation of torsional stiffnesses requires further investigations. Therefore, the primary focus is now confined to the examination of the effects of various parameters on the torsional stiffness (GJ) of wing sections. One of the main problems in determining the torsional stiffness using the 2D analysis through BOXMXES for a wing section with cut-out stems from the fact that the relevant portion of the wing box cross section containing the cut could not be removed because the section would then become an open section which is not the real case to represent the actual wing as the cut-out does not extend through the neighbouring sections along the span wise direction of the wing. The problem is further compounded by a number of other reasons which are explained next. Altogether the following parameters are included in the investigation: (i) the presence of the manholes (cut-outs for access panels) appearing in the lower skin, (ii) the rigidity of the ribs to retain the aerofoil shape, (iii) the taper ratio of the wing planform and the taper ratio of the depth of the wing from root to tip and (iv) the sweep angle of the leading edge. In order to obtain an accurate measure of the torsional stiffness GJ and to make some engineering judgement on the influence of each of the above parameters on GJ, the in-depth investigation was undertaken by using FEMAP/NASTRAN together with the application of the classical theory of aircraft structures. The results from the above two methods (one numerical and the other theoretical) are compared and contrasted with some discussion. It should be recognised that in the numerical method using FEMAP/NASTRAN, the torsional stiffness GJ is obtained for a typical element of certain length by cantilevering the element at its one end and applying a pure bending moment or a pure torque (pure, as closely as possible) at the other end. This inevitably involves the length of the element as a parameter in the data. By contrast, in the theoretical method the torsional stiffness is simply a matter of cross sectional parameter without involving the length of the element in the data. A part of the numerical investigation simulated the non-warping of the cross section by assuming the ribs to be rigid. A number of case studies have been conducted with primary emphasis on the torsional stiffness GJ as indicated and these are explained next. It is to be noted that the case studies from 1 through 8 correspond to wing sections of metallic constructions (i.e. aluminium alloy) with no cut-outs (manholes) whereas the case studies 9 and 10 are focused on the shape, size and material of composite wing of similar dimensions of Section 16 with and without cut-outs (manholes). For comparative purposes case study 9 included parallel investigations using aluminium material alongside the original composite material of the wing whereas case study 10 is solely for composite material. For each of the case studies, a general description showing the relevant dimensions is illustrated in Figure 3.4 and the corresponding data for the dimensions of a to l are shown in Table 3.15. Further details of each of the case studies are given in Appendix C.

The definitions of taper ratio and its values for each of the relevant cases which have taper are given in Table 3.16. The leading edge is considered to be on the right hand side of the box whereas the trailing edge is on the left hand side (see Figure 3.4). Also the front of the box is considered to be the tip and the rear to be the root in the analysis when imposing the boundary conditions.

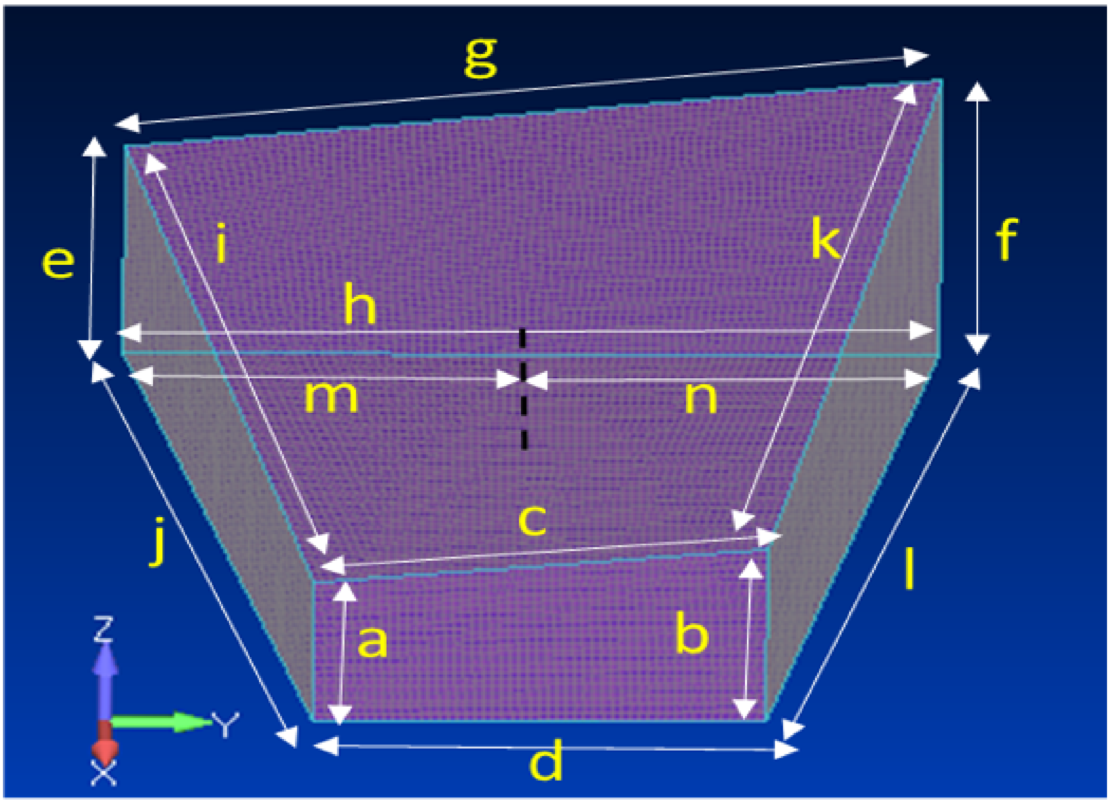

Figure 3.4: A general description of principal dimensions covering all 10 case studies.

Table 3.15: Principal dimensions for each of the 10 case studies.

Parameters	Case studies									
(m)	1	2	3	4	5	6	7	8	9	10
a	0.2	0.2	0.2	0.2	0.2	0.2	0.2	0.2	0.217	0.217
b	0.2	0.2	0.2	0.2	0.3	0.25	0.25	0.2	0.290	0.290
c	0.5	0.5	0.5	0.5	0.51	0.502	0.502	0.5	1.338	1.338
d	0.5	0.5	0.5	0.5	0.5	0.5	0.5	0.5	1.342	1.342
e	0.2	0.2	0.2	0.2	0.3	0.3	0.3	0.2	0.224	0.224
f	0.2	0.2	0.2	0.2	0.4	0.4	0.4	0.2	0.300	0.300
g	0.5	0.5	0.9	0.9	0.51	0.906	0.906	0.585	1.398	1.398
h	0.5	0.5	0.9	0.9	0.5	0.9	0.9	0.585	1.402	1.402
i	1.0	1.0	1.02	1.0	1.005	1.025	1.0	0.22	0.584	0.584
j	1.0	1.0	1.0	1.0	1.0	1.198	1.05	0.22	0.584	0.584
k	1.0	1.0	1.02	1.077	1.005	1.308	1.087	0.236	0.590	0.590
l	1.0	1.0	1.02	1.077	1.0	1.02	1.077	0.236	0.591	0.591

Table 3.16: Taper ratio for case studies referring to Figure 3.5 and Table 3.15.

Taper	Case studies									
ratio	1	2	3	4	5	6	7	8	9	10
(h-d)/l	0	0	0.39	0.37	0.00	0.39	0.37	0.36	0.10	0.10
(g-c)/k	0	0	0.39	0.37	0.00	0.31	0.37	0.36	0.10	0.10
(g-c)/i	0	0	0.39	0.40	0.00	0.39	0.40	0.39	0.10	0.10
(h-d)/j	0	0	0.39	0.40	0.00	0.39	0.40	0.39	0.10	0.10
(e-a)/i	0	0	0.00	0.00	0.10	0.10	0.10	0.00	0.01	0.01
(e-a)/j	0	0	0.00	0.00	0.10	0.08	0.10	0.00	0.01	0.01
(f-b)/k	0	0	0.00	0.00	0.10	0.11	0.14	0.00	0.02	0.02
(f-b)/l	0	0	0.00	0.00	0.10	0.15	0.14	0.00	0.02	0.02
(e-f)/g	0	0	0.00	0.00	-0.20	-0.11	-0.11	0.00	-0.05	-0.05
(e-f)/h	0	0	0.00	0.00	-0.20	-0.11	-0.11	0.00	-0.05	-0.05
(a-b)/c	0	0	0.00	0.00	-0.20	-0.10	-0.10	0.00	-0.05	-0.05
(a-b)/d	0	0	0.00	0.00	-0.20	-0.10	-0.10	0.00	-0.05	-0.05

3.4.7 Case studies

Some explanations of each of the case studies are given below:

3.4.7.1 Case study 1 (metallic)

In this case study, a rectangular metallic wing box of constant cross section and a given element length is considered in the finite element analysis using FEMAP/NASTRAN to establish the torsional stiffness *GJ* (see Figure C1 of Appendix C). The left hand end of the element is cantilevered and the front face is loaded by two equal and opposite forces in the front and the rear so as to produce a pure torque about the shear centre and thus making sure that the loading caused no bending displacement of the cross section, but only twisting deformation. A certain amount of trial and error was required to produce a pure twist. The torsional stiffness *GJ* is then evaluated by using standard procedure, relating the applied torque to the rate of twist of the element. In this case study, the in-plane displacements of the front and rear faces are both restrained first and then unrestrained later when computing the torsional stiffness. However, this restriction does not prevent the torsional rotation. This essentially means that the ribs are rigid in the former and flexible in the latter. For theoretical calculation of the torsion constraint *J* which requires only the 2-D cross sectional details, the rear and the front face data are used to obtain *GJ* and an average value was worked out at the midpoint so as to make the results somehow comparable with the 3-D FEMAP/NASTRAN results. This strategy is consistently used for the rest of the case studies.

3.4.7.2 Case study 2 (metallic)

Case study 2 is essentially the same as case study 1 except that a refined mesh in FEMAP/NASTRAN is used to ensure that the convergence of results. Further refinement of the mesh did not alter the results to any appreciable extent. Therefore, the mesh in case study 2 is consistently used to ensure the accuracy of the results. Figure C2 of Appendix C corresponds to case study 2 and they are merely a duplication of Figure C1 of Appendix C with the understanding that case study 2 is simply based on refined mesh generation.

3.4.7.3 Case study 3 (metallic)

As the wing planform tapers, case study 3 principally focuses on the effect of taper ratio on the torsional stiffness *GJ* of the wing. In this particular case, only the wing planform taper is considered whereas the depth-wise taper in the span wise direction which is generally small is not taken into account by assuming the depth to be constant (see Figure C3 of Appendix C). As in the case of case studies 1 and 2, the beam element of Figure

C3 of Appendix C for case study 3 is still metallic and its rear end is cantilevered when applying a pure torque on the front face about a point which is as close to the shear centre as possible. (As before, this is achieved by trial and error method ensuring that the application of the load produces only torsional rotation and not any bending displacement). The wing planform tapers for both leading and trailing edges for this case as can be seen in Figure C3 of Appendix C.

3.4.7.4 Case study 4 (metallic)

Case study 4 is similar but different from case study 3 in the sense that the wing planform is not doubly tapered, but singly tapered linearly on the front which is essentially the leading edge as shown in Figure C4 of Appendix C. The trailing edge is assumed to be straight as shown. In this way, the case study 4 focuses on the effect of sweep on the torsional stiffness (GJ) of the section. As in previous cases, the beam element of Figure C4 of Appendix C for case study 4 is still metallic and its rear end is cantilevered when applying a pure torque on the front face about a point which is as close to the shear centre as possible. Case study 4 has an unsymmetrical cross section which is evident from the Figure C4 of Appendix C.

3.4.7.5 Case study 5 (metallic)

Case study 5 principally focuses on the effect of depth-wise taper ratio on the torsional stiffness GJ of the wing. In this particular case, only the depth-wise taper is considered whereas the wing planform remains constant (see Figure C5 of Appendix C). As in the case of previous case studies, the beam element for case study 5 is still metallic and its rear end is cantilevered when applying a pure torque on the front face about a point which is as close to the shear centre as possible. The depth-wise change in dimension is taken into account for both leading and trailing edges for this case as can be seen in Figure C5 of Appendix C.

3.4.7.6 Case study 6 (metallic)

Case study 6 is concerned with the effect of taper ratio for both leading edge and trailing edge on the torsional stiffness GJ of the wing. In this case both the wing planform as well as the depth-wise taper is in the span wise direction (see Figure C6 of Appendix C). As in the case of previous case studies, the beam element of Figure C6 of Appendix C is based on aluminium material. As before the rear end of the element is cantilevered when applying a pure torque on the front face about a point which is as close to the shear centre as possible.

3.4.7.7 Case study 7 (metallic)

Case study 7 is similar but different from case study 6 in the sense that the trailing edge is assumed to be straight whereas the leading edge is linearly tapered as shown in Figure C7 of Appendix C. Obviously the case study 7 focuses on the effect of sweep only. Here again, the beam element of Figure C7 of Appendix C for the case study 7 is still metallic and its rear end is cantilevered when applying a pure torque on the front face about a point which is as close to the shear centre as possible. Case study 7 has an unsymmetrical cross section which is evident from the Figure C7 of Appendix C.

3.4.7.8 Case study 8 (metallic)

Case study 8 in many ways is similar but different from case study 4 in the sense that dimensions are different even though the general layout is same. The trailing edge is assumed to be straight whereas the leading edge is linearly tapered as shown in Figure C8 of Appendix C. As in previous cases, the beam element of Figure C8 of Appendix C for case study 8 is still metallic and its rear end is cantilevered when applying a pure torque on the front face about a point which is as close to the shear centre as possible. Note that the case study 8 has an unsymmetrical cross section.

3.4.7.9 Case study 9 (metallic and composite)

Case study 9 is based on similar dimensions of composite wing at section 16, but without the presence of stringers and has four subcases: (a) Subcase 1 – wing box with cut-out (manhole) made up of aluminium, (b) Subcase 2 – wing box without cut-out (no manhole) made up of aluminium, (c) Subcase 3- wing box with cut-out made up of composite and (d) Subcase 4 – wing box without cut-out made up of composite (see Figure C9 of Appendix C). All of these 4 subcases of the wing box are created using FEMAP/NASTRAN. However, some simplifying assumptions are made in that the wing box dimensions are considered to be made up of corner nodes of the actual aircraft wing box so that the wing box surfaces are straight lines rather than curved lines whereas in the actual composite wing box both the upper and lower skin surfaces are curved. The dimension and location of the cut-out (manhole) are identical with the composite wing box. The relevant data for case study 9 are given in Figure C9 of Appendix C. This case study focuses on the effect of manhole on the torsional stiffness GJ for the composite wing and the differences it makes when using isotropic material as opposed to composites. Note that for case study 9, the rib is considered to be rigid for both metallic and composite subcases.

3.4.7.10 Case study 10 (composite)

Case study 10 is a portion of the actual composite wing which is actually Section 16 of the wing which unlike case study 9 includes the stringers. In essence, case study 10 has all the essential features covered in previous case studies (see Figure C10 of Appendix C). In all of the previous case studies the skin thicknesses were assumed to be constant, but for this case study, the upper skin, lower skin and the front spar have the same thickness whereas the rear spar and the ribs have different thicknesses that are representative of the original composite wing model. However, case study 10 has also two subcases: (a) Subcase 1 - wing box is made of composites and the ribs are considered elastic and made of composites, (b) Subcase 2 - wing box is made of composites, but the ribs are rigid, modelled by artificially increasing the elastic constants to a larger value. In the above two subcases, the presence of the manhole has been taken into account.

3.4.7.11 Discussion of results

The results of the first 8 case studies described above are shown in Table 3.7. The results of Table 3.17 shows that for case studies 1 and 2, the discrepancy between the results from FEMAP/NASTRAN and classical theory is quite small, notably within engineering accuracy, but for case studies 3 and 4, the difference in results is quite substantial. The results using classical theory were obtained by multiplying the (effective) shear rigidity with torsion constant J evaluated from $J = \frac{4A^2}{\oint \frac{ds}{t}}$ with A being the cell area and the integration $\oint \frac{ds}{t}$ is carried out all around the cross section. This could be attributed to the fact that the taper ratio for these two cases is significant which can alter the results sufficiently. Also, it should be noted that case 3 has doubly tapered and its GJ values are lot higher for case 4 which was singly tapered. Similar trends were observed for case studies 5 to 8 which had the added complexity of sweep angle in addition to the taper ratio. From case studies 6 and 7, it can be observed that the depth-wise taper does not contribute much to the GJ difference. The big differences in results in part, are due to the small element size chosen and the localise effect of the load applied when working out the stiffness. The GJ results for case studies 1 to 8 are shown in Figure 3.5 in a histogram plot. Case studies 6 and 7 show large differences between the GJ values at the tip and the root due to the differences in the dimensions at the two respective cross sections (see Figure C6 and C7 of Appendix C).

Table 3.17: The computed torsional stiffness GJ using FEMAP/NASTRAN and the corresponding values using classical theory for cases 1 to 8.

Cases	FEMAP/NASTRAN GJ (Nm^2)		Classical theory GJ (Nm^2)			% diff (Elastic)	% diff (Rigid)
	Elastic rib	Rigid rib	At tip	At root	Average		
1	5.14E+06	5.74E+06	5.40E+06	5.40E+06	5.40E+06	5	-6
2	5.00E+06	5.74E+06	5.40E+06	5.40E+06	5.40E+06	7	-6
3	6.82E+06	8.31E+06	5.40E+06	1.11E+07	8.27E+06	18	0
4	5.95E+06	6.47E+06	5.40E+06	1.11E+07	8.27E+06	28	22
5	7.62E+06	8.52E+06	7.82E+06	1.35E+07	1.07E+07	29	20
6	9.41E+06	1.18E+07	6.59E+06	2.99E+07	1.83E+07	48	36
7	9.32E+06	1.14E+07	6.59E+06	2.99E+07	1.83E+07	49	38
8	5.10E+06	7.11E+06	5.40E+06	6.59E+06	6.00E+06	15	-19

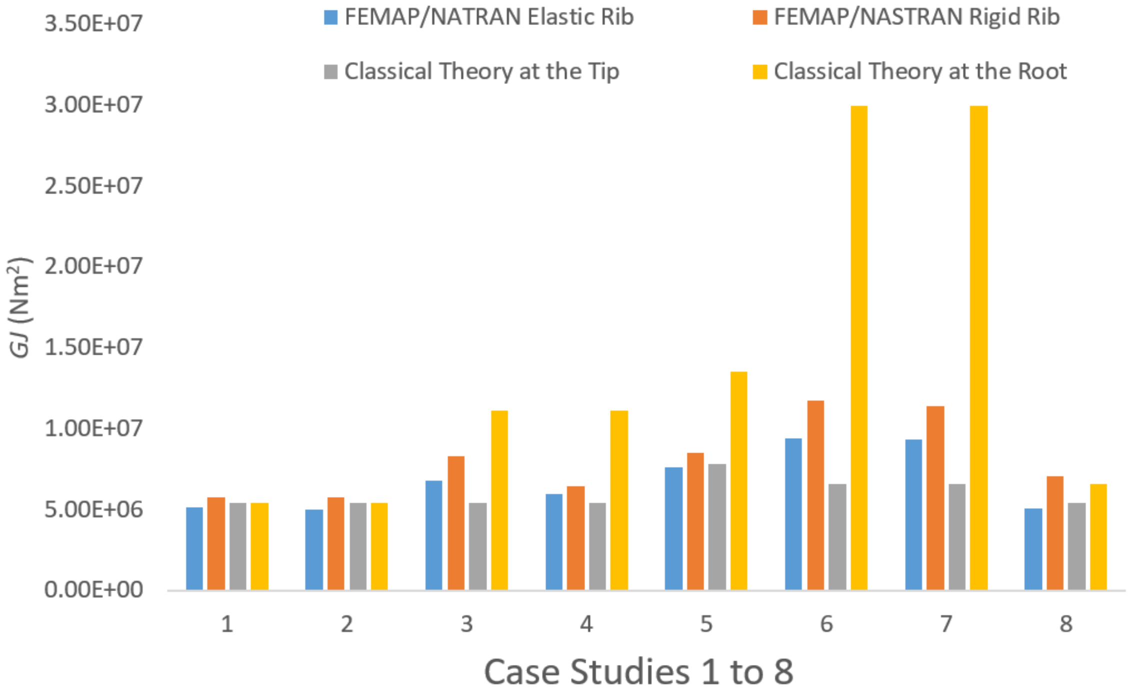

Figure 3.5: Distribution of torsional stiffness GJ for the first 8 case studies.

The case studies 9 and 10 (see Figures C9 and C10 of Appendix C) corresponds to Section 16 of the composite wing for which the former is representative of Section 16 of the composite wing but has no stringer attached and also the curved surfaces of the upper and lower skins are represented by straight surfaces. (This is in contrast to case study 10 which has all the components of the Section 16 of the composite wing both from geometrical and material properties points of view). The results for case studies 9(a) to 9(d) are given

Table 3.18: The computed torsional stiffness *GJ* using FEMAP/NASTRAN (Case 9).

Case study 9	FEMAP/NASTRAN results GJ (Nm^2)
(a) With manhole (aluminium)	4.03E+07
(b) Without manhole (aluminium)	4.15E+07
(c) With manhole (composite)	4.95E+07
(d) Without manhole (composite)	5.05E+07

in Table 3.18 and Figure 3.6 which clearly indicate that the effect of cut-out (manhole) is small both for aluminium and composite sections. These sections have similar dimensions to those of Section 16 of the composite wing as mentioned except that the stringers have not been taken into account in the stiffness analysis.

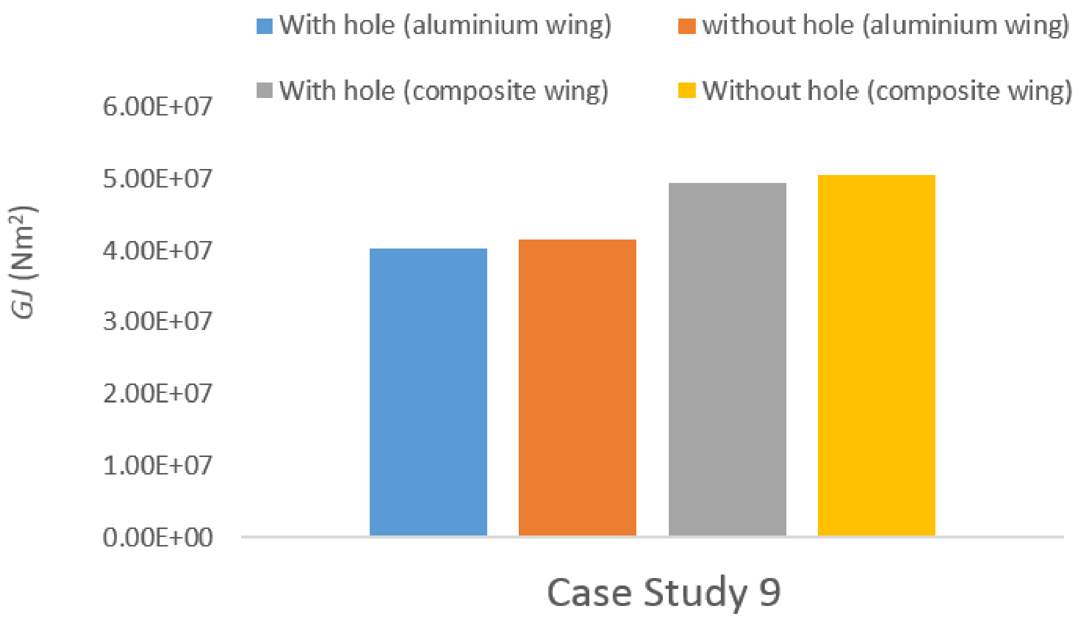

Figure 3.6: Torsional stiffness *GJ* for case study 9.

The final set of results for the torsional stiffness *GJ* concerning case study 10 (which corresponds to an exact replica of Section 16 of the composite wing including the stringers and cut-out) are given in Table 3.19 and Figure 3.7. The case studies 10(a) and 10(b) are for Section 16 of composite wing with elastic and rigid ribs, respectively. Clearly the results from case study 10 reveal that the FEMAP/NASTRAN stiffness results are very different from the classical theory results, particularly when the results from FEMAP /NASTRAN are based on rigid rib. The exact reason for this has not identified and the matter needs further investigation. The probable cause could be in part due to the use of

Table 3.19: The computed torsional stiffness *GJ* using FEMAP/NASTRAN and the corresponding values using classical theory for case study 10.

Case study 10 for Section 16 of composite wing						
FEMAP/NASTRAN GJ (Nm^2)		Classical theory GJ (Nm^2)			% diff (Elastic)	% diff (Rigid)
Elastic rib	Rigid rib	At tip	At root	Average		
3.53E+07	4.88E+07	3.14E+07	3.54E+07	3.34E+07	-6	-46

exceptionally small element and the application of the loading point to produce a pure torque about the centre of twist or shear centre.

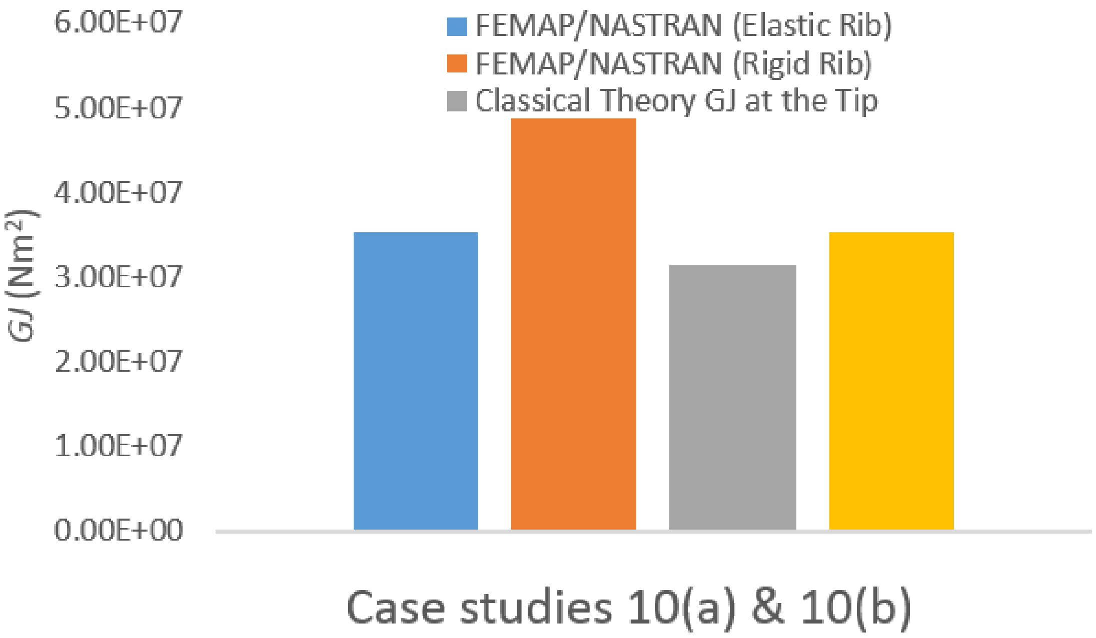

Figure 3.7: Torsional stiffness *GJ* for section 16 of the composite wing using FEMAP /NASTRAN analysis and classical theory.

3.4.8 Effects of bending-torsion coupling stiffnesses on the flutter speed and frequency

One of the most interesting and intriguing features in composite wing design is the fact that the bending-torsion coupling stiffness K can be taken advantage of to enhance the flutter characteristics. In the absence of accurately computed torsional stiffness GJ of the composite wing, a small, but limited flutter analysis has been carried out to show the effects of K on the flutter speed and flutter frequency of composite wing. A non-dimensional parameter α given by $\alpha = \frac{K^2}{EI \times GJ}$, $(0 < \alpha < 1)$ is defined to show some representative results. The stiffness data used and the non-dimensional parameter α are given in Table 3.20. The results of the flutter analysis using CALFUN by varying the non-dimensional parameter α are given in Table 3.21. Clearly, the Table 3.21 shows that significant changes in flutter speed and flutter frequency are possible as a result of the bending-torsion coupling stiffness parameter. Also it should be noted that bending-torsion coupling does not exist in metallic wing.

Table 3.20: Bending, torsional and bending-torsion coupling stiffness data used in CALFUN.

Bending and torsional stiffnesses		Coupling stiffness $\boldsymbol{K}$ and $\alpha = \frac{K^2}{EI \times GJ}$, $(0<\alpha<1)$				
EI (Nm^2)	GJ (m^2)	$K(\alpha=0)$	$K(\alpha=0.01)$	$K(\alpha=0.25)$	$K(\alpha=0.50)$	$K(\alpha=0.75)$
1.96E+06	1.51E+06	0.0	1.72E+05	8.61E+05	1.22E+06	1.49E+06
4.39E+06	4.73E+06	0.0	4.56E+05	2.28E+06	3.22E+06	3.95E+06
9.31E+06	1.24E+07	0.0	1.08E+06	5.38E+06	7.61E+06	9.32E+06
1.85E+07	2.75E+07	0.0	2.25E+06	1.13E+07	1.59E+07	1.95E+07
2.70E+07	6.06E+07	0.0	4.05E+06	2.02E+07	2.86E+07	3.51E+07
9.48E+07	2.19E+08	0.0	1.44E+07	7.21E+07	1.02E+08	1.25E+08
2.11E+08	3.25E+08	0.0	2.62E+07	1.31E+08	1.85E+08	2.27E+08

Table 3.21: Bending-torsion coupling effects on flutter speed and flutter frequency.

	K(α=0)	K(α=0.01)	K(α=0.25)	K(α=0.50)	K(α=0.75)
Flutter Speed (m/s)	366.75	368.25	375	386	278.25
Flutter Frequency (Hz)	8.05	8.01	7.46	6.68	11.96

3.5 Conclusions

It can be concluded that special attention needs to be paid to validate and improve the model of calculating a wing box stiffness using BOXMXES based on 2D thin-walled box beam theory. For validation purpose, a modelling method has been developed for extracting the *EI* and *GJ* values from the FEMAP/NASTRAN model of the 3D wing box. It should be noted that 2D model does not take into account manhole in its analysis. Based on the results obtained, the maximum difference between the *EI* obtained from the 2D BOXMXES model and the 3D FEMAP/NASTRAN model is around 36%. It is also noted that such large difference only occurs in the inboard wing made of double cell wing box with large geometric variation. For the outboard wing made of single cell boxes, the maximum *EI* difference is about 21%. The maximum difference between the *GJ* obtained from the 2D BOXMXES model and the 3D FEMAP/NASTRAN model remains about 55% in the inboard wing. For the outboard wing, the maximum difference is around 28%. From the parametric study of the geometric effect on the 2D model stiffness, it is clear that the geometric features such as cut-outs, sweep, taper ratio, flexible ribs in the 3D of the wing box have significant effects on the torsional stiffness, *GJ*, especially the presence of taper along the wing planform contributes more to the torsional stiffness than other parameters such as manholes, rigidity of ribs and sweep angle.

Chapter 4

High aspect ratio aircraft wings

4.1 Introduction to free vibration and flutter analysis of high aspect ratio metallic aircraft wings

In this chapter, the free vibration and flutter behaviour of a range of high aspect ratio metallic aircraft wings are investigated. The theory is already given in Chapter 1. The variety of aircraft analysed is quite diverse and includes sailplane, light aircraft trainer and transport aircraft. The wings of these aircraft are sufficiently slender with aspect ratios ranging typically between 6 and 30. As a consequence, they are easily prone to vibration and other dynamic problems. In this respect, free vibration and flutter analysis of aircraft wings, particularly those with high aspect ratios is indeed an important area of research. Furthermore, it is one of the mandatory airworthiness requirements, laid down by the aviation authorities. Sailplane, light aircraft trainer and transport airliner wings are typical examples for which the free vibration and flutter analysis is of great significance. For high aspect ratio wings such as the ones described above, the bending (EI) and torsional stiffnesses (GJ) play significant roles which affect the modal behaviour. Additionally, the engine masses and their locations can also be significant parameters to influence the modal analysis. The purpose of this chapter is to carry out a detailed analysis and investigate the free vibration and flutter behaviour for a range of high aspect ratio aircraft wings by applying the dynamic stiffness method.

One of the motivations for modal analysis of aircraft wings originates from the fact that it is a fundamental prerequisite to carry out an aeroelastic or response analysis, when using the normal mode method. There are some published literature which elucidates the importance of this research [5, 29, 30]. The current research focuses first on the free vibration and flutter analysis of eight aircraft wings, namely those of two sailplanes, two light aircraft trainers and four transport aircraft by using the bending and torsional stiffness data calculated from the original design of each aircraft wing. Next, the bending and torsional stiffnesses of the original wings are altered between +25% and -25% insteps of 5% and their subsequent effects on the modal behaviour of the wings and flutter analysis are carried out. This is followed by further investigation wherein the engine mass and its location wherever applicable, are varied and the free vibration and flutter behaviour is re-examined. In each case, the wing is idealised as an assembly of bending-torsional coupled beams for which the frequency dependent dynamic stiffness matrix is well established [12, 13]. The investigation needed considerable efforts for data preparation to model each of the aircraft wings. Once the data preparation was completed, a detailed parametric study with the variations of bending and torsional stiffnesses, the engine mass and its location wherever applicable was undertaken and the free vibration and flutter analysis was carried out on each of the wings. The results shows some interesting trends which are discussed and commented on in this chapter.

4.2 Particulars of the aircraft considered for the analysis

Using the dynamic stiffness method for a bending-torsion coupled beam mentioned in Chapter 1 of this thesis, three categories of aircraft wings with cantilever boundary condition at the root are analysed for their free vibration and flutter characteristics. In the first category, a class of high aspect ratio, high performance sailplane wings are considered. A typical layout of such a sailplane is shown in Figure 4.1. Some particulars of the two sailplanes (S_1 and S_2) are given in Table 4.1. The second category of aircraft wings analysed belongs to two light aircraft trainers. A general layout of these two light aircraft trainers (L_1 and L_2) is shown in Figure 4.2, and Table 4.2 gives their particulars. The third category of aircraft wings analysed belongs to transport airliners. A typical layout of such aircraft is shown in Figure 4.3. Four wings of transport airliners (T_1, T_2, T_3 and T_4) with particulars given in Table 4.3 are analysed. The wide range of aircraft analysed has marked differences in their specification and other properties, particularly, the operating empty weight (OWE) and the maximum take off weight (MTOW) are very different. Figure 4.4 represents the three different categories of aircraft in logarithmic scale to show the wide variety of high aspect ratio aircraft considered for the analysis.

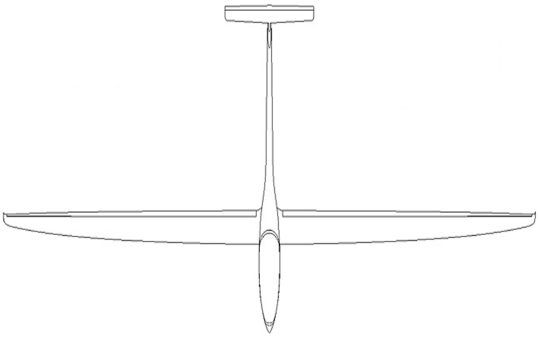

Figure 4.1: A general lay-out of a typical sailplane.

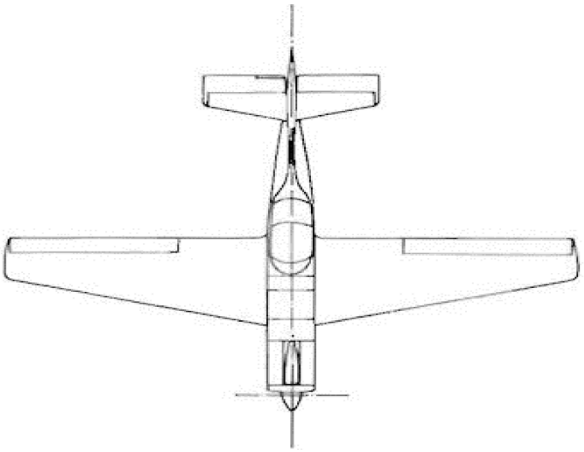

Figure 4.2: A general lay-out of a typical light aircraft trainer aircraft.

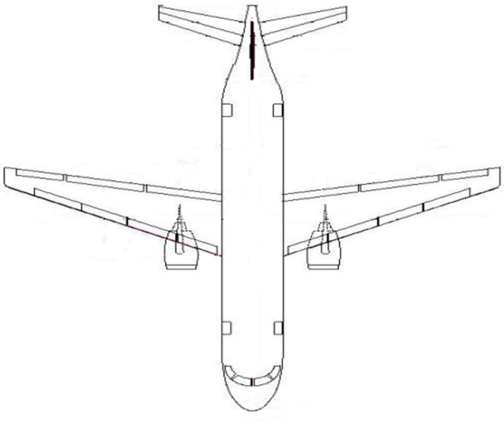

Figure 4.3: A general lay-out of a typical transport aircraft.

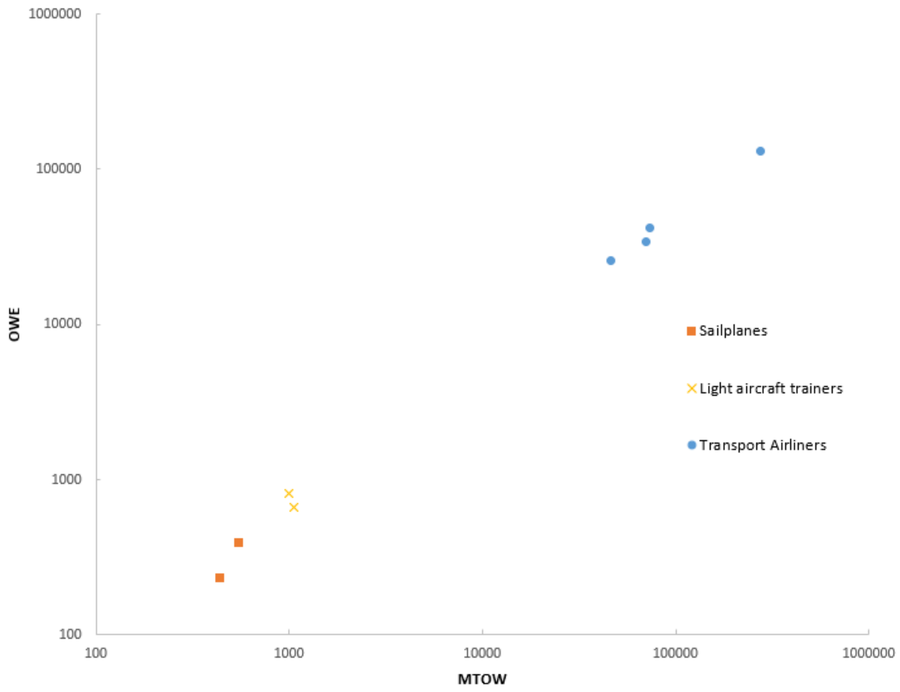

Figure 4.4: Three different categories of aircraft represented in logarithmic scale (OWE - operating empty weight, MTOW - maximum take-off weight).

Table 4.1: Particulars of sailplanes.

Parameters	Sailplane	
	Sailplane-S_1	Sailplane-S_2
Wing Span (m)	22	15
Wing Area (m^2)	15.44	10.05
Aspect Ratio	31.35	22.4
Wing Root Chord (m)	1.0	0.9
Wing Tip Chord (m)	0.4	0.4
Sweep angle (deg)	0	0
Length overall (m)	7.6	6.72
Height Overall (m)	2.0	2.0
Weight Empty (kg)	390	234
Max Take-off weight (kg)	550	440
Max Wing Loading (kg/m^2)	37	36
Max Cruising Speed (knots)	135	105

Table 4.2: Particulars of trainers (Light aircraft).

Parameters	Light aircraft trainers	
	Trainer-L_1	Trainer-L_2
Wing Span (m)	10	10
Wing Area (m^2)	12	15
Aspect Ratio	8.3	6.7
Wing Root Chord (m)	1.5	1.9
Wing Tip Chord (m)	0.9	0.9
Sweep angle (deg)	2.3	8.36
Length overall (m)	7.08	8.05
Height Overall (m)	2.73	2.7
Weight Empty (kg)	669	808
Max Take-off weight (kg)	1066	1000
Max Cruising Speed (knots)	130	155

Table 4.3: Particulars of transport airliners.

Parameters	Transport airliner			
	T_1	T_2	T_3	T_4
Wing Span (m)	40	30	35	60
Wing Area (m^2)	162	93	123	362
Aspect Ratio	10	9	10	10
Wing Root Chord (m)	5.0	5.5	6.0	10.5
Wing Tip Chord (m)	2.5	1.5	1.5	2.5
Sweep angle (deg)	0	28	28	28
Length overall (m)	30	36	38	60
Height Overall (m)	12	11	12	17
Weight Empty (kg)	34,000	26,000	42,000	130,000
Max Take-off weight (kg)	70,000	46,000	74,000	275,000
Max Wing Loading (kg/m^2)	434	511	600	760
Max Cruising Speed (knots)	348	529	516	569
Range (nmi)	2835	2400	2592	8000

4.3 Stiffness distribution, mode shapes and flutter results for unmodified wings

As essential data required for the free vibration analysis, Figure 4.5 represents the stiffness distribution (bending (EI) and torsional (GJ) stiffnesses) of the sailplanes S_1 and S_2, respectively. Figure 4.6 illustrates the first five natural frequencies and mode shapes of S_1 and S_2 showing the bending displacements by solid black lines and torsional displacements by broken red lines. Clearly the first three modes of both sailplanes are essentially the bending mode whereas the fourth mode for each wing is a torsional one. By contrast, the fifth mode is bending for sailplane S_1 but a coupled mode for sailplane S_2.

Now turning attention to the light aircraft trainers L_1 and L_2, Figure 4.7 represents their stiffness distributions (bending (EI) and torsional (GJ) stiffnesses) which were used to compute their natural frequencies and mode shapes. Figure 4.8 illustrates the first five natural frequencies and mode shapes of L_1 and L_2, respectively showing the bending displacements by solid black lines and torsional displacements by broken red lines. Clearly for light aircraft trainer L_1, the first four modes are the bending modes while the fifth mode is a torsional one. By contrast, for light aircraft trainer L_2, the first two modes are bending, third and fifth modes are torsional while the fourth mode is coupled.

Next the free vibration analysis of the transport aircraft wings is carried out. Figure 4.9 represents the stiffness distribution (bending (EI) and torsional (GJ) stiffnesses) of the transport aircraft wings T_1, T_2, T_3, and T_4, respectively, which were used to compute their natural frequencies and mode shapes. Figure 4.10 illustrates the first five natural frequencies and mode shapes of the transport airliners T_1, T_2, T_3, and T_4 showing the bending displacements by solid black lines and torsional displacements by broken red lines. For the transport airliner T_1, the first two modes are the bending modes, third mode is coupled, fourth mode is bending and the fifth mode is torsional. For T_2 wing, the first three modes are predominantly the bending modes, fourth and fifth modes are coupled. For T_3 wing, the first three modes are dominated by bending but the fourth and the fifth modes are essentially torsional. For T_4 wing, the first two and the fourth modes are the bending dominated whereas the third and the fifth modes are torsional.

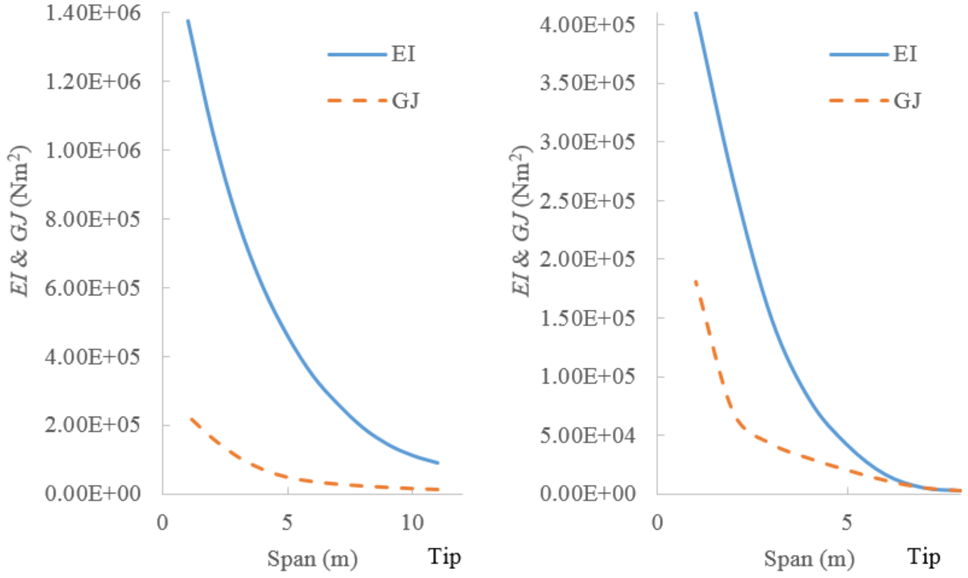

Stiffness distribution of sailplane S_1 Stiffness distribution of sailplane S_2

Figure 4.5: Stiffness distributions of sailplane wings.

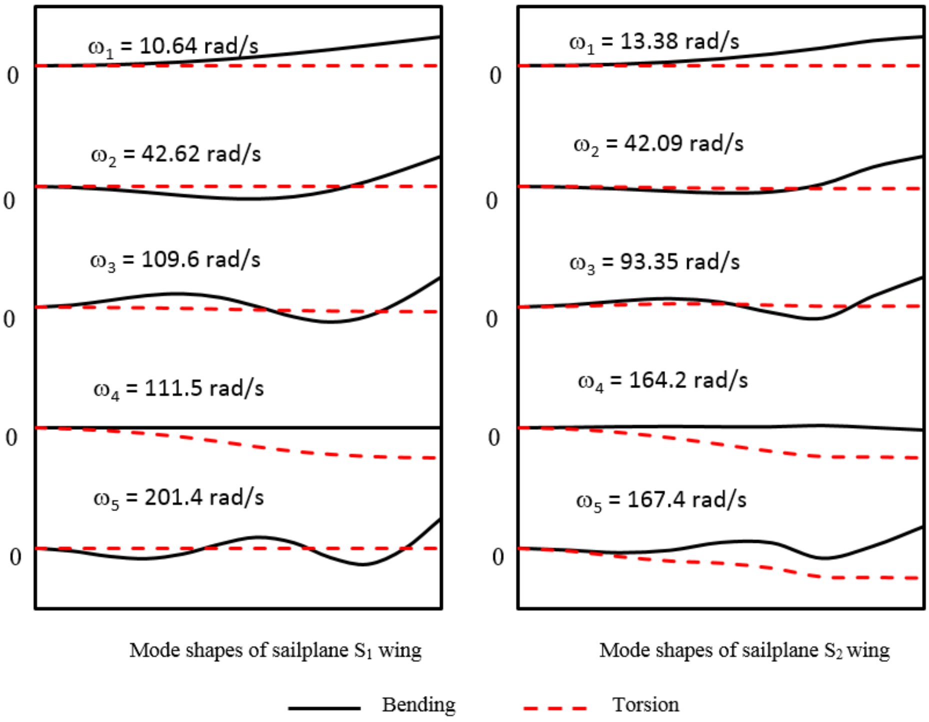

Mode shapes of sailplane S_1 wing Mode shapes of sailplane S_2 wing

Figure 4.6: Mode shapes of sailplane wings.

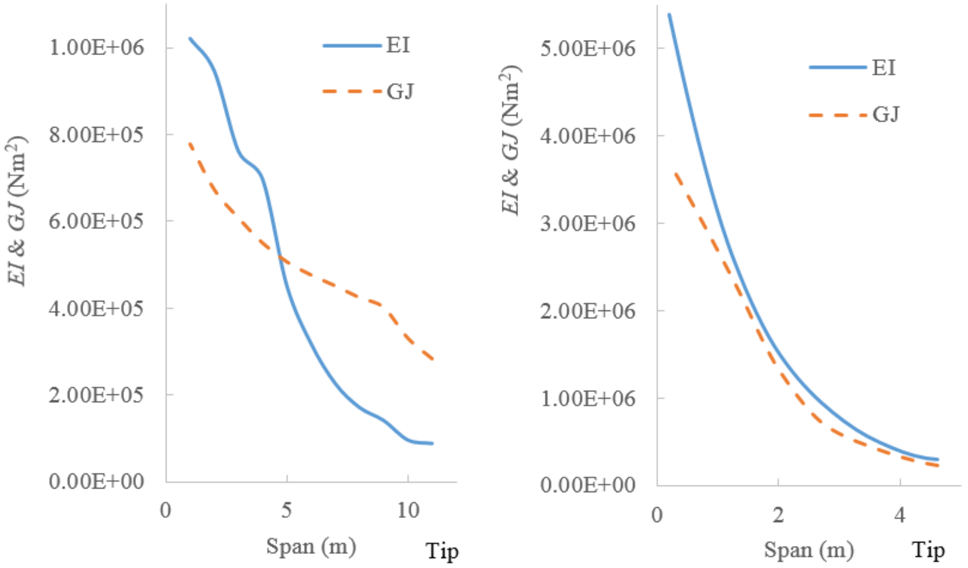

Stiffness distribution of light aircraft trainer L$_1$ Stiffness distribution of light aircraft trainer L$_2$

Figure 4.7: Stiffness distribution of light aircraft trainers.

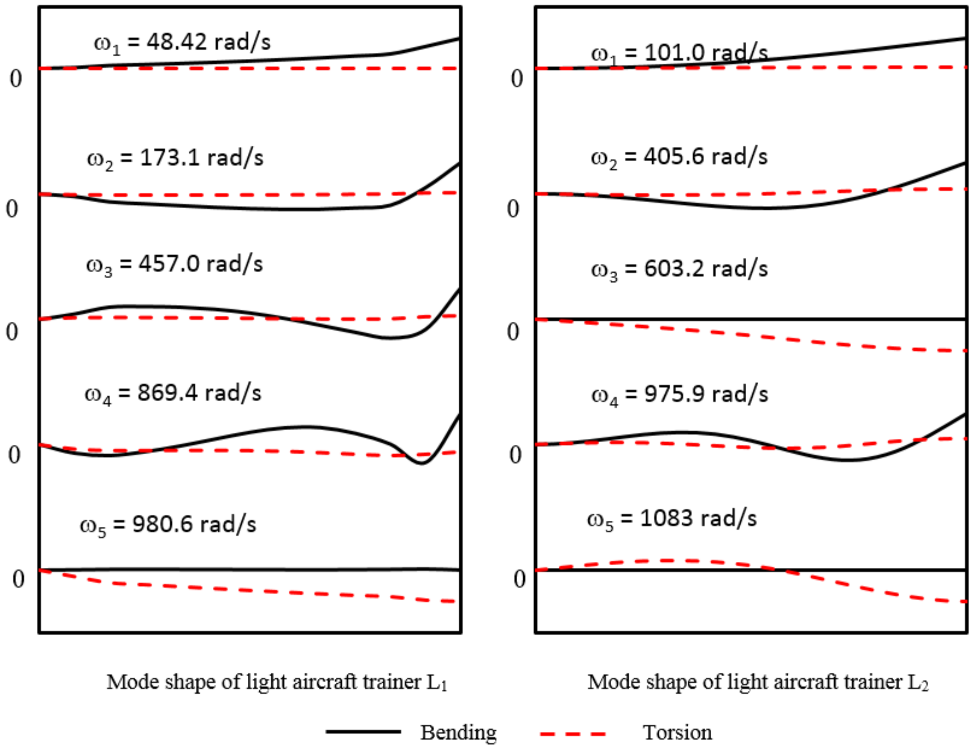

Mode shape of light aircraft trainer L$_1$ Mode shape of light aircraft trainer L$_2$

Figure 4.8: Mode shapes of light aircraft trainer.

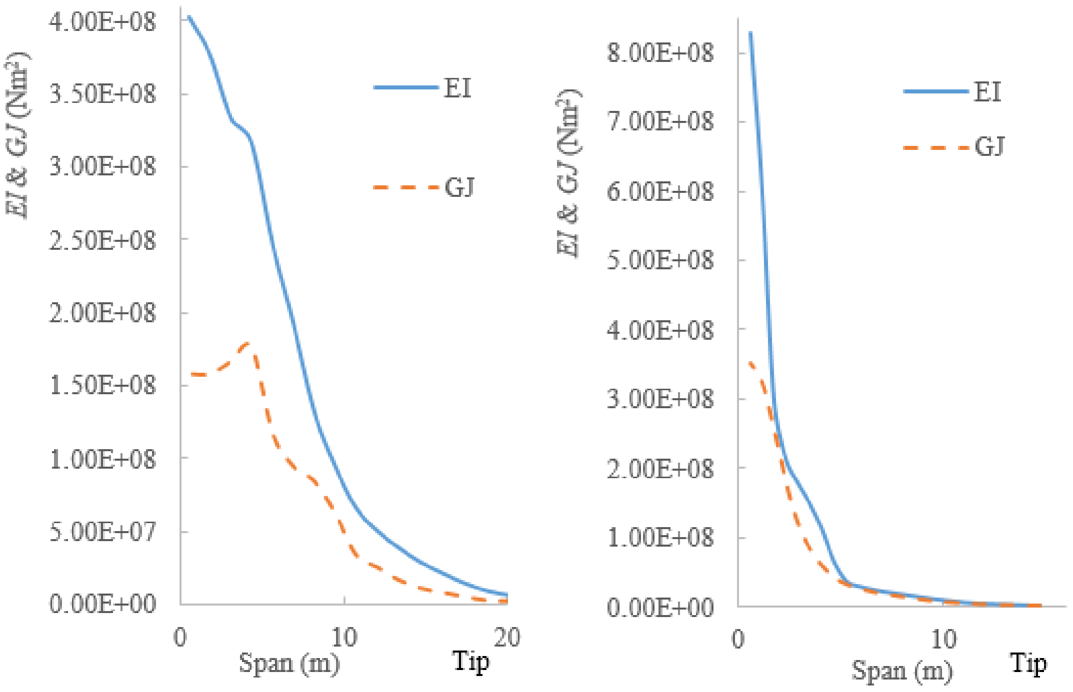

Stiffness distribution of transport airliner T$_1$ Stiffness distribution of transport airliner T$_2$

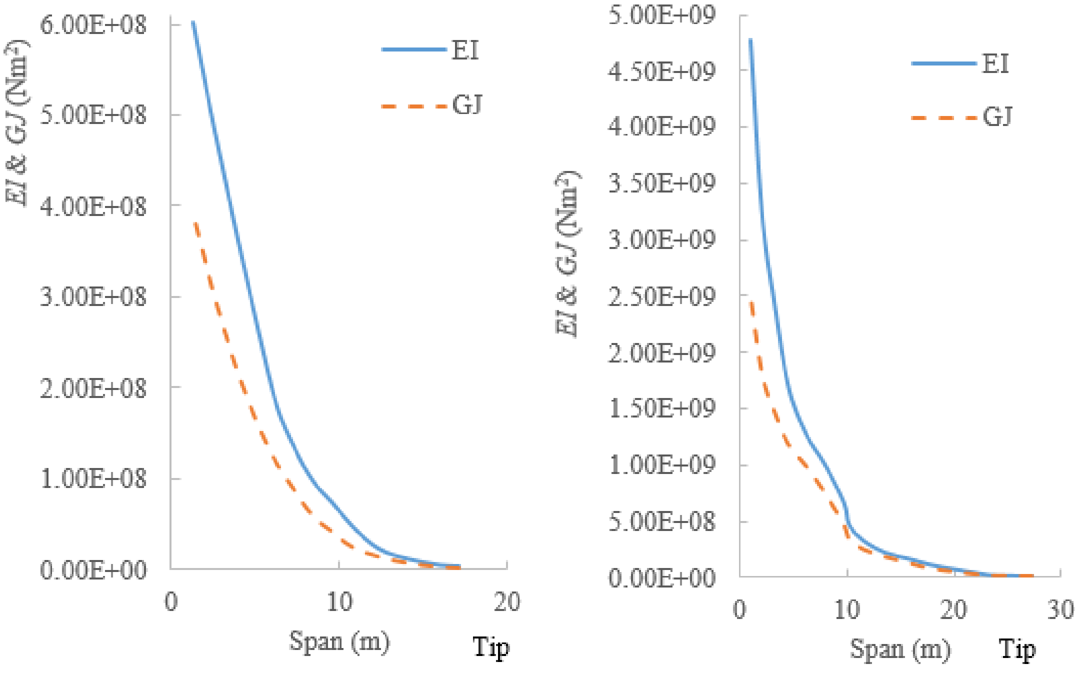

Stiffness distribution of transport airliner T$_3$ Stiffness distribution of transport airliner T$_4$

Figure 4.9: Stiffness distributions of transport airliner.

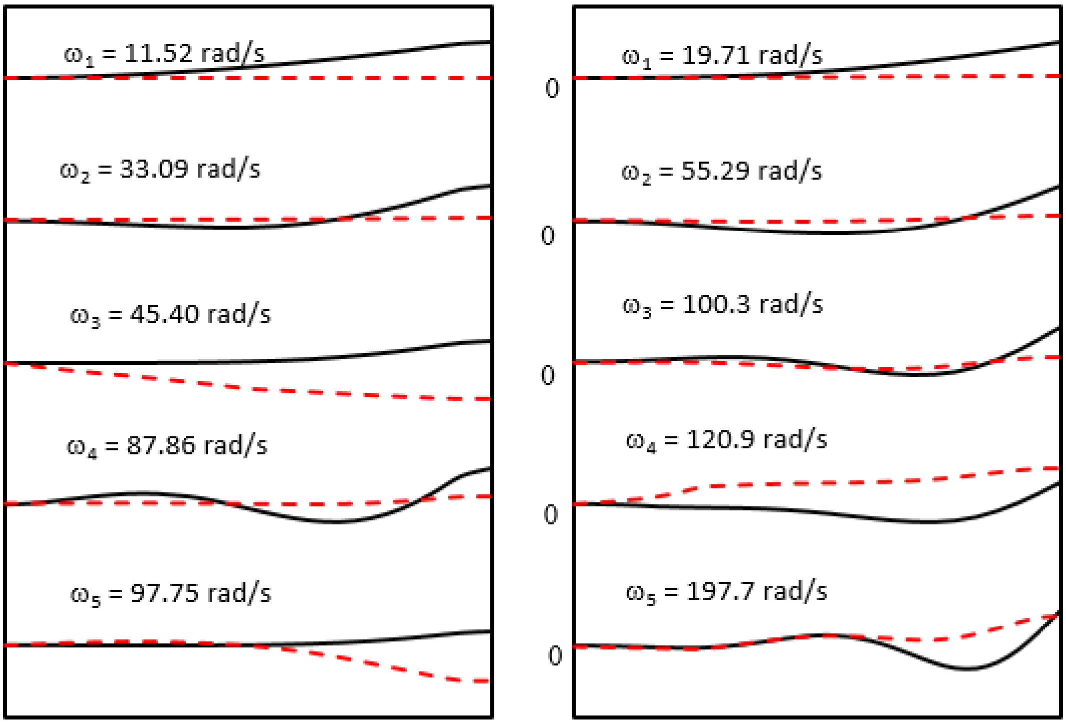

Mode shape of transport airliner T_1

Mode shape of transport airliner T_2

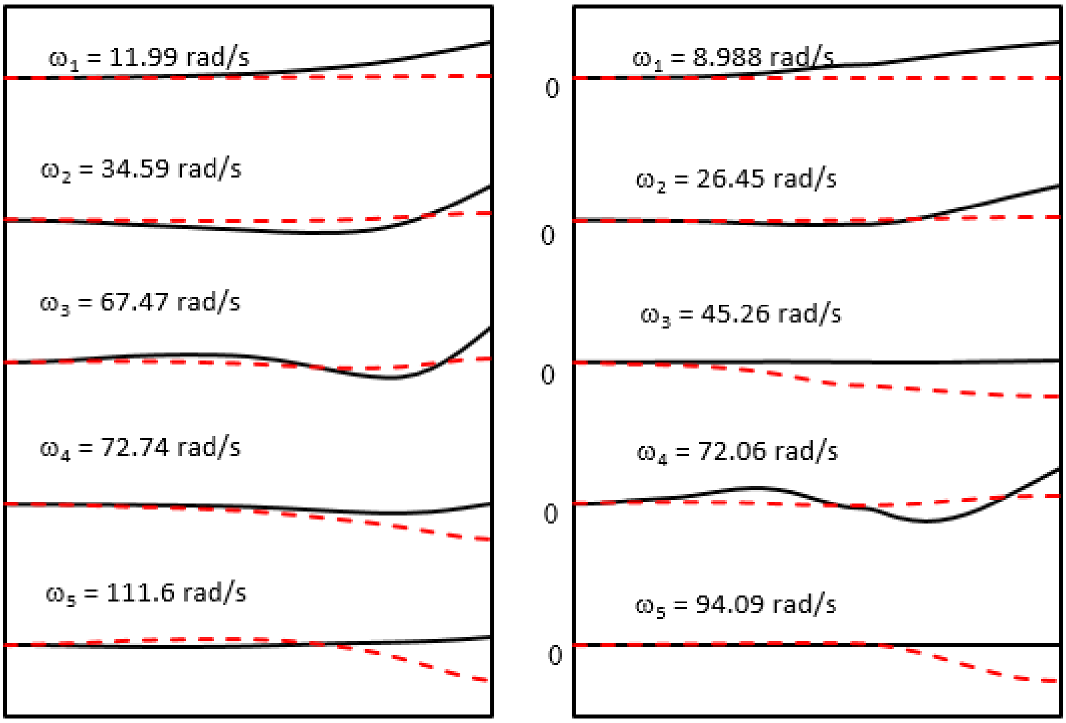

Mode shape of transport airliner T_3

Mode shape of transport airliner T_4

Figure 4.10: Mode shapes of transport airliner.

The first five natural frequencies for all of the aircraft wings (S_1, S_2, L_1, L_2, T_1, T_2, T_3 and T_4) are given in Table 4.4. The letters B and T used in the table and elsewhere in the thesis indicate bending and torsion dominated modes respectively whereas the letter C indicates a bending torsion coupled mode. Following the free vibration analysis, the flutter analysis is carried out next for all of the three categories of aircraft. Table 4.5 gives the flutter speed and flutter frequencies of the two sailplanes (S_1 and S_2), two light trainer aircraft (L_1 and L_2) and four transport airliner (T_1, T_2, T_3 and T_4).

Table 4.4: First five natural frequencies of the baseline aircraft wings.

Aircraft category	Natural frequencies (ω_i) (rad/s)				
	ω_1	ω_2	ω_3	ω_4	ω_5
Sailplane S_1	10.64 (B)	42.62 (B)	109.6 (B)	111.5 (T)	201.4 (B)
Sailplane S_2	13.38 (B)	42.09 (B)	93.35 (B)	164.2 (T)	167.4 (C)
Light aircraft trainer L_1	48.42 (B)	173.1 (B)	457.0 (B)	869.4 (B)	980.6 (T)
Light aircraft trainer L_2	101.0 (B)	405.6 (B)	603.2 (T)	975.9 (C)	1083 (T)
Transport airliner T_1	11.52 (B)	33.09 (B)	45.40 (C)	87.86 (B)	97.75 (T)
Transport airliner T_2	19.71 (B)	55.29 (B)	100.3 (B)	120.9 (C)	197.7 (C)
Transport airliner T_3	11.99 (B)	34.59 (B)	67.47 (B)	72.74 (T)	111.6 (T)
Transport airliner T_4	8.988 (B)	26.45 (B)	45.26 (T)	72.06 (B)	94.09 (T)

Table 4.5: Flutter speed and flutter frequency of the baseline aircraft wings.

Aircraft category	Flutter speed V_s (m/s)	Flutter frequency (ω) (rad/s)
Sailplane S_1	71	53.70
Sailplane S_2	77	76.16
Light aircraft trainer L_1	1543	59.96
Light aircraft trainer L_2	1065	298.9
Transport Airliner T_1	249	28.77
Transport Airliner T_2	411	78.56
Transport Airliner T_3	284	42.44
Transport Airliner T_4	385.8	46.50

4.4 Variations of bending and torsional stiffnesses on aircraft wings

Next, a detailed parametric study is carried out by varying the bending and torsional stiffnesses of each wing for all of the three categories of aircraft (sailplanes, light aircraft trainers and transport airliners). The stiffness properties are varied between -25% to 25% in steps of 5% and both free vibration and flutter analyses are carried out. Representative results are given in Tables 4.6 to 4.37. Tables 4.6 to 4.9 represents the results obtained for sailplane S_1, Tables 4.10 to 4.13 represents the results obtained for sailplane S_2, Tables 4.14 to 4.17 represents the results obtained for light aircraft trainer L_1, Tables 4.18 to 4.21 represents the results obtained for light aircraft trainer L_2, Tables 4.22 to 4.25 represents the results obtained for transport airliner T_1, Tables 4.26 to 4.29 represents the results obtained for transport airliner T_2, Tables 4.30 to 4.33 represents the results obtained for transport airliner T_3 and Tables 4.34 to 4.37 represents the results obtained for transport airliner T_4.

For sailplane S_1, the first five natural frequencies due to the variation of EI and GJ are presented in Tables 4.6 and 4.7 respectively. Clearly it can be seen from the tables, that when bending stiffness EI is varied bending dominated modes vary significantly but torsional dominated modes vary only slightly. Similarly when torsional stiffness GJ is varied torsion dominated modes vary significantly while bending dominated modes vary slightly. This phenomenon as expected is observed for all other aircraft wings.

From Table 4.6, it is clear that for the S_1 sailplane the first, second and fifth modes are bending modes for the original configuration. Interesting results can be observed for the third and the fourth modes. The nature of these modes does not change when the bending stiffness EI is decreased. However, these modes swap from bending to torsion when the bending stiffness EI is increased as can be seen in the table. The fourth mode remains torsional when EI is decreased and becomes bending modes when EI is increased. With respect to the variation of GJ shown in Table 4.7, the nature of the first, second and fifth modes remains unchanged as bending modes. By contrast, the third mode changes from bending to torsion when the GJ is reduced while it remains bending as the GJ is increased. The fourth mode changes from torsion to bending as the GJ is decreased while it remains torsional as the GJ is increased. It should be noted from the results that the stiffness variation causes modal interchanges (flip over) between bending and torsion as evident from Tables 4.6 and 4.7.

Table 4.6: The effects of the variation of *EI* on the natural frequencies of S_1 wing.

Variation in *EI* (%)	ω_i (rad/s)				
	ω_1	ω_2	ω_3	ω_4	ω_5
-25	9.216 (B)	36.91 (B)	94.96 (B)	111.5 (T)	174.4 (B)
-20	9.519 (B)	38.12 (B)	98.07 (B)	111.5 (T)	180.1 (B)
-15	9.812 (B)	39.29 (B)	101.1 (B)	111.5 (T)	185.7 (B)
-10	10.09 (B)	40.43 (B)	104.0 (B)	111.5 (T)	191.1 (B)
-5	10.37 (B)	41.54 (B)	106.9 (B)	111.5 (T)	196.3 (B)
0	10.64 (B)	42.62 (B)	109.6 (B)	111.5 (T)	201.4 (B)
5	10.91 (B)	43.67 (B)	111.5 (T)	112.4 (B)	206.4 (B)
10	11.16 (B)	44.69 (B)	111.5 (T)	114.9 (B)	211.2 (B)
15	11.41 (B)	45.70 (B)	111.5 (T)	117.6 (B)	215.9 (B)
20	11.66 (B)	46.69 (B)	111.5 (T)	120.1 (B)	220.6 (B)
25	11.89 (B)	47.65 (B)	111.5 (T)	122.6 (B)	225.2 (B)

Table 4.7: The effects of the variation of *GJ* on the natural frequencies of S_1 wing.

Variation in *GJ* (%)	ω_i (rad/s)				
	ω_1	ω_2	ω_3	ω_4	ω_5
-25	10.64 (B)	42.62 (B)	96.59 (T)	109.6 (B)	201.4 (B)
-20	10.64 (B)	42.62 (B)	99.76 (T)	109.6 (B)	201.4 (B)
-15	10.64 (B)	42.62 (B)	102.8 (T)	109.6 (B)	201.4 (B)
-10	10.64 (B)	42.62 (B)	105.8 (T)	109.6 (B)	201.4 (B)
-5	10.64 (B)	42.62 (B)	108.7 (T)	109.7 (B)	201.4 (B)
0	10.64 (B)	42.62 (B)	109.6 (B)	111.5 (T)	201.4 (B)
5	10.64 (B)	42.62 (B)	109.6 (B)	114.3 (T)	201.4 (B)
10	10.64 (B)	42.62 (B)	109.6 (B)	116.9 (T)	201.4 (B)
15	10.64 (B)	42.62 (B)	109.6 (B)	119.6 (T)	201.4 (B)
20	10.64 (B)	42.62 (B)	109.6 (B)	122.2 (T)	201.4 (B)
25	10.64 (B)	42.62 (B)	109.6 (B)	124.7 (T)	201.4 (B)

Table 4.8 represents the flutter speed and flutter frequency obtained due to the variation of *EI* and Table 4.9 represents the flutter speed and flutter frequency obtained due to the variation of *GJ* for sailplane S_1. It can be seen from Table 4.8 that variation of *EI* does not affect flutter speed much, but for Table 4.9 it can be observed that as *GJ* value increases

flutter speed increases. However, when GJ value decreases flutter speed also decreases, this is to be expected because torsional stiffness GJ generally plays a greater role in flutter analysis and increasing GJ increases the flutter speed.

Table 4.8: The effects of the variation of EI on the flutter analysis of S_1 wing.

Variation in EI (%)	Flutter speed V_s (m/s)	Flutter frequency ω (rad/s)
-25	71.09	53.26
-20	71.07	53.34
-15	71.05	53.42
-10	71.02	53.52
-5	71.00	53.61
0	71.00	53.70
5	71.00	53.17
10	71.00	53.85
15	71.00	53.93
20	71.00	54.06
25	71.00	54.08

Table 4.9: The effects of the variation of GJ on the flutter analysis of S_1 wing.

Variation in GJ (%)	Flutter speed V_s (m/s)	Flutter frequency ω (rad/s)
-25	61.5	46.94
-20	63.5	48.38
-15	65.5	49.68
-10	67.4	51.1
-5	69.2	52.5
0	71.0	53.70
5	72.8	54.96
10	74.5	56.1
15	76.2	57.34
20	77.8	58.49
25	79.5	59.64

For sailplane S_2, the first five natural frequencies computed by varying EI and GJ are shown in Tables 4.10 and 4.11 respectively. From the results in Table 4.10, it is clear that the first, second and third modes are always bending modes. The fourth mode changes from torsional to a coupled one as the *EI* is decreased, while this mode remains torsional as the *EI* is increased. The fifth mode changes from coupled to a torsional one as the *EI* is decreased, while the mode shapes remain as coupled as the *EI* is increased. With respect to the variation of *GJ* in Table 4.11, the modes corresponding to the first, second and third natural frequencies remain unchanged as bending modes regardless of the variations within the range. The fourth mode remains torsional as the *GJ* is decreased while it changes from torsional to coupled modes as the *GJ* is increased. The fifth mode remains as coupled as the *GJ* is decreased while it changed from coupled to torsional as the *GJ* is increased. Here again, the modal interchanges (flip over) between torsional and coupled modes are prevalent as a result of the *GJ* variations, see Tables 4.10 and 4.11.

Table 4.10: The effects of the variation of *EI* on the natural frequencies of S_2 wing.

Variation in *EI* (%)	ω_i (rad/s)				
	ω_1	ω_2	ω_3	ω_4	ω_5
-25	11.59 (B)	36.49 (B)	81.05 (B)	145.3 (C)	164.3 (T)
-20	11.97 (B)	37.69 (B)	83.67 (B)	149.9 (C)	164.3 (T)
-15	12.33 (B)	38.84 (B)	86.19 (B)	154.4 (C)	164.4 (T)
-10	12.69 (B)	39.95 (B)	88.65 (B)	158.7 (C)	164.5 (T)
-5	13.04 (B)	41.04 (B)	91.03 (B)	162.6 (C)	164.9 (T)
0	13.38 (B)	42.09 (B)	93.35 (B)	164.2 (T)	167.4 (C)
5	13.71 (B)	43.12 (B)	95.61 (B)	164.4 (T)	171.3 (C)
10	14.03 (B)	44.13 (B)	97.80 (B)	164.5 (T)	175.1 (C)
15	14.34 (B)	45.11 (B)	99.95 (B)	164.6 (T)	178.8 (C)
20	14.65 (B)	46.07 (B)	102.0 (B)	164.7 (T)	182.5 (C)
25	14.95 (B)	47.01 (B)	104.1 (B)	164.7 (T)	186.1 (C)

Table 4.11: The effects of the variation of GJ on the natural frequencies of S_2 wing.

Variation in GJ (%)	ω_i (rad/s)				
	ω_1	ω_2	ω_3	ω_4	ω_5
-25	13.37 (B)	42.03 (B)	93.01 (B)	142.7 (T)	166.2 (C)
-20	13.38 (B)	42.04 (B)	93.17 (B)	147.3 (T)	166.5 (C)
-15	13.38 (B)	42.06 (B)	93.17 (B)	151.8 (T)	166.7 (C)
-10	13.38 (B)	42.07 (B)	93.24 (B)	156.1 (T)	166.9 (C)
-5	13.38 (B)	42.08 (B)	93.30 (B)	160.3 (T)	167.1 (C)
0	13.38 (B)	42.09 (B)	93.35 (B)	164.2 (T)	167.4 (C)
5	13.38 (B)	42.10 (B)	93.39 (B)	166.8 (C)	169.0 (T)
10	13.38 (B)	42.11 (B)	93.44 (B)	167.2 (C)	172.6 (T)
15	13.38 (B)	42.12 (B)	93.48 (B)	167.4 (C)	176.4 (T)
20	13.38 (B)	42.13 (B)	93.51 (B)	167.5 (C)	180.1 (T)
25	13.38 (B)	42.14 (B)	93.54 (B)	167.6 (C)	183.7 (T)

Table 4.12 shows the flutter speed and flutter frequency obtained due to the variation of EI and Table 4.13 represents the flutter speed and flutter frequency obtained due to the variation of GJ for sailplane S_2. It can be seen from Table 4.12 that the variation of EI does not affect the flutter speed to any appreciable extent, but for Table 4.13 it can be observed that as GJ value increases flutter speed increases and when GJ value decreases flutter speed decreases, which is as expected. The same trend was observed for the sailplane S_1. Thus from the flutter point of view, the general characteristics of these two sailplanes are similar.

Table 4.12: The effects of the variation of EI on the flutter analysis of S_2 wing.

Variation in EI (%)	Flutter speed V_s (m/s)	Flutter frequency ω (rad/s)
-25	76.0	82.71
-20	76.0	84.78
-15	77.0	76.11
-10	77.0	76.12
-5	77.0	76.14
0	77.0	76.16
5	77.0	76.18
10	77.0	76.21
15	77.0	76.23
20	77.0	76.25
25	77.0	76.27

Table 4.13: The effects of the variation of GJ on the flutter analysis of S_2 wing.

Variation in GJ (%)	Flutter speed V_s (m/s)	Flutter frequency ω (rad/s)
-25	67.5	64.73
-20	69.6	67.17
-15	71.6	69.47
-10	73.6	71.71
-5	75.5	73.79
0	77.0	76.16
5	79.0	77.98
10	81.1	79.60
15	83.0	81.5
20	84.7	83.3
25	86.4	85.0

For light aircraft trainer L_1, the first five natural frequencies due to the variation of EI and GJ are presented in Tables 4.14 and 4.15 respectively. In Table 4.14, it is clear that the first, second and third are always bending modes while the fifth mode is always torsional. However, the fourth mode remains bending as the EI is decreased, but this mode changes from bending to coupled modes as the EI is increased except for the case when the increase in EI is 25% for which the mode is torsional. With respect to the variation of GJ the results shown in Table 4.15 reveal an interesting picture. The first, second and third natural frequencies of the L_1 wing remain unchanged as bending modes while the fifth mode remains as torsional for most of the cases except when the GJ is reduced by 25% for which the mode becomes coupled as can be seen. By contrast, the fourth mode remains to be bending dominant as the GJ is increased, but when GJ is reduced the mode becomes coupled until the reduction is 15%, beyond which the mode becomes torsional. Table 4.16 gives the flutter speed and flutter frequency obtained due to the variation of EI and Table 4.17 represents the flutter speed and flutter frequency obtained due to the variation of GJ for light aircraft trainer L_1. It can be seen from Table 4.16 that as EI value increases flutter speed increases and when EI value decreases flutter speed decreases thus flutter speed varies proportional to any change in bending stiffness EI, similarly for Table 4.17 it can be observed that as GJ value increases flutter speed increases and when GJ value decreases flutter speed decreases, thus flutter speed varies proportional to torsional stiffness GJ. It should be noted that GJ plays a major role than EI, because the variation in flutter speed is a lot higher than EI when GJ is used.

Table 4.14: The effects of the variation of *EI* on the natural frequencies of L_1 wing.

Variation in *EI* (%)	ω_i (rad/s)				
	ω_1	ω_2	ω_3	ω_4	ω_5
-25	41.93 (B)	149.9 (B)	395.8 (B)	753.3 (B)	980.2 (T)
-20	43.31 (B)	154.8 (B)	408.8 (B)	778.0 (B)	980.3 (T)
-15	44.64 (B)	159.6 (B)	421.4 (B)	801.8 (B)	980.3 (T)
-10	45.93 (B)	164.2 (B)	433.6 (B)	825.0 (B)	980.4 (T)
-5	47.19 (B)	168.7 (B)	445.5 (B)	847.5 (B)	980.5 (T)
0	48.42 (B)	173.1 (B)	457.0 (B)	869.4 (B)	980.6 (T)
5	49.61 (B)	177.4 (B)	468.3 (B)	890.8 (C)	980.7 (T)
10	50.78 (B)	181.6 (B)	479.3 (B)	911.5 (C)	980.9 (T)
15	51.92 (B)	185.6 (B)	490.1 (B)	931.7 (C)	981.3 (T)
20	53.04 (B)	189.6 (B)	500.6 (B)	950.9 (C)	982.1 (T)
25	54.13 (B)	193.5 (B)	510.9 (B)	967.8 (T)	984.8 (T)

Table 4.15: The effects of the variation of *GJ* on the natural frequencies of L_1 wing.

Variation in *GJ* (%)	ω_i (rad/s)				
	ω_1	ω_2	ω_3	ω_4	ω_5
-25	48.42 (B)	173.1 (B)	456.9 (B)	846.9 (T)	871.7 (C)
-20	48.42 (B)	173.1 (B)	457.0 (B)	865.6 (T)	880.8 (T)
-15	48.42 (B)	173.1 (B)	457.0 (B)	868.5 (C)	905.0 (T)
-10	48.42 (B)	173.1 (B)	457.0 (B)	869.0 (C)	930.6 (T)
-5	48.42 (B)	173.1 (B)	457.0 (B)	869.3 (C)	955.9 (T)
0	48.42 (B)	173.1 (B)	457.0 (B)	869.4 (B)	980.6 (T)
5	48.42 (B)	173.1 (B)	457.0 (B)	869.6 (B)	1005 (T)
10	48.42 (B)	173.1 (B)	457.0 (B)	869.6 (B)	1028 (T)
15	48.42 (B)	173.1 (B)	457.0 (B)	869.7 (B)	1051 (T)
20	48.42 (B)	173.1 (B)	457.1 (B)	869.7 (B)	1074 (T)
25	48.42 (B)	173.1 (B)	457.1 (B)	869.8 (B)	1096 (T)

Table 4.16: The effects of the variation of *EI* on the flutter analysis of L_1 wing.

Variation in *EI* (%)	Flutter speed V_s (m/s)	Flutter frequency ω (rad/s)
-25	1509	63.98
-20	1516	63.00
-15	1522	62.46
-10	1535	61.45
-5	1535	60.93
0	1543	59.96
5	1556	58.50
10	1556	57.98
15	1571	56.40
20	1584	54.95
25	1600	52.90

Table 4.17: The effects of the variation of *GJ* on the flutter analysis of L_1 wing.

Variation in *GJ* (%)	Flutter speed V_s (m/s)	Flutter frequency ω (rad/s)
-25	1388	44.89
-20	1405	48.93
-15	1460	51.02
-10	1479	54.49
-5	1518	56.92
0	1543	59.96
5	1572	62.49
10	1605	64.44
15	1632	66.74
20	1670	68.49
25	1694	70.47

For the light aircraft trainer L_2, the first five natural frequencies due to the variation of *EI* and *GJ* are presented in Tables 4.18 and 4.19 respectively. In Table 4.18, it can be seen that the first and second modes are always bending modes while the third and fifth modes are torsional except for the 25% increase in *EI* of the fifth mode for which the mode is coupled. The fourth mode remains by and large a coupled mode except for the lone case when the increase in *EI* is 25%, for which the mode is torsional. With respect to the variation of *GJ* the natural frequencies are shown in Table 4.19. The first and second modes remains unchanged as bending and the third mode also remains unchanged as torsion. However, the fourth mode changes its character from coupled to torsional only when the *GJ* is reduced by 20% and 25%. The fifth mode is basically a torsional mode for majority of the cases of *GJ* variations except when the *GJ* is reduced by 25% for which the mode becomes a coupled one.

Table 4.18: The effects of the variation of *EI* on the natural frequencies of L_2 wing.

Variation in *EI* (%)	ω_i (rad/s)				
	ω_1	ω_2	ω_3	ω_4	ω_5
-25	87.55 (B)	351.4 (B)	602.9 (T)	845.6 (C)	1082 (T)
-20	90.41 (B)	362.9 (B)	602.9 (T)	873.2 (C)	1082 (T)
-15	93.18 (B)	374.0 (B)	603.0 (T)	900.1 (C)	1083 (T)
-10	95.86 (B)	384.9 (B)	603.1 (T)	926.1 (C)	1083 (T)
-5	98.47 (B)	395.4 (B)	603.2 (T)	951.4 (C)	1083 (T)
0	101.0 (B)	405.6 (B)	603.2 (T)	975.9 (C)	1083 (T)
5	103.5 (B)	415.6 (B)	603.3 (T)	999.9 (C)	1083 (T)
10	105.9 (B)	425.3 (B)	603.4 (T)	1023 (C)	1084 (T)
15	108.3 (B)	434.8 (B)	603.4 (T)	1046 (C)	1084 (T)
20	110.6 (B)	444.1 (B)	603.5 (T)	1067 (C)	1085 (T)
25	112.8 (B)	453.2 (B)	603.6 (T)	1081 (T)	1094 (C)

Table 4.19: The effects of the variation of *GJ* on the natural frequencies of L_2 wing.

Variation in *GJ* (%)	ω_i (rad/s)				
	ω_1	ω_2	ω_3	ω_4	ω_5
-25	100.9 (B)	405.3 (B)	522.8 (T)	937.9 (T)	976.6 (C)
-20	100.9 (B)	405.4 (B)	539.8 (T)	966.5 (T)	978.6 (T)
-15	100.9 (B)	405.5 (B)	556.4 (T)	975.0 (C)	999.8 (T)
-10	101.0 (B)	405.5 (B)	572.4 (T)	975.7 (C)	1028 (T)
-5	101.0 (B)	405.6 (B)	588.0 (T)	975.9 (C)	1056 (T)
0	101.0 (B)	405.6 (B)	603.2 (T)	975.9 (C)	1083 (T)
5	101.0 (B)	405.6 (B)	618.1 (T)	976.1 (C)	1109 (T)
10	101.1 (B)	405.7 (B)	632.5 (T)	976.2 (C)	1136 (T)
15	101.1 (B)	405.7 (B)	646.7 (T)	976.2 (C)	1161 (T)
20	101.1 (B)	405.7 (B)	660.5 (T)	976.3 (C)	1186 (T)
25	101.1 (B)	405.7 (B)	674.1 (T)	976.3 (C)	1210 (T)

Table 4.20 represents the flutter speed and flutter frequency obtained due to the variation of EI and Table 4.21 represents the flutter speed and flutter frequency obtained due to the variation of GJ for light aircraft trainer L_2. It can be seen from Table 4.20 that as EI value increases flutter speed increases and when EI value decreases flutter speed decreases, thus flutter speed varies proportional to any change in bending stiffness EI, also, it should be noted that the change in flutter speed is very small. For Table 4.21 it can be observed that as GJ value increases flutter speed increases and when GJ value decreases flutter speed decreases, thus flutter speed varies proportional to torsional stiffness GJ. Also the variation in flutter speed due to torsional stiffness GJ is more evident. The same trend was observed for the light aircraft trainer L_1. Thus from the flutter point of view, the general characteristics of these two light aircraft trainers are similar.

Table 4.20: The effects of the variation of EI on the flutter analysis of L_2 wing.

Variation in EI (%)	Flutter speed V_s (m/s)	Flutter frequency ω (rad/s)
-25	1061	294.0
-20	1063	295.1
-15	1064	295.6
-10	1067	297.0
-5	1066	298.1
0	1065	298.9
5	1065	299.6
10	1065	300.1
15	1065	300.9
20	1067	301.5
25	1067	302.1

Table 4.21: The effects of the variation of GJ on the flutter analysis of L_2 wing.

Variation in GJ (%)	Flutter speed V_s (m/s)	Flutter frequency ω (rad/s)
-25	925.2	262.5
-20	954.2	270.2
-15	980.0	277.5
-10	1007	284.2
-5	1038	292.1
0	1065	298.9
5	1093	305.6
10	1117	311.2
15	1141	317.2
20	1163	323.2
25	1187	329.8

For transport airliner T_1, the first five natural frequencies computed by varying the EI and GJ are presented in Tables 4.22 and 4.23, respectively. In Table 4.22, it can be seen that the first and second modes are always bending modes while the third mode is always coupled. For the fourth mode, it can be seen that as EI decreases the mode remains as bending, but it changes from bending to coupled and finally to torsion as EI is increased. The fifth mode changes from torsion to coupled for the entire range of EI variation. In Table 4.23, it can be seen that the first and second modes are bending while the third mode is coupled for all the cases. However, for the fourth mode, it can be seen that as GJ is decreased the mode changes from bending to coupled and finally towards torsion, but it remains as a bending mode when GJ is increased. By contrast, the fifth mode changes from torsion to coupled modes when GJ is increased or decreased except for the lone case when the reduction in GJ is -25% for which the mode becomes bending. The interesting phenomena of modal interchanges are again observed in the results of Tables 4.22 and 4.23.

Table 4.22: The effects of the variation of *EI* on the natural frequencies of T_1 wing.

Variation in *EI* (%)	ω_i (rad/s)				
	ω_1	ω_2	ω_3	ω_4	ω_5
-25	9.983 (B)	28.69 (B)	45.37 (C)	76.27 (B)	97.64 (C)
-20	10.31 (B)	29.63 (B)	45.38 (C)	78.74 (B)	97.66 (C)
-15	10.63 (B)	30.53 (B)	45.38 (C)	81.13 (B)	97.68 (C)
-10	10.93 (B)	31.41 (B)	45.39 (C)	83.45 (B)	97.71 (C)
-5	11.23 (B)	32.26 (B)	45.39 (C)	85.68 (B)	97.73 (C)
0	11.52 (B)	33.09 (B)	45.40 (C)	87.86 (B)	97.75 (T)
5	11.81 (B)	33.89 (B)	45.40 (C)	89.98 (B)	97.77 (C)
10	12.09 (B)	34.68 (B)	45.41 (C)	92.04 (B)	97.79 (C)
15	12.36 (B)	35.45 (B)	45.42 (C)	94.04 (C)	97.82 (C)
20	12.62 (B)	36.19 (B)	45.43 (C)	95.97 (C)	97.86 (C)
25	12.88 (B)	36.93 (B)	45.44 (C)	97.61 (T)	98.14 (C)

Table 4.23: The effects of the variation of *GJ* on the natural frequencies of T_1 wing.

Variation in *GJ* (%)	ω_i (rad/s)				
	ω_1	ω_2	ω_3	ω_4	ω_5
-25	11.52 (B)	33.01 (B)	39.36 (C)	84.74 (T)	87.46 (B)
-20	11.52 (B)	33.03 (B)	40.64 (C)	87.31 (T)	87.78 (C)
-15	11.52 (B)	33.05 (B)	41.88 (C)	87.65 (C)	90.20 (C)
-10	11.53 (B)	33.06 (B)	43.08 (C)	87.74 (B)	92.78 (C)
-5	11.52 (B)	33.08 (B)	44.26 (C)	87.81 (B)	95.29 (C)
0	11.52 (B)	33.09 (B)	45.40 (C)	87.86 (B)	97.75 (T)
5	11.53 (B)	33.09 (B)	46.51 (C)	87.90 (B)	100.1 (C)
10	11.53 (B)	33.10 (B)	47.60 (C)	87.94 (B)	102.5 (C)
15	11.53 (B)	33.11 (B)	48.67 (C)	87.98 (B)	104.8 (C)
20	11.53 (B)	33.12 (B)	49.71 (C)	88.01 (B)	106.9 (C)
25	11.53 (B)	33.12 (B)	50.73 (C)	88.03 (B)	109.2 (C)

Table 4.24 represents the flutter speed and flutter frequency obtained due to the variation of *EI* and Table 4.25 represents the flutter speed and flutter frequency obtained due to the variation of *GJ* for transport airliner T_1. It can be seen from Table 4.24 that as *EI* value varies flutter speed fluctuates, the flutter speed tends to increase for minor change in *EI* values for both cases of either increase or decrease but the flutter speed decreases

for major variation in *EI* values. For Table 4.25 it can be observed that as *GJ* changes, the flutter speed tends to increase for minor change in *GJ* values but the flutter speed decreases for major variation in *GJ* values.

Table 4.24: The effects of the variation of *EI* on the flutter analysis of T_1 wing.

Variation in *EI* (%)	Flutter speed V_s (m/s)	Flutter frequency ω (rad/s)
-25	195	38.88
-20	193	39.49
-15	195	39.38
-10	193	39.99
-5	258	29.13
0	249	28.77
5	244	28.85
10	264	35.13
15	260	36.32
20	234	29.44
25	200	42.00

Table 4.25: The effects of the variation of *GJ* on the flutter analysis of T_1 wing.

Variation in *GJ* (%)	Flutter speed V_s (m/s)	Flutter frequency ω (rad/s)
-25	181	36.50
-20	179	37.50
-15	185	37.88
-10	228	27.38
-5	260	33.13
0	249	28.77
5	263	29.63
10	203	42.00
15	208	42.38
20	212	43.35
25	217	43.99

For transport airliner T_2, the first five natural frequencies due to the variation of *EI* and *GJ* are presented in Tables 4.26 and 4.27 respectively. In Table 4.26, It can be seen that the first, second and third modes are always bending while the fourth and fifth modes are always coupled modes. Surprisingly, there is no change in the characterisation of the modes due to the variation of *EI* for the entire range. Table 4.27, which shows the effects of the variation of *GJ* on the first five natural frequencies reveal similar characteristics in that the nature of the modes remains unchanged due to *GJ* variations.

Table 4.26: The effects of the variation of *EI* on the natural frequencies of T_2 wing.

Variation in *EI* (%)	ω_i (rad/s)				
	ω_1	ω_2	ω_3	ω_4	ω_5
-25	17.09 (B)	48.15 (B)	87.41 (B)	119.5 (C)	176.7 (C)
-20	17.64 (B)	49.64 (B)	90.14 (B)	119.8 (C)	181.4 (C)
-15	18.18 (B)	51.13 (B)	92.81 (B)	120.1 (C)	185.9 (C)
-10	18.71 (B)	52.56 (B)	95.37 (B)	120.4 (C)	190.1 (C)
-5	19.21 (B)	53.95 (B)	97.85 (B)	120.7 (C)	194.1 (C)
0	19.71 (B)	55.29 (B)	100.3 (B)	120.9 (C)	197.7 (C)
5	20.19 (B)	56.60 (B)	102.6 (B)	121.1 (C)	201.3 (C)
10	20.66 (B)	57.86 (B)	104.8 (B)	121.4 (C)	204.5 (C)
15	21.13 (B)	59.11 (B)	107.0 (B)	121.6 (C)	207.6 (C)
20	21.57 (B)	60.31 (B)	109.2 (B)	121.9 (C)	210.3 (C)
25	22.02 (B)	61.51 (B)	111.3 (B)	122.1 (C)	212.9 (C)

Table 4.27: The effects of the variation of *GJ* on the natural frequencies of T_2 wing.

Variation in *GJ* (%)	ω_i (rad/s)				
	ω_1	ω_2	ω_3	ω_4	ω_5
-25	19.68 (B)	54.87 (B)	99.14 (B)	106.1 (C)	187.8 (C)
-20	19.68 (B)	54.98 (B)	99.47 (B)	109.2 (C)	190.5 (C)
-15	19.69 (B)	55.07 (B)	99.72 (B)	112.3 (C)	192.7 (C)
-10	19.70 (B)	55.15 (B)	99.93 (B)	115.2 (C)	194.7 (C)
-5	19.70 (B)	55.23 (B)	100.1 (B)	118.1 (C)	196.3 (C)
0	19.71 (B)	55.29 (B)	100.3 (B)	120.9 (C)	197.7 (C)
5	19.71 (B)	55.34 (B)	100.4 (B)	123.6 (C)	199.0 (C)
10	19.71 (B)	55.39 (B)	100.5 (B)	126.3 (C)	200.1 (C)
15	19.72 (B)	55.44 (B)	100.6 (B)	128.9 (C)	201.1 (C)
20	19.72 (B)	55.48 (B)	100.7 (B)	131.5 (C)	201.9 (C)
25	19.72 (B)	55.52 (B)	100.8 (B)	134.1 (C)	202.8 (C)

Table 4.28 represents the flutter speed and flutter frequency obtained due to the variation of *EI* and Table 4.29 represents the flutter speed and flutter frequency obtained due to the variation of *GJ* for transport airliner T_2. It can be seen from Table 4.28 that as *EI* value increases flutter speed decreases gradually and when *EI* value decreases flutter speed increases gradually, it can be said that the flutter speed varies inversely proportional to any change in bending stiffness *EI*, also, it should be noted that the change in flutter speed is very small. For Table 4.29 it can be observed that as *GJ* value increases flutter speed increases and when *GJ* value decreases flutter speed decreases, thus flutter speed varies proportional to torsional stiffness *GJ*. It should be noted that T_2 consists of single engine on its wing.

Table 4.28: The effects of the variation of *EI* on the flutter analysis of T_2 wing.

Variation in *EI* (%)	Flutter speed V_s (m/s)	Flutter frequency ω (rad/s)
-25	414	78.99
-20	413	78.69
-15	413	78.64
-10	413	78.27
-5	412	78.21
0	411	78.56
5	410	79.05
10	409	78.80
15	409	78.67
20	409	78.66
25	409	78.64

Table 4.29: The effects of the variation of *GJ* on the flutter analysis of T_2 wing.

Variation in GJ (%)	Flutter speed V_s (m/s)	Flutter frequency ω (rad/s)
-25	355	66.03
-20	366	70.41
-15	377	71.85
-10	387	76.96
-5	399	75.91
0	411	78.56
5	421	79.01
10	429	86.14
15	441	82.34
20	452	86.92
25	462	86.24

For the transport airliner T_3, the first five natural frequencies due to the variation of *EI* and *GJ* are shown in Tables 4.30 and 4.31 respectively. In Table 4.30, it can be seen that the first and second modes are always bending modes. However, for the third mode when *EI* is decreased, the mode always remains bending whereas when *EI* is increased, the modes remain bending until the increase is 10%, beyond which the modes become coupled. The fourth mode remains torsional for decrease in the *EI* values but it becomes a coupled mode when *EI* is increased on or above the 10% value. Now the fifth mode is always the torsional mode for any increase of the *EI* value but it becomes a coupled mode when *EI* is reduced by 10% or more. The results for the *GJ* variation are shown in Table 4.31. It can be observed that the first and second modes are always bending modes. For the third mode, if the *GJ* is decreased the mode changes from bending to coupled and then finally to torsional for -15%, -20% and -25% variations, respectively. The character of this mode remains unchanged when *GJ* is increased. For the fourth mode when *GJ* decreases, the mode becomes coupled from 10% reduction and beyond. However, when *GJ* increases the mode remains always torsional. With regard to the fifth mode, any decrease in *GJ* does not alter the basic torsional nature of the mode but when *GJ* is increased beyond 5% the mode becomes coupled.

Table 4.30: The effects of the variation of *EI* on the natural frequencies of T_3 wing.

Variation in *EI* (%)	ω_i (rad/s)				
	ω_1	ω_2	ω_3	ω_4	ω_5
-25	10.39 (B)	30.03 (B)	58.77 (B)	72.51 (T)	107.9 (C)
-20	10.73 (B)	31.00 (B)	60.63 (B)	72.55 (T)	110.1 (C)
-15	11.06 (B)	31.94 (B)	62.43 (B)	72.59 (T)	110.9 (C)
-10	11.38 (B)	32.85 (B)	64.17 (B)	72.63 (T)	111.3 (C)
-5	11.69 (B)	33.73 (B)	65.85 (B)	72.68 (T)	111.5 (T)
0	11.99 (B)	34.59 (B)	67.47 (B)	72.74 (T)	111.6 (T)
5	12.28 (B)	35.42 (B)	69.02 (B)	72.82 (T)	111.8 (T)
10	12.57 (B)	36.23 (B)	70.46 (B)	72.95 (C)	111.9 (T)
15	12.85 (B)	37.03 (B)	71.68 (C)	73.28 (C)	112.0 (T)
20	13.13 (B)	37.79 (B)	72.33 (C)	74.13 (C)	112.1 (T)
25	13.39 (B)	38.55 (B)	72.56 (C)	75.36 (C)	112.2 (T)

Table 4.31: The effects of the variation of *GJ* on the natural frequencies of T_3 wing.

Variation in *GJ* (%)	ω_i (rad/s)				
	ω_1	ω_2	ω_3	ω_4	ω_5
-25	11.98 (B)	34.45 (B)	62.98 (T)	67.16 (C)	97.38 (T)
-20	11.98 (B)	34.48 (B)	64.90 (C)	67.40 (C)	100.4 (T)
-15	11.98 (B)	34.52 (B)	66.47 (C)	67.91 (C)	103.3 (T)
-10	11.99 (B)	34.54 (B)	67.13 (B)	69.26 (T)	106.2 (T)
-5	11.99 (B)	34.57 (B)	67.35 (B)	70.98 (T)	108.9 (T)
0	11.99 (B)	34.59 (B)	67.47 (B)	72.74 (T)	111.6 (T)
5	11.99 (B)	34.60 (B)	67.56 (B)	74.48 (T)	114.3 (T)
10	11.99 (B)	34.62 (B)	67.63 (B)	74.19 (T)	116.8 (C)
15	11.99 (B)	34.63 (B)	67.69 (B)	77.86 (T)	119.1 (C)
20	11.99 (B)	34.65 (B)	67.74 (B)	79.50 (T)	121.3 (C)
25	11.99 (B)	34.66 (B)	67.79 (B)	81.11 (T)	123.0 (C)

Table 4.32 represents the flutter speed and flutter frequency obtained due to the variation of *EI* and Table 4.33 represents the flutter speed and flutter frequency obtained due to the variation of *GJ* for transport airliner T_3. It can be seen from Table 4.32 that as *EI* value increases flutter speed decreases and when *EI* value decreases flutter speed increases, it can be said that the flutter speed varies inversely proportional to any change in bending stiffness *EI*, also, it should be noted that the change in flutter speed is very small. For Table 4.33 it can be observed that as *GJ* value increases flutter speed increases and when *GJ*

value decreases flutter speed decreases, thus flutter speed varies proportional to torsional stiffness *GJ*. It should be noted that T_3 consists of single engine on its wing. This is similar to the characteristics observed in transport airliner T_2.

Table 4.32: The effects of the variation of *EI* on the flutter analysis of T_3 wing.

Variation in *EI* (%)	Flutter speed V_s (m/s)	Flutter frequency ω (rad/s)
-25	286	41.14
-20	286	41.36
-15	285	41.64
-10	285	41.84
-5	285	42.02
0	284	42.44
5	284	42.64
10	284	42.99
15	283	43.34
20	283	43.52
25	283	43.87

Table 4.33: The effects of the variation of *GJ* on the flutter analysis of T_3 wing.

Variation in *GJ* (%)	Flutter speed V_s (m/s)	Flutter frequency ω (rad/s)
-25	245	38.44
-20	253	39.26
-15	261	40.01
-10	269	40.93
-5	277	41.53
0	284	42.44
5	292	43.08
10	299	43.92
15	306	44.68
20	313	45.47
25	320	46.23

For transport airliner T_4, the first five natural frequencies due to the variation of *EI* and *GJ* are presented in Tables 4.34 and 4.35 respectively. In Table 4.34, it can be seen from the mode shapes analysed that the first, second and fourth modes are always bending while third and fifth modes are always torsional. There is virtually no changes in the character of the modes due to the variation of *EI*. In Table 4.35, similar observations are made when *GJ* is varied. Clearly, the first, second and fourth modes are always bending while third and fifth modes are always torsional.

Table 4.34: The effects of the variation of *EI* on the natural frequencies of T_4 wing.

Variation in *EI* (%)	ω_i (rad/s)				
	ω_1	ω_2	ω_3	ω_4	ω_5
-25	7.784 (B)	22.90 (B)	45.26 (T)	62.41 (B)	94.08 (T)
-20	8.039 (B)	23.65 (B)	45.26 (T)	64.46 (B)	94.09 (T)
-15	8.286 (B)	24.38 (B)	45.26 (T)	66.44 (B)	94.09 (T)
-10	8.526 (B)	25.09 (B)	45.26 (T)	68.37 (B)	94.09 (T)
-5	8.760 (B)	25.78 (B)	45.26 (T)	70.24 (B)	94.09 (T)
0	8.988 (B)	26.45 (B)	45.26 (T)	72.06 (B)	94.09 (T)
5	9.210 (B)	27.09 (B)	45.26 (T)	73.84 (B)	94.09 (T)
10	9.426 (B)	27.74 (B)	45.26 (T)	75.58 (B)	94.09 (T)
15	9.638 (B)	28.36 (B)	45.26 (T)	77.28 (B)	94.09 (T)
20	9.846 (B)	28.97 (B)	45.26 (T)	78.94 (B)	94.09 (T)
25	10.05 (B)	29.57 (B)	45.26 (T)	80.57 (B)	94.09 (T)

Table 4.35: The effects of the variation of *GJ* on the natural frequencies of T_4 wing.

Variation in *GJ* (%)	ω_i (rad/s)				
	ω_1	ω_2	ω_3	ω_4	ω_5
-25	8.988 (B)	26.45 (B)	39.19 (T)	72.06 (B)	81.49 (T)
-20	8.988 (B)	26.45 (B)	40.48 (T)	72.06 (B)	84.16 (T)
-15	8.988 (B)	26.45 (B)	41.73 (T)	72.06 (B)	86.75 (T)
-10	8.988 (B)	26.45 (B)	42.94 (T)	72.06 (B)	89.26 (T)
-5	8.988 (B)	26.45 (B)	44.12 (T)	72.06 (B)	91.71 (T)
0	8.988 (B)	26.45 (B)	45.26 (T)	72.06 (B)	94.09 (T)
5	8.988 (B)	26.45 (B)	46.38 (T)	72.06 (B)	96.41 (T)
10	8.988 (B)	26.45 (B)	47.47 (T)	72.06 (B)	98.68 (T)
15	8.988 (B)	26.45 (B)	48.54 (T)	72.07 (B)	100.9 (T)
20	8.988 (B)	26.45 (B)	49.58 (T)	72.07 (B)	103.1 (T)
25	8.988 (B)	26.45 (B)	50.60 (T)	72.07 (B)	105.2 (T)

Table 4.36 represents the flutter speed and flutter frequency obtained due to the variation of *EI* and Table 4.37 represents the flutter speed and flutter frequency obtained due to the variation of *GJ* for transport airliner T_4. It can be seen from Table 4.36 that as *EI* value increases flutter speed decreases and when *EI* value decreases flutter speed increases and it can be said that the flutter speed varies inversely proportional to bending stiffness *EI*. For Table 4.37 it can be observed that as *GJ* value increases flutter speed increases and when *GJ* value decreases flutter speed decreases, thus flutter speed varies proportional to torsional stiffness *GJ*. This is similar with respect to the characteristics observed in other transport airliners.

Table 4.36: The effects of the variation of *EI* on the flutter analysis of T_4 wing.

Variation in *EI* (%)	Flutter speed V_s (m/s)	Flutter frequency ω (rad/s)
-25	392	45.46
-20	391	45.66
-15	389	45.82
-10	389	46.00
-5	388	46.26
0	386	46.50
5	386	46.54
10	384	46.71
15	380	46.49
20	370	42.50
25	370	42.67

Table 4.37: The effects of the variation of *GJ* on the flutter analysis of T_4 wing.

Variation in *GJ* (%)	Flutter speed V_s (m/s)	Flutter frequency ω (rad/s)
-25	318	37.37
-20	331	38.16
-15	339	39.00
-10	363	44.46
-5	375	45.46
0	386	46.50
5	397	47.48
10	407	48.41
15	418	49.28
20	428	50.10
25	438	51.00

4.5 Effects due to the variation of engine mass and its location

Next, a parametric study is carried out for transport airliner wings by varying the engine mass and its location. Both sailplanes and the light aircraft trainer wings have been excluded because they do not have any engines on them. Thus, only the transport airliner wings are considered in the parametric study based on the changes of engine masses and their locations. It should be noted that among the four transport airliners, T_1 and T_4 have two engines on each of their wings whereas T_2 and T_3, each has a single engine mounted on each of their wings. A variation between -25% to 25% in steps of 5% is allowed and for the engine locations, some realistic distances from the wing root and the current locations of the engines are considered. The first five natural frequencies with the identifications of the modes and the flutter analysis are presented in Tables 4.38 to 4.45 which are discussed next. The results corresponding to the original mass and its location of the baseline wing are shown in bold.

For the transport airliner T_1, the first five natural frequencies due to the variation of engine masses and its locations are presented in Tables 4.38 and 4.39 respectively. It should be noted that the transport airliner T_1 has two engines on its wing and the masses of each of the two engines are equally increased by the same proportion as indicated in Table 4.38. In Table 4.38, it can also be seen that the first, second and fourth modes are always bending while third mode is always coupled and fifth mode is always torsional. There is no change in their modal characteristics due to the variation of engine mass. Flutter speed increases as engine mass is increased and the flutter speed decreases as engine mass is decreased, thus flutter speed varies directly proportional to change in engine mass. Table 4.39 shows that the first, second and fourth modes are always bending while the third mode is coupled and the fifth mode is torsional. Here also, there is no change in their modal characteristics due to the variation of engine location. It can be seen as the two engines are brought closer (9.53, 6.93), lowest flutter speed occurred and when the two engines are separated apart (12.07, 4.32), highest flutter speed occurred. Overall it can be noted that the right balance in engine mass and location provides the best flutter speed, this can be observed in other aircraft wings analysed too.

Table 4.38: The effects of the variation of engine mass on the natural frequencies, flutter speeds and flutter frequencies of T_1.

Variation in engine mass (%)	ω_i (rad/s)					Flutter speed, Vs (m/s)	Flutter frequency, ω (rad/s
	ω_1	ω_2	ω_3	ω_4	ω_5		
-25	11.97 (B)	34.55 (B)	45.40 (C)	92.02 (B)	97.76 (T)	237	30.63
-20	11.88 (B)	34.22 (B)	45.40 (C)	91.17 (B)	97.76 (T)	240	30.13
-15	11.79 (B)	33.91 (B)	45.40 (C)	90.32 (B)	97.75 (T)	242	29.87
-10	11.70 (B)	33.62 (B)	45.40 (C)	89.49 (B)	97.75 (T)	245	29.38
-5	11.61 (B)	33.35 (B)	45.40 (C)	88.67 (B)	97.75 (T)	248	29.08
0	**11.52 (B)**	**33.09 (B)**	**45.40 (C)**	**87.86 (B)**	**97.75 (T)**	**249**	**28.77**
5	11.44 (B)	32.84 (B)	45.40 (C)	87.07 (B)	97.75 (T)	251	28.44
10	11.36 (B)	32.61 (B)	45.40 (C)	86.28 (B)	97.75 (T)	255	28.05
15	11.28 (B)	32.39 (B)	45.40 (C)	86.28 (B)	97.75 (T)	256	27.63
20	11.20 (B)	32.17 (B)	45.40 (C)	86.28 (B)	97.75 (T)	256	27.37
25	11.12 (B)	31.97 (B)	45.39 (C)	84.01 (B)	97.74 (T)	259	26.88

Table 4.39: The effects of the variation of engine location on the natural frequencies, flutter speeds and flutter frequencies of T_1.

Location of engine 1 from wing root (m)	Location of engine 2 from wing root (m)	ω_i (rad/s)					Flutter speed, Vs (m/s)	Flutter frequency, ω (rad/s)
		ω_1	ω_2	ω_3	ω_4	ω_5		
12.07	5.59	10.73 (B)	34.40 (B)	42.45 (C)	79.79 (B)	92.83 (T)	254	27.63
12.07	4.32	10.80 (B)	35.10 (B)	42.96 (C)	86.25 (B)	95.67 (T)	256	27.92
10.80	6.93	11.36 (B)	32.13 (B)	44.05 (C)	86.87 (B)	97.10 (T)	252	28.84
10.80	**5.59**	**11.52 (B)**	**33.09 (B)**	**45.40 (C)**	**87.86 (B)**	**97.75 (T)**	**249**	**28.77**
10.80	4.32	11.61 (B)	33.78 (B)	46.17 (C)	93.66 (B)	98.95 (T)	246	29.49
9.53	6.93	12.00 (B)	31.79 (B)	45.62 (C)	91.88 (B)	96.55 (T)	234	26.47
9.53	5.59	12.18 (B)	32.85 (B)	47.28 (C)	91.66 (B)	96.91 (T)	252	27.81

For the transport airliner T_2, the first five natural frequencies due to the variation of engine mass and its location are presented in Tables 4.40 and 4.41 respectively. It should be noted that the transport airliner T_2 has single engine on its wing. In Table 4.40, it can be seen that the first, second and third modes are always bending while the fifth mode is always coupled. Also, the fourth mode is coupled but as its engine mass is reduced to 25% it change to torsional. Flutter speed increases as engine mass is increased and the flutter speed decreases as engine mass is decreased, thus flutter speed varies directly proportional to change in engine mass. In Table 4.41, It can be seen that the first and second modes are always bending while the third mode changes from bending to coupled as the engine is moved towards the wing tip but remains bending as the engine is moved towards wing root. The fourth mode changes from coupled to torsional as the engine is moved towards the wing root. Also the fourth mode changes from coupled to bending as the engine is move towards wing tip. The fifth mode remains coupled as the engine is moved towards the root but changed to bending when it is moved towards wing tip. It can be seen as the engine is brought closer to the wing root, the flutter speed is increased and as the engine is moved away from the root, the flutter speed is decreased.

Table 4.40: The effects of the variation of engine mass on the natural frequencies, flutter speeds and flutter frequencies of T_2.

Variation in engine mass (%)	ω_i (rad/s)					Flutter speed, Vs (m/s)	Flutter frequency, ω (rad/s
	ω_1	ω_2	ω_3	ω_4	ω_5		
-25	19.75 (B)	57.27 (B)	104.5 (B)	121.6 (T)	199.7 (C)	409	77.85
-20	19.74 (B)	56.87 (B)	103.5 (B)	121.5 (C)	199.2 (C)	409	78.00
-15	19.73 (B)	56.47 (B)	102.7 (B)	121.3 (C)	198.8 (C)	410	78.14
-10	19.72 (B)	56.08 (B)	101.8 (B)	121.1 (C)	198.4 (C)	410	78.28
-5	19.71 (B)	55.68 (B)	101.0 (B)	121.0 (C)	198.1 (C)	410	78.43
0	**19.71 (B)**	**55.29 (B)**	**100.3 (B)**	**120.9 (C)**	**197.7 (C)**	**411**	**78.56**
5	19.70 (B)	54.90 (B)	99.53 (B)	120.8 (C)	197.4 (C)	411	78.71
10	19.69 (B)	54.51 (B)	98.84 (B)	120.7 (C)	197.2 (C)	411	78.83
15	19.68 (B)	54.13 (B)	98.20 (B)	120.7 (C)	196.9 (C)	411	78.94
20	19.67 (B)	53.76 (B)	97.59 (B)	120.6 (C)	196.6 (C)	411	79.06
25	19.67 (B)	53.38 (B)	97.01 (B)	120.5 (C)	196.4 (C)	411	79.18

Table 4.41: The effects of the variation of engine location on the natural frequencies, flutter speeds and flutter frequencies of T_2.

Location of engine from wing root (m)	ω_i (rad/s)					Flutter speed, Vs (m/s)	Flutter frequency, ω (rad/s)
	ω_1	ω_2	ω_3	ω_4	ω_5		
6.41	18.50 (B)	41.36 (B)	75.43 (C)	103.9 (B)	217.9 (B)	344	72.58
5.48	19.11 (B)	44.68 (B)	86.04 (C)	101.1 (T)	215.4 (C)	358	85.84
5.15	19.47 (B)	49.18 (B)	95.22 (B)	104.4 (C)	206.3 (C)	380	80.77
4.37	**19.71 (B)**	**55.29 (B)**	**100.3 (B)**	**120.9 (C)**	**197.7 (C)**	**411**	**78.56**
3.66	19.81 (B)	59.88 (B)	107.5 (B)	139.8 (T)	194.9 (C)	414	78.85
2.95	19.86 (B)	62.64 (B)	117.7 (B)	160.4 (T)	200.5 (C)	416	80.12
2.22	19.88 (B)	63.85 (B)	125.8 (B)	181.8 (T)	214.8 (C)	416	81.67

For the transport airliner T_3, the first five natural frequencies due to the variation of engine mass and its location are presented in Tables 4.42 and 4.43 respectively. It should be noted that the transport airliner T_3 has single engine on its wing. Clearly it can be seen from the Table 4.42, all the natural frequencies are virtually unaltered due to the variation of engine mass. It can also be seen that the first, second and third modes are always bending while fourth and fifth modes are always torsional. It can be seen any change in engine mass reduces the flutter speed. In Table 4.43, it can be seen that the first and the second modes are always bending and the fifth mode is always torsional. The third mode changes from bending to coupled and then to torsional as the engine is moved towards the wing root and it remains bending when it is moved towards the wing tip. The fourth modes change from torsional to coupled and then to bending as the engine is moved towards the wing root and it remains torsional when it is moved towards the wing tip. It can be seen as the engine is brought closer to the wing root, the flutter speed is increased and as the engine is moved away from the root, the flutter speed is decreased.

Table 4.42: The effects of the variation of engine mass on the natural frequencies, flutter speeds and flutter frequencies of T_3.

Variation in engine mass (%)			ω_i (rad/s)			Flutter speed, Vs (m/s)	Flutter frequency, ω (rad/s
	ω_1	ω_2	ω_3	ω_4	ω_5		
-25	12.00 (B)	35.08 (B)	69.74 (B)	72.78 (T)	112.5 (T)	272	44.48
-20	12.00 (B)	34.98 (B)	69.27 (B)	72.77 (T)	112.4 (T)	273	44.17
-15	12.00 (B)	34.88 (B)	68.80 (B)	72.76 (T)	112.2 (T)	274	43.88
-10	11.99 (B)	34.78 (B)	68.35 (B)	72.75 (T)	112.0 (T)	274	43.71
-5	11.99 (B)	34.68 (B)	67.90 (B)	72.75 (T)	111.8 (T)	275	43.44
0	**11.99 (B)**	**34.59 (B)**	**67.47 (B)**	**72.74 (T)**	**111.6 (T)**	**284**	**42.44**
5	11.99 (B)	34.49 (B)	67.04 (B)	72.74 (T)	111.5 (T)	276	43.14
10	11.98 (B)	34.39 (B)	66.63 (B)	72.73 (T)	111.3 (T)	277	43.00
15	11.98 (B)	34.29 (B)	66.23 (B)	72.73 (T)	111.1 (T)	277	42.87
20	11.98 (B)	34.19 (B)	65.83 (B)	72.73 (T)	111.0 (T)	278	42.74
25	11.98 (B)	34.09 (B)	65.45 (B)	72.73 (T)	110.8 (T)	278	42.71

Table 4.43: The effects of the variation of engine location on the natural frequencies, flutter speeds and flutter frequencies of T_3.

Location of engine from wing root (m)			ω_i (rad/s)			Flutter speed, Vs (m/s)	Flutter frequency, ω (rad/s)
	ω_1	ω_2	ω_3	ω_4	ω_5		
5.99	11.83 (B)	31.01 (B)	63.16 (B)	70.09 (T)	105.1 (T)	257	36.61
5.20	11.93 (B)	32.98 (B)	64.45 (B)	71.65 (T)	107.8 (T)	279	42.91
4.40	**11.99 (B)**	**34.59 (B)**	**67.47 (B)**	**72.74 (T)**	**111.6 (T)**	**284**	**42.44**
3.29	12.02 (B)	35.94 (B)	72.95 (C)	73.95 (C)	118.1 (T)	284	42.88
2.18	12.04 (B)	36.47 (B)	73.92 (T)	77.49 (B)	122.1 (T)	285	42.98

For the transport airliner T_4, the first five natural frequencies due to the variation of engine masses and its locations are presented in Tables 4.44 and 4.45 respectively. It should be noted that the transport airliner T_4 has two engines on its wing. Note that, the masses of each of the two engines are equally increased by the same proportion as indicated in Table 4.44. Clearly it can be seen from the Table 4.44, all the natural frequencies variation is quite small due to the variation of the engine masses from -25% to +25%. It can also be seen from the mode shapes analysed that the first, second and fourth modes are always bending while third and fifth modes are torsional. There is no change in their modes due

to the variation of engine mass. It can be seen that as the engine mass is decreased, flutter speed increases and as the engine mass is increased, the flutter speed decreases.
For Table 4.45, It can be seen that the first, second and fourth modes are always bending while third and fifth modes are always torsional. There is no appreciable change in the modal characteristics due to the variation of the engine positions. It can be seen as the two engines are brought closer, low flutter speed occurs not the lowest though and when the two engines are separated apart, high value for flutter speed occurs and it can be noticed that the lowest or highest flutter speed does not occur solely on the basis of engine location.

Table 4.44: The effects of the variation of engine mass on the natural frequencies, flutter speeds and flutter frequencies of T_4.

Variation in engine mass (%)	ω_i (rad/s)					Flutter speed, Vs (m/s)	Flutter frequency, ω (rad/s
	ω_1	ω_2	ω_3	ω_4	ω_5		
-25	9.324 (B)	26.98 (B)	45.26 (T)	73.25 (B)	94.09 (T)	387	46.50
-20	9.254 (B)	26.86 (B)	45.26 (T)	73.01 (B)	94.09 (T)	387	46.50
-15	9.186 (B)	26.75 (B)	45.26 (T)	72.77 (B)	94.09 (T)	386	46.50
-10	9.118 (B)	26.64 (B)	45.26 (T)	72.54 (B)	94.09 (T)	386	46.50
-5	9.052 (B)	26.54 (B)	45.26 (T)	72.30 (B)	94.09 (T)	386	46.50
0	**8.988 (B)**	**26.45 (B)**	**45.26 (T)**	**72.06 (B)**	**94.09 (T)**	**386**	**46.50**
5	8.924 (B)	26.35 (B)	45.26 (T)	71.83 (B)	94.09 (T)	386	46.50
10	8.862 (B)	26.26 (B)	45.26 (T)	71.59 (B)	94.09 (T)	386	46.50
15	8.801 (B)	26.18 (B)	45.26 (T)	71.36 (B)	94.09 (T)	385	46.49
20	8.741 (B)	26.09 (B)	45.26 (T)	71.13 (B)	94.09 (T)	385	46.50
25	8.682 (B)	26.01 (B)	45.26 (T)	70.89 (B)	94.09 (T)	385	46.49

Table 4.45: The effects of the variation of engine location on the natural frequencies, flutter speeds and flutter frequencies of T_4.

Location of engine 1 from wing root (m)	Location of engine 2 from wing root (m)	ω_i (rad/s) ω_1	ω_2	ω_3	ω_4	ω_5	Flutter speed, Vs (m/s)	Flutter frequency, ω (rad/s)
17.6	5.6	8.811 (B)	26.69 (B)	45.07 (T)	70.65 (B)	94.31 (T)	479	29.14
17.6	4.6	8.814 (B)	26.73 (B)	45.08 (T)	72.67 (B)	94.35 (T)	477	29.20
17.1	7.4	8.972 (B)	26.30 (B)	45.22 (T)	66.62 (B)	94.00 (T)	390	46.51
17.1	**5.6**	**8.988 (B)**	**26.45 (B)**	**45.26 (T)**	**72.06 (B)**	**94.09 (T)**	**386**	**46.50**
17.1	4.6	8.991 (B)	26.48 (B)	45.28 (T)	74.15 (B)	94.13 (T)	386	46.50
15.8	7.4	9.400 (B)	25.92 (B)	45.82 (T)	68.11 (B)	93.73 (T)	433	43.00
15.8	4.6	9.418 (B)	26.08 (B)	45.87 (T)	72.88 (B)	93.82 (T)	428	42.99

It should be noted that unlike the cases for T_2 and T_3 wings which carry single engine, the analysis of the aircraft with two engines on each of its wing reveals that there would be no appreciable change in their modal characteristics as a consequence of reasonably realistic variations of engine masses and their locations.

4.6 Conclusions

Using the dynamic stiffness method for the theoretical development and the Wittrick-Williams algorithm as the solution technique, the modal behaviour of a wide range of aircraft wings has been investigated which includes two sailplane, two light aircraft trainer and four transport airliner wings. Natural frequencies, mode shapes and flutter analysis for the wings are presented and the results are discussed in detail. The bending and torsional stiffnesses of each wing are varied between +25% and -25% in steps of 5% and their subsequent effects on the natural frequencies, mode shapes and flutter speed are investigated which showed significant changes in results and some interesting trends. As an overview of the results observed in the analysis it can be said that for sailplanes, the variation of *EI* does not affect the flutter speed to any appreciable extent while the flutter speed varies proportional to the change in *GJ*. For light aircraft trainers, the flutter speed varies proportional to both *EI* and *GJ*. For transport airliner, the flutter speed varies inversely proportional to change in *EI* and directly proportional to change in *GJ*. Overall *GJ* variation affects flutter speed more than *EI* variation. An interesting feature of this particular investigation reveals that the modal interchanges or flip-overs between bending, torsional and/or coupled modes can occur as a result of the variations which can have profound influence in aeroelastic studies. Subsequent parametric studies on the effects of variation of engine mass and its location that are applicable to the transport airliners showed that the natural frequencies, mode shapes and flutter speed can be changed to some appreciable extent to make provision for the avoidance of aeroelastic problems. It can be concluded that the right balance in engine mass and location provides the best flutter speed.

Chapter 5

Whole aircraft analysis

5.1 Introduction to free vibration and flutter analysis using whole aircraft configuration

In the final stage of the investigation described in section A, the whole aircraft configuration for free vibration and flutter analysis is considered as opposed to wing only analysis using cantilever boundary condition at the root described in Chapter 4. Two different types of idealisations are used to model the whole aircraft configuration in this chapter. In the first type of idealisation, the mass and inertia of the fuselage, tailplane, fin and rudder are modelled as lumped mass and lumped inertia connected at the wing elastic axis and fuselage centreline intersection and thus allowing for the rigid body motions. The second type of idealisation is a detailed model wherein the fuselage, tailplane, fin and rudder are each modelled as bending-torsion coupled beams. For the first type of idealisation only the symmetric motion involving heave and pitch is considered whereas, for the second type of the idealisation, both symmetric and antisymmetric motions are considered so that the heave and pitch as well as the rolling freedoms are taken into account. Also for the first type of idealisation, a parametric study by varying the magnitude of the lumped mass and inertia at the wing elastic axis and fuselage centreline intersection is carried out and the subsequent effects of the modal and flutter behaviour of the aircraft are examined. For the second type of idealisation, only an illustrative configuration using 16 elements for the wing, 18 elements for the fuselage, 8 elements for the tailplane and 6 elements for the fin and rudder are used in the analysis to serve as an example. It should be noted that for this second type of idealisation, only the structural effects of the fuselage, tailplane, fin and rudder are included and no account for the aerodynamic effects apart from the wing is considered, i.e., unsteady aerodynamic effects arising from the fuselage, tailplane, fin and rudder are disregarded. The FORTRAN program called BIGCALFUN is used to analyse the whole aircraft configuration. In the illustrative example for the results that follows is

Table 5.1: Particulars of transport airliner.

Parameters	Transport airliner
Wing Span (m)	40
Wing Area (m^2)	162
Aspect Ratio	10
Wing Root Chord (m)	5.0
Wing Tip Chord (m)	2.5
Sweep angle (deg)	0
Length overall (m)	30
Height Overall (m)	12
Weight Empty (kg)	34,000
Max Take-off weight (kg)	70,000
Max Wing Loading (kg/m^2)	434
Max Cruising Speed (knots)	348
Range (nmi)	2835

that of a transport airliner for which some pertinent details are given in Table 5.1.

5.2 Results for the free vibration and flutter analysis using model Type I

As explained above, the model Type I considers the whole aircraft configuration by lumping the fuselage, tailplane, fin and rudder masses and their inertias at the nodal point of the wing and fuselage centreline intersection, as shown in Figure 5.1, without representing the fuselage, tailplane, fin and rudder by individual bending-torsion coupled beam elements unlike the case for the wing. The initial values of the data for the lumped mass and pitching moment of inertia for the rest of the aircraft other than the wing, for the original aircraft were taken to be 15,000 kg and 70,000 kgm^2, respectively. These values were halved because only one symmetric half of the aircraft was considered for the analysis. The bending (EI) and torsional (GJ) stiffnesses along the span for this transport aircraft are illustrated in Figure 5.2.

The first ten natural frequencies and mode shapes of the aircraft were computed. As the aircraft was completely free and exhibiting natural vibrations in symmetric motion, the first two natural frequencies turned out to be zero (from a numerical standpoint, the value was exceedingly small and close to zero) corresponding to the rigid body modes in heave and pitch. The first five elastic modes ω_3 to ω_7 are illustrated in Figure 5.3, where

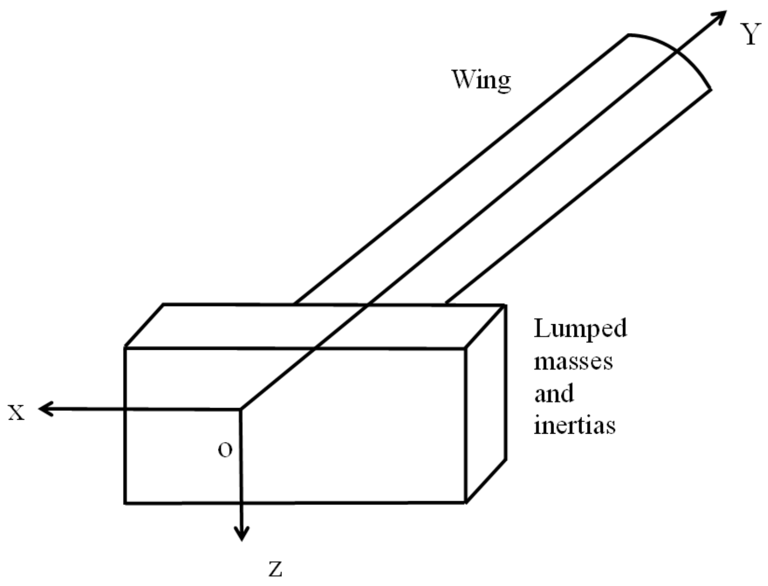

Figure 5.1: Representation of lumped masses and inertias of fuselage, tailplane, fin and rudder for half of an aircraft.

Table 5.2: The flutter results for transport airliner.

	Transport airliner	
	Whole aircraft configuration	Cantilevered aircraft wing configuration
Flutter Speed (m/s)	203.3	249.0
Flutter Frequency (rad/s)	51.63	28.77

the bending and torsional displacements are respectively shown by solid black lines and broken red lines. The first three elastic modes are basically bending dominated modes, whereas the fourth elastic one is a coupled mode. By contrast the fifth elastic mode is more or less a torsional mode. In the subsequent flutter analysis, these elastic modes as well as the two rigid body modes in heave and pitch were included. The results of the analysis for the whole aircraft configuration showing flutter speed and flutter frequency are shown in Table 5.2 alongside the results computed by using the cantilever model.

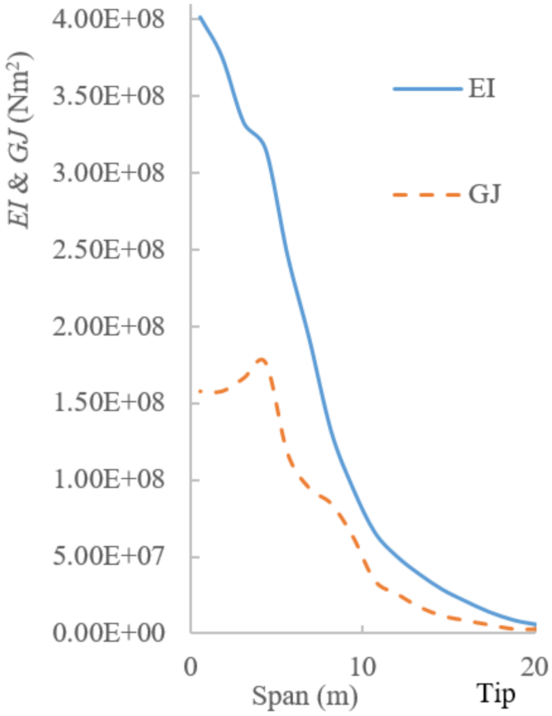

Figure 5.2: Stiffness distributions.

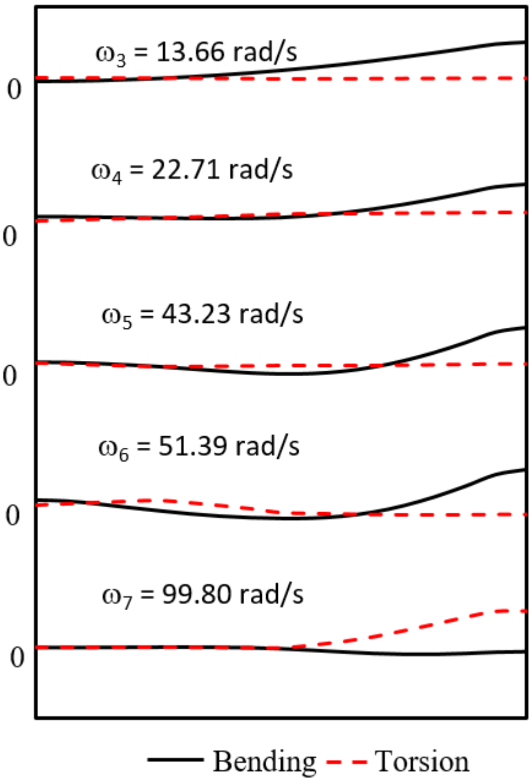

Figure 5.3: Mode shape of an aircraft wing.

5.3 Effects of fuselage mass and inertia on transport airliner

Next, a parametric investigation is carried out by keeping the wing properties constant but by varying the connected lumped mass and inertia at the wing and fuselage centreline section. Both lumped mass and lumped inertia parameters are varied up to ±25% in steps of 5% relative to the original values and the natural frequencies corresponding to the elastic modes as well as the flutter speed and flutter frequency and the results when lumped inertia is at ±25% are shown in Tables 5.3 and 5.4. The investigation shows that such variations did not make any appreciable difference to the natural frequencies, flutter speeds and flutter frequencies. The fuselage, tailplane, fin and rudder masses and inertias were not increased or decreased beyond ±25% because it was thought to be unrealistic.

Table 5.3: The effects of the variation of fuselage mass for -25% of inertia for a transport airliner.

Variation of fuselage mass (%)	Moment of inertia (%)	ω_i (rad/s)								Flutter speed (m/s)	Flutter frequency (rad/s)
		ω_3	ω_4	ω_5	ω_6	ω_7	ω_8	ω_9	ω_{10}		
-25	-25	14.02	23.15	43.40	52.35	99.81	106.6	188.4	209.9	202.8	52.13
-20	-25	13.94	23.10	43.39	52.13	99.81	106.4	188.2	209.9	203.6	52.13
-15	-25	13.87	23.07	43.38	51.93	99.81	106.3	188.0	209.9	205.3	52.13
-10	-25	13.80	23.03	43.38	51.75	99.80	106.1	187.9	209.9	204.9	51.63
-5	-25	13.73	23.00	43.37	51.58	99.80	106.0	187.7	209.9	203.5	51.63
0	-25	13.67	22.97	43.36	51.43	99.80	105.9	187.6	209.9	202.8	51.63
5	-25	13.62	22.94	43.35	51.29	99.80	105.7	187.4	209.9	204.2	51.63
10	-25	13.56	22.91	43.35	51.16	99.80	105.6	187.3	209.9	205.5	51.63
15	-25	13.51	22.89	43.34	51.04	99.80	105.6	187.2	209.9	206.5	51.13
20	-25	13.46	22.87	43.33	50.93	99.80	105.5	187.1	209.9	205.7	51.13
25	-25	13.42	22.85	43.33	50.82	99.80	105.4	187.0	209.9	204.8	51.13

Table 5.4: The effects of the variation of fuselage mass for 25% of inertia for a transport airliner.

Fuselage mass (%)	Moment of inertia (%)	ω_i (rad/s)								Flutter speed (m/s)	Flutter frequency (rad/s)
		ω_3	ω_4	ω_5	ω_6	ω_7	ω_8	ω_9	ω_{10}		
-25	25	14.01	22.74	43.19	52.29	99.81	106.6	188.4	209.9	202.6	52.13
-20	25	13.93	22.69	43.18	52.07	99.81	106.4	188.2	209.9	204.4	52.13
-15	25	13.85	22.65	43.17	51.87	99.81	106.3	188.0	209.9	204.9	51.63
-10	25	13.78	22.62	43.17	51.68	99.80	106.1	187.9	209.9	203.3	51.63
-5	25	13.72	22.59	43.16	51.52	99.80	106.0	187.7	209.9	202.1	51.63
0	25	13.66	22.56	43.15	51.36	99.80	105.9	187.6	209.9	203.6	51.63
5	25	13.60	22.53	43.15	51.22	99.80	105.7	187.4	209.9	205.0	51.63
10	25	13.55	22.50	43.14	51.09	99.80	105.6	187.3	209.9	205.9	51.13
15	25	13.49	22.48	43.13	50.97	99.80	105.5	187.2	209.9	204.9	51.13
20	25	13.45	22.46	43.13	50.86	99.80	105.5	187.1	209.9	204.0	51.13
25	25	13.40	22.43	43.12	50.76	99.80	105.4	187.0	209.9	203.1	51.13

5.4 Results for the free vibration and flutter analysis using model Type II

The Type II model for the whole aircraft configuration includes bending-torsion coupled beams elements for all the components of the aircraft namely, fuselage, tail plane, fin and rudder. The model also includes the effect of the lumped mass or inertia such as that of an engine. A schematic diagram of such a model is shown in Figure 5.4 for one symmetric half of the aircraft.

It should be noted that for the symmetric case, all out of plane displacements and rotations (Δ_y, Θ_x, Θ_z) on the enforced plane of symmetry will be zero whereas for the anti-symmetric case, all in plane displacements and rotations (Δ_x, Δ_z, Θ_y) on the enforced plane of symmetry will be zero. The stick model configuration having 16 elements for the wing, 18 elements for the fuselage, 8 elements for the tailplane and 6 elements for the fin and rudder are used in the analysis for both the symmetric and antisymmetric cases. When computing the flutter speed and flutter frequency only the wing modes which included the fundamental bending and fundamental torsion were considered, but the rigid body modes were implemented in the analysis for both symmetric and antisymmetric cases. In addition to the rigid body modes of the whole aircraft, five elastic modes of the wings were included in the flutter analysis. The results for the flutter speed and flutter frequencies for both symmetric and antisymmetric cases are shown in Table 5.5.

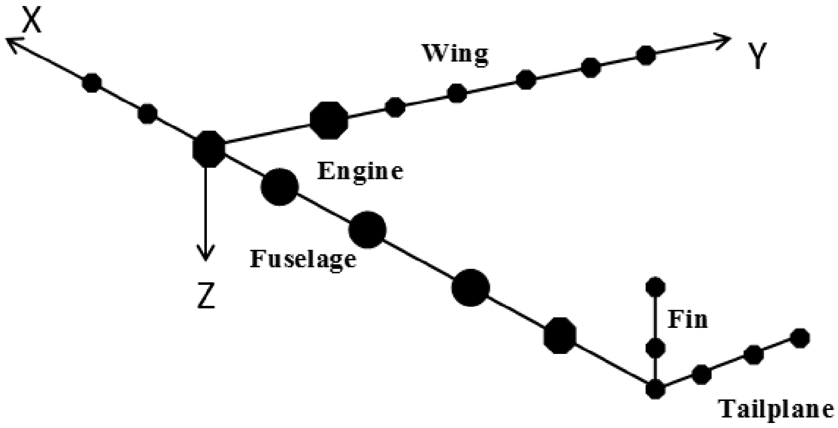

Figure 5.4: Bending-Torsion coupled beam idealisation for one symmetric half of an aircraft.

Clearly, the antisymmetric flutter speed for the whole aircraft configuration is significantly lower than the symmetric case as shown in Table 5.5 which is not unusual. It should be noted that the unsteady aerodynamic forces arising from the tailplane for the symmetric

Table 5.5: Flutter speed and flutter frequency for the whole aircraft configuration using Type II.

	Transport airliner		
	Symmetric whole aircraft configuration	Antisymmetric whole aircraft configuration	Cantilevered aircraft wing configuration
Flutter speed (m/s)	248.8	174.5	249.0
Flutter frequency (rad/s)	48.12	32.45	28.77

case and fin and rudder for the antisymmetric case were not taken into account in the flutter analysis.

For the symmetric flutter analysis of whole aircraft configuration, the rigid body modes in heave and pitch have been included along with five elastic modes whereas for the antisymmetric flutter analysis for the whole aircraft configuration, the rigid body modes in rolling motion is accounted for during the flutter analysis. Clearly, when a wing only analysis is carried out with cantilever end condition, the symmetric and antisymmetric cases cannot be properly covered, let alone the non-inclusion of the rigid body modes due to the fixity of the built-in end of the aircraft wing.

5.5 Conclusions

Using the dynamic stiffness method for the theoretical development and the Wittrick-Williams algorithm as the solution technique, the free vibration and flutter analysis for whole aircraft configuration has been carried out. Two model types have been considered for whole aircraft analysis. In the first type of analysis masses and inertia are lumped at the wing and fuselage centreline intersection and for the second type of analysis both symmetric and antisymmetric motions are considered for whole aircraft modelled as bending-torsion coupled beams. Also a parametric study is carried out by varying lumped masses and inertias between +25% and -25% in steps of 5% and their subsequent effects on the natural frequencies, mode shapes and flutter speed are investigated for the first type of aircraft model. It can be seen from the results that their contribution to natural frequencies, flutter speeds and flutter frequencies are very minimal.

Section B

An overview and layout of Section B

Free vibration analysis is of great importance in the design of aeronautical, civil, automobile and marine engineering structures, amongst the others. These structures are often idealised by beam elements such as the case with high aspect ratio aircraft wings. The traditional finite element method (FEM) is generally used when carrying out the static and dynamic analysis of beam and other structures. Clearly the order of the mass and stiffness matrices in the FEM decides the number of natural frequencies that can be meaningfully computed. The higher order natural frequencies and mode shapes, will of course, be considerably less accurate. It should be noted that there is a powerful alternative to FEM as well the classical method, which has no restriction on higher order natural frequency computation and yet it retains the exactness of results. The alternative is that of the dynamic stiffness method (DSM) which is elegant and versatile and can be used to analyse the free vibration behaviour of complex structures. The DSM is different, but in many ways similar to the FEM in that it has analogous procedure for assembling structural properties of individual structural elements. However, a major difference exists between the DSM and the FEM which is that the former is unaffected by the number of elements used in the analysis and always gives exact results whereas the latter is mesh dependent and the accuracy of results depends on the number of elements used in the analysis. For instance, one single structural element can be used in the DSM to compute any number of natural frequencies without any loss of accuracy which, of course, is impossible in the FEM. The uncompromising accuracy of the DSM stems from the fact that the frequency dependent shape function used to derive the element dynamic stiffness matrix of a structural element comes from the exact solution of the governing differential equation of motion of the element undergoing free natural vibration. The overall frequency dependent dynamic stiffness matrix of the final structure is obtained by assembling the individual dynamic stiffness matrices of all constituent elements in the structure, in the usual way as in the case of the FEM, but the formulation leads to a non-linear eigenvalue problem and the natural frequencies are generally extracted by applying the well-established algorithm of Wittrick and William. Section B deals with fundamental research in dynamic stiffness formulation and its application. Each chapter is self-contained and consists of a brief introduction, literature review, theory, discussion of computed results and conclusions.

The layout of this Section B is as follows. Chapter 6 deals with the free vibration analysis of functionally graded beams and frameworks which is followed by Chapter 7 for which the subject matter is free vibration of cracked beam. Next in Chapter 8, analytical development of advanced beam model incorporating Rayleigh-Love and Timoshenko beam theories is given precedence. Finally Chapter 9 deals with the theoretical, analytical and computational development of the free vibration analysis of axial-bending coupled beams.

Chapter 6

Functionally graded beams

6.1 Introduction to functionally graded beams (FGBs)

A functionally graded material (FGM) may be characterised by the variation in composition and structure gradually over volume, resulting in corresponding changes in the properties of the material. The materials can be designed for specific function and applications. It consists of pure form of each component, hence the properties of all components can be fully utilised. In recent years interest in functionally graded material (FGM) has grown enormously. The progress made in understanding this material has been phenomenal. In conventional laminated composite structures, homogeneous elastic laminae are bonded together to obtain enhanced mechanical and material properties. The anisotropic constitution of laminated composite structures often results in stress concentrations near material and geometric discontinuities which can lead to damage in the form of delamination, matrix cracking and adhesive bond separation. FGMs are a class of composites that have a continuous variation of material properties from one surface to another and thus alleviate the stress concentrations found in laminated composites. The gradation in properties of the material reduces thermal stresses, residual stresses and stress concentration factors.

In general, FGMs are composite materials with a microscopically inhomogeneous character. Continuous changes in their microstructure distinguish FGMs from conventional composite materials [1]. One great advantage of FGM is that the properties vary gradually in a continuous manner within the material so that there is no abrupt change or mismatch of the properties. By contrast, fibre-reinforced laminated composite materials have different characteristics. The problem of delamination does not exist in FGM whereas it can be very much prevalent in composite laminates. For example, FGM can be designed in a way to have the properties of ceramic at one end and those of metal at the other so that the thermal resistance of ceramic and the mechanical behaviour of metal can be exploited to guarantee structural integrity.

The free vibration analysis of functionally graded beams (FGBs) and frameworks containing FGBs is carried out by applying the dynamic stiffness method and deriving the elements of the dynamic stiffness matrix in explicit algebraic form. The stated rule that the material properties of the FGBs vary continuously through the thickness according to the power law forms the fundamental basis of the governing differential equations of motion in free vibration. The differential equations are solved in closed analytical form when the free vibratory motion is harmonic. The dynamic stiffness matrix is then formulated by relating the amplitudes of forces to those of the displacements at the two ends of the beam. Next, the explicit algebraic expressions for the dynamic stiffness elements are derived with the help of symbolic computation. Finally the Wittrick-Williams algorithm is applied as solution technique to solve the free vibration problems of FGBs with uniform cross-section, stepped FGBs and frameworks consisting of FGBs. Some numerical results are validated against published results, but in the absence of published results for frameworks containing FGBs, consistency checks on the reliability of results are performed.

6.2 Literature review

Researchers have been continually motivated to use various techniques and methodologies to deal with this exciting material in order to enhance its state-of-the-art. There are now excellent books [1–4] available on the subject. As potential application of FGM, beams which are extensively used in civil, mechanical, aeronautical and other branches of engineering as principal load carrying structural members can be investigated for their free vibration characteristics. Investigators have expended considerable efforts which have led to the insurgence of massive literature on the free vibration behaviour of functionally graded beams (FGBs). A number of theories and methodologies have been proposed to study the free vibration characteristics of FGBs. Foremost amongst these are the applications of direct analytical procedure using the governing differential equations of motion [5–8], finite element [9, 10], Rayleigh-Ritz [11], finite volume [12, 13], differential quadrature [14], differential transformation [15] and transfer function [16, 17] methods. Recently the dynamic stiffness method (DSM) has also been proposed [18, 19].

The current research stems from the previously published DSM theories. The entire formulation using DSM is accomplished in the real domain as opposed to previous formulations which used complex arithmetic when developing the element dynamic stiffness matrices [18, 19]. Another important further development included is the derivation of explicit algebraic expressions for the dynamic stiffness elements using symbolic computation [20–22]. The explicit expressions for the dynamic stiffness elements are particularly useful in optimisation studies and also when some, but not all of the stiffnesses are needed. Of particular significance of this investigation is the application of DSM to analyse the free vibration characteristics of stepped FGBs and frameworks containing FGBs. The solution technique used in the DSM is robust, particularly when the well-established algorithm of Wittrick and Williams [23], known as Wittrick-Williams algorithm in the literature, is applied. The algorithm ensures that no natural frequency of the structure is missed, and it has featured in literally hundreds of papers. It is worth noting that earlier investigations on the free vibration of FGBs were focused on individual FGBs except for a few isolated cases where stepped FGBs with collinear axes were reported [24, 25]. Accordingly, the literature on the free vibration of frameworks containing FGBs is virtually non-existent. The current part of this research focuses to fill this gap.

6.3 Theoretical formulation

In a right-handed Cartesian coordinate system, Figure 6.1 shows a uniform rectangular cross-section FGB of length L, width b and thickness h. The beam material has Young's Modulus E and mass density ρ which can vary through the thickness direction (Z) of the cross-section according to the following power law distribution [17, 19, 26]:

$$E(z) = (E_t - E_b)\left(\frac{z}{h} + \frac{1}{2}\right)^k + E_b, \qquad \rho(z) = (\rho_t - \rho_b)\left(\frac{z}{h} + \frac{1}{2}\right)^k + \rho_b \tag{6.1}$$

where E_t and E_b are the Young's moduli, and ρ_t and ρ_b are the densities at the top and bottom surfaces of the beam, respectively.

In Equation 6.1, k ($k \geq 0$) is the power law index parameter which indicates the material property variation through the beam thickness. The parameter k has been extensively discussed in the literature [27, 28] and hence it is not elaborated here. However, three special cases maybe observed. Clearly $k = 1$ indicates a linear variation of the composition between the top and bottom surfaces of the beam, $k = 0$ represents the case when the beam is made of full material of the top surface whereas infinite k represents the case when the beam is made of full material of the bottom surface.

6.3.1 Governing differential equations of motion and its solution

The classical Bernoulli-Euler theory is considered here so that the effects of shear deformation and rotary inertia that are relevant to the Timoshenko beam theory are assumed to be small and hence disregarded in the analysis. Referring to Figure 6.1, the displacements u_1, v_1 and w_1 along the X, Y and Z directions of a point on the cross-section are given by [17, 29]:

$$u_1 = 0, v_1(y,z,t) = v(y,t) - z\frac{\partial w(y,t)}{\partial y}, w_1(y,z,t) = w(y,t) \tag{6.2}$$

where v and w are the corresponding displacements of a point on the neutral axis of the beam. It should be noted that due to the variation of the material properties through the thickness, the neutral axis would no longer be at the central line of the beam cross-section [30, 31].

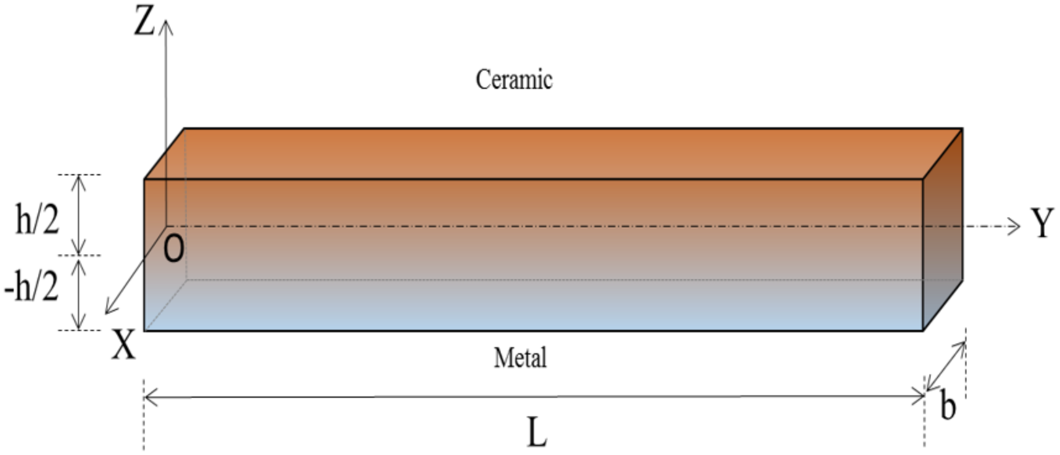

Figure 6.1: Coordinate system and dimensions of a functionally graded beam.

Using the displacement field given by Equation 6.2 and through the application of Hamilton's principle, the governing differential equations of motion in free vibration of the FGB are given by [17, 19]

$$-B_0\ddot{v} + B_1\ddot{w}' + A_0v'' - A_1w''' = 0, \qquad -B_0\ddot{w} - B_1\ddot{v}' + B_2\ddot{w}'' + A_1v''' - A_2w'''' = 0 \quad (6.3)$$

where

$$A_i = \int z^i E(z)dA, \qquad B_i = \int z^i \rho(z)dA \qquad (i = 0,\ 1,\ 2) \quad (6.4)$$

The natural boundary conditions from the Hamiltonian formulation [17, 19] give the following expressions for axial force F, shear force S and bending moment M as follows:

$$F = -A_0v' + A_1w'', \qquad S = B_1\ddot{v} - A_1v'' - B_2\ddot{w}' + A_2w''', \qquad M = A_1v' - A_2w'' \quad (6.5)$$

Clearly, due to the use of FGM, the axial (v) and bending motions (w) are coupled as evident from Equations 6.3 and 6.5.
Assuming harmonic oscillation so that

$$v(y,t) = V(y)e^{i\omega t}, w(y,t) = W(y)e^{i\omega t} \quad (6.6)$$

where ω is the angular or circular frequency, $V(y)$ and $W(y)$ are the amplitudes of (v) and (w) , respectively.

Introducing the differential operator $D = \frac{d}{d\xi}$ and the non-dimensional length ξ as:

$$\xi = \frac{y}{L} \tag{6.7}$$

The differential equations of motion in Equations 6.3 can now be written as:

$$\left.\begin{aligned} &(B_0\omega^2L^3 + A_0LD^2)V(\xi) - (B_1\omega^2L^2D + A_1D^3)W(\xi) = 0 \\ &(B_1\omega^2L^3D + A_1LD^3)V(\xi) + (B_0\omega^2L^4 - B_2\omega^2L^2D^2 - A_2D^4)W(\xi) = 0 \end{aligned}\right\} \tag{6.8}$$

By combining the above two differential equations, it is possible to obtain a sixth order ordinary differential equation satisfying both $V(\xi)$ and $W(\xi)$ to give:

$$(D^6 + aD^4 - bD^2 - c)H = 0 \tag{6.9}$$

where

$$H = V(\xi) \text{ or } W(\xi) \tag{6.10}$$

and

$$a = \frac{2A_1B_1 - A_0B_2 - A_2B_0}{A_1^2 - A_0A_2}L^2\omega^2, b = \frac{B_0B_2\omega^2 - A_0B_0 - B_1^2\omega^2}{A_1^2 - A_0A_2}L^4\omega^2, c = -\frac{B_0^2}{A_1^2 - A_0A_2}L^6\omega^4 \tag{6.11}$$

By assuming the solution in the form $H = e^{\lambda\xi}$ the characteristic or auxiliary equation of the differential equation Equation 6.9 can be expressed as

$$\lambda^6 + a\lambda^4 - b\lambda^2 - c = 0 \tag{6.12}$$

Equation 6.12 can be reduced to a cubic equation to give

$$\mu^3 + a\mu^2 - b\mu - c = 0 \tag{6.13}$$

where

$$\mu = \lambda^2 \tag{6.14}$$

Using an approach similar to the one described in [32, 33], it can be shown that the three roots of the cubic equation (Equation 6.13) are real and the solution for H in Equation 6.9 can be expressed in terms of trigonometric and hyperbolic functions. This is advantageous when deriving the explicit expressions for the dynamic stiffness elements of the FGB. Explicit expressions are particularly useful when some, but not all of the stiffness elements are needed, e.g. sensitivity analysis in optimisation studies. Thus if the roots [34] of Equation 6.13 are α, β and γ, the solution for H is given by

$$H(\xi) = C_1\cosh\alpha\xi + C_2\sinh\alpha\xi + C_3\cos\beta\xi + C_4\sin\beta\xi + C_5\cos\gamma\xi + C_6\sin\gamma\xi \tag{6.15}$$

where

$$\alpha = \left[2\left(\frac{q}{3}\right)^{\frac{1}{2}}\cos\frac{\phi}{3} - \frac{a}{3}\right]^{\frac{1}{2}} \quad \beta = \left[2\left(\frac{q}{3}\right)^{\frac{1}{2}}\cos\frac{\pi-\phi}{3} + \frac{a}{3}\right]^{\frac{1}{2}} \quad \gamma = \left[2\left(\frac{q}{3}\right)^{\frac{1}{2}}\cos\frac{\pi+\phi}{3} + \frac{a}{3}\right]^{\frac{1}{2}} \tag{6.16}$$

with

$$q = b + \frac{a^2}{3} \tag{6.17}$$

and

$$\phi = \cos^{-1}\left[\frac{27c - 9ab - 2a^3}{2\left(a^2+3b\right)^{\frac{3}{2}}}\right] \tag{6.18}$$

$H(\xi)$ of Equation 6.15 represents the solution for both axial displacement $V(\xi)$ and bending displacement $W(\xi)$, containing different sets of constants as follows

$$V(\xi) = Q_1\cosh\alpha\xi + Q_2\sinh\alpha\xi + Q_3\cos\beta\xi + Q_4\sin\beta\xi + Q_5\cos\gamma\xi + Q_6\sin\gamma\xi \tag{6.19}$$

$$W(\xi) = R_1\cosh\alpha\xi + R_2\sinh\alpha\xi + R_3\cos\beta\xi + R_4\sin\beta\xi + R_5\cos\gamma\xi + R_6\sin\gamma\xi \tag{6.20}$$

The two different sets of constants Q_1-Q_6 and R_1-R_6 can be related with the help of any one of the two of Equations 6.8 to give

$$\begin{gathered} Q_1 = \left(\tfrac{k_\alpha}{L}\right)R_2, \quad Q_3 = \left(\tfrac{k_\beta}{L}\right)R_4, \quad Q_5 = \left(\tfrac{k_\gamma}{L}\right)R_6\ , \\ Q_2 = \left(\tfrac{k_\alpha}{L}\right)R_1, \quad Q_4 = -\left(\tfrac{k_\beta}{L}\right)R_3, \quad Q_6 = -\left(\tfrac{k_\gamma}{L}\right)R_5 \end{gathered} \tag{6.21}$$

where

$$k_\alpha = \tfrac{\alpha\left(A_1\alpha^2+B_1\omega^2L^2\right)}{\left(A_0\alpha^2+B_0\omega^2L^2\right)}, \quad k_\beta = \tfrac{\beta\left(A_1\beta^2-B_1\omega^2L^2\right)}{\left(A_0\beta^2-B_0\omega^2L^2\right)}, \quad k_\gamma = \tfrac{\gamma\left(A_1\gamma^2-B_1\omega^2L^2\right)}{\left(A_0\gamma^2-B_0\omega^2L^2\right)} \tag{6.22}$$

With the help of Equations 6.5, 6.19 and 6.20, the expressions for bending rotation $\theta(\xi)$, axial force $F(\xi)$, bending moment $M(\xi)$, and shear force $S(\xi)$ can be obtained after some simplification, as

$$\begin{aligned} \theta(\xi) = \tfrac{W'(\xi)}{L} = \left(\tfrac{1}{L}\right)\{&R_1\alpha\sinh\alpha\xi + R_2\alpha\cosh\alpha\xi - R_3\beta\sin\beta\xi + R_4\beta\cos\beta\xi \\ &-R_5\gamma\sin\gamma\xi + R_6\gamma\cos\gamma\xi\} \end{aligned} \tag{6.23}$$

$$\begin{aligned} F(\xi) = -\tfrac{A_0}{L}\left(V' - \tfrac{A_1}{A_0L}W''\right) = \left(\tfrac{A_0}{L}\right)\{&-R_1\tfrac{e_\alpha}{L}\cosh\alpha\xi - R_2\tfrac{e_\alpha}{L}\sinh\alpha\xi + R_3\tfrac{e_\beta}{L}\cos\beta\xi \\ &+R_4\tfrac{e_\beta}{L}\sin\beta\xi + R_5\tfrac{e_\gamma}{L}\cos\gamma\xi + R_6\tfrac{e_\gamma}{L}\sin\gamma\xi\} \end{aligned} \tag{6.24}$$

$$\begin{aligned} M(\xi) = -\tfrac{A_2}{L^2}\left(W'' - \tfrac{A_1L}{A_2}V'\right) = -\left(\tfrac{A_2}{L^2}\right)\{&-R_1g_\alpha\cosh\alpha\xi - R_2g_\alpha\sinh\alpha\xi + R_3g_\beta\cos\beta\xi \\ &+R_4g_\beta\sin\beta\xi + R_5g_\gamma\cos\gamma\xi + R_6g_\gamma\sin\gamma\xi\} \end{aligned} \tag{6.25}$$

$$\begin{aligned} S(\xi) &= \tfrac{A_2}{L^3}\left(W''' + \tfrac{B_2L^2\omega^2}{A_2}W' - \tfrac{A_1L}{A_2}V'' - \tfrac{B_1L^3\omega^2}{A_2}V\right) \\ &= \tfrac{A_2}{L^3}\left\{R_1f_\alpha\sinh\alpha\xi + R_2f_\alpha\cosh\alpha\xi + R_3f_\beta\sin\beta\xi - R_4\cos\beta\xi + R_5\sin\gamma\xi - R_6\cos\gamma\xi\right\} \end{aligned} \tag{6.26}$$

where

$$e_\alpha = \alpha k_\alpha - A_1\alpha^2/A_0, \qquad e_\beta = \beta k_\beta - A_1\beta^2/A_0, \qquad e_\gamma = \gamma k_\gamma - A_1\gamma^2/A_0 \tag{6.27}$$

$$g_\alpha = \alpha^2 - \alpha k_\alpha A_1/A_2, \qquad g_\beta = \beta^2 - \beta k_\beta A_1/A_2, \qquad g_\gamma = \gamma^2 - \gamma k_\gamma A_1/A_2 \tag{6.28}$$

$$\begin{aligned} f_\alpha &= \alpha^3 - \alpha^2 k_\alpha A_1/A_2 + \alpha\omega^2 L^2 B_2/A_2 - k_\alpha \omega^2 L^2 B_1/A_2 \\ f_\beta &= \beta^3 - \beta^2 k_\beta A_1/A_2 - \beta\omega^2 L^2 B_2/A_2 + k_\beta \omega^2 L^2 B_1/A_2 \\ f_\gamma &= \gamma^3 - \gamma^2 k_\gamma A_1/A_2 - \gamma\omega^2 L^2 B_2/A_2 + k_\gamma \omega^2 L^2 B_1/A_2 \end{aligned} \tag{6.29}$$

6.3.2 Dynamic stiffness formulation

The dynamic stiffness matrix of the FGB can now be formulated by applying natural boundary conditions for displacements and forces at the ends of the beam. Referring to the sign convention for positive axial force, shear force and bending moment shown in Figure 6.2, the boundary conditions for displacements and forces, see Figure 6.3, are:

$$At \ \ \xi = 0: \quad V = V_1, \ \ W = W_1, \ \ \theta = \theta_1, F = F_1, \ \ S = S_1, \ \ M = M_1 \tag{6.30}$$

$$At \ \ \xi = 1: \quad V = V_2, \ \ W = W_2, \ \ \theta = \theta_2, F = -F_2, \ \ S = -S_2, \ \ M = -M_2 \tag{6.31}$$

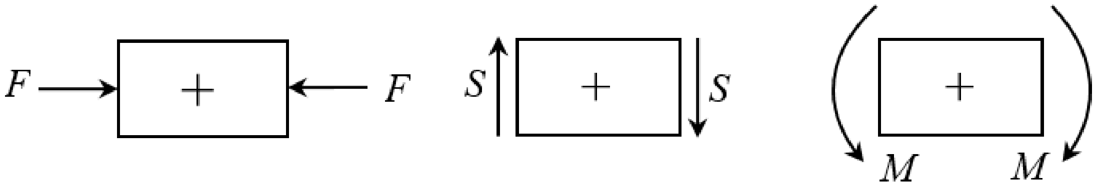

Figure 6.2: Sign convention for positive axial force F, shear force S and bending moment M.

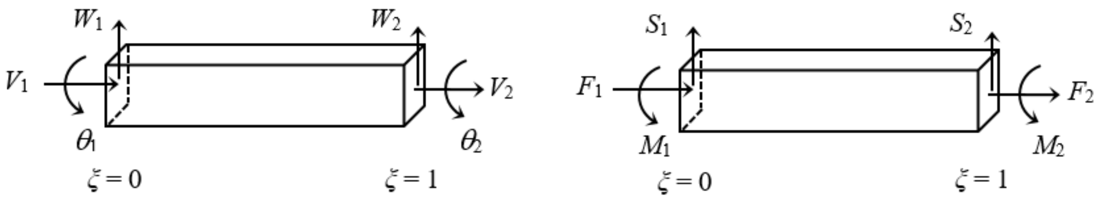

(a) Displacements (b) Forces

Figure 6.3: Boundary conditions for displacements and forces.

The displacement vector δ and the force vector **P** can be expressed as:

$$\delta = [V_1 \ \ W_1 \ \ \theta_1 \ \ V_2 \ \ W_2 \ \ \theta_2]^T, P = [\ F_1 \ \ S_1 \ \ M_1 \ \ F_2 \ \ S_2 \ M_2\ ]^T \tag{6.32}$$

where the upper script T denotes a transpose.

The relationship between the displacement δ and the constant vector **R** can be obtained by using Equations 6.19 -6.23 and Equations 6.30-6.31 to give,

$$\delta = B\,R \tag{6.33}$$

where

$$B = \begin{bmatrix} 0 & \frac{k_\alpha}{L} & 0 & \frac{k_\beta}{L} & 0 & \frac{k_\gamma}{L} \\ 1 & 0 & 1 & 0 & 1 & 0 \\ 0 & \frac{\alpha}{L} & 0 & \frac{\beta}{L} & 0 & \frac{\gamma}{L} \\ \frac{k_\alpha S_{h\alpha}}{L} & \frac{k_\alpha C_{h\alpha}}{L} & -\frac{k_\beta S_\beta}{L} & \frac{k_\beta C_\beta}{L} & -\frac{k_\gamma S_\gamma}{L} & \frac{k_\gamma C_\gamma}{L} \\ C_{h\alpha} & S_{h\alpha} & C_\beta & S_\beta & C_\gamma & S_\gamma \\ \frac{\alpha S_{h\alpha}}{L} & \frac{\alpha C_{h\alpha}}{L} & -\frac{\beta S_\beta}{L} & \frac{\beta C_\beta}{L} & -\frac{\gamma S_\gamma}{L} & \frac{\gamma C_\gamma}{L} \end{bmatrix} \tag{6.34}$$

with

$$C_{h\alpha} = \cosh\alpha, \quad S_{h\alpha} = \sinh\alpha, \quad C_\beta = \cos\beta, \quad S_\beta = \sin\beta, \quad C_\gamma = \cos\gamma, \quad S_\gamma = \sin\lambda \tag{6.35}$$

Similarly, the relationship between the force vector **P** and the constant vector **R** can be obtained using Equations 6.24-6.26 and Equations 6.30-6.31 to give

$$P = A\,R \tag{6.36}$$

where

$$A = \begin{bmatrix} -\frac{W_1 e_\alpha}{L} & 0 & \frac{W_1 e_\beta}{L} & 0 & \frac{W_1 e_\gamma}{L} & 0 \\ 0 & W_3 f_\alpha & 0 & -W_3 f_\beta & 0 & -W_3 f_\gamma \\ -W_2 g_\alpha & 0 & W_2 g_\beta & 0 & W_2 g_\gamma & 0 \\ \frac{W_1 e_\alpha C_{h\alpha}}{L} & \frac{W_1 e_\alpha S_{h\alpha}}{L} & -\frac{W_1 e_\beta C_\beta}{L} & -\frac{W_1 e_\beta S_\beta}{L} & -\frac{W_1 e_\gamma C_\gamma}{L} & -\frac{W_1 e_\gamma S_\gamma}{L} \\ -W_3 f_\alpha S_{h\alpha} & -W_3 f_\alpha C_{h\alpha} & -W_3 f_\beta S_\beta & W_3 f_\beta C_\beta & -W_3 f_\gamma S_\gamma & W_3 f_\gamma C_\gamma \\ W_2 g_\alpha C_{h\alpha} & W_2 g_\alpha S_{h\alpha} & -W_2 g_\beta C_\beta & -W_2 g_\beta S_\beta & -W_2 g_\gamma C_\gamma & -W_2 g_\gamma S_\gamma \end{bmatrix} \tag{6.37}$$

By eliminating the constant vector **R** from Equations 6.33 and 6.36, **P** and δ can be related to give the dynamic stiffness matrix relationship of the FGB as

$$P = K\,\delta \tag{6.38}$$

where

$$\mathrm{K} = \mathrm{A}\,\mathrm{B}^{-1} \tag{6.39}$$

is the required dynamic stiffness matrix with elements k_{ij} ($i = 1, 2, 3..6; j = 1, 2, 3,..6$). With the help of symbolic computation [20, 22], the matrix **B** of Equation 6.34 was inverted algebraically and the inverted matrix was pre-multiplied by the matrix **A** of Equation 6.37 in order to generate the explicit expressions for each of the elements of the dynamic stiffness matrix **K**. The stiffness expressions are simplified very considerably by means of symbolic computations.

The above 6×6 frequency dependent dynamic stiffness matrix **K** of Equation 6.39 can now be used to compute the natural frequencies and mode shapes of either an individual FGB or an assembly of FGBs for different boundary conditions. A reliable and accurate method of solving the problem is to apply the Wittrick-Williams algorithm [23] which is well suited for the application of DSM. The algorithm uses the Sturm sequence property of the dynamic stiffness matrix to ensure that no natural frequencies of the structure analysed are missed. Basically the algorithm [23] gives the number of natural frequencies of a structure that lie below an arbitrarily chosen trial frequency specified by the user. As successive trial frequencies can be chosen by the user, this simple feature of the algorithm can be exploited to bracket any natural frequency between its upper and lower bounds to any desired accuracy. The results given in the next section were computed by applying the Wittrick-Williams algorithm as the customary solution technique.

6.4 Results and discussion

The first set of results was obtained for a uniform FGB with different boundary conditions with the letters C, F and S denoting clamped, free and simple-support at each end of the beam. Four classical boundary conditions are investigated, namely, clamped-free (C-F), simply-supported (S-S), clamped-simply support (C-S) and clamped-clamped (C-C). The simple support (S) boundary condition is assumed to be equivalent to a pinned support which prevents both flexural and axial displacements. A wide range of investigations was carried out by varying the length to thickness ratio (L/h) and the power law index k of the FGB which controls the material property distribution through thickness. However, only selected results are given when presenting because existing literature already covers a huge amount of data for natural frequencies and mode shapes with the variations of L/h and k, see for example [17]. For brevity, only the results for L/h =10 and k = 0.5 have been used here, but the theory has been extensively validated against published results.

In order to make the results universal and also to be consistent with the published results, the following non-dimensional natural frequency parameter is defined

$$\lambda_i = \omega_i \frac{L^2}{h} \sqrt{\frac{\rho_b}{E_b}} \tag{6.40}$$

where ω_i is the i^{th} angular natural frequency in rad/s, ρ_b and E_b are density and Young's modulus of the bottom surface of the FGB.

Table 6.1: Non-dimensional natural frequencies (λ_i) of a uniform FGB with $L/h = 10$ and $k = 0.5$ for different boundary conditions.

Boundary conditions	Non-dimensional natural frequencies $\left(\lambda_i = \frac{\omega_i L^2}{h}\sqrt{\frac{\rho_b}{E_b}}\right)$									
	λ_1		λ_2		λ_3		λ_4		λ_5	
	Present	Ref.[30]	Present	Ref.[30]	Present	Ref.[30]	Present	Ref.[30]	Present	Ref.[30]
C-F	1.721	1.660	10.657	10.284	27.280	27.265	29.280	28.303	55.876	54.033
S-S	4.820	4.788	19.036	18.328	41.954	40.603	54.561	53.830	72.554	70.782
C-S	7.521	7.295	24.036	23.228	49.074	47.264	54.559	54.580	81.560	79.070
C-C	10.903	10.530	29.598	28.624	54.561	54.565	56.723	54.944	91.046	88.349

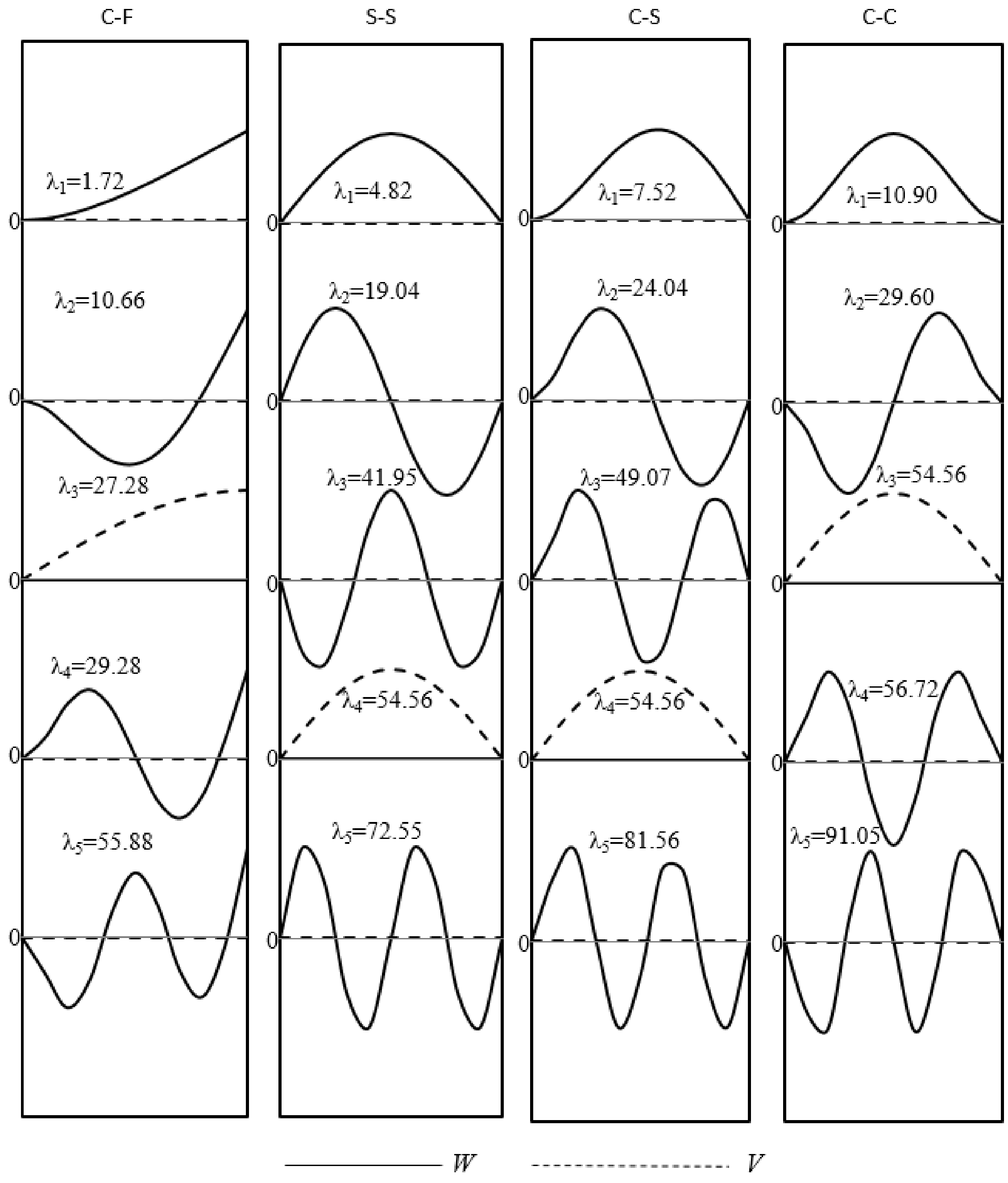

Figure 6.4: Natural frequencies and mode shapes of FGB with L/h = 10, k = 0.5 for different boundary conditions (C-Clamped, F-Free, S-Simple support).

Table 6.1 shows the first five natural frequencies of the FGB with L/h = 10 and k = 0.5 for C-F, S-S, C-S and C-C boundary conditions alongside the results reported in a recently published paper [30]. The close agreement between the results from the current investigation and the published ones is clearly evident. The maximum discrepancy between the two sets of results is less than 4%. The corresponding mode shapes shown in Figure 6.4, reveal that for the C-F and C-C boundary conditions, the first, second, fourth and fifth

Table 6.2: Dimensionless fundamental natural frequency of a stepped FGB with $k = 0.5$ for different step ratios and boundary conditions.

Boundary conditions	Non-dimensional fundamental natural frequency $\left(\lambda_i = \frac{\omega_i L^2}{h}\sqrt{\frac{\rho_b}{E_b}}\right)$					
	L_1/L = 0.25		L_1/L = 0.5		L_1/L = 0.75	
	Present	Ref.[38]	Present	Ref.[38]	Present	Ref.[38]
C-F	1.365	1.381	2.050	2.073	2.124	2.148
S-S	2.431	2.460	2.731	2.763	3.909	3.954
C-S	5.525	5.600	5.476	5.541	5.963	6.037
C-C	7.780	7.897	7.265	7.358	8.377	8.487

modes are essentially bending (solid line) modes whereas the third one is axial (dashed line). By contrast, for the S-S and C-S boundary conditions, the first, second, third and fifth modes are basically bending modes and the fourth one axial.

The next set of results was obtained for a stepped beam (see Figure 6.5) made of FGM, for which some comparative results are available in the literature. The DSM theory developed in this chapter can easily account for such problems with any step location, thickness variation and boundary conditions. However, for brevity only the results for stepped FGB with step locations $L_1 = 0.25$L, $L_1 = 0.5$L and $L_1 = 0.75$L (see Figure 6.5) and the power law index $k = 0.5$ are presented in Table 6.2 together with the published results [38]. Note that for consistency, FGM type-II of Ref. [25] is used so that the results are directly comparable. Clearly, the results from the current investigation are in close agreement with those of [25].

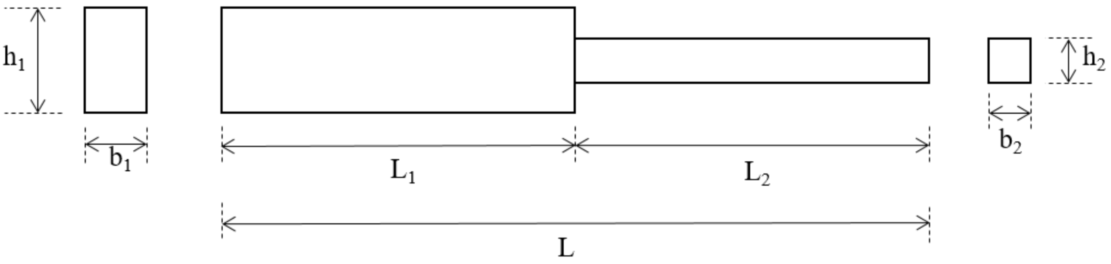

Figure 6.5: A stepped functionally graded beam.

The final set of results was obtained for a portal frame consisting of three beam members AB, BC and CD as shown in Figure 6.6. The natural frequencies of this frame are available in the literature [35] when all the three beam members of the frame are made of isotropic material and the supports at both points A and D are either clamped (built-in) or pinned (simply-supported). These results are based on exact analytical theory. Using the current theory, results are obtained for both the boundary conditions C-C and S-S at A and D, respectively and making (i) all the three members AB, BC and CD isotropic (which is achieved by substituting the power-law index parameter k to zero and using both the top and bottom surface material properties to be the same and isotropic), (ii) AB and CD isotropic, but BC made of FGM, (iii) BC isotropic and AB and CD made of FGM and (iv) AB, BC and CD are all made of FGM. When computing numerical results, all three members of the portal frame are assumed to have the same rectangular cross-section and length. The width and depth (height) of the cross-section are taken to be 0.04 m and 0.02 m, respectively and length of each member is set to 1m. When any of the beam members is isotropic, it is considered to be made of steel with Young's modulus 200 GPa and density 7500 kg/m^3 whereas if it is made of FGM, the bottom surface is considered to be steel with the above properties and the top surface ceramic with Young's modulus 380 GPa and density 3960 kg/m^3. The computed natural frequencies are non-dimensionalised with respect to the metallic properties to give

$$\lambda_i = \omega_i \sqrt{\frac{\rho A L^4}{EI}} \tag{6.41}$$

The results of the investigation when all members of the portal frame (see Figure 6.6) are metallic, are given in Table 6.3 showing the first three non-dimensional natural frequencies of the frame when the points A and D are clamped (C-C) or simply-supported (S-S), together with the results reported in Ref. [35]. The agreement between the sets of results in Table 6.3 is excellent. Table 6.4 shows the three non-dimensional natural frequencies when the vertical members AB and CD and the horizontal member BC of the frame are made of either isotropic metal or FGM in turn, as indicated, and the points A and D are clamped (C-C). Similar results are obtained for the case when the points A and D of Figure 6.6 are simply-supported (S-S). The results for the S-S case are shown in Table 6.5. Clearly the results shown in Tables 6.4 and 6.5 when compared to Table 6.3 indicate that significant changes in natural frequencies can occur as a result of using functionally graded beams. This can have profound influence in the design of fire-resistant multi-storey and multi-bay building structures.

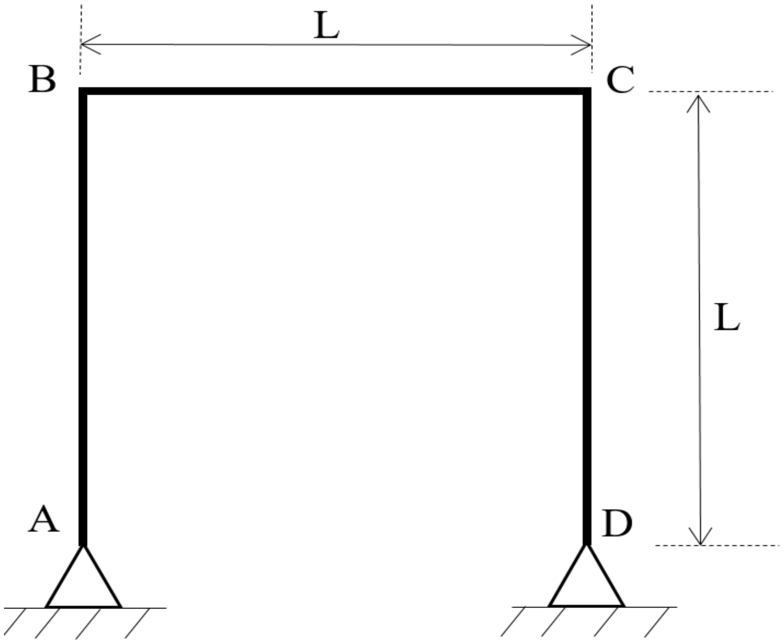

Figure 6.6: A portal frame.

Table 6.3: Non-dimensional natural frequencies of a portal frame made of metallic members.

Boundary conditions at A and D	Non-dimensional natural frequencies ($\lambda_i = \omega_i \sqrt{\frac{\rho A L^4}{EI}}$)					
	λ_1		λ_2		λ_3	
	Present	Ref.[44]	Present	Ref.[44]	Present	Ref.[44]
C-C	3.204	3.205	12.639	12.648	20.627	20.629
S-S	1.463	1.463	9.866	9.870	14.854	14.856

Table 6.4: Non-dimensional natural frequencies of portal frame made of metal and FGM with built-in boundary conditions at A and D for different *k* values.

k	Non-dimensional natural frequency ($\lambda_i = \omega_i \sqrt{\frac{\rho A L^4}{EI}}$)								
	Frame type with different categories of constituent members AB, BC and CD								
	AB, CD: metallic; BC: FGM			BC: metallic; AB, CD: FGM			AB, BC, CD: FGM		
	λ_1	λ_2	λ_3	λ_1	λ_2	λ_3	λ_1	λ_2	λ_3
0.5	3.711	15.226	22.470	4.046	14.879	28.255	4.841	19.089	31.137
1.0	3.585	14.677	22.065	3.869	14.461	26.323	4.412	17.390	28.355
5.0	3.360	13.602	21.344	3.553	13.634	23.203	3.741	14.749	24.054

Table 6.5: Non-dimensional natural frequencies of portal frame made of metal and FGM with simple-support boundary conditions at A and D for different *k* values.

k	Non-dimensional natural frequency ($\lambda_i = \omega_i \sqrt{\frac{\rho A L^4}{EI}}$)								
	Frame type with different categories of constituent members AB, BC and CD								
	AB, CD: metallic; BC: FGM			BC: metallic; AB, CD: FGM			AB, BC, CD: FGM		
	λ_1	λ_2	λ_3	λ_1	λ_2	λ_3	λ_1	λ_2	λ_3
0.5	1.694	11.083	16.282	1.831	12.617	20.301	2.211	14.906	22.434
1.0	1.640	10.848	15.961	1.752	12.025	18.917	2.015	13.583	20.438
5.0	1.541	10.375	15.394	1.610	10.921	16.694	1.708	11.518	17.334

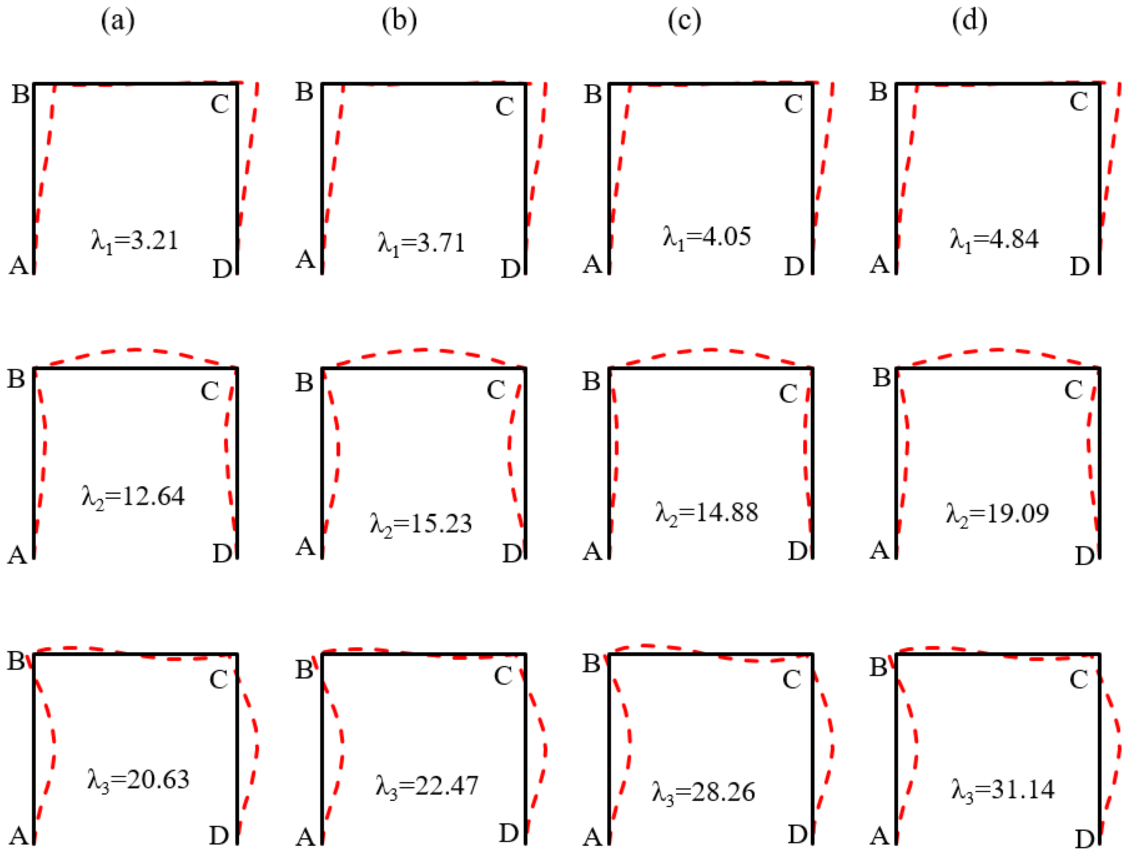

Figure 6.7: Natural frequencies and mode shapes of portal frame for various cases with points A and D built-in. (a) AB, BC and CD are all metallic, (b) AB and CD are metallic, but BC is FGM, (c) AB and CD are FGM, but BC is metallic, (d) AB, BC and CD are all FGM.

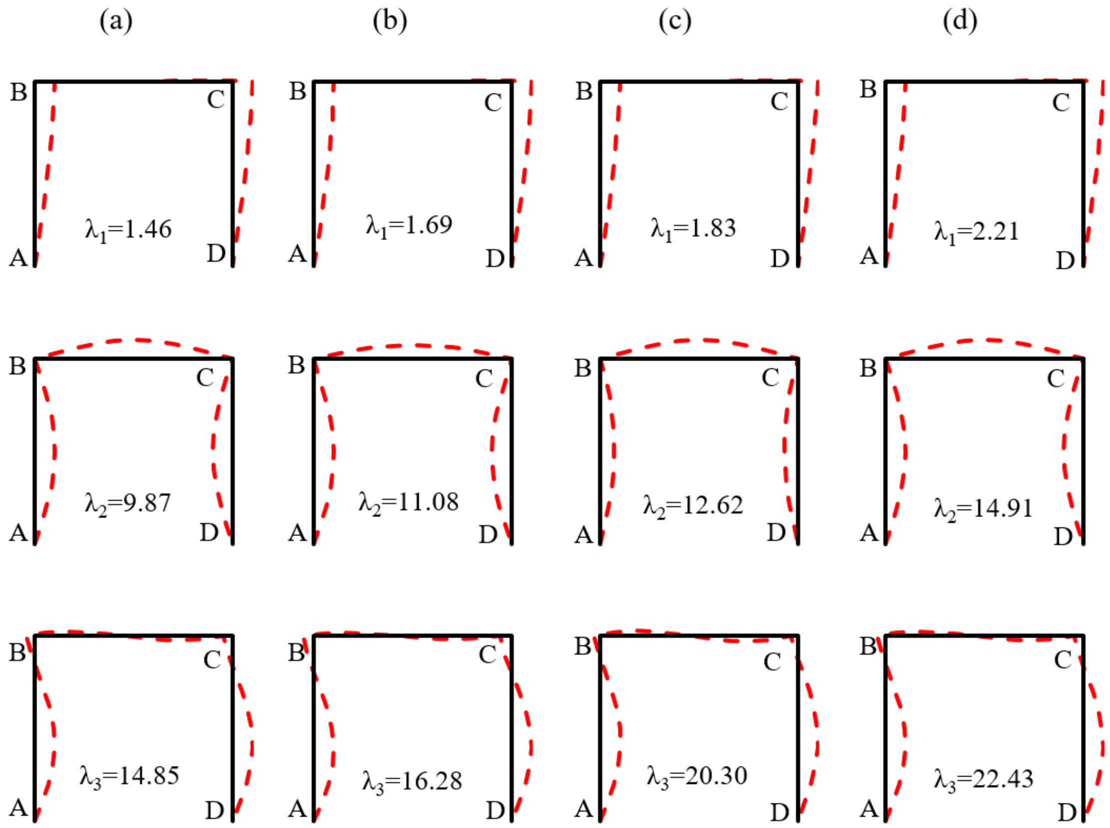

Figure 6.8: Natural frequencies and mode shapes of portal frame for various cases with points A and D simply-supported. (a) AB, BC and CD are all metallic, (b) AB and CD are metallic, but BC is FGM, (c) AB and CD are FGM, but BC is metallic, (d) AB, BC and CD are all FGM.

For illustrative purposes, representative mode shapes for the portal frame of Figure 6.6 are presented in Figures 6.7 and 6.8 when the points A and D of the frame are built-in (clamped) and simply-supported, respectively. The power law index parameter k is set to 0.5 when computing the mode shapes. Figures 6.7(a) and 6.8(a) represent the mode shapes when all three members of the portal frame are metallic whereas Figures 6.7(b) and 6.8(b) shows the mode shapes when the columns AB and CD are metallic, but the beam BC is made of FGM. By contrast Figures 6.7(c) and 6.8(c) show the mode shapes for the case when the beam BC of the portal frame is metallic, but its columns AB and CD are made of FGM. Finally, Figures 6.7(d) and 6.8(d) show the mode shapes when all three members of the portal frame are made of FGM. Although the basic nature of the mode shapes for the portal frame remains the same depending on the order of the natural frequency on a case to case basis, significant changes in the natural frequencies are found to occur when using FGM as evident from Figures 6.7 and 6.8. As expected the first mode of the portal frame in each case is a sway mode with the frame oscillating between left and right with virtually no elastic displacement of the central beam. The second mode shows elastic deformations of all three members with no nodal point or any point of inflection within any member. By contrast, the third mode reveals somehow a different picture in that a node with zero displacement appears towards the top end of each columns whereas a node for the beam appears near its centre. The mode shapes shown in Figures 6.7 and 6.8 are typical, as expected from the modal analysis of a portal frame and they are in accord with similar mode shapes reported by other investigators [35, 36].

6.5 Conclusions

The dynamic stiffness matrix of a functionally graded beam is developed by deriving explicit expressions for the individual stiffness elements in explicit algebraic form. This is achieved through the application of symbolic computation. The dynamic stiffness theory is applied by using the Wittrick-Williams algorithm as solution technique to compute the natural frequencies and mode shapes of some representative problems of uniform functionally gradient beams, for which the material properties are considered to vary continuously in the thickness direction according to a power law distribution. A stepped beam made of functionally graded material is also investigated for its free vibration characteristics. The results show good agreement with published results. Importantly, the theory has been applied to study the free vibration behaviour of a portal frame with its constituent members made of both isotropic and functionally graded material (FGM). The investigation has shown that significant changes in the free vibration behaviour are possible by using FGM. The literature on the free vibration of frameworks containing FGBs is virtually non-existent and this chapter addresses this problem and fills a gap in the literature by analysing a portal frame. The developed theory can be applied to analyse high-rise building structures made of FGM which has advantageous mechanical properties of metal and virtuous fire-resistant characteristics of ceramic and it is in this context, the investigation carried out is expected to be most useful.

Chapter 7

Free vibration of cracked beam

7.1 Introduction to free vibration of cracked beam

Investigation into the static, dynamic and buckling behaviour of cracked beams has aroused continuing interest amongst researchers. This is because the subject matter is of considerable practical importance in engineering design to ensure safety and integrity of load carrying structures that are vulnerable to cracks and other damages. The reduction in the strength and stiffness properties of a structure due to the presence of single or multiple cracks can be dangerous and may lead to catastrophic structural failures under both static and dynamic loads. This has inspired the current research to carry out a parametric investigation into the free vibration characteristics of a cracked beam using the dynamic stiffness method. As a fundamental prerequisite, first the dynamic stiffness matrix of a cracked beam is formulated through the application of the compliance properties of the crack. Basically, the cracked beam is idealised by connecting two Bernoulli-Euler beams at the crack location where a local flexibility matrix representing the crack is introduced. The dynamic stiffness matrix of the combined system is then developed. Once the dynamic stiffness matrix of the cracked beam is identified, the free vibration problem is then formulated. The formulation leads to a non-linear eigenvalue problem for which the Wittrick-Williams algorithm being ideally suited as solution technique, is applied to yield natural frequencies and mode shapes of the cracked beam for different boundary conditions. The first set of numerical results are obtained to validate the theory. This is achieved by comparing results from the current theory with those available in the published literature. Next a detailed parametric study is carried out by changing the crack location, crack depth and boundary conditions of the beam. The results are discussed and the chapter concludes with some significant remarks.

7.2 Literature review

The literature review on the dynamic behaviour of cracked beams suggests that there is a need to develop more accurate theories based on fracture mechanics and elastodynamics to underpin the effects of cracks on the dynamic behaviour of structures. A selective sample of the literature is surveyed next. Gudmundson [37], Ju and Mimovich [38] in their investigation showed how changes in natural frequencies and mode shapes can help to determine the location and scale of defects resulting from a damaged or cracked structure. In particular, Gudmundson [37, 39] used perturbation as well as transfer matrix method to study the influence of small cracks on the free vibration behaviour of slender structures. By contrast, Chondros et al [40] developed a continuous cracked beam theory for free vibration analysis. Their basic assumption was that the crack caused a continuous change in flexibility in its neighbourhood which they modelled by incorporating a consistent displacement field with singularity. Christides and Barr [41] on the other hand, used a modified Bernoulli-Euler theory to include the effect of a crack of simple geometric form by considering an exponential decay in the stress field due to the presence of the crack. A different, but related approach in which a crack in structural member such as a beam, is represented by a mass-less spring-like element located at the crack location, became popular due to much effort by Dimarogonas and Papadopoulos [42] and Papadopoulos and Dimarogonas [43–45] in the eighties, amongst others. Other notable contributors to this field who have used finite element, analytical and semi-analytical methods are Tharp [46], Miyazaki [47], Liang et al [48], Lee and Ng [49], Bamnios and Trochides [50], Kisa et al [51], Kisa and Brandon [52], Zheng and Kessissoglou [53], Loya et al [54], Viola et al [55] and Bouboulas and Anifantis [56].

The current investigation is based on the dynamic stiffness method in conjunction with a flexibility approach to model a cracked beam in order to investigate its free vibration characteristics. In essence, the cracked beam is modelled by a combination of two segments represented by Bernoulli-Euler theory (one on the left side of the crack and the other on the right side of the crack) connected together by a crack element of zero length whose compliance (flexibility) and subsequent stiffness properties are established using fracture mechanics theory. The flexibility properties are derived by making use of the fact that compliances are related to energy release rate and stress intensities [57–59]. At the crack location, the construction of a nodal stiffness matrix with the help of the compliance properties resulting from the crack is an essential part of the present theory. The frequency-dependent dynamic stiffness matrices of the adjoining Bernoulli-Euler beam elements are assembled together with the nodal stiffness matrix of the crack to form the global dynamic stiffness matrix of the (entire) cracked beam. The well-established algorithm of Wittrick and Williams [23] is finally applied to yield natural frequencies and mode shapes of the cracked beam. For illustrative purposes, a cantilever cracked beam for which some comparative results are available in the literature is analysed to confirm the validity and accuracy of the proposed theory.

7.3 Theoretical formulation

A cantilever cracked beam is shown in Figure 7.1 (Note that the theory developed can be applied to other boundary conditions, but the cantilever boundary condition shown here is only for convenience.) Figure 7.1 shows the coordinate system of a cracked beam ABCD with a crack shown through the depth (thickness) located between two closely spaced points B and C which are at a distance L_1 from the origin. The beam is assumed to be prismatic and of rectangular cross-section with width b, depth h, and length L, respectively. It is allowed to deflect in the XY plane undergoing axial displacement (δx), bending displacement (δy), and bending rotation (θ). (The theory developed can be applied to other cross-sections, but the rectangular cross-section is chosen for convenience.) The extensional (axial) and bending (flexural) rigidities of the intact (undamaged) beam are EA and EI, respectively, where A (= bh) is the area, I (= $bh^3/12$) is the second moment of area of the beam cross-section with E, the Young's modulus of beam material. The mass per unit length of the beam is $m = \rho A$ where ρ is the density of material.

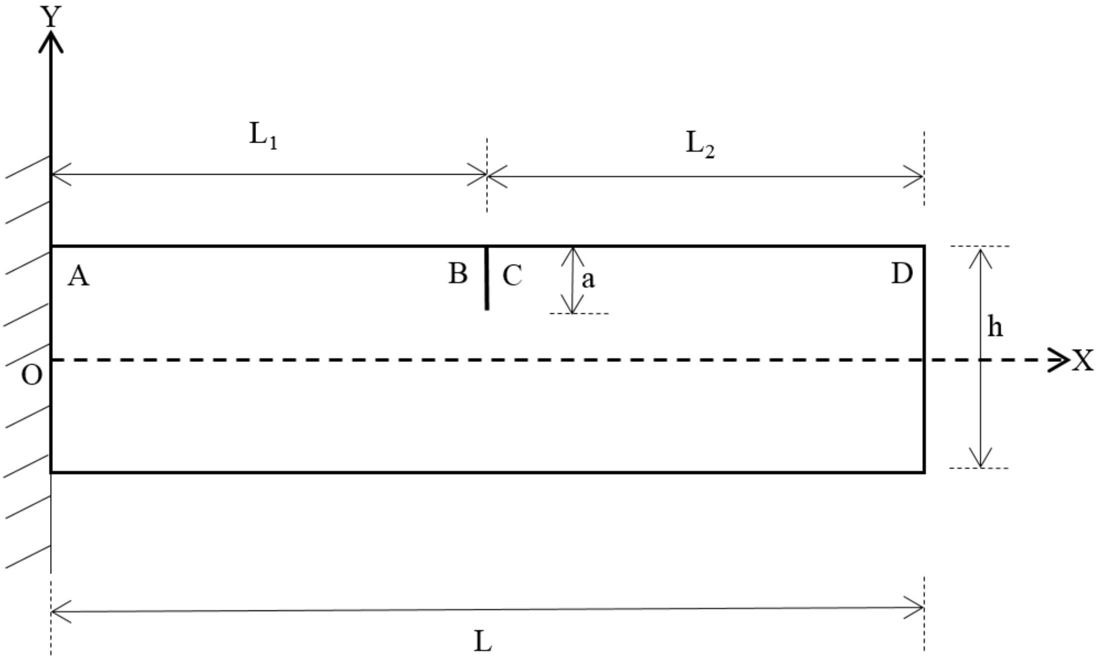

Figure 7.1: Notation and coordinate system of a cracked cantilevered beam.

The cracked beam shown in Figure 7.1 is idealised into three structural elements denoted by letters (a), (b) and (c) having lengths L_1, L_2 and L_3, respectively, as shown in Figure

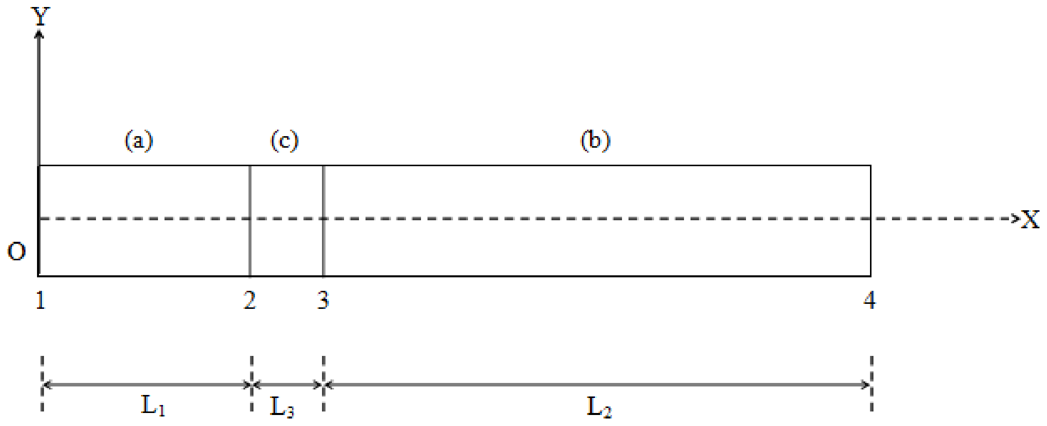

Figure 7.2: Node numbering and member (element) lettering of a cracked beam.

7.2. Thus, the cracked beam is represented by two Bernoulli-Euler beam elements (a) and (b), connected together by a crack element (c). In addition to the element (member) lettering, the figure also shows the node numbering of the entire cracked beam. As shown in the Figure 7.2, nodes 1 and 2 are connected by a beam element (a), nodes 2 and 3 are connected by a crack element (c) whereas nodes 3 and 4 are connected by a beam element (b). For clarity and subsequent development of the theory, the (fictitious) length of the crack element is assumed to be L_3 instead of zero. This fictitious length is irrelevant and have no consequence on the theory. This is because the crack is located at a point on the axis of the beam and the flexibility matrix introduced at that point is not considered to be an explicit function of length. The associated stiffness matrix of the element (c) will be computed from the compliance matrix at the crack, which will eventually turn out to be a nodal stiffness matrix rather than a conventional element stiffness matrix connecting two nodes and separated by a distance. The crack element's compliance (flexibility) and subsequent stiffness properties are established using fracture mechanics theory. At the crack location, the construction of a nodal stiffness matrix with the help of the compliance properties resulting from the crack is an essential part of the present theory. An in house program is developed by using dynamic stiffness matrix for the crack element and then by using the Wittrick-Williams Algorithm, it became possible to ascertain how many natural frequencies of a structure lie below an arbitrarily chosen trial frequency. This simple feature of the algorithm is exploited to advantage to converge upon any required natural frequency to any desired accuracy.

The dynamic stiffness matrix of a freely vibrating beam element (e) connecting nodes i and j, see Figure 7.3, relates the amplitudes of forces $\mathbf{p}_\mathrm{i}$ and $\mathbf{p}_\mathrm{j}$ to those of the displacements δ_i and δ_j at the ends i and j of the element. In the usual matrix notation and referring

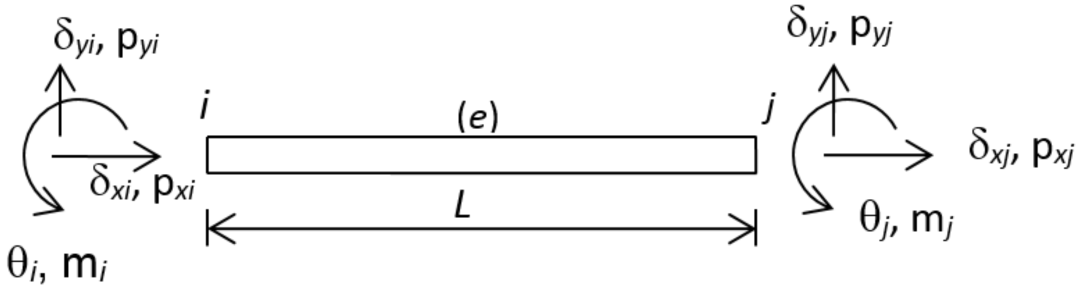

Figure 7.3: Forces and displacements at the ends of a beam element e connecting nodes *i* and *j*.

to Figure 7.3, the relationship can be expressed as

$$\begin{bmatrix} p_i \\ p_j \end{bmatrix} = \begin{bmatrix} k^e_{11} & k^e_{12} \\ k^e_{21} & k^e_{22} \end{bmatrix} \begin{bmatrix} \delta_i \\ \delta_j \end{bmatrix} \tag{7.1}$$

where

$$p_i = \left\{p_{xi}, p_{yi}, m_i\right\}^T p_j = \left\{p_{xj}, p_{yj}, m_j\right\}^T \tag{7.2}$$

$$\delta_i = \left\{\delta_{xi}, \delta_{yi}, \theta_i\right\}^T \delta_j = \left\{\delta_{xj}, \delta_{yj}, \theta_j\right\}^T$$

p$_{xi}$ and p$_{xj}$ are axial force, p$_{yi}$ and p$_{yj}$ are shear forces and m$_i$ and m$_j$ are bending moments, T denotes a transpose.

The dynamic stiffness elements of the sub-matrices $\mathbf{k}^e{}_{11}$ and $\mathbf{k}^e{}_{12}$ of Equation 7.1 are frequency dependent and are given by [60]

$$k^e_{11} = \begin{bmatrix} a_1 & 0 & 0 \\ 0 & b_1 & d_1 \\ 0 & d_1 & c_1 \end{bmatrix} \; and \;\; k^e_{12} = \begin{bmatrix} e_1 & 0 & 0 \\ 0 & f_1 & h_1 \\ 0 & -h_1 & g_1 \end{bmatrix} \tag{7.3}$$

where the elements a_1 to h_1 are in terms of the beam parameters as follows

$$a_1 = (EA/L)\nu \cot \nu; \qquad b_1 = (EI\lambda^3/L^3)(\sin\lambda\cosh\lambda + \cos\lambda\sinh\lambda)/Z \tag{7.4}$$

$$c_1 = (EI\lambda/L)(\sin\lambda\cosh\lambda - \cos\lambda\sinh\lambda)/Z; \qquad d_1 = (EI\lambda^2/L^2)\sin\lambda\sinh\lambda/Z \tag{7.5}$$

$$e_1 = -(EA/L)\nu \cos ec\nu; \qquad f_1 = -(EA\lambda^3/L^3)(\sin\lambda + \sinh\lambda)/Z \tag{7.6}$$

$$g_1 = (EI\lambda/L)(\sinh\lambda - \sin\lambda)/Z; \qquad h_1 = (EI\lambda^2/L^2)(\cosh\lambda - \cos\lambda)/Z \tag{7.7}$$

with

$$\nu = \omega L(m/EA)^{1/2}; \qquad \lambda = (m\omega^2L^4/EI)^{1/4}; \qquad Z = 1 - \cos\lambda\cosh\lambda \tag{7.8}$$

where ω is the circular (or angular) frequency, and L, m, EA and EI are the element (member) length, mass per unit length, extensional (axial) rigidity and flexural rigidity, respectively.

$\mathbf{k}^e{}_{22}$ in Equation 7.1 can be obtained from $\mathbf{k}^e{}_{11}$ by writing $-d_1$ for d_1 in Equation 7.3 and $\mathbf{k}^e{}_{21}$ is the transpose of $\mathbf{k}^e{}_{12}$.

For a given trial frequency, it is thus possible to compute the dynamic stiffness elements of members (a) and (b) in Figure 7.2 by substituting the appropriate lengths L_1 and L_2 in Equations 7.1-7.8, respectively.

The stiffness matrix for the crack element (c) in Figure 7.2 can be obtained from the 3×3 flexibility matrix **C** given as

$$C = \begin{bmatrix} C_{11} & 0 & 0 \\ 0 & C_{22} & 0 \\ 0 & 0 & C_{33} \end{bmatrix} \tag{7.9}$$

There are literally dozens of papers which deal with the derivation of the flexibility matrix by integrating the stress intensity factor. In particular, Zheng and Kessissoglou [53] have given explicit expressions for the elements C_{11}, C_{22} and C_{33} for both rectangular and circular cross-section beams in terms of the cross-sectional dimensions (width b and depth h for a rectangle, and radius r for a circle) and the crack length a through the depth. For plane strain problems and for a rectangular cross-section shown in Figure 7.4, these expressions for crack-length over depth ratios within the range 0≤ a/h ≥ 0.5 are taken from [53] and written as follows

$$c_{11} = \frac{1-\mu^2}{Eb}F(1,1)\, c_{22} = \frac{1-\mu^2}{Eb}F(2,2)\, c_{33} = \frac{1-\mu^2}{Eb}F(3,3) \tag{7.10}$$

where μ is the Poisson's ratio, E is the Young's modulus and *F(1,1)*, *F(2,2)* and *F(3,3)* are non-dimensional functions given by [53]

$$F(1,1) = e^{\frac{1}{(1-\xi)}} \left(\begin{array}{c} -0.326584 \times 10^{-5}\xi + 1.455190\xi^2 - 0.984690\xi^3 + 4.895396\xi^4 \\ -6.501832\xi^5 + 12.792091\xi^6 - 26.723556\xi^7 + 35.073593\xi^8 \\ -34.954632\xi^9 + 9.054062\xi^{10} \end{array} \right) \tag{7.11}$$

$$F(2,2) = e^{\frac{1}{(1-\xi)}} \left(\begin{array}{c} -0.326018 \times 10^{-6}\xi + 1.454954\xi^2 - 1.455784\xi^3 - 0.421981\xi^4 \\ -0.279522\xi^5 + 0.455399\xi^6 - 2.432830\xi^7 + 5.427219\xi^8 \\ -6.643057\xi^9 + 4.466758\xi^{10} \end{array} \right) \tag{7.12}$$

$$F(3,3) = e^{\frac{1}{(1-\xi)}} \left(\begin{array}{c} -0.219628 \times 10^{-4}\xi + 52.37903\xi^2 - 130.2483\xi^3 + 308.442769\xi^4 \\ -602.445544\xi^5 + 939.044538\xi^6 - 1310.95029\xi^7 + 1406.52368\xi^8 \\ -1067.4998\xi^9 + 391.536356\xi^{10} \end{array} \right) \tag{7.13}$$

where

$$\xi = a/h \tag{7.14}$$

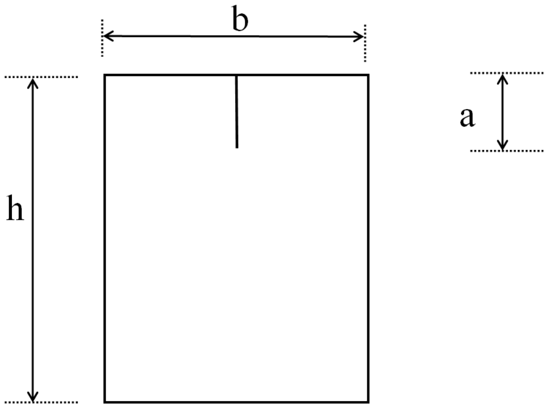

Figure 7.4: Cross-sectional dimensions and crack length of a cracked beam.

is the non-dimensional crack length.

Once the flexibility matrix **C** of the crack element given by Equation 7.9 is known, a nodal 6×6 stiffness matrix $\mathbf{k}^c$ at the crack location can be constructed by using the inverse of **C** as follows

$$k^c = \begin{bmatrix} C^{-1} & -C^{-1} \\ -C^{-1} & C^{-1} \end{bmatrix} \tag{7.15}$$

Using the above stiffness matrix, the force-displacement relationship at the left hand and right-hand ends of the crack element can now be related as

$$\begin{bmatrix} p_L \\ p_R \end{bmatrix} = \begin{bmatrix} k_{11}^c & k_{12}^c \\ k_{21}^c & k_{22}^c \end{bmatrix} \begin{bmatrix} \delta_L \\ \delta_R \end{bmatrix} \tag{7.16}$$

where

$$p_L = \{p_{xL}, p_{yL}, m_L\}^T; \quad p_R = \{p_{xR}, p_{yR}, m_R\}^T; \quad \delta_L = \{\delta_{xL}, \delta_{yL}, \theta_L\}^T; \quad \delta_R = \{\delta_{xR}, \delta_{yR}, \theta_R\}^T \tag{7.17}$$

and

$$\mathbf{k}_{11}^c = \mathbf{k}_{22}^c = -\mathbf{k}_{12}^c = -\mathbf{k}_{21}^c = \mathbf{C}^{-1} \tag{7.18}$$

Note that the stiffness matrix $\mathbf{k}^c$ corresponds to a crack element of zero length. Thus the length L_3 appearing in Figure 7.2 for the crack element is irrelevant and hence can be disregarded.

Referring to Figure 7.2 and using Equations 7.1-7.13, the frequency dependent dynamic stiffness matrix $\mathbf{K}(\omega)$ of the cracked beam can now be formed in the usual way by assembling the element stiffness matrices of two Bernoulli-Euler beams (a) and (b) (connecting nodes 1 and 2, and 3 and 4, respectively) and one crack element (c), connecting nodes 2 and 3). In matrix notation, the assembled stiffness matrix $\mathbf{K}(\omega)$ that will lead to an eigenvalue problem can be expressed symbolically as follows.

$$K(\omega) = \begin{bmatrix} k_{11}^a & k_{12}^a & 0 & 0 \\ k_{21}^a & k_{22}^a + k_{11}^c & k_{12}^c & 0 \\ 0 & k_{21}^c & k_{22}^c + k_{11}^b & k_{12}^b \\ 0 & 0 & k_{21}^b & k_{22}^b \end{bmatrix} \tag{7.19}$$

Appropriate boundary conditions at nodes 1 and 4 in Figure 7.2, can be applied by deleting the particular rows and columns of $\mathbf{K}(\omega)$, corresponding to zero displacements in order to compute the natural frequencies and mode shapes of individual cases such as cantilever, simply-supported and clamped-clamped cracked beams. (Note that for a free-free cracked beam, the whole $\mathbf{K}(\omega)$ matrix must be used for the eigenvalue problem.) The dynamic stiffness matrix of Equation 7.19 can now be used to compute the natural frequencies and mode shapes of cracked beams with various end conditions. A non-uniform cracked beam can also be analysed for its free vibration characteristics by idealising it as an assemblage of many uniform cracked beams. An accurate and reliable method of calculating the natural frequencies and mode shapes of a structure using the dynamic stiffness method is to apply the well-known algorithm of Wittrick and Williams [23] which has been featured in numerous papers.

7.4 Results and discussion

The theory developed above is applied to a cantilever cracked beam of rectangular cross-section (Figure 7.1) for which some comparative results are available in the literature [51] which is used to verify the results obtained in this chapter. The data used for the analysis are taken from Ref. [51] and are as follows: L = 0.2 m, b = 0.025 m, h = 0.0078 m, E = 216 GPa, μ = 0.28 and ρ = 7850 kgm^{-3} so that $EA = 4.2120\times10^7$ N, EI = 213.548 Nm^2, m = ρbh = 1.5308 kgm^{-1}. (Note that the notations used in Ref. [51] for width and depth of the beam cross-section are, d and b which are b and h in this chapter.) Also two principal non-dimensional parameters are defined when presenting the numerical results. These are non-dimensional crack length, ξ =a/h and non-dimensional crack location, $\zeta = L_1$/L. Representative results are computed by examining the effects of the crack location, crack depth and boundary condition and are given below in Tables 7.1-7.4. Table 7.1 shows the results obtained for various boundary conditions C-F, S-S, C-S and C-C for the first three natural frequencies when the non-dimensional crack location ζ is fixed at 0.2 and the non-dimensional crack length ξ is varied as 0.2, 0.4, 0.6 and 0.8. It can be seen that as the non-dimensional crack length increases, natural frequencies decreases gradually for all boundary conditions. At lower non-dimensional crack length of ξ = 0.2, higher value of natural frequencies occurs. Clamped-Clamped boundary condition gives higher value of natural frequencies than other boundary conditions and then Clamped- Simple support gives higher value than Simple-simple and Cantilever cases and Simple-Simple support gives higher value than Cantilever for all non-dimensional crack lengths as can be seen from Table 7.1. Similar results are observed for all other Tables 7.2, 7.3 and 7.4 and it can be seen as crack location ζ increases the value of natural frequencies increases gradually too with highest value occurs at crack location $\zeta = 0.8$.

Table 7.1: Natural frequencies with various boundary conditions at crack location, $\zeta = 0.2$.

Boundary condition	Crack location ($\zeta = L_1$/L = 0.2)											
	Non-dimensional crack length (ξ)											
	0.2			0.4			0.6			0.8		
	ω_1 (rad/s)	ω_2 (rad/s)	ω_3 (rad/s)	ω_1 (rad/s)	ω_2 (rad/s)	ω_3 (rad/s)	ω_1 (rad/s)	ω_2 (rad/s)	ω_3 (rad/s)	ω_1 (rad/s)	ω_2 (rad/s)	ω_3 (rad/s)
C-F	1022.5	6503.1	18129	972.8	6492.3	17848	854.1	6462.1	17200	639.5	6375.2	16099
S-S	2899.5	11506	25898	2848.8	11029	24974	2702.6	9937.9	23379	2316.5	8277.9	21706
C-S	4544.8	14710	30457	4520.0	14572	29496	4462.9	14235	27638	4360.1	13569	25506
C-C	6602.4	18121	35286	6589.3	17837	34097	6554.5	17181	31957	6464.6	16065	29749

Table 7.2: Natural frequencies with various boundary conditions at crack location, $\zeta = 0.4$.

Boundary condition	Crack location ($\zeta = L_1$/L = 0.4)											
	Non-dimensional crack length (ξ)											
	0.2			0.4			0.6			0.8		
	ω_1 (rad/s)	ω_2 (rad/s)	ω_3 (rad/s)	ω_1 (rad/s)	ω_2 (rad/s)	ω_3 (rad/s)	ω_1 (rad/s)	ω_2 (rad/s)	ω_3 (rad/s)	ω_1 (rad/s)	ω_2 (rad/s)	ω_3 (rad/s)
C-F	1031.8	6441.3	18098	1010.1	6237.0	17740	949.8	5798.5	17015	802.4	5016.2	16034
S-S	2876.4	11597	26085	2754.2	11412	25643	2451.2	11007	24679	1869.5	10392	23157
C-S	4531.6	14603	30740	4463.8	14151	30597	4298.6	13236	30190	3999.4	12040	28950
C-C	6555.0	18086	35559	6393.6	17714	35118	6023.5	16957	34114	5429.5	15932	32156

Table 7.3: Natural frequencies with various boundary conditions at crack location, ζ = 0.6.

Boundary condition	Crack location (ζ = L_1/L = 0.6)											
	Non-dimensional crack length (ξ)											
	0.2			0.4			0.6			0.8		
	ω_1 (rad/s)	ω_2 (rad/s)	ω_3 (rad/s)	ω_1 (rad/s)	ω_2 (rad/s)	ω_3 (rad/s)	ω_1 (rad/s)	ω_2 (rad/s)	ω_3 (rad/s)	ω_1 (rad/s)	ω_2 (rad/s)	ω_3 (rad/s)
C-F	1036.6	6419.0	18070	1030.9	6139.9	17633	1013.7	5468.2	16761	959.1	4284.7	15617
S-S	2876.4	11597	26085	2754.2	11412	25643	2451.2	11007	24679	1869.5	10392	23157
C-S	4495.7	14726	30486	4316.7	14638	29604	3902.1	14430	27845	3212.0	14018	25593
C-C	6555.0	18086	35559	6393.6	17714	35118	6023.5	16957	34114	5429.5	15932	32156

Table 7.4: Natural frequencies with various boundary conditions at crack location, ζ = 0.8.

Boundary condition	Crack location (ζ = L_1/L = 0.8)											
	Non-dimensional crack length (ξ)											
	0.2			0.4			0.6			0.8		
	ω_1 (rad/s)	ω_2 (rad/s)	ω_3 (rad/s)	ω_1 (rad/s)	ω_2 (rad/s)	ω_3 (rad/s)	ω_1 (rad/s)	ω_2 (rad/s)	ω_3 (rad/s)	ω_1 (rad/s)	ω_2 (rad/s)	ω_3 (rad/s)
C-F	1038.1	6488.4	18021	1037.6	6425.6	17362	1036.2	6229.6	15648	1031.2	5601.5	12641
S-S	2899.5	11506	25898	2848.8	11029	24974	2702.6	9937.9	23379	2316.5	8277.9	21706
C-S	4521.6	14548	30440	4416.7	13918	29506	4126.9	12583	27955	3452.8	10805	26293
C-C	6602.4	18121	35286	6589.3	17837	34097	6554.5	17181	31957	6464.6	16065	29749

Table 7.5: Natural frequencies with various boundary conditions for intact beam.

Intact beam	ω_1 (rad/s)	ω_2 (rad/s)	ω_3 (rad/s)
C-F	1038.214	6506.374	18218.04
	1037.0 [64]	6458.3 [64]	17961 [64]
S-S	2914.31	11657.24	26228.79
C-S	4553.631	14755.43	30781.34
C-C	6606.3	18209.89	35703.06

Table 7.5 shows the value of first three natural frequencies for various boundary conditions of an intact (no cracks) beam. The result of the cantilever case is compared with Ref [51] where it can be observed that the results obtained using the current theory are very close to the published results (The maximum discrepancy is around 1.8%). It should be noted that the results obtained by using the dynamic stiffness method is exact and the small difference that exists with the reference [51] may be attributed to the fact that the present theory is based on an exact dynamic stiffness method whereas the theory used in Ref [51] is an approximate one (i.e. FEM).

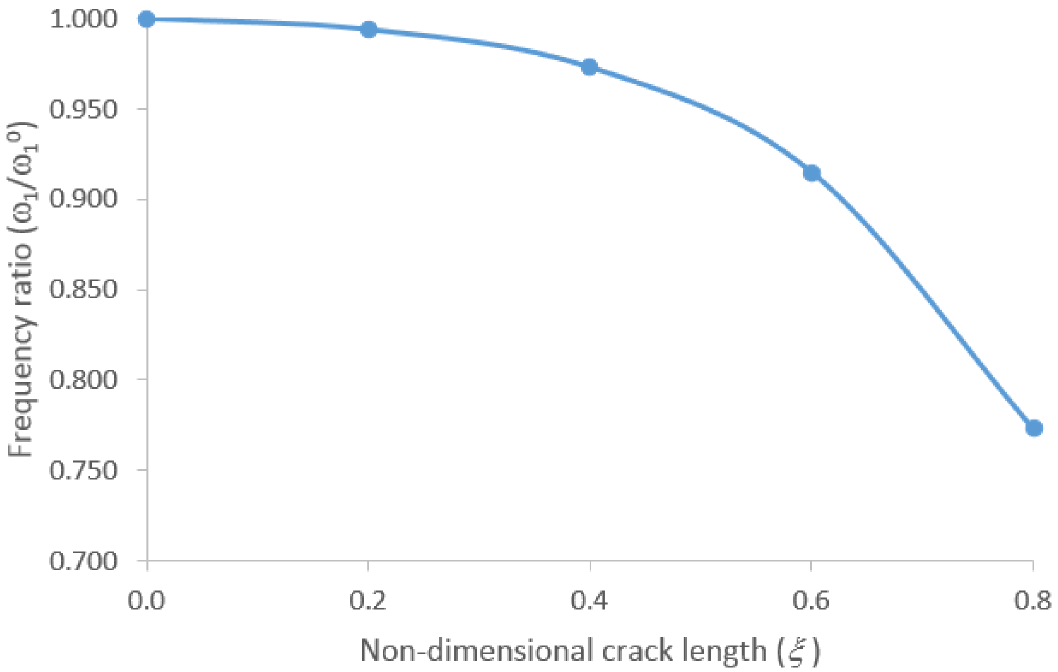

Figure 7.5: The natural frequency ratio between the cracked beam and the intact beam for the fundamental mode of a cantilever cracked beam having non-dimensional crack length $\xi = 0.4$.

Figure 7.5 shows the natural frequency ratio between the crack beam and the intact beam for the fundamental natural frequency ω_1 relative to that of the intact beam ω_1^0 of a cantilever cracked beam when the non-dimensional crack length is $\xi = 0.4$. It can be seen that the fundamental frequency drops as non-dimensional crack length increases, which is observed in Table 7.2 too. So it can be said that the effect of non-dimensional crack length is significant on the fundamental natural frequency of the cantilever cracked beam. Similar observations were made for higher natural frequencies and for other boundary conditions which was not shown in the form of figures for brevity but can be observed from Tables 7.1-7.4. These observations were also reported by a number of earlier investigators [51, 52, 61].

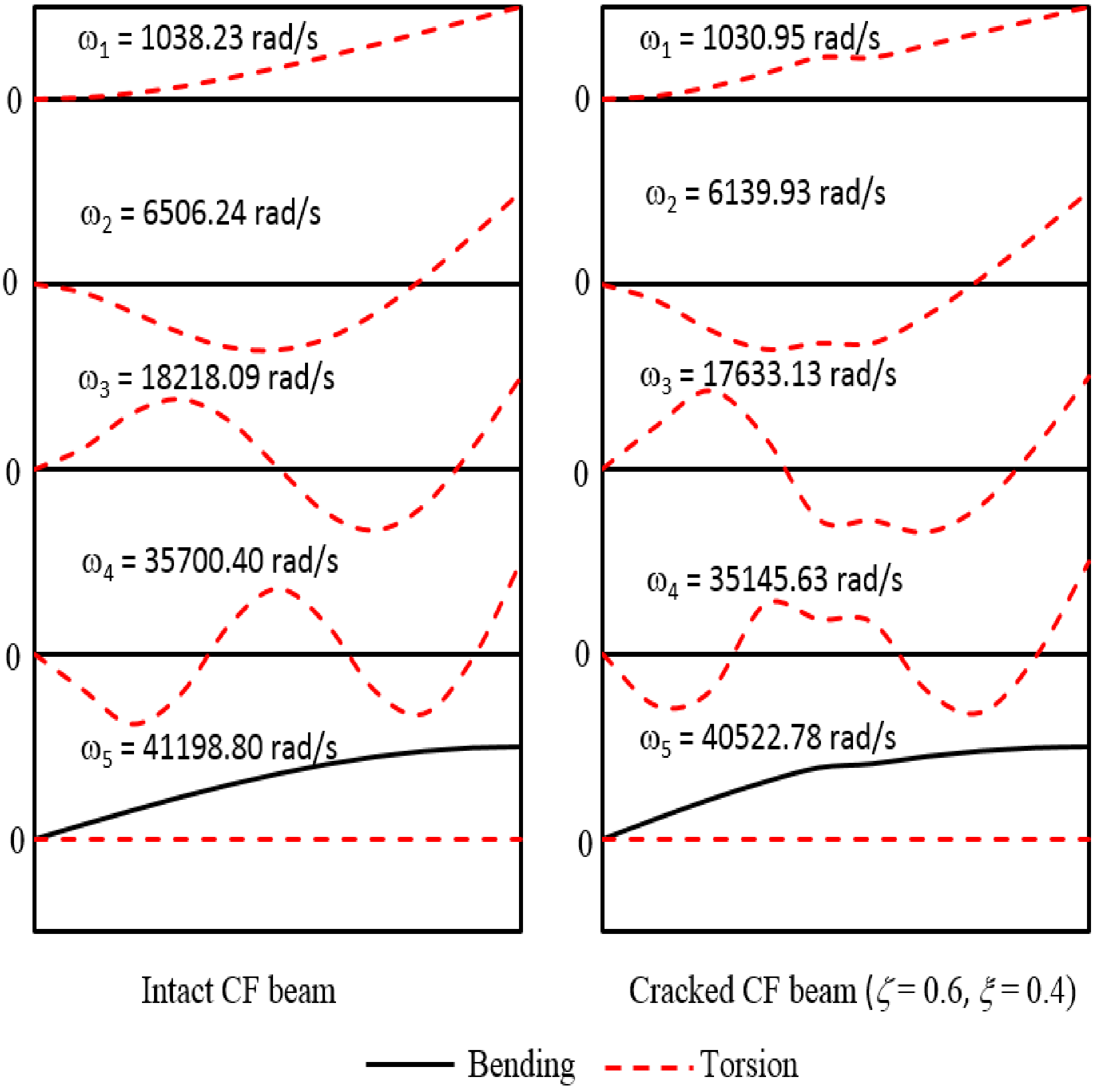

Figure 7.6: Mode shapes of intact and cracked C-F beam.

The final set of results was obtained to illustrate the mode shapes of the cracked beam. The first five natural frequencies and mode shapes of the cantilever are shown in Figure

7.6 when the crack is located at $\zeta = 0.6$ and the non-dimensional crack length is $\xi = 0.4$. The bending displacements for the cracked beam and the intact beam are shown such that bending is represented by black solid lines and torsion mode is shown as red dashed lines.

7.5 Conclusions

Using the dynamic stiffness method and Bernoulli-Euler beam theory, the free vibration behaviour of a cracked beam is investigated. In the development of the theory, the cracked beam is idealised by two intact beams joined together and by introducing a flexibility matrix of the crack at the joint. The formulation leads to a non-linear eigenvalue problem and was solved by applying the Wittrick-Williams algorithm. A parametric study by varying the crack location, crack depth and boundary conditions is carried out and the results showing the natural frequencies and mode shapes are illustrated. The investigation has shown that the crack location, crack depth and boundary conditions have significant effects on the natural frequencies and modes shapes of a cracked beam. The natural frequencies of intact beam for cantilever boundary condition are readily available in the existing literature and in this research natural frequencies of intact beam for simply supported, clamped-pinned and clamped-clamped boundary conditions have been obtained for cracked beams and contrasted against the results of intact beams. The theory developed can be extended to frame works and other building structures and within the context of structural health monitoring purposes, the developed theory is expected to be most useful.

Chapter 8

Combined Rayleigh-Love and Timoshenko theories

8.1 Introduction for a beam incorporating Rayleigh-Love and Timoshenko theories

In this chapter, an exact dynamic stiffness matrix for a beam is developed by integrating the Rayleigh-Love theory for longitudinal vibration into the Timoshenko theory for bending vibration. It should be noted that no one appears to have made any attempt to combine Rayleigh-Love bar and Timoshenko beam theories particularly when investigating the free vibration characteristics of frameworks. This will be important within the high frequency range when using the SEA technique. In the formulation, the Rayleigh-Love theory accounted for the transverse inertia in longitudinal vibration whereas the Timoshenko beam theory accounted for the effects of shear deformation and rotating inertia in bending vibration.

The dynamic stiffness matrix is developed by solving the governing differential equations of motion in free vibration of a Rayleigh-Love bar and a Timoshenko beam and then imposing the boundary conditions for displacements and forces. Next the two dynamic stiffness theories are combined using a unified notation. The ensuing dynamic stiffness matrix is subsequently used for free vibration analysis of uniform and stepped bars as well as frameworks through the application of the Wittrick-Williams algorithm as solution technique. Illustrative examples are given to demonstrate the usefulness of the theory and some of the computed results are compared with published ones and this chapter closes with some concluding remarks.

8.2 Literature review

Free vibration analysis in the high frequency range is of great importance to assess the flow of vibrational energy in structures, particularly when the widely accepted Statistical Energy Analysis (SEA) method [62, 63] is used. Research in this area is further motivated by the fact that the modal density required for the energy flow analysis in structures is generally very high in the high frequency range. To this end there are several research papers in the published literature on the energy flow analysis in classical structures such as bars [64], beams [65], membranes [66] and plates [67] which emphasize the need for high frequency vibration analysis. For accurate and efficient high frequency vibration analysis, these publications highlight the inadequacy of the traditional finite element method (FEM) which is somehow limited to low and perhaps medium frequency range unless high-precision, good quality finite elements are used which may become computationally very expensive.

The dynamic stiffness matrix of the element used to investigate the free vibration behaviour of plane frames [68, 69] was obtained by separate consideration of axial and bending deformation and then combining the two together in matrix form. In these earlier works, when the axial stiffnesses were incorporated into the bending stiffnesses to construct the dynamic stiffness matrix of an individual element, only classical theory for longitudinal free vibration of bars which ignores the transverse inertia effect was used. This is generally justified, particularly in the low and probably in the medium frequency range, but for high frequency vibration, the so-called Rayleigh-Love theory [70, 71] which accounts for the effects of transverse inertia during longitudinal vibration and the Timoshenko theory [69] which accounts for the effects of shear deformation and rotatory inertia during bending vibration need to be considered. This is particularly important when applying the widely accepted SEA technique for which the high frequency vibration problem must be modelled properly [62, 63]. In this respect, the traditional FEM may become inaccurate.

From a historical perspective, it was Lord Rayleigh [72] who first recognised the importance of transverse inertia on the longitudinal free vibration of bars, particularly at high frequencies. Many years later, Love [73] shed further lights on Lord Rayleigh's work which eventually took the name Rayleigh-Love theory and the research took significant turn to wave propagation and vibrational energy analysis [65, 74, 75] of bars in longitudinal motion. No one appears to have made any attempt to combine the Rayleigh-Love bar analysis with flexure, particularly when investigating the free vibration characteristics of frameworks. This will be important within the high frequency range when using the SEA technique. The purpose of this chapter is to fill this gap in the literature. First, the dynamic stiffness matrix of a Rayleigh-Love bar is developed from the fundamental equation of motion in longitudinal free vibration. Then the developed dynamic stiffness matrix of the Rayleigh-Love bar is integrated with the dynamic stiffness matrix of a Timoshenko beam [76–78] which accounts for the effects of shear deformation and rotatory inertia to allow for the free vibration analysis of individual members and plane frames in the low, medium and high frequency range through the application of the Wittrick-Williams algorithm [23] as solution technique. Using the developed theory, a wide range of problems is solved and some of the computed results are compared with published literature.

It should be noted that there are no specific hard boundaries between the regimes of low, medium and high frequencies, but a useful descriptor which gives an indicative guidance to frequency range is the vibrational wavelength when compared to the overall length of the structure. Thus an engineering judgement can be reasonably made based on the product of the wave number and a typical length of the structure, which is essentially the Helmholtz number. Large values of this number represent the high frequency range whereas lower values determine the low to medium frequency range. For the type of problems investigated in this chapter, the low to medium range of frequencies is characterised to be below 1500 Hz whereas frequencies above this value constitute the high frequency range.

8.3 Development of dynamic stiffness formulation

The dynamic stiffness matrix of a structural element essentially relates the amplitudes of the forces to those of the corresponding displacements at the nodes of the harmonically vibrating structural element. The axial deformation of a Rayleigh-Love bar and the bending deformations of a Timoshenko beam are considered uncoupled and treated independently so that the derivation of the dynamic stiffness matrix for each of them can be carried out separately, and later integrated.

8.3.1 Dynamic stiffness matrix of a Rayleigh-Love bar

A uniform Rayleigh-Love bar of length L is shown in Figure 8.1 in a rectangular right handed Cartesian co-ordinate system with the X-axis coinciding with the axis of the bar. Note that Figure 8.1 can also be used to represent a beam which is also a two-noded line element like a bar element. The essential difference between a bar and a beam element is that the former can sustain only axial load whereas the latter can take bending and shear load, as well as the axial load. In other words, in any local coordinate system such as the one shown in Figure 8.1, a bar element can undergo only axial deformation whereas a beam element can undergo bending displacement, bending rotation as well as axial deformation. Now the governing differential equation of motion of the Rayleigh-Love bar in free axial (or longitudinal) vibration can be derived by using Hamilton's principle as the first step towards the dynamic stiffness formulation. The focus area of the derivation in this section is, of course, on the axial stiffnesses only.

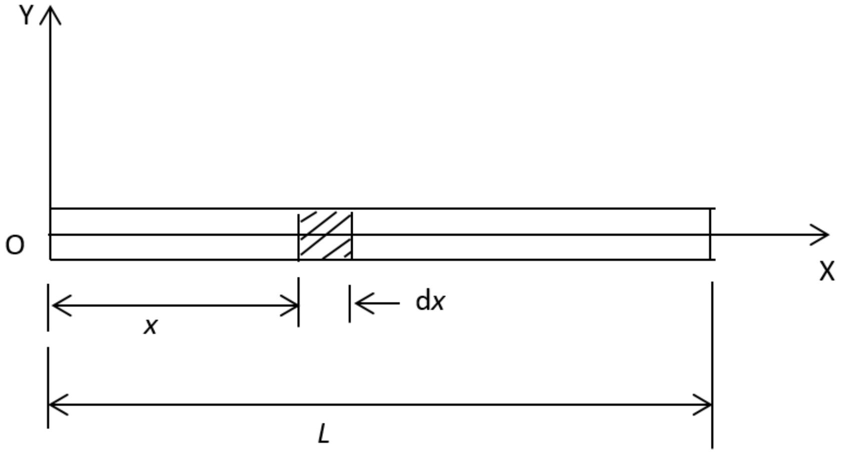

Figure 8.1: Coordinate system and notation for a Rayleigh-Love bar and a Timoshenko beam.

Referring to Figure 8.1 and noting that if u is the axial displacement at a distance x from the origin, the kinetic and potential energies of the bar T_{bar} and V_{bar} are respectively given by [71, 79]

$$T_{\mathrm{bar}} = \frac{1}{2}\int_0^L \left[\rho A\left(\frac{\partial u}{\partial t}\right)^2 + \rho I_P \nu^2\left(\frac{\partial^2 u}{\partial x \partial t}\right)^2\right] dx \tag{8.1}$$

and

$$V_{\mathrm{bar}} = \frac{1}{2}\int_0^L EA\left(\frac{\partial u}{\partial x}\right)^2 dx \tag{8.2}$$

where ρ is the density of the bar material, A is the cross-sectional area of the bar so that ρA represents the mass per unit length, I_P is the polar second moment of area so that ρI_P represents the polar mass moment of inertia per unit length, E is the Young's modulus of the bar material so that EA represents the axial or extensional rigidity of the bar and ν is the Poisson's ratio of the bar material.

Hamilton's principle states

$$\delta \int_{t_1}^{t_2} (T_{\mathrm{bar}} - V_{\mathrm{bar}}) dt = 0 \tag{8.3}$$

where t_1 and t_2 are the time interval in the dynamic trajectory, and δ is the usual variational operator.

The governing differential equations of motion of the Rayleigh-Love bar and the associated boundary condition in free vibration can now be derived by substituting the kinetic (T_{bar}) and potential (V_{bar}) energy expressions of Equations 8.1 and 8.2 into Equation 8.3, using the δ operator, integrating by parts and then collecting terms. In an earlier publication, the entire procedure to generate the governing differential equations of motion and natural boundary conditions for bar or beam type structures was automated by Banerjee et al [22] by applying symbolic computation. In this way, the governing differential equation of motion of the Rayleigh-Love bar is obtained as [71, 79]

$$EA\frac{\partial^2 u}{\partial x^2} - \rho A\frac{\partial^2 u}{\partial t^2} + \rho I_P \nu^2 \frac{\partial^4 u}{\partial x^2 \partial t^2} = 0 \tag{8.4}$$

As a by-product of the Hamiltonian formulation, the expression for the axial force $f(x, t)$ follows from the natural boundary condition to give [71, 79]

$$f(x,t) = -EA\frac{\partial u}{\partial x} - \rho I_P \nu^2 \frac{\partial^3 u}{\partial x \partial t^2} \tag{8.5}$$

If harmonic oscillation is assumed, then

$$u(x,t) = U(x)e^{i\omega t} \tag{8.6}$$

where ω is the angular or circular frequency, and $U(x)$ are the amplitudes of u.
Substituting Equation 8.6 into Equation 8.5 gives

$$(EA - \rho I_P \nu^2 \omega^2)\frac{d^2 U}{dx^2} + \rho A \omega^2 U = 0 \tag{8.7}$$

As a result of the harmonic oscillation assumption, the amplitude $F(x)$ of the force $f(x, t)$ in Equation 8.5 becomes

$$F(x) = -(EA - \rho I_P \nu^2 \omega^2)\frac{dU}{dx} \tag{8.8}$$

Introducing the differential operator $D = d/d\xi$ and the non-dimensional length ξ as

$$\xi = \frac{x}{L} \tag{8.9}$$

Equation 8.7 becomes

$$(D^2 + \gamma^2)U = 0 \tag{8.10}$$

where

$$\gamma^2 = \frac{\alpha^2}{1-\beta^2} \tag{8.11}$$

with

$$\alpha^2 = \frac{\rho A \omega^2 L^2}{EA}; \qquad \beta^2 = \frac{\rho I_P \nu^2 \omega^2}{EA} \tag{8.12}$$

The expression for the amplitude of the axial force in Equation 8.8 using Equations 8.9 and 8.12 becomes

$$F(\xi) = -\frac{EA}{L}(1-\beta^2)\frac{dU}{d\xi} \tag{8.13}$$

The solution of the differential equation, Equation 8.10 is given by

$$U(\xi) = C_1 \sin\gamma\xi + C_2 \cos\gamma\xi \tag{8.14}$$

where C_1 and C_2 are constants.
The expression for axial force $F(\xi)$ can now be expressed by substituting Equation 8.14 into Equation 8.13 to give

$$F(x) = F(\xi) = -\frac{EA}{L}(1-\beta^2)\gamma(C_1\cos\gamma\xi - C_2\sin\gamma\xi) \tag{8.15}$$

Now referring to Figure 8.2, the boundary conditions for displacements and forces can be applied as follows.

$$At\ \ x = 0\ \ (i.e.\ \ \xi = 0),\ \ U = \Delta_{x1}\ \ and\ \ F = F_{x1} \tag{8.16}$$

$$At\ \ x = L\ \ (i.e.\ \ \xi = 1),\ \ U = \Delta_{x2}\ \ and\ \ F = -F_{x2} \tag{8.17}$$

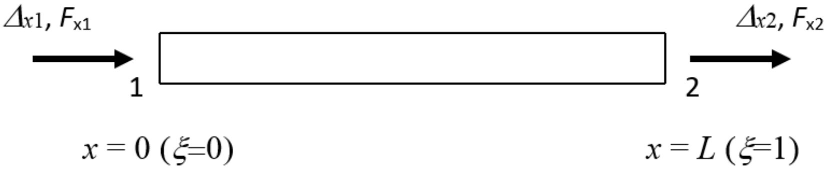

Figure 8.2: Boundary conditions for displacements and forces in axial vibration for a Rayleigh-Love bar.

Substituting Equations 8.16 and 8.17 into Equations 8.14 and 8.15, the following matrix relationships can be obtained

$$\begin{bmatrix} \Delta_{x1} \\ \Delta_{x2} \end{bmatrix} = \begin{bmatrix} 0 & 1 \\ \sin\gamma & \cos\gamma \end{bmatrix} \begin{bmatrix} C_1 \\ C_2 \end{bmatrix} \tag{8.18}$$

and

$$\begin{bmatrix} F_{x1} \\ F_{x2} \end{bmatrix} = \frac{EA}{L}\gamma(1-\beta^2) \begin{bmatrix} -1 & 0 \\ \cos\gamma & -\sin\gamma \end{bmatrix} \begin{bmatrix} C_1 \\ C_2 \end{bmatrix} \tag{8.19}$$

The constants C_1 and C_2 can now be eliminated from Equations 8.18 and 8.19 to give the dynamic stiffness matrix of an axially vibrating Rayleigh-Love bar relating amplitudes of the forces and displacements at its ends as follows:

$$\begin{bmatrix} F_{x1} \\ F_{x2} \end{bmatrix} = \begin{bmatrix} a_1 & a_2 \\ a_2 & a_1 \end{bmatrix} \begin{bmatrix} \Delta_{x1} \\ \Delta_{x2} \end{bmatrix} \tag{8.20}$$

where the elements of the 2×2 dynamic stiffness matrix are given by

$$a_1 = \frac{EA}{L}\gamma\left(1-\beta^2\right)\cot\gamma\,, \qquad a_2 = -\frac{EA}{L}\gamma\left(1-\beta^2\right)\operatorname{cosec}\gamma \tag{8.21}$$

It should be noted that the Rayleigh-Love theory has a limitation that β^2 in Equations 8.11 and 8.12 must be less than one which is usually the case, otherwise, the solution of Equation 8.10 would not be harmonic and hence no oscillatory motion will take place. This limitation has been pointed out in the literature, e.g. see Equation 13 of [80].

8.3.2 Dynamic stiffness matrix of a Timoshenko beam

The dynamic stiffness matrix of a Timoshenko beam has already been published in the literature [76–78] in a rather longwinded and complicated manner, the details of which are not repeated here. However, for clarity, completeness and importantly to make this chapter self-contained, the existing literature is concisely congregated and simplified. The procedure is briefly summarised below.

Considering Figure 8.1 to be the Timoshenko beam under investigation with bending rigidity EI, mass per unit length ρA and length L, undergoing bending displacement w and bending rotation θ, the expressions for kinetic and potential energies T_{beam} and V_{beam} are respectively given by [81]

$$T_{\text{beam}} = \frac{1}{2}\int_0^L \rho A\left(\frac{\partial w}{\partial t}\right)^2 dx + \frac{1}{2}\int_0^L \rho I\left(\frac{\partial \theta}{\partial t}\right)^2 dx \tag{8.22}$$

$$V_{\text{beam}} = \frac{1}{2}\int_0^L EI\left(\frac{\partial \theta}{\partial x}\right)^2 dx + \frac{1}{2}\int_0^L kAG\gamma^2 dx \tag{8.23}$$

In Equations 8.22 and 8.23, ρI is the rotatory inertia per unit length about the bending axis, kAG is the shear rigidity of the beam with k being the shear correction (also known as the shape factor) and γ is the angle of shear deformation which is essentially the shearing strain. It should be noted that in the Timoshenko beam formulation the total slope $\frac{\partial w}{\partial x}$ is the sum of both bending slope θ and the slope due to shear γ [81] so that

$$\frac{\partial w}{\partial x} = \theta + \gamma \tag{8.24}$$

or

$$\gamma = \frac{\partial w}{\partial x} - \theta \tag{8.25}$$

Thus, the potential energy V_{beam} of Equation 8.22 becomes

$$V_{\text{beam}} = \frac{1}{2}\int_0^L EI\left(\frac{\partial \theta}{\partial x}\right)^2 dx + \frac{1}{2}\int_0^L kAG\left(\frac{\partial w}{\partial x} - \theta\right)^2 dx \tag{8.26}$$

Substituting the expressions for the kinetic and potential energies T_{beam} and V_{beam} from Equations 8.22 and 8.26 into Hamilton's principle expressed in Equation 8.3 and then integrating by parts and collecting terms yield the governing differential equations of motion and the associated boundary conditions providing the expressions for bending moment (M) and shear force (S) as follows [81]. *Governing differential equations*

$$-\rho A\frac{\partial^2 w}{\partial t^2}+kAG\frac{\partial}{\partial x}\left(\frac{\partial w}{\partial x}-\theta\right)=0 \tag{8.27}$$

$$-\rho I\frac{\partial^2 \theta}{\partial t^2}+EI\frac{\partial^2 \theta}{\partial x^2}+kAG\left(\frac{\partial w}{\partial x}-\theta\right) \tag{8.28}$$

Natural boundary conditions Shear force:

$$v=-kAG\left(\frac{\partial w}{\partial x}-\theta\right)=EI\frac{\partial^2 \theta}{\partial x^2}-\rho I\frac{\partial^2 \theta}{\partial t^2} \tag{8.29}$$

Bending moment:

$$m=-EI\frac{\partial \theta}{\partial x} \tag{8.30}$$

Introducing the non-dimensional length $\xi = x/L$ and assuming harmonic oscillation so that

$$w\left(x,t\right)=W(\xi)e^{i\omega t} \tag{8.31}$$

$$\theta\left(x,t\right)=\Theta(\xi)e^{i\omega t} \tag{8.32}$$

where $W(\xi)$ and $Q(\xi)$ are the amplitudes of the bending displacement and bending rotation of the harmonically vibrating Timoshenko beam.

Equations 8.27 and 8.28 can now be combined to give a fourth order ordinary differential equation as follows which is identically satisfied by both $W(\xi)$ and $Q(\xi)$

$$\left[D^4+b^2\left(r^2+s^2\right)D^2-b^2\left(1-b^2r^2s^2\right)\right]H=0 \tag{8.33}$$

where

$$D=\frac{d}{d\xi}=\frac{1}{L}\frac{d}{dx} \tag{8.34}$$

$$b^2=\frac{\rho A\omega^2L^4}{EI};\qquad r^2=\frac{I}{AL^2};\qquad s^2=\frac{EI}{kAGL^2} \tag{8.35}$$

and

$$H=W\ \ or\ \ \Theta \tag{8.36}$$

If a trial solution $H = e^{\lambda\xi}$ is assumed where λ is a constant, yet to be known, the auxiliary or characteristic equation of the differential Equation 8.33 is given by

$$\lambda^4+b^2\left(r^2+s^2\right)\lambda^2-b^2\left(1-b^2r^2s^2\right)=0 \tag{8.37}$$

Equation 8.37 is quartic in λ, but quadratic in λ^2 so that

$$\lambda^2=\frac{-b^2\left(r^2+s^2\right)\pm\sqrt{\left\{b^2\left(r^2+s^2\right)\right\}^2+4b^2\left(1-b^2r^2s^2\right)}}{2}$$

$$= \frac{-b^2\left(r^2+s^2\right) \pm \sqrt{\left\{b^2\left(r^2-s^2\right)\right\}^2+4b^2}}{2} \tag{8.38}$$

Clearly λ^2 will be always real and for the negative value of the expression under the square root sign of Equation 8.38, one of the two values of λ^2 will be always negative, resulting in two imaginary roots of λ which will lead to part of the solution of Equation 8.33 in terms of trigonometric functions whereas the other value of λ^2 when using the positive value before the square root sign can be either positive or negative depending on whether the square root expression in Equation 8.38 is bigger than or smaller than $b^2(r^2+s^2)$. If this second value of λ^2 is positive which is usually the case, the two roots of λ^2 will be real, yielding the remaining solution of Equation 8.33 in terms of hyperbolic functions so that the two of the four integration constants in the solution will be connected to trigonometric functions and the other two to hyperbolic functions. However, for exceptionally high frequencies or for exceptionally squat beams, the second value of λ^2 can be negative like the first one which will give the entire solution of Equation 8.33 in terms of trigonometric functions only. The two sets of solutions and their conditionality are explained below.
The expression for λ^2 in Equation 8.38 can be expressed in the following alternative form

$$\lambda^2 = \frac{b^2}{2}\left\{-\left(r^2+s^2\right) \pm \sqrt{\left(r^2+s^2\right)^2+\frac{4}{b^2}\left(1-b^2r^2s^2\right)}\right\} \tag{8.39}$$

It is clear from Equation 8.39 that if $b^2r^2s^2 < 1$, one of the values of λ^2 will be negative and the other value will be positive whereas if $b^2r^2s^2 > 1$, they both will be negative. Thus the solutions for bending displacement W and bending rotation Θ for these two cases resulting from the differential equation of Equation 8.33 are given by

1. $b^2r^2s^2 < 1$

$$W(\xi) = A_1\cos\Phi + A_2\sin\Phi + A_3\cosh\Lambda + A_4\sinh\Lambda \tag{8.40}$$

$$\Theta(\xi) = B_1\cos\Phi + B_2\sin\Phi + B_3\cosh\Lambda + B_4\sinh\Lambda \tag{8.41}$$

2. $b^2r^2s^2 > 1$

$$W(\xi) = A_1\cos\Phi + A_2\sin\Phi + A_3\cos\Lambda + A_4\sin\Lambda \tag{8.42}$$

$$\Theta(\xi) = B_1\cos\Phi + B_2\sin\Phi + B_3\cos\Lambda + B_4\sin\Lambda \tag{8.43}$$

where

$$\Phi^2 = \frac{b^2\left(r^2+s^2\right)}{2} + \frac{b^2}{2}\sqrt{\left(r^2+s^2\right)^2+\frac{4}{b^2}\left(1-b^2r^2s^2\right)} \tag{8.44}$$

and

$$j\Lambda^2 = -\frac{b^2\left(r^2+s^2\right)}{2} + \frac{b^2}{2}\sqrt{\left(r^2+s^2\right)^2+\frac{4}{b^2}\left(1-b^2r^2s^2\right)} \tag{8.45}$$

with

$$j = 1 \;\; for \;\; b^2r^2s^2 < 1; \;\; j = -1 \;\; for \;\; b^2r^2s^2 > 1 \tag{8.46}$$

and A_1 - A_4 and B_1 - B_4 are two different sets of constants.
It should be noted from Equation 8.35 that

$$b^2r^2s^2 = \frac{\rho I \omega^2}{kAG} \tag{8.47}$$

For most of the practical problems, $b^2r^2s^2$ will be less than one unless ω is exceptionally large. This is because the shear rigidity kAG is generally much bigger than the rotatory inertia per unit length ρI for any realistic cross-section and beam material, but nevertheless, the solutions given by Equations 8.42 and 8.43 are included in the theory to cover the exceptional case when $b^2r^2s^2$ is greater than one.
With the help of Equation 8.27 or 8.28 and the solution given by Equations 8.40-8.43, it can be shown that the two sets of constants A_1 - A_4 and B_1 - B_4 are related. Using Equation 8.27, the following relationships between B_1 - B_4 and A_1 - A_4 are obtained.

$$B_1 = \frac{k_\Phi}{L}A_2; \quad B_2 = -\frac{k_\Phi}{L}A_1; \quad B_3 = \frac{k_\Lambda}{L}A_4; \quad B_4 = j\frac{k_\Lambda}{L}A_3 \tag{8.48}$$

where

$$k_\Phi = \left(\frac{\Phi^2 - b^2s^2}{\Phi}\right); \qquad k_\Lambda = \left(\frac{\Lambda^2 + jb^2s^2}{\Lambda}\right) \tag{8.49}$$

Because of the harmonic oscillation hypothesis adopted for the freely vibrating Timoshenko beam as indicated by Equations 8.31 and 8.32 and also by the introduction of the non-dimensional length $\xi = x/L$, the expressions for the amplitudes of the shear force (V) and bending moment (M) arising from Equations 8.29, 8.30 and 8.48 will take the following form.

$$V = \frac{EI}{L^2}\left(\frac{d^2\Theta}{d\xi^2} - b^2r^2\Theta\right) = \frac{EI}{L^3}\left(A_1e_\Phi \sin\Phi\xi - A_2e_\Phi \cos\Phi + jA_3e_\Lambda \sin\Lambda\xi + A_4e_\Lambda \cos\Lambda\xi \quad \right) \tag{8.50}$$

$$M = -\frac{EI}{L^2}\frac{d\Theta}{d\xi} = -\frac{EI}{L^2}\left(-A_1\Phi k_\Phi \cos\Phi\xi - A_2\,\Phi k_\Phi \sin\Phi\xi + jA_3\,\Lambda k_\Lambda \cos\Lambda\xi \; + jA_4\Lambda k_\Lambda \sin\Lambda\xi\right) \tag{8.51}$$

where

$$e_\Phi = \left(\Phi^2 - b^2r^2\right)k_\Phi; \qquad e_\Lambda = j\left(\Lambda^2 + jb^2r^2\right)k_\Lambda \tag{8.52}$$

and j and k_ϕ, k_Λ have already been defined in Equations 8.46 and 8.49, respectively.
Now from the expressions for the amplitudes of displacements W and Θ given by Equations 8.40 - 8.43 and the corresponding forces V and M given by Equations 8.50 and 8.51, the dynamic stiffness matrix of the Timoshenko beam can be formulated by applying the boundary conditions in algebraic form relating the amplitudes of forces and displacements.

Referring to Figure 8.3, the boundary conditions for the displacements and forces can be applied as follows

$$At \;\; x = 0 \;\; (i.e. \;\; \xi = 0), \;\; W = \Delta_{y1}, \;\; \Theta = \Theta_1, \;\; V = F_{y1} \;\; and \;\; M = M_1 \tag{8.53}$$

$$At \;\; x = L \;\; (i.e. \;\; \xi = 1), \;\; W = \Delta_{y2}, \;\; \Theta = \Theta_2, \;\; V = -F_{y2} \;\; and \;\; M = -M_2 \tag{8.54}$$

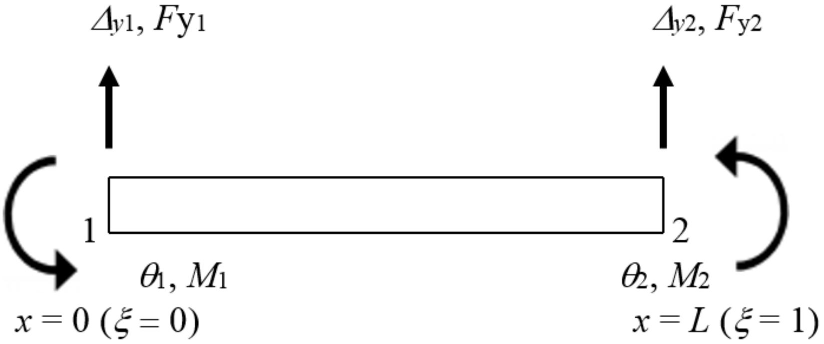

Figure 8.3: Boundary conditions for displacements and forces for a Timoshenko beam.

Substituting Equations 8.53 and 8.54 into Equations 8.40 - 8.43 and Equations 8.50 and 8.51, the following two matrix equations are obtained for displacements and forces, respectively, in terms of the constants A_1 - A_4.

$$\begin{bmatrix} \Delta_{y1} \\ \Theta_1 \\ \Delta_{y2} \\ \Theta_2 \end{bmatrix} = \begin{bmatrix} 1 & 0 & 1 & 0 \\ 0 & k_\Phi/L & 0 & k_\Lambda/L \\ C & S & \overline{C} & \overline{S} \\ -k_\Phi S/L & k_\Phi C/L & jk_\Lambda S/L & k_\Lambda C/L \end{bmatrix} \begin{bmatrix} A_1 \\ A_2 \\ A_3 \\ A_4 \end{bmatrix} \tag{8.55}$$

or

$$\mathbf{\Delta} = \mathbf{Q}A \tag{8.56}$$

and

$$\begin{bmatrix} F_{y1} \\ M_1 \\ F_{y2} \\ M_2 \end{bmatrix} = \begin{bmatrix} 0 & -W_3 e_\Phi & 0 & W_3 e_\Lambda \\ W_2 \Phi k_\Phi & 0 & -jW_2 \Lambda k_\Lambda & 0 \\ -W_3 e_\Phi S & W_3 e_\Phi C & -jW_3 e_\Lambda \overline{S} & -W_3 e_\Lambda \overline{C} \\ -W_2 \Phi k_\Phi C & -W_2 \Phi k_\Phi S & jW_2 \Lambda k_\Lambda \overline{C} & jW_2 \Lambda k_\Lambda \overline{S} \end{bmatrix} \begin{bmatrix} A_1 \\ A_2 \\ A_3 \\ A_4 \end{bmatrix} \tag{8.57}$$

or

$$\mathbf{F} = \mathbf{RA} \tag{8.58}$$

where

$$S = \sin\Phi; \quad C = \cos\Phi \tag{8.59}$$

$$\overline{S} = sinh \;\; \Lambda; \quad \overline{C} = cosh \;\; \Lambda \quad b^2 r^2 s^2 < 1 (j = 1)$$

$$\overline{S} = sin\ \Lambda; \quad \overline{C} = cos\ \Lambda \quad b^2r^2s^2 > 1(j = -1) \tag{8.60}$$

and

W_1, W_2 and W_3 are defined as follows

$$W_1 = \frac{EI}{L}; \; W_2 = \frac{EI}{L^2}; \quad W_3 = \frac{EI}{L^3} \tag{8.61}$$

The constants A_1 - A_4 can now be eliminated from Equations 8.55 and 8.57 to give the 4×4 dynamic stiffness matrix of the Timoshenko beam. This can be achieved by inverting the square matrix of Equation 8.55, i.e. **Q** matrix of Equation 8.56 and pre-multiplying it with the square matrix of Equation 8.57, i.e. **R** matrix and performing the matrix operation $\mathbf{RQ^{-1}}$ numerically to give the dynamic stiffness matrix. Alternatively, the matrix inversion and matrix multiplication procedures can be carried out symbolically (algebraically) to generate explicit expressions for each of the stiffness elements of the dynamic stiffness matrix to give.

$$\begin{bmatrix} F_{y1} \\ M_1 \\ F_{y2} \\ M_2 \end{bmatrix} = \begin{bmatrix} d_1 & d_2 & d_4 & d_5 \\ d_2 & d_3 & -d_5 & d_6 \\ d_4 & d_5 & d_1 & -d_2 \\ -d_5 & d_6 & -d_2 & d_3 \end{bmatrix} \begin{bmatrix} \Delta_{y1} \\ \Theta_1 \\ \Delta_{y2} \\ \Theta_2 \end{bmatrix} \tag{8.62}$$

where

$$\begin{aligned} d_1 &= W_3 b^2 \Gamma (C\overline{S} + \eta S\overline{C})/(\Lambda\Phi) \\ d_2 &= W_2 Z\Gamma \left\{(\Phi + j\eta\Lambda)\, S\overline{S} - (\Lambda - \eta\Phi)\left(1 - C\overline{C}\right)\right\} / (\Lambda + \eta\Phi) \\ d_3 &= W_1 \Gamma \left(S\overline{C} - j\eta C\overline{S}\right) \\ d_4 &= -W_3 b^2 \Gamma (\overline{S} + \eta S)/(\Lambda\Phi) \\ d_5 &= W_2 Z\Gamma(\overline{C} - C) \\ d_6 &= W_1 \Gamma \left(j\eta\overline{S} - S\right) \end{aligned} \tag{8.63}$$

with

$$\begin{aligned} Z = \Phi - b^2s^2/\Phi; \quad \eta = Z/(j\Lambda + b^2s^2/\Lambda); \\ \Gamma = [\Lambda + \eta\Phi]/[2\eta(1 - C\overline{C}) + (1 - j\eta^2)S\overline{S}] \end{aligned} \tag{8.64}$$

8.3.3 Combination of axial and bending stiffnesses

A simple superposition is now possible to put the axial and bending dynamic stiffnesses together in order to express the force-displacement relationship of the combination of a Rayleigh-Love bar and a Timoshenko beam. Superposing Figures 8.2 and 8.3 to give Figure 8.4 and then using Equations 8.20 and 8.62, one obtains the dynamic stiffness matrix of the combination of a Rayleigh-Love bar incorporating the axial stiffnesses, and a

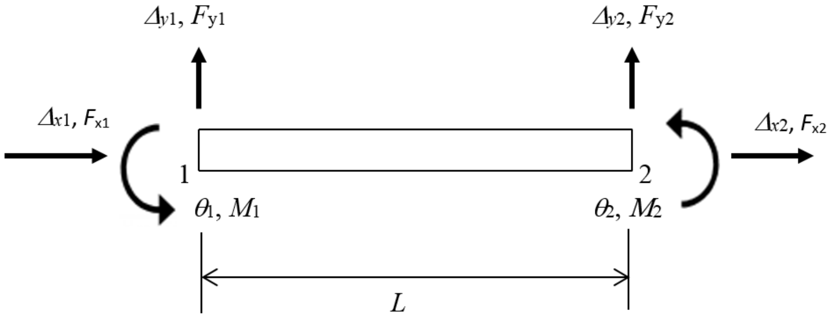

Figure 8.4: Amplitudes of displacements and forces at the ends of a combined Rayleigh-Love bar and a Timoshenko beam.

Timoshenko beam incorporating the bending stiffness to enable the free vibration analysis of plane frames to be made.

Referring to Figure 8.4 and Equations 8.20 and 8.62, the resulting dynamic stiffness matrix is given by

$$\begin{bmatrix} F_{x1} \\ F_{y1} \\ M_1 \\ F_{x2} \\ F_{y2} \\ M_2 \end{bmatrix} = \begin{bmatrix} a_1 & 0 & 0 & a_2 & 0 & 0 \\ 0 & d_1 & d_2 & 0 & d_4 & d_5 \\ 0 & d_2 & d_3 & 0 & -d_5 & d_6 \\ a_2 & 0 & 0 & a_1 & 0 & 0 \\ 0 & d_4 & -d_5 & 0 & d_1 & -d_2 \\ 0 & d_5 & d_6 & 0 & -d_2 & d_3 \end{bmatrix} \begin{bmatrix} \Delta_{x1} \\ \Delta_{y1} \\ \Theta_1 \\ \Delta_{x2} \\ \Delta_{y2} \\ \Theta_2 \end{bmatrix} \tag{8.65}$$

or

$$\mathbf{F} = \mathbf{K}\boldsymbol{\Delta} \tag{8.66}$$

where **F** and **Δ** are respectively the force and displacement vectors and **K** is the frequency dependent 6×6 dynamic stiffness matrix whose elements $k(i, j)$ $(i = 1,2,\ldots 6; j = 1,2,\ldots 6)$ are given by a_1, a_2 and d_1 - d_6 defined in Equations 8.21 and 8.63, respectively. Note that **K** is symmetric as expected.

8.4 Application of the dynamic stiffness matrix

8.4.1 The Wittrick-Williams algorithm

The main features of the Wittrick-Williams algorithm and its basic working principles are briefly summarised as follows which have been already explained in Section A 1.2.1.2. The algorithm has essentially two components, one is the so-called sign count $\mathbf{s}\{\mathbf{K_f}\}$ and the other is the so-called j_0 count.

Suppose that ω denotes the circular (or angular) frequency of a vibrating structure, then according to the Wittrick-Williams algorithm [23], j, the number of natural frequencies passed, as ω is increased from zero to ω^*, is given by

$$j = j_0 + s\{K_f\} \tag{8.67}$$

where $\mathbf{K_f}$,the overall dynamic stiffness matrix of the wing whose elements depend on ω and is evaluated at $\omega = \omega^*$; $\mathbf{s}\{\mathbf{K_f}\}$ is the number of negative elements on the leading diagonal of $\mathbf{K_f^\Delta}$, $\mathbf{K_f^\Delta}$ is the upper triangular matrix obtained by applying the usual form of Gauss elimination to $\mathbf{K_f}$, and j_0 is the number of natural frequencies of the wing still lying between $\omega = 0$ and $\omega = \omega^*$ when the displacement components to which $\mathbf{K_f}$ corresponds are all zeros. (Note that the structure can still have natural frequencies when all its nodes are clamped, because exact member equations allow each individual member to displace between nodes with an infinite number of degrees of freedom, and hence infinite number of natural frequencies between nodes.) Thus

$$j_0 = \Sigma j_m \tag{8.68}$$

where j_m is the number of natural frequencies between $\omega = 0$ and $\omega = \omega^*$ for an individual component member with its ends fully clamped, while the summation extends over all members of the structure. Thus, with the knowledge of Equations 8.67 and 8.68, it is possible to ascertain how many natural frequencies of a structure lie below an arbitrarily chosen trial frequency. This simple feature of the algorithm (coupled with the fact that successive trial frequencies can be chosen by the user to bracket a natural frequency) can be used to converge on any required natural frequency to any desired (or specified) accuracy.

8.4.2 The significance of the j_0 count in the Wittrick-Williams algorithm

As explained in section 8.1, one of the requirements for the application of the Wittrick-Williams algorithm is to acquire the needed information about the Clamped-Clamped natural frequencies of individual elements in a structures (the so-called j_0 count) so as to enable the free vibration analysis to be carried out in a flawless and robust manner. However, the determination of the natural frequencies using the Wittrick-Williams algorithm is predominantly based on the sign count $\mathbf{s}\{\mathbf{K_f}\}$ described in section 8.1. The j_0 count of Equation 8.68 is not always needed, particularly if the clamped-clamped natural frequency of none of the constituent members in the structure is exceeded within the frequency range of interest. One way of avoiding the computation of j_0 is to split the structure into large number of elements so that the clamped-clamped natural frequencies of all individual elements become exceptionally high and thus will not be exceeded by any frequency of practical interest. Nevertheless, j_0 count of the algorithm is not really a peripheral issue, particularly for achieving computational efficiency and avoiding further unnecessary discretisation of the structure. The need to compute j_0 stems from the fact that the DSM allows infinite number of natural frequencies to be accounted for when all the nodes of the structure are fully restrained and yet one or more structural members can vibrate freely on their own between the nodes resulting in $\delta = \mathbf{0}$ modes in the eigenvalue equation $[\mathbf{K_D}]\{\delta\} = \mathbf{0}$.

8.4.3 Clamped-Clamped natural frequencies of a Rayleigh-Love bar

The clamped-clamped natural frequencies of a Rayleigh-Love bar can be obtained from Equations 8.14 and 8.15 by substituting the boundary conditions of displacements to zero at both ends or alternatively by putting the determinant of the square matrix of Equation 8.18 to zero, yielding the frequency equation as

$$\sin\gamma \;= 0 = \sin n\pi \tag{8.69}$$

Thus, proceeding in the same way as in the case of classical Bernoulli-Euler bar [60] the number of clamped-clamped natural frequencies j_R of a Rayleigh-Love bar lying below an arbitrarily chosen trial frequency ω^* is given by

$$j_R = highest\;\;integer < \frac{\gamma}{\pi} \tag{8.70}$$

8.4.4 Clamped-Clamped natural frequencies of a Timoshenko beam

For a Timoshenko beam, the number of clamped-clamped natural frequencies exceeded by the trial frequency ω^* can be established using the procedure described in [69] to give

$$j_T \;= j_c - \left[2 - sg\left\{d_3\right\} - sg\left\{d_3 - \frac{d_6^2}{d_3}\right\}\right]/2 \tag{8.71}$$

where sg{ } is +1 or -1 depending on the sign of the quantity within the curly bracket, d_3 and d_6 have already been defined in Equation 8.63 and j_c is given by

$$\begin{aligned} j_c &= j_d \;\; for\;\; b^2r^2s^2 < 1 \\ j_c &= j_d + j_e \;\; for\;\; b^2r^2s^2 \geq 1 \end{aligned} \tag{8.72}$$

with

$$\begin{aligned} j_d &= highest\;\;integer < \frac{\phi}{\pi} \\ j_e &= highest\;\;integer < \frac{\Lambda}{\pi} + 1 \end{aligned} \tag{8.73}$$

In Equation 8.73, ϕ and Λ have already been defined in Equations 8.44 and 8.45 respectively. Thus the number of clamped-clamped natural frequencies j_m exceeded by an individual member by the trial frequency ω^* with the inclusion of the Rayleigh-Love bar and the Timoshenko beam theories is given by

$$j_m = j_R + j_T \tag{8.74}$$

Now the root count j_0 of Equation 8.68 can be computed using the Equation 8.68 where the summation Σ over m is extended to include all elements in the structure.

8.5 Results and discussion

Numerical examples are given for three different types of problems. Example-1 is focused on the natural frequencies of a freely vibrating uniform Rayleigh-Love bar in longitudinal motion with clamped-clamped and cantilever boundary conditions. This is followed by example-2 which is that of a stepped bar taken from the literature. This problem is analysed using both the classical Bernoulli Euler and the Rayleigh-Love theories. Finally example-3 demonstrates the free vibration characteristics of a plane frame for which the dynamic stiffness matrix for each constituent element is based on both Rayleigh-Love and Timoshenko theories as well as classical Bernoulli Euler theories.

8.5.1 Free longitudinal vibration of a uniform bar

Using the notations given in section 8.3.1, the natural frequencies of a Rayleigh-Love bar with both ends clamped can be obtained from Equation 8.14 by substituting $U(\xi)$ to zero at both $\xi = 0$ and $\xi = 1$ and making appropriate substitution for γ to give the n^{th} natural frequency ω_n as

$$\omega_n = \sqrt{\frac{n^2\pi^2}{\left(1 + \frac{\nu^2 I_p n^2\pi^2}{AL^2}\right)}\left(\frac{EA}{\rho AL^2}\right)} \tag{8.75}$$

where $n = 1, 2, 3, \ldots$. The corresponding natural frequencies for the classical Bernoulli-Euler with clamped-clamped boundary conditions can be found in standard texts [79] given by

$$\omega_{n_0} = n\pi\sqrt{EA/\left(\rho AL^2\right)} \tag{8.76}$$

The ratio between the natural frequencies for the clamped-clamped bar obtained from the Rayleigh-Love and classical Bernoulli-Euler theories can be expressed with the help of Equations 8.75 and 8.76 to give

$$\frac{\omega_n}{\omega_{n_0}} = \frac{1}{\sqrt{1 + \frac{\nu^2 n^2\pi^2}{\left(\frac{L}{r}\right)^2}}} \tag{8.77}$$

where r is defined as the radius of gyration expressed as

$$r = \sqrt{\frac{I_p}{A}} \tag{8.78}$$

Proceeding in a similar way and imposing appropriate boundary conditions, the natural frequency ratio for a cantilever bar using the Rayleigh-Love and classical Bernoulli-Euler theories can be expressed as

$$\frac{\omega_n}{\omega_{n_0}} = \frac{1}{\sqrt{1 + \frac{(2n-1)^2\pi^2\nu^2}{4\left(\frac{L}{r}\right)^2}}} \tag{8.79}$$

The validity of the Equations 8.77 and 8.79 has been further confirmed by using the developed dynamic stiffness matrix of a Rayleigh-Love bar shown in Equation 8.20.
Clearly Equations 8.77 and 8.79 indicate that the natural frequency ratio $\frac{\omega_n}{\omega_{n_0}}$ is dependent on the Poisson's ratio ν of the bar material as well as the slenderness ratio L/r of the bar. The Poisson's ratio ν for an isotropic material is generally constant and maybe assumed to be 0.3 which is used here in the analysis.
Figures 8.5 and 8.6 shows the variation of the ratio of the first five natural frequencies using the Rayleigh-Love and classical Bernoulli-Euler theories against the slenderness ratio L/r for the clamped-clamped and cantilever bar respectively. Clearly for smaller values of slenderness ratios and for higher natural frequencies, the classical Bernoulli-Euler theory is considerably less accurate. The errors incurred in the fifth natural frequency when using the classical Bernoulli-Euler theory are 27% and 24% for the clamped-clamped and cantilever bar respectively when the slenderness ratio is 5. It should be noted that in the Statistical Energy Analysis (SEA) for which modal density in the high frequency range is required, the classical Bernoulli-Euler theory can be inadequate.

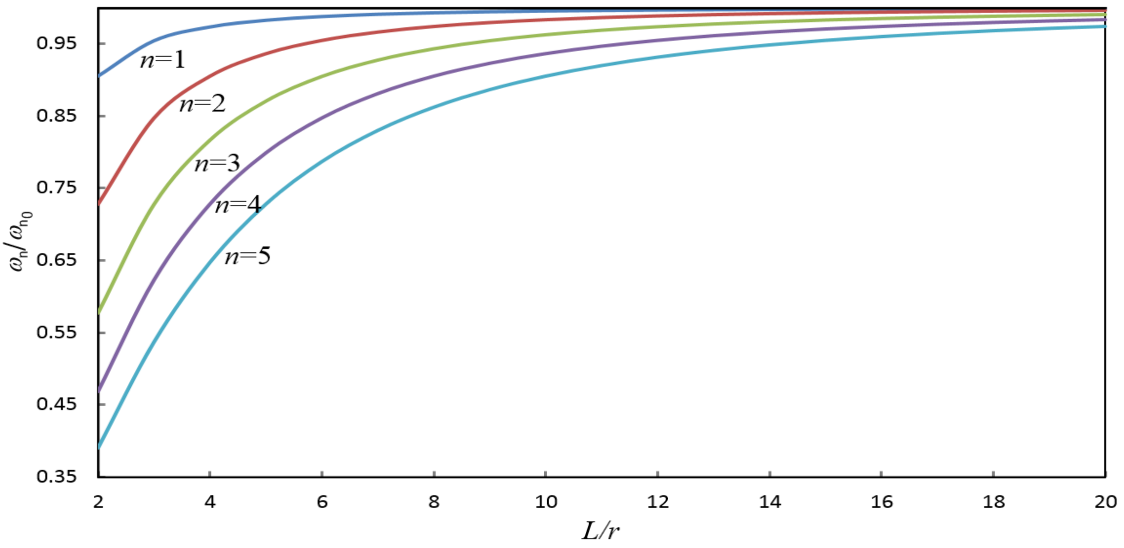

Figure 8.5: The first five natural frequency ratios using the Rayleigh-Love and classical Bernoulli-Euler theories for a clamped-clamped bar in axial vibration. ω_n = natural frequency using Rayleigh-Love theory; ω_{n_0} = natural frequency using classical Bernoulli-Euler theory.

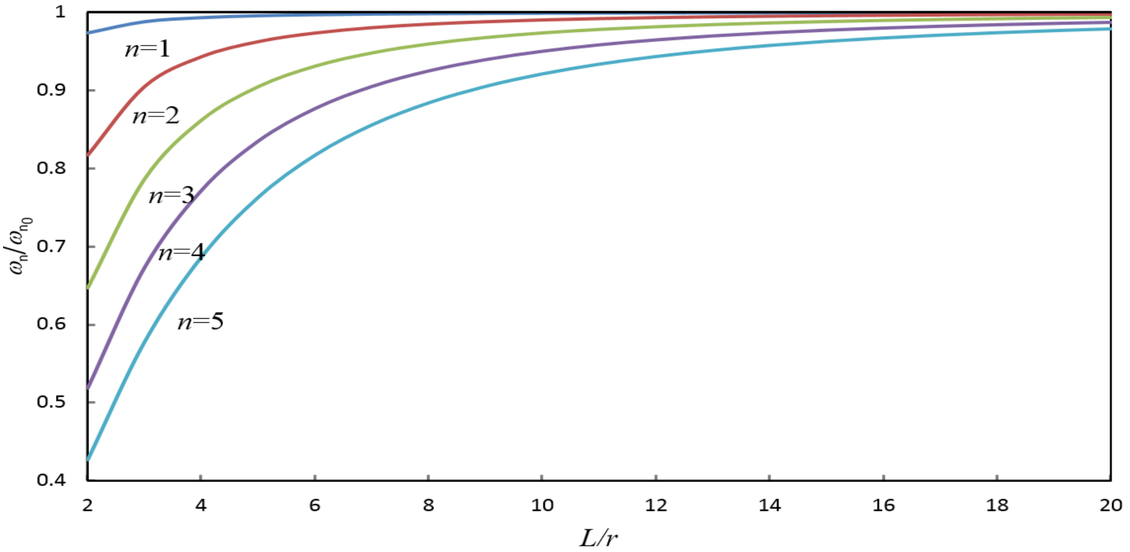

Figure 8.6: The first five natural frequency ratios using the Rayleigh-Love and classical Bernoulli-Euler theories for a cantilever bar in axial vibration mode. ω_n = natural frequency using Rayleigh-Love theory; ω_{n_0} = natural frequency using classical Bernoulli-Euler theory.

8.5.2 Free longitudinal vibration of a stepped bar

A stepped bar (example-2) which is taken from [82] and shown in Figure 8.7 is analysed for its free vibration characteristics in longitudinal motion using the developed dynamic stiffness matrix. The stepped bar is cantilevered at the left hand end as shown and consists of three individual bars of solid circular cross-section with different geometrical dimensions and material properties for each. The essential data required for the analysis are: radius of cross-section (r_i), length (l_i), Young's modulus (E_i), density (ρ_i) and Poisson's ratio (ν_i) (i representing the segment or element number). It should be noted that radius of cross section (r_i) used in this section is different from radius of gyration used in previous section for uniform bar.

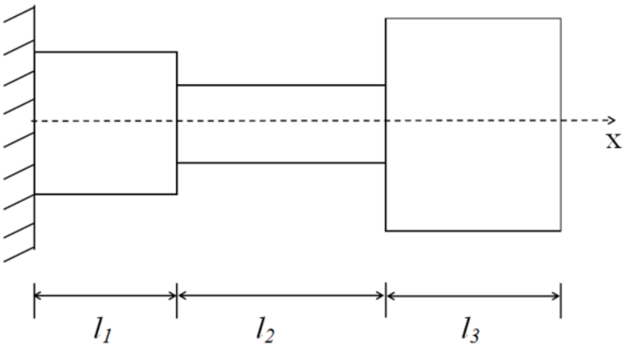

Figure 8.7: A three-stepped bar for free vibration analysis.

The numerical values for the data taken from [92] are: r_1 = 0.05m, r_2 = 0.03m, r_3 = 0.075m, l_1 = 0.05m, l_2 = 0.17m, l_3 = 0.13m, E_1 = 200×10^9 Pa, E_2 = 70×10^9 Pa, E_3=100×10^9 Pa, ρ_1 = 7.85×103 kg/m^3, ρ_2 = 2.7×103 kg/m^3, ρ_3 = 8.4×103 kg/m^3, ν_1= 0.30, ν_2 = 0.33, ν_3 = 0.34.

The first four natural frequencies computed using the Rayleigh-Love dynamic stiffness theory are shown in column 2 of Table 8.1 alongside the results reported in [82] shown in column 3. The corresponding natural frequencies computed using classical Bernoulli-Euler dynamic stiffness theory [60] are also shown in the parenthesis in column 2. Although the agreement of the results between the present theory and those of [82] are good for the second and fourth natural frequencies (the differences are well within 3%), but for the first and third natural frequencies there are some discrepancies which are around 13% and 15% respectively. The fundamental natural frequency of the bar quoted in [82] is well above the corresponding natural frequency obtained from the classical Bernoulli-Euler theory. This is surely in error because the effect of the transverse inertia presumably accounted for in [82] is expected to diminish the natural frequency and not increase it. The mode shapes corresponding to the four natural frequencies using the present theory are

Table 8.1: Natural frequencies of a stepped bar in longitudinal vibration (results from the conventional classical theory are shown in the parenthesis in column 2).

Frequency number	Natural frequency (*Hz*)	
	Current theory	Ref. [82]
1	1184.312 (1184.39)	1362.79
2	11732.86 (12509.42)	11679.6
3	14503.42 (15002.56)	12640.5
4	20014.45 (24187.29)	19461.9

shown in Figure 8.8 by black solid lines which are in broad agreement with the ones reported in [82]. The mode shapes shown by red dashed lines are those computed using the classical Bernoulli-Euler theory. Clearly, the first three mode shapes have undergone very little change as the result of using the present theory as opposed to the classical Bernoulli-Euler theory, but the fourth mode being a higher order mode has turned out to be significantly different, as expected. The exact reason for the discrepancies in the first and third natural frequencies were unable to be pinpointed when the results are compared with those of [82], but it should be recognised that the series solution approach used in [82] is different from the dynamic stiffness methodology developed in this chapter. It is to be noted that both the Rayleigh-Love and the classical Bernoulli-Euler theories give almost the same results for the fundamental natural frequency, but the differences in the second, third and fourth frequencies are 7%, 4% and 21% respectively. Understandably, the classical Bernoulli-Euler theory overestimates the natural frequencies whereas the more refined Rayleigh-Love theory which accounts for the added transverse and lateral inertia of the bar yields lower values of the natural frequencies which is apparently contradicted by the result for the fundamental natural frequency reported in [82].

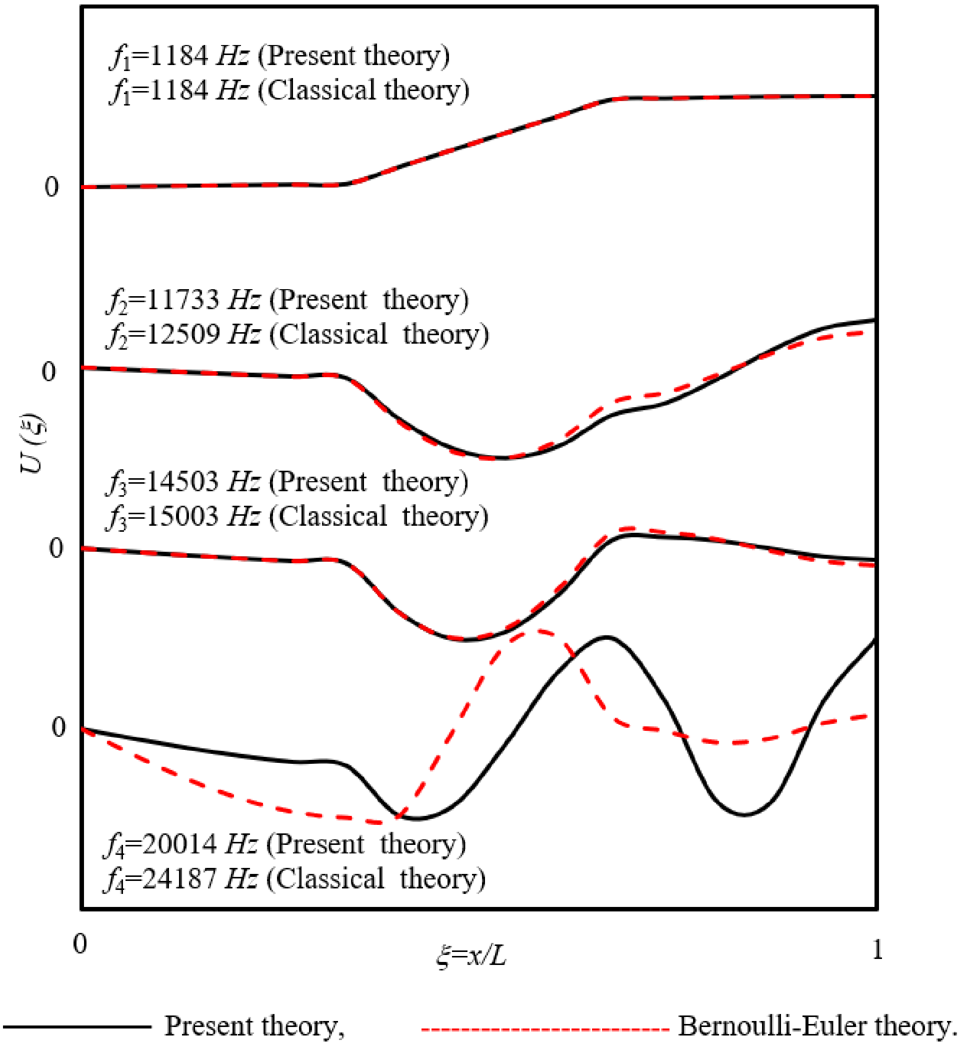

Figure 8.8: Natural frequencies and mode shapes of the three-stepped bar of Figure 8.7.

8.5.3 Free vibration of a plane frame

The final set of results was obtained using example-3 which is that of a plane frame shown in Figure 8.9. Each element of the frame has the same uniform geometrical, cross sectional and material properties and the data used in the analysis are as follows: EI = 4.0×10^6 Nm^2, $EA = 8.0\times10^8$ N, $kAG = 2.0\times10^8$ N, $\rho A = 30$ kg/m, $\rho I_p = 0.157$ kgm, ν = 1/3, $k = 2/3$.

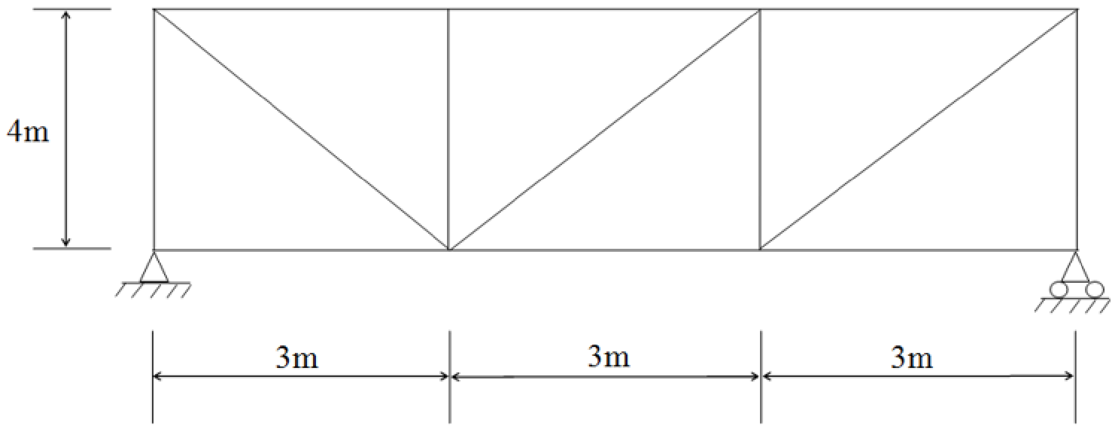

Figure 8.9: A plane frame for free vibration analysis using Rayleigh-Love and Timoshenko theories.

A wide range of the natural frequencies of the frame was computed using the present theory as well as the classical Bernoulli-Euler theory. Apart from the computation of the first five natural frequencies which were sequentially chosen, the higher order natural frequencies were sparingly and sparsely chosen so as to cover the order of the natural frequencies between 50^{th} and 400^{th}. The results are shown in Table 8.2. Clearly, higher the order of the frequency, higher the incurred error due to using the classical Bernoulli-Euler theory. The first five natural frequencies of the frame are virtually unaltered. As expected, the classical Bernoulli-Euler theory overestimates the natural frequencies.

One of the potential application areas of the theory developed in this chapter is the Statistical Energy Analysis (SEA) for which accurate natural frequency predictions in the low, medium and high frequency range are essential. To this end, the uncompromising accuracy of the dynamic stiffness method developed in this chapter by applying the Rayleigh-Love and Timoshenko theories is further demonstrated by computing the number of natural frequencies of the frame (see Figure 8.10) which lies within the frequency ranges of $0 < f_i \leq 1kHz$, $0 < f_i \leq 2kHz$, $0 < f_i \leq 3kHz$ and up to $0 < f_i \leq 10kHz$ which cover low, medium and high frequency bands. Figure 8.10 shows the frequency distribution, i.e. the modal density of the frame. It will be difficult to obtain these results with such accuracy using conventional finite element method.

Table 8.2: Natural frequencies of plane frame.

Frequency range	Natural frequency number (i)	Natural frequency fi (Hz)	
		Rayleigh-Love and Timoshenko theory	Classical Bernoulli-Euler theory
Low	1	35.38	35.77
	2	38.56	39.10
	3	41.98	42.56
	4	50.73	51.39
	5	53.14	53.94
Medium	50	565.54	600.97
	60	635.28	709.09
	70	828.95	934.39
	80	964.48	1136.00
	90	1108.90	1301.20
	100	1306.80	1521.40
High	150	2151.10	2732.30
	200	3047.50	4089.50
	250	3940.30	5585.00
	300	4859.70	7152.20
	350	5767.40	8744.80
	400	6112.80	10495.0

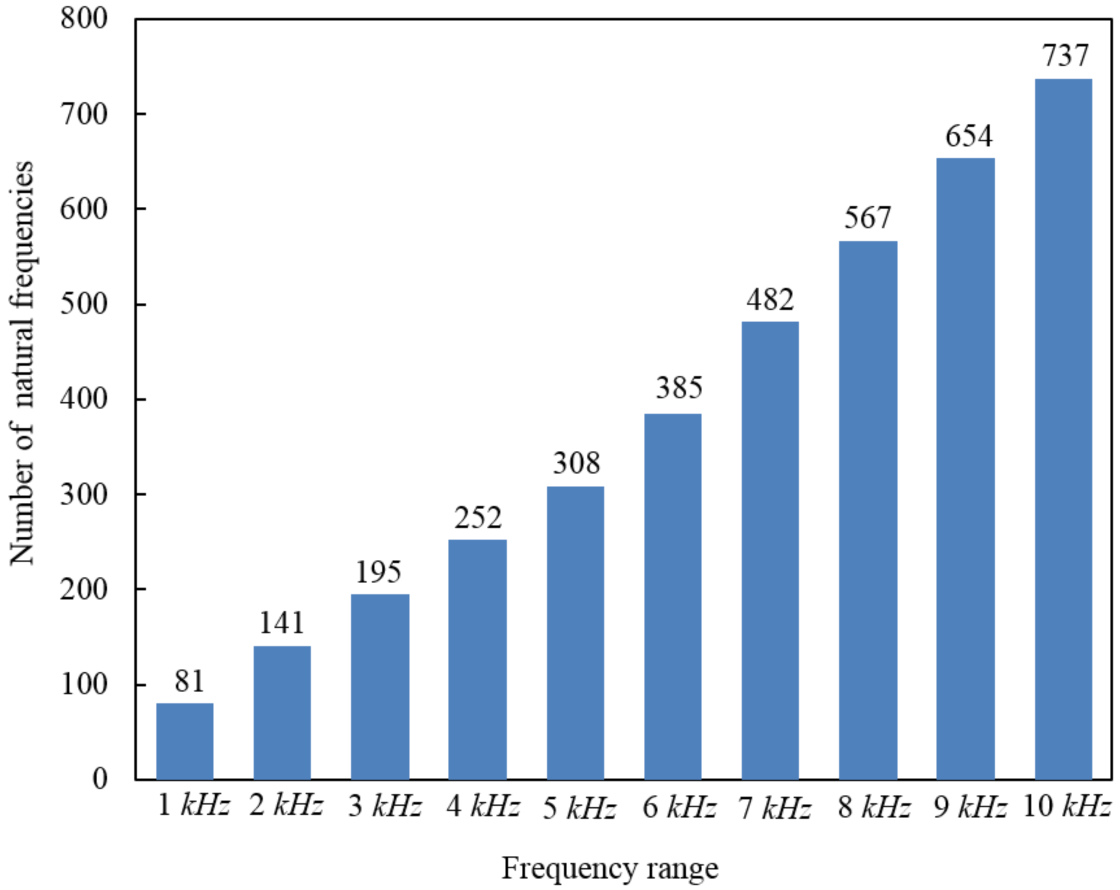

Figure 8.10: Modal density of plane frame.

8.6 Conclusions

Starting from the derivations of the governing differential equations of motion in free vibration, the dynamic stiffness matrix of a beam using both the Rayleigh-Love and Timoshenko theories has been developed. With the help of the Wittrick-Williams algorithm as solution technique, the theory is applied to investigate the free vibration behaviour of a uniform Rayleigh-Love bar, a stepped Rayleigh-Love bar, and a framework for which the modal density distribution is presented by capturing its natural frequencies in the low, medium and high frequency range. Some representative mode shapes of the stepped bar are also illustrated. The theory developed is particularly helpful when carrying out high frequency free vibration analysis of skeletal structures. A potential application of the research described in this chapter falls within the area of statistical energy analysis for which the knowledge of modal density distributions in the high frequency range is essential.

Chapter 9

Coupled axial-bending DSM for beam elements

9.1 Introduction to coupled axial-bending dynamic stiffness matrix for beam elements

Generally for aeroelastic optimisation the coupling between the axial and bending deformations was ignored because the axial stiffness of an aircraft wing in comparison with its bending and torsional stiffnesses is generally much higher which results in negligibly small axial displacement, unlike the relatively larger bending and torsional displacements. Consequent on this, the axial natural frequencies of aircraft wings are expected to be so high that to all intents and purposes such frequencies will be beyond the range of practical interest. This is particularly true from an aeroelastic standpoint of high aspect ratio aircraft wings for which flutter generally occurs due to the coalescence of the bending and torsional modes with insignificant interaction from the axial modes. The possibility of axial-bending coupling in aircraft wings is indeed very remote. However, there is a different class of problems in civil engineering structures for which the axial-bending coupling cannot be ignored. This establishes the need for the development of new theories for free and/or forced vibration analysis of structures incorporating the axial-bending coupling effects. For instance, beam structures used in the construction industry with channel, Tee, angle and other cross-sections that have non-coincident centroid and shear centre will inevitably exhibit coupling between the axial and bending deformations during their free and/or forced vibratory motions. Paradoxically some of these cross-sections with smaller dimensions are used as stiffeners attached to the skins, spars and ribs of aircraft wings. It is rather surprising that the literature covering the free and forced vibration behaviour of axial-bending coupled beams is scarce despite the considerable importance of the topic, the purpose of this chapter is to fill this gap.

9.2 Literature review

A sample of published papers that are available in the literature and somehow relevant to this chapter is reviewed in chronological order. Yigit and Christoforou [83] studied the transverse vibration of an oil-well drill string by modelling it as a slender axial-bending coupled beam with its lower portion simply-supported. They used an assumed modes method when deriving the governing differential equations of motion of the axial-bending coupled beam which included the non-linear coupling terms. Han and Benaroya [84] investigated the coupled transverse-axial vibration of a compliant tower modelled as a beam with a concentrated mass at the free end. They formulated the problem using nonlinear coupled theory but concluded that the linear theory could be adequate even when the axial motion was no longer negligible. Trindade et al [85] examined the non-linear vibration of a drill-string modelled by a vertical slender cylinder, clamped in its upper extreme, pinned in its lower extreme and constrained inside the outer cylinder in its lower portion. They applied the Karhunen-Loeve decomposition to simulate the dynamics of the system and emphasized the importance of including the axial-bending coupling terms when studying the vibration characteristics of drill-strings. A couple of years later Sampaio et al [86] published a related paper in which they used a geometrically non-linear model to simulate the axial-torsional coupled vibration of drill-strings. By contrast, Ginsberg [87] considered the axial-transverse vibration of a beam by introducing different amounts of coupling between the axial and transverse displacements through suitable choice of the boundary condition. The manipulation of the boundary conditions was achieved by employing a simple support at one end of the beam and a tilted roller support at the other when carrying out the analysis to obtain the natural frequencies, mode shapes and the forced response of the beam. Lenci and Rega [88] provided a detailed account of the axial-transverse coupled vibration of Timoshenko beams with arbitrary slenderness and axial boundary conditions by using an asymptotic method. They highlighted both the nonlinear and linear behaviour of the axial-transverse coupled Timoshenko beams. Lei et al [89] investigated the dynamic properties of a two-layered axial-bending coupled Timoshenko beam for which the mass and stiffness distributions through the thickness of the beam cross-section were non-uniform. Later Ni and Hua [90] extended the work of Lei et al [89] to include multi-layered beams with arbitrary boundary conditions when carrying out the coupled axial-bending vibration analysis. Different, but related research on advanced beam theories has also been reported in the literature. For instance, Carrera and his colleagues [91] have used a unified formulation, called Carrera Unified Formulation (CUF) in the literature, which has the capability to capture the axial-bending coupling of a beam when the shear centre and the centroid of its cross-section are not coincident. On the other hand, based on a three-dimensional approach, Lee and McClure [92] have used finite element method to analyse an L section beam undergoing large elasto-plastic deformation. No one appears to have made any attempt to solve the free vibration problem of axial-bending coupled beams by using the dynamic stiffness method (DSM) which is well known for its accuracy and computational efficiency [32, 93, 94]. The purpose of this chapter is to fill this gap in the literature. Starting from the derivation of the governing differential equations of motion, the dynamic stiffness matrix of an axial-bending coupled beam is developed. The resulting dynamic stiffness matrix is exploited through the application of the Wittrick-Williams algorithm [23] as solution technique to compute the natural frequencies and mode shapes of an illustrative example of axial-bending coupled beam for various boundary conditions. The results are contrasted with those obtained from the classical beam theory which ignores the axial-bending coupling effects.

9.3 Theoretical development

The dynamic stiffness matrix of a beam element coupled in axial and bending deformations is derived in the following steps by using linear small deflection theory. First the governing differential equations of motion in free vibration of the beam and the associated natural boundary conditions are derived using Hamilton's principle. Next the governing differential equations are solved in an exact sense so that the solutions representing the displacements and forces are expressed in explicit analytical (algebraic) form. Finally, through an algebraic procedure, the frequency-dependent dynamic stiffness matrix of the axial-bending coupled beam is formulated by applying the boundary conditions for the amplitudes of displacements and forces at the ends of the beam so that the force-displacement relationship is achieved for the harmonically vibrating beam to enable free vibration analysis of such beams and their assembles to be made.

9.3.1 Derivation of the governing differential equations of motion and natural boundary conditions

Figure 9.1 shows in a right-handed Cartesian coordinate system, the notation and geometrical parameters of a uniform axial-bending coupled beam of length L exhibiting free natural vibration in the YZ plane with Y-axis coinciding with the beam axis. The coupling between axial and bending displacements essentially occurs due to non-coincident centroid and shear centre denoted by the letters G_c and E_s respectively, as shown. The mass axis and the elastic axis of the beam which are respectively the loci of the centroid and shear centre of the beam cross-section are separated by a distance z_α as shown. Note that the inverted T-section shown in Figure 9.1 is only for convenience and the theory developed in this chapter can be applied to other cross-sections which exhibit coupling between axial and bending deformation in a 2D plane. A carefully selected sample of such cross-sections is shown in Figure 9.2. The method developed below is focused on axial-bending coupling only and other forms of couplings arising from shear, torsion and warping effects are not included in the theory. The principal assumptions made are those of linear small deflection theory and also that the cross section of the beam is singly symmetric. In the formulation, the contributions of shear stress and transverse normal stress are assumed to be small and hence neglected in the analysis. The beam deforms only in one plane and any form of non-linearity arising from large deflections and/or geometric stiffness due to the presence of any axial load is not considered in this chapter, but interested readers are referred to [83–85] which provide useful information on the development of non-linear beam models.

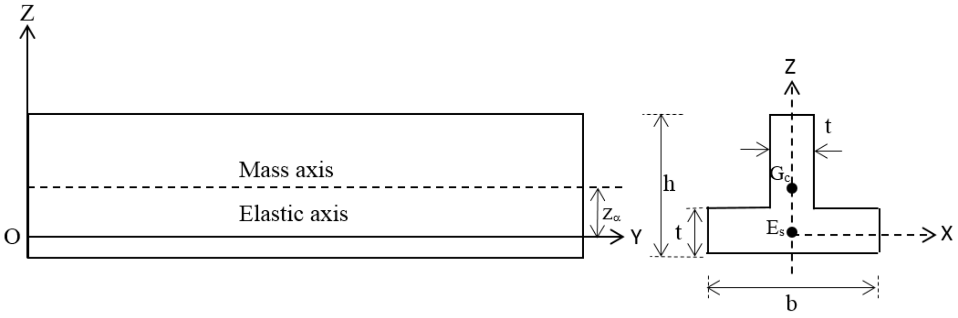

Figure 9.1: Coordinate system and notation for an axial-bending coupled beam. G_c : Centroid, E_s : Shear centre.

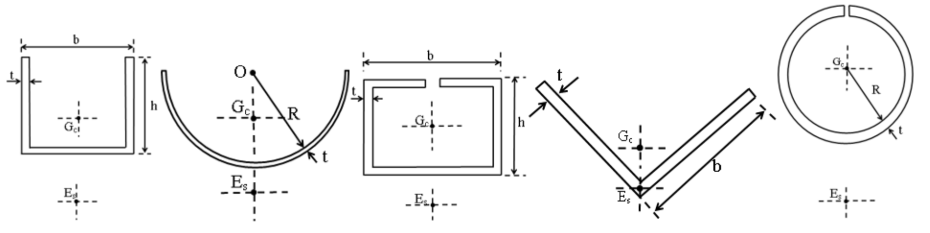

(a) Channel (b) Semi-Circle (c) Open Box (d) Angle (e) Open-Circle

Figure 9.2: Samples of beam cross sections with non-coincident centroid and shear centre.

If v, w and θ are axial displacement, bending displacement and bending rotation of a point at a distance y from the origin and at a height z from the elastic axis, i.e. the point (y, z) in the coordinate system (Figure 9.1), one can write

$$v = v_0 - z w_0{}', \quad w = w_0 \tag{9.1}$$

where v_0 and w_0 are the corresponding displacement components of the point (y, 0) on the Y-axis (i.e. the elastic axis) and a prime denotes differentiation with respect to y. (Note that v and v_0 represent the displacement components and must not be confused with the velocity.)

Using linear, small deflection elasticity theory, the expression for the strain ε_y in the Y-direction can be expressed as

$$\varepsilon_y = v_0{}' - z w_0{}'' \tag{9.2}$$

The potential or strain energy of the beam is given by

$$U = \frac{1}{2}\int_0^L \int_A E\varepsilon_y^2 dA dy \tag{9.3}$$

where E is the Young's modulus of the beam material and the integrations are carried out over the beam cross-sectional area A and length L. Note that the effect of shear deformation is assumed to be small and hence, neglected in the analysis.

Substituting ε_y from Equation 9.2 into Equation 9.3, and integrating over the beam cross-section, we obtain

$$U = \frac{1}{2}\int_0^L EA[v_0{}']^2 - 2EAz_\alpha v_0{}' w_0{}'' + EI_e[w_0{}'']^2 dy \tag{9.4}$$

where A and I_e are the area of cross-section and second moment of area about the elastic axis so that EA and EI_e are the extensional and bending stiffnesses of the beam, respectively.

The kinetic energy of the beam is given by

$$T = \frac{1}{2}\int_0^L \int_A \rho\left\{(\dot{v})^2 + (\dot{w})^2\right\} dy \tag{9.5}$$

where ρ is the density of the beam material and an over dot represents differentiation with respect to time t.

Equation 9.5 with the help of Equation 9.1 becomes

$$T = \frac{1}{2}\int_0^L \left\{\rho A(\dot{v}_0)^2 - 2\rho A z_\alpha \dot{v}_0 \dot{w}_0' + \rho I_e\left(\dot{w}_0'\right)^2 + \rho A(\dot{w}_0)^2\right\} dy \tag{9.6}$$

Hamilton's principle states

$$\delta \int_{t_1}^{t_2} (T - U) dt = 0 \tag{9.7}$$

where t_1 and t_2 are the time interval in the dynamic trajectory, and δ is the usual variational operator.

The governing differential equations of motion for the axial-bending coupled beam and the associated boundary condition in free vibration can now be derived by substituting the potential (U) and kinetic (T) energy expressions of Equations 9.4 and 9.6 into Equation 9.7, using the δ operator, integrating by parts and then collecting terms. In an earlier publication, the entire procedure to generate the governing differential equations of motion and natural boundary conditions for bar or beam type structures was automated by Banerjee et al [22] by applying symbolic computation. In this way, the governing differential equations of motion of the axial-bending coupled beam and the associated natural boundary conditions are obtained as follows. *Governing differential equations:*

$$EAv_0'' - EAz_\alpha w_0''' - \rho A\ddot{v}_0 + \rho A z_\alpha \ddot{w}_0' = 0 \tag{9.8}$$

$$EI_e w_0'''' - EAz_\alpha v_0''' + \rho A\ddot{w}_0 + \rho A z_\alpha \ddot{v}_0' - \rho I_e \ddot{w}_0'' = 0 \tag{9.9}$$

Natural boundary conditions: Axial force:

$$F = -EAv_0' + EAz_\alpha w_0'' \tag{9.10}$$

Bending moment:

$$M = -EI_e w_0'' + EAz_\alpha v_0' \tag{9.11}$$

Shear force:

$$S = EI_e w_0''' - EAz_\alpha v_0'' + \rho A z_\alpha \ddot{v}_0 - \rho I_e \ddot{w}_0' \tag{9.12}$$

Assuming harmonic oscillation with circular or angular frequency ω rad/s, one can write

$$v_0 = Ve^{i\omega t}, \qquad w_0 = We^{i\omega t} \tag{9.13}$$

where V and W are the amplitudes of the axial and bending displacements, respectively. Substituting Equation 9.13 into Equations 9.8 and 9.9 and introducing the non-dimensional length $\xi = y/L$ and the differential operator $D = \frac{d}{d\xi}$, yield the following ordinary differential equations in V and W

$$\left(\omega^2\rho A + \frac{EA}{L^2}D^2\right)V - \left(\frac{\omega^2\rho A z_\alpha}{L}D + \frac{EAz_\alpha}{L^3}D^3\right)W = 0 \tag{9.14}$$

$$\left(\frac{\omega^2\rho A z_\alpha}{L}D + \frac{EAz_\alpha}{L^3}D^3\right)V + \left(\omega^2\rho A - \frac{\omega^2\rho I_e}{L^2}D^2 - \frac{EI_e}{L^4}D^4\right)W = 0 \tag{9.15}$$

It is now possible to eliminate either V or W from Equations 9.14 and 9.15 to give the following sixth order ordinary differential equation which is identically satisfied by both V and W.

$$\left(D^6 + a_1 D^4 + b_1 D^2 - c_1\right)H = 0 \tag{9.16}$$

where

$$H = V \;\; or \;\; W \tag{9.17}$$

and

$$a_1 = \frac{\left\{a^2 + b^2\left(r_0^2 - 2\mu^2\right)\right\}}{1 - \frac{b^2\mu^2}{a^2}}; \quad b_1 = \frac{b^2\left\{a^2\left(r_0^2 - \mu^2\right) - 1\right\}}{1 - \frac{b^2\mu^2}{a^2}}; \quad c_1 = \frac{a^2b^2}{1 - \frac{b^2\mu^2}{a^2}} \tag{9.18}$$

with

$$a^2 = \frac{\rho A\omega^2 L^2}{EA}; \quad b^2 = \frac{\rho A\omega^2 L^4}{EI_e}; \quad r_0^2 = \frac{I_E}{AL^2} = \frac{a^2}{b^2}; \quad \mu^2 = \frac{z_\alpha^2}{L^2} \tag{9.19}$$

By assuming the solution in the form $H = e^{\lambda\xi}$ where λ is a constant, yet to be determined, the characteristic or auxiliary equation of the differential equation, Equation 9.16 can be expressed as

$$\lambda^6 + a_1\lambda^4 + b_1\lambda^2 - c_1 = 0 \tag{9.20}$$

The polynomial equation, Equation 9.20 can be reduced to a cubic and solved analytically using standard procedure [107]. By taking the square root of the three roots of the cubic, which could be real or complex, the six roots $r_j \quad (j = 1,\ 2, \cdots,\ 6)$ of the characteristic or auxiliary equation Equation 9.20 can be computed leading to the solutions of the differential equation, Equation 9.16 as:

$$V(\xi) = \sum_{j=1}^{6} R_j e^{r_j\xi}; \qquad W(\xi) = \sum_{j=1}^{6} Q_j e^{r_j\xi} \tag{9.21}$$

where R_j and Q_j $(j = 1,\ 2, \cdots, 6)$ are two sets of different constants which can be related to each other by using Equations 9.14 and 9.15. The relationship between R_j and Q_j is obtained as:

$$Q_j = \alpha_j R_j \tag{9.22}$$

where

$$\alpha_j = \frac{\mu b^2 r_j\left(a^2 + r_j^2\right)}{a^2\left\{r_j^4 - b^2\left(1 - r_0^2 r_j^2\right)\right\}} \tag{9.23}$$

The constant vectors **Q** and **R** can be written as:

$$\mathbf{Q} = [Q_1\ Q_2\ Q_3\ Q_4\ Q_5\ Q_6]^T; \qquad \mathbf{R} = [R_1\ R_2\ R_3\ R_4\ R_5\ R_6]^T \tag{9.24}$$

where the upper suffix T denotes a transpose.
The amplitude of the bending rotation in terms of R_j is:

$$\Theta = \frac{dW}{dy} = \frac{1}{L}\frac{dW}{d\xi} = \frac{1}{L}\sum_{j=1}^{6} r_j\alpha_j R_j e^{r_j\xi} \tag{9.25}$$

The amplitudes of the axial force (F), shear force (S) and bending moment (M) are obtained in terms of R_j using Equations 9.10-9.13 and Equations 9.18 and 9.19 as

$$F = -\frac{EA}{L}\left(\frac{dV}{d\xi} - \mu\frac{d^2W}{d\xi^2}\right) = -\frac{EA}{L}\sum_{j=1}^{6} r_j\left(1 - \mu\alpha_j r_j\right) R_j\, e^{r_j\xi} \tag{9.26}$$

$$\begin{aligned} S &= \frac{EI}{L^3}\left(\frac{d^3W}{d\xi^3} + b^2 r_0^2 \frac{dW}{d\xi} - \frac{\mu b^2}{a^2}\frac{dV}{d\xi} + \mu b^2 V\right) \\ &= \frac{EI}{L^3}\sum_{j=1}^{6}\left\{\alpha_j r_j\left(r_j^2 + b^2 r_0^2\right) - \mu\left(b^2 + \frac{r_j^2}{r_0^2}\right)\right\} R_j\, e^{r_j \xi} \end{aligned} \tag{9.27}$$

$$M = -\frac{EI}{L^2}\left(\frac{d^2W}{d\xi^2} - \frac{\mu}{r_0^2}\frac{dV}{d\xi}\right) = -\frac{EI}{L^2}\sum_{j=1}^{6} r_j\left(\alpha_j r_j - \frac{\mu}{r_0^2}\right)\sum_{j=1}^{6} R_j e^{r_j \xi} \tag{9.28}$$

9.3.2 Dynamic stiffness formulation

The dynamic stiffness matrix of the axial-bending coupled beam can now be formulated by applying the boundary conditions for displacements and forces at the ends of the beam. Referring to the sign convention for positive axial force, shear force and bending moment shown in Figure 9.3, the boundary conditions for displacements and forces, see Figure 9.4, are:

$$At\ \ \xi = 0:\ \ V = V_1;\ \ W = W_1;\ \ \Theta = \Theta_1;\ \ F = F_1;\ \ S = S_1;\ \ and\ \ M = M_1 \tag{9.29}$$

$$At\ \ \xi = 1:\ \ V = V_2;\ \ W = W_2;\ \ \Theta = \Theta_2;\ \ F = -F_2;\ \ S = -S_2;\ \ and\ \ M = -M_2 \tag{9.30}$$

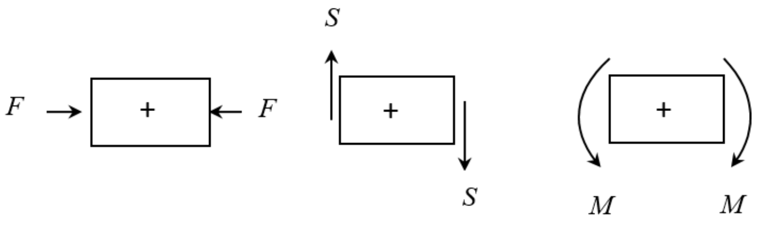

Figure 9.3: Sign convention for positive axial force F, shear force S and bending moment M.

The displacement vector δ and the force vector $\mathbf{P}$ of the beam connecting the ends 1 and 2, see Figure 9.4, can be expressed as:

$$\boldsymbol{\delta} = [V_1\ W_1\ \Theta_1\ V_2\ W_2\ \Theta_2]^T; \qquad \mathbf{P} = [F_1\ S_1\ M_1\ F_2\ S_2\ M_2]^T \tag{9.31}$$

The relationship between the displacement δ and the constant vector $\mathbf{R}$ is now obtained using Equations 9.21-9.23, 9.25 and Equations 9.29-9.30 to give

$$\boldsymbol{\delta} = \mathbf{B}\,\mathbf{R} \tag{9.32}$$

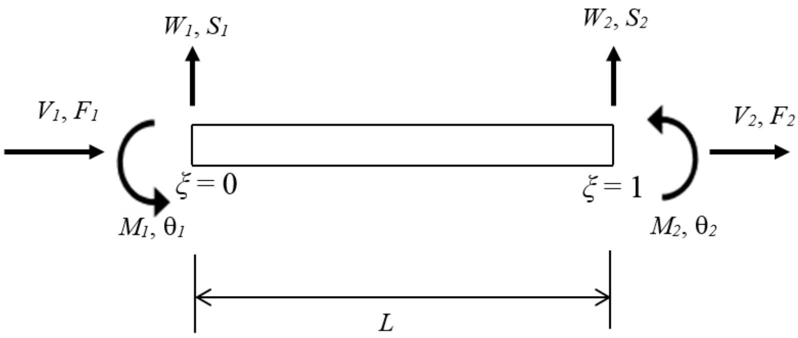

Figure 9.4: Boundary condition for displacements and forces for an axial-bending coupled beam.

where

$$\mathbf{B} = \begin{bmatrix} 1 & 1 & 1 & 1 & 1 & 1 \\ \alpha_1 & \alpha_2 & \alpha_3 & \alpha_4 & \alpha_5 & \alpha_6 \\ r_1\alpha_1/L & r_2\alpha_2/L & r_3\alpha_3/L & r_4\alpha_4/L & r_5\alpha_5/L & r_6\alpha_6/L \\ e^{r_1} & e^{r_2} & e^{r_3} & e^{r_4} & e^{r_5} & e^{r_6} \\ \alpha_1 e^{r_1} & \alpha_2 e^{r_2} & \alpha_3 e^{r_3} & \alpha_4 e^{r_4} & \alpha_5 e^{r_5} & \alpha_6 e^{r_6} \\ r_1\alpha_1 e^{r_1}/L & r_2\alpha_2 e^{r_2}/L & r_3\alpha_3 e^{r_3}/L & r_4\alpha_4 e^{r_4}/L & r_5\alpha_5 e^{r_5}/L & r_6\alpha_6 e^{r_6}/L \end{bmatrix} \tag{9.33}$$

Similarly, the relationship between the force vector **P** and the constant vector **R** is obtained using Equations 9.26-9.30 to give

$$\mathbf{P} = \mathbf{A}\,\mathbf{R} \tag{9.34}$$

where elements of each row of the **A** matrix are indicated by the first of the two subscripts as given below with *j* representing the column number.

$$a_{1j} = -\frac{EA}{L}\left\{r_j\left(1-\mu\alpha_j r_j\right)\right\}; \qquad a_{2j} = \frac{EI}{L^3}\left\{\alpha_j r_j\left(r_j^2+b^2r_0^2\right)-\mu\left(b^2+\frac{r_j^2}{r_0^2}\right)\right\};$$

$$a_{3j} = -\frac{EI}{L^2}\left\{r_j(\alpha_j r_j-\frac{\mu}{r_0^2})\right\}; \;\; a_{4j} = \frac{EA}{L}\left\{r_j\left(1-\mu\alpha_j r_j\right)\right\}e^{r_j}; \tag{9.35}$$

$$a_{5j} = -\frac{EI}{L^3}\left\{\alpha_j r_j\left(r_j^2+b^2r_0^2\right)-\mu\left(b^2+\frac{r_j^2}{r_0^2}\right)\right\}e^{r_j}; \;\; a_{6j} = \frac{EI}{L^2}\left\{r_j(\alpha_j r_j-\frac{\mu}{r_0^2})\right\}e^{r_j};$$

By eliminating the constant vector **R** from Equations 9.32 and 9.34, **P** and δ can now be related to give the dynamic stiffness matrix relationship of the axial-bending coupled beam as

$$\mathbf{P} = \mathbf{K}\,\boldsymbol{\delta} \tag{9.36}$$

where

$$\mathbf{K} = \mathbf{A}\,\mathbf{B}^{-1} \tag{9.37}$$

is the required frequency-dependent dynamic stiffness matrix. It should be noted that the resulting dynamic stiffness matrix **K** of Equation 9.37 will be always symmetric and real [95] with imaginary part of each element being zero although the matrices **A** and **B** are complex and asymmetric. The expanded dynamic stiffness matrix giving the relationship between the amplitudes of the forces to those of the displacements can be expressed in the following way.

$$\begin{bmatrix} F_1 \\ S_1 \\ M_1 \\ F_2 \\ S_2 \\ M_2 \end{bmatrix} = \begin{bmatrix} k_{11} & k_{12} & k_{13} & k_{14} & k_{15} & k_{16} \\ k_{12} & k_{22} & k_{23} & k_{24} & k_{25} & k_{26} \\ k_{13} & k_{23} & k_{33} & k_{34} & k_{35} & k_{36} \\ k_{14} & k_{24} & k_{34} & k_{44} & k_{45} & k_{46} \\ k_{15} & k_{25} & k_{35} & k_{45} & k_{55} & k_{56} \\ k_{16} & k_{26} & k_{36} & k_{46} & k_{56} & k_{66} \end{bmatrix} \begin{bmatrix} V_1 \\ W_1 \\ \Theta_1 \\ V_2 \\ W_2 \\ \Theta_2 \end{bmatrix} \tag{9.38}$$

or

$$\begin{bmatrix} \mathbf{P_1} \\ \mathbf{P_2} \end{bmatrix} = \begin{bmatrix} \mathbf{K_{11}} & \mathbf{K_{12}} \\ \mathbf{K_{21}} & \mathbf{K_{22}} \end{bmatrix} \begin{bmatrix} \boldsymbol{\Delta_1} \\ \boldsymbol{\Delta_2} \end{bmatrix} \tag{9.39}$$

where $\mathbf{K_{11}}$, $\mathbf{K_{12}}$, $\mathbf{K_{21}}$ and $\mathbf{K_{22}}$ are all submatrices of order 3×3 each and $\mathbf{P_1}$ and $\mathbf{P_2}$ are force vectors of node 1 (left-hand end) and node 2 (right-hand end) and $\boldsymbol{\Delta_1}$ and $\boldsymbol{\Delta_2}$ are the corresponding displacement vectors, respectively.

The above frequency dependent dynamic stiffness matrix **K** can now be used to compute the natural frequencies and mode shapes of either an individual axial-bending coupled beam, or an assembly of axial-bending coupled beams for different boundary conditions. A reliable and accurate method of solving the eigenvalue problem is to apply the Wittrick-Williams algorithm [23] which is well suited for the DSM applications. The algorithm uses the Sturm sequence property of the dynamic stiffness matrix and ensures that no natural frequencies of the structure analysed are missed.

9.4 Results and discussion

The dynamic stiffness theory developed above is now applied to investigate the free vibration behaviour of a carefully chosen axial-bending coupled beam. The beam has a channel cross-section as shown in Figure 9.2(a). Four classical boundary conditions of the beam are investigated, which are clamped-free (C-F), pinned-pinned (P-P), clamped-pinned (C-P) and clamped-clamped (C-C).

The dimensions for the channel section, see Figure 9.2(a), are taken as: width (b) = 10 cm, height (h) = 10 cm and thickness (t) = 0.5 cm. The length of the beam is taken to be

1 m. The material used is steel with Young's modulus E = 200 GPa and density ρ =7850 kg/m^3. When preparing data, the stiffness, mass and other geometrical properties of the channel section are calculated as follows:

(i) Axial stiffness (EA) = 2.9×10^8 N, (ii) Bending stiffness (EI_e) = 1.965×10^6 Nm^2, (iii) Mass per unit length (ρA) = 11.383 kg/m, (iv) Rotatory inertia per unit length (ρI_e) = 0.07713 kgm and (iv) Elastic axis off-set from the mass axis (z_α) = 0.075616 m. Based on these data and referring to Figure 9.2(a), it can be ascertained that the elastic axis and mass axis are respectively 0.090356 m and 0.01474 m below the mid-length of the sides with height h. It should be noted that the nature of the coupling in inertial only and the stiffness coupling is ignored in the model.

The first five natural frequencies of the beam using the present theory are shown in Table 9.1 together with the corresponding results computed by using the classical beam theory for C-F, P-P, C-P and C-C boundary conditions. It should be noted that when computing results to simulate the classical beam theory as a degenerate case of the present theory, the elastic axis off-set from the mass axis (z_α) was set to a small number close to zero (typically of the order of 10^{-6}) in order to avoid numerical overflow and the bending stiffness for the input data was recalculated about the centroidal axis to give EI_g = 3.0689×10^5 Nm^2. The results for the classical beam theory case were further checked up to the accuracy quoted in Table 9.1 by using the results quoted in standard text (for example, see page 278 of [96]). These were also checked with the help of the computer program published by Williams and Howson [60] who used the traditional uncoupled classical beam theory when applying the dynamic stiffness method. The discrepancies in the result for the five natural frequencies between the classical beam theory and the present theory are shown in Table 9.1 for each set of the boundary conditions. The percentage difference is given relative to the present theory. Clearly, unacceptably large errors can incur due to using the classical beam theory as shown in the table.

In order to confirm the correctness of the natural frequencies shown in Table 9.1 additional checks has been performed due to the absence of comparative results in the literature. This was carried out by using the individual elements of the dynamic stiffness matrix of Equations 9.38 and 9.39 and imposing the necessary boundary conditions. For instance, the determinant formed by the matrix $\mathbf{K_{11}}$ (or $\mathbf{K_{22}}$) of Equation 9.38 was set to zero to represent the cantilever boundary condition (C-F) and the determinant value was then computed for a wide range of frequencies. The zeroes of the determinant established the natural frequencies of the cantilever beam as an alternative method without resorting to the Wittrick-Williams algorithm [23] as solution technique. The latter of course, is robust and has a much wider applicability. For instance, a non-uniform axial-bending coupled beam or a framework consisting of several axial-bending coupled beams can be modelled as an assembly of many uniform axial-bending coupled beams to form the overall dynamic stiffness matrix of the final structure to which the Wittrick-Williams algorithm can be applied to compute the natural frequencies and mode shapes in a straightforward manner. This cannot be easily accomplished by using the determinant method. An illustrative example of the determinant plot for the above C-F beam is shown in Figure 9.5 where its first two natural frequencies are identified at 575.85 rad/s (91.65 *Hz*) and 3557.2 rad/s (566.15 *Hz*), respectively by tracking the zeroes of the determinant $|\mathbf{K_{11}}|$ when it crosses the horizontal axis representing the frequency. These two natural frequencies agreed completely with the C-F results reported in column 2 of Table 9.1. These results were further checked by imposing the boundary conditions in Equations 9.32-9.33 and Equations 9.34-9.35 and tracking the zeroes of the 6×6 determinant formed by the first three rows of B matrix and the last three rows of A matrix which together essentially represent the cantilever boundary conditions with the left hand end built-in and the right hand end free. Further checks were performed for other boundary conditions, the details of which are not reported here for brevity.

Table 9.1: Natural frequencies of a channel section beam for different boundary conditions using present theory and classical beam theory.

	Natural frequency f_i (Hz)											
	C-F			P-P			C-P			C-C		
Frequency number (i)	Present theory	Classical beam theory	% diff	Present theory	Classical beam theory	% diff	Present theory	Classical beam theory	% diff	Present theory	Classical beam theory	% diff
1	91.65	91.88	0.25	452.65	257.93	75.5	476.49	402.93	18.3	580.88	584.69	0.65
2	566.15	575.84	1.68	801.88	1031.7	22.3	1273.7	1305.8	2.46	1573.7	1611.7	2.36
3	1261.9	1261.9	0.00	1882.3	2321.4	18.9	1951.0	2523.8	22.7	2523.8	2523.8	0.00
4	1550.1	1612.4	3.86	2311.3	2523.8	8.42	2894.8	2724.4	6.25	3005.9	3159.7	4.87
5	2944.6	3159.6	6.80	3793.4	4126.9	8.08	4023.4	4658.8	13.6	4804.5	5047.5	4.81

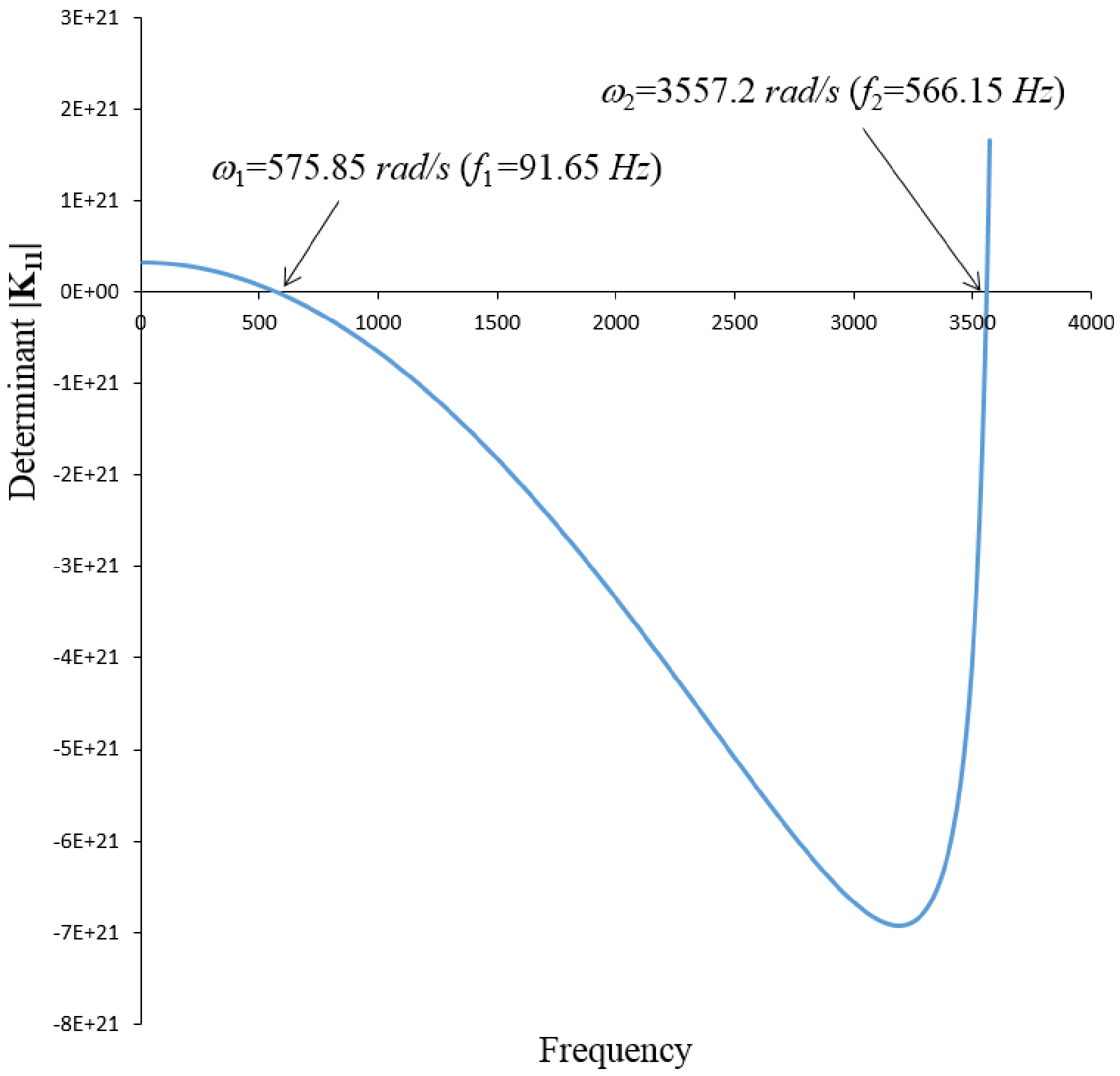

Figure 9.5: Determinant plot of $\mathbf{K}_{11}$ to locate the first two natural frequencies of the cantilever channel section beam.

The mode shapes corresponding to the natural frequencies of Table 9.1 were computed using the present theory and the classical beam theory. Results for the C-F, P-P, C-P and C-C boundary conditions are illustrated in Figures 9.6-9.9, respectively. Clearly the modes generated by the classical beam theory are uncoupled for all cases, as expected. By contrast, the present theory shows substantial coupling between the axial and bending deformation in most of the cases. For the C-F case, the first mode is predominantly bending with very little axial deformation whereas the second, fourth and the fifth modes are heavily coupled. However, the third mode is essentially an axial mode with no bending displacement present. It should be noted that pure axial mode is possible for the C-F boundary condition. This is because the axial inertial forces can be possibly balanced by the elastic forces arising from the axial deformations only without involving any bending deformation. For this C-F boundary conditions, a direct comparison between the results computed by the present theory and the classical beam theory indicates that a relatively small change in the natural frequency due to the application of the two theories, can cause substantial changes in the mode shapes. In particular, the fourth and fifth modes shown in Figure 9.6 are heavily coupled in axial and bending motions when using the present theory, but the percentage differences in the corresponding natural frequencies for these two modes when compared with the classical uncoupled classical beam theory are only around 4% and 7%, respectively. Similar observations were made for other boundary conditions. Interestingly, in an earlier investigation on the free vibration behaviour of twisted beams, it was shown that even a substantial amount of twist (up to 30 degrees) caused very little difference to the natural frequencies, but significant changes to the mode shapes (see Figure 4 of [97]).

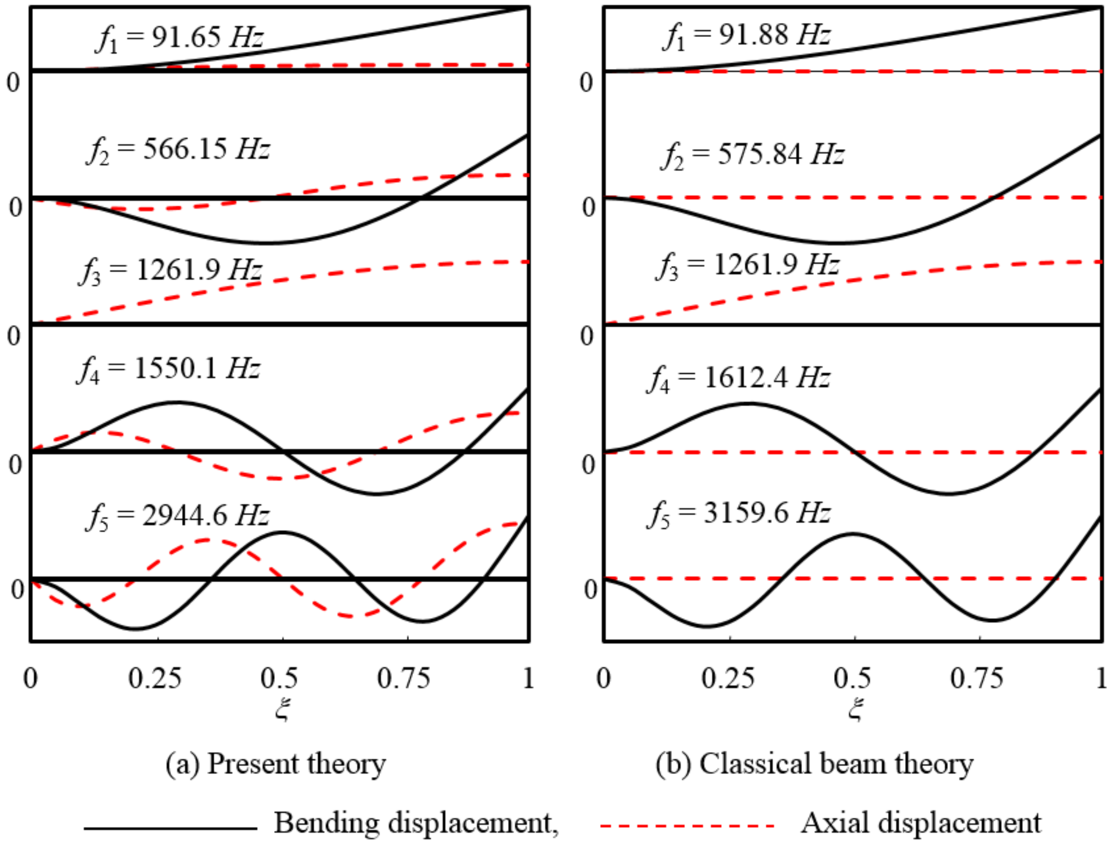

(a) Present theory

(b) Classical beam theory

Figure 9.6: The first five natural frequencies and mode shapes for the channel-section beam using present theory and classical beam theory for cantilever boundary condition.

The results shown in Table 9.1 clearly indicate that the errors incurred in the natural frequencies for the pinned-pinned (P-P) boundary condition of the channel section beam can be very large when applying the classical beam theory as opposed to the present theory.

A percentage error of around 75% in the fundamental natural frequency is astonishing which makes the classical beam theory inapplicable for this type of problem. The coupling arising from different modes of vibration can make huge differences in the natural frequencies when the simple minded classical beam theory is used. For instance, Bishop et al [98] reported 396% error in the second natural frequency when they investigated coupled bending and torsional vibration of uniform beams and compared their results with those obtained from classical beam theory, see Table 3 of their paper. The mode shapes corresponding to the first five natural frequencies of the beam with P-P boundary condition are shown in Figure 9.7 which reveal that unlike the classical beam theory, the present theory yields heavily coupled modes. It should be noted that pure axial modes are not possible for this P-P boundary condition. The absence of pure axial modes and large discrepancies in results between the present theory and the classical beam theory for this case can be attributed to the fact that the pinned support which is applied at the shear centre of the beam (instead of the centroid) prevents both axial and bending deformations but allows bending rotation. Based on the mode shapes shown in Figure 9.7, the following observations can be made. The first and second modes using the present theory and the classical beam theory have some degree of resemblance, but the magnitudes of the natural frequencies are very different and of course, the coupling between the axial and bending deformation is non-existent in the classical beam theory, see Figure 9.7(b). By contrast the third mode computed from the present theory, see Figure 9.7(a), does not seem to have a suitable counterpart computed from the classical beam theory, whereas the fourth mode from the present theory has a natural frequency which is close to the third natural frequency computed from the classical beam theory and the bending deformations for the two cases are similar, but the axial deformation is non-existent in the classical beam theory, as expected. The fifth mode shape for this P-P case resulting from the present theory and the classical beam theory are somehow very different, but the corresponding natural frequencies are not so widely different.

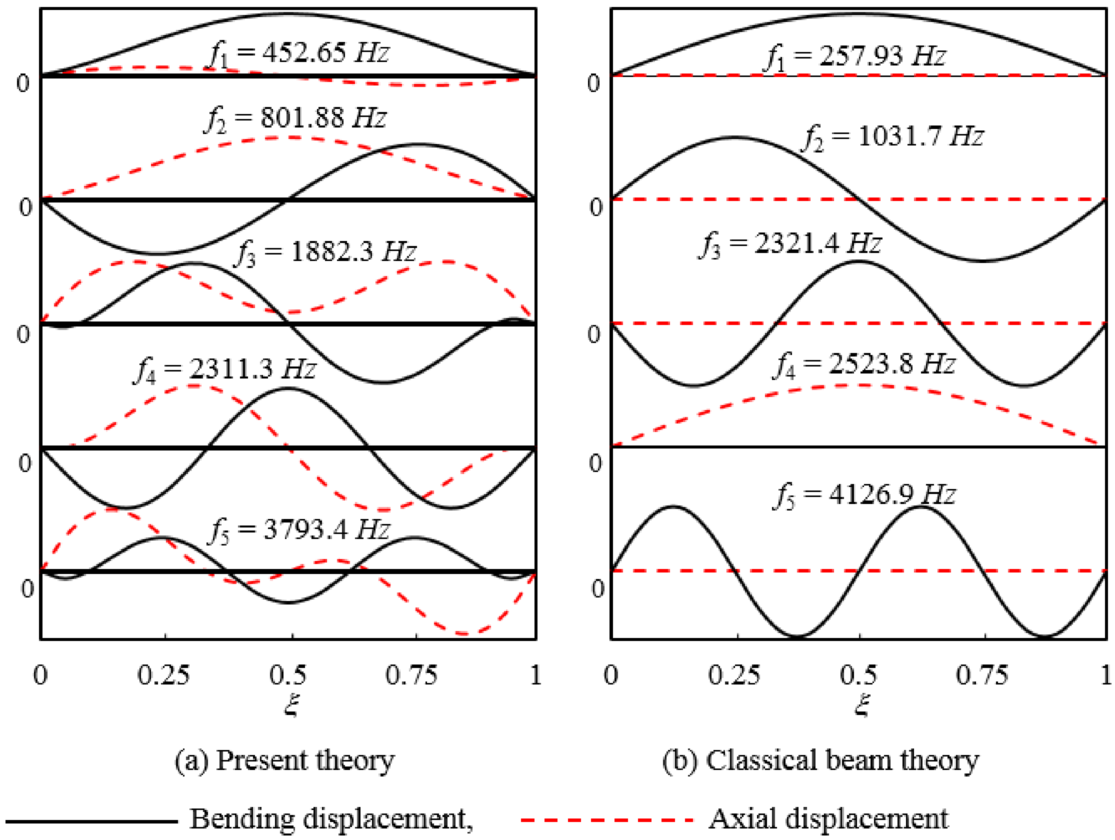

Figure 9.7: The first five natural frequencies and mode shapes for the channel-section beam using present theory and classical beam theory for pinned-pinned boundary condition.

The next set of results comprising the natural frequencies for the clamped-pinned (C-P) boundary conditions using the present theory and the classical beam theory are shown in columns 8 and 9 of Table 9.1, respectively with the percentage differences given in the 10th column. Clearly, the errors due to using the classical beam theory are significant, but not as great as was in the case of P-P boundary condition. The mode shapes for the five natural frequencies for this C-P case are shown in Figure 9.8 which illustrate the presence of substantial coupling between the axial and bending deformation when using the present theory whereas there is no coupling present when using classical beam theory, as expected. Pure axial mode arising from the classical beam theory (third mode of Figure 9.8) is essentially a coupled mode which the present theory is capable to detect. As explained in the previous paragraph, the presence of a pinned support at any end of the beam at its shear centre prevents the occurrence of any pure axial mode when using the present theory.

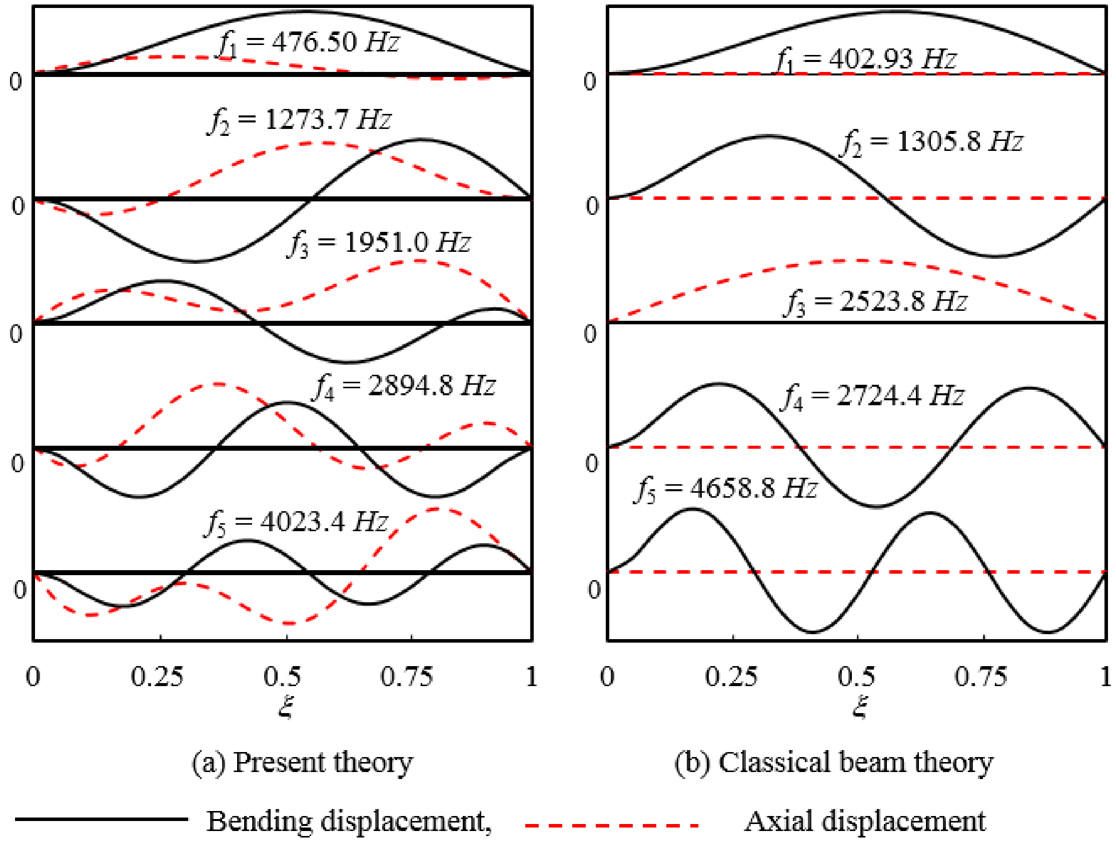

(a) Present theory (b) Classical beam theory

Figure 9.8: The first five natural frequencies and mode shapes for the channel-section beam using present theory and classical beam theory for clamped-pinned boundary condition.

The final set of results was obtained for the clamped-clamped (C-C) boundary conditions for which the first five natural frequencies have already been shown in columns 11 and 12 of Table 9.1 using both the present and classical beam theories. The percentage difference relative to the present theory is shown in the 13^{th} column of the table. The corresponding mode shapes are shown in Figure 9.9 which illustrate substantial coupling between the axial and bending deformations in the first, second, fourth and fifth mode captured by the present theory. The classical beam theory naturally fails to predict such couplings as expected, which is demonstrated by the mode shapes shown in Figure 9.9. The third mode is however, a pure axial mode captured by both theories. It should be recognised that the C-C boundary condition can produce a pure axial mode as was the case with C-F boundary condition. This is because the clamped support at the ends of the beam allows neither bending displacement nor bending rotation which makes it possible for the beam to freely vibrate in the axial direction only as a distinctive case.

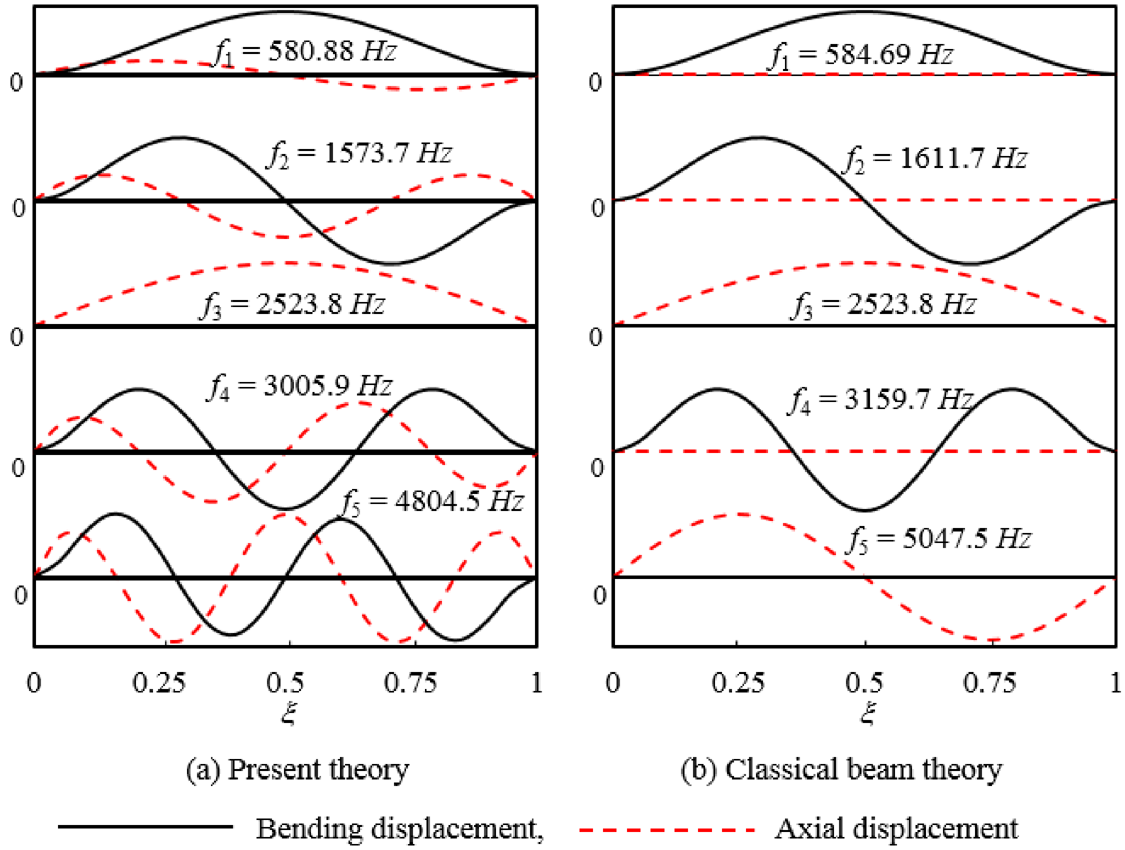

(a) Present theory

(b) Classical beam theory

Figure 9.9: The first five natural frequencies and mode shapes for the channel-section beam using present theory and classical beam theory for clamped-clamped boundary condition.

9.4.1 Further investigation to validate the theory and results

The natural frequencies computed by the dynamic stiffness method developed in this chapter and shown in Table 9.1 were checked by alternative methods which are based on the imposition of boundary conditions for displacements and forces (see Equations 9.21, 9.25 and 9.26-9.28) and subsequently making use of the usual determinant plot, without resorting to the dynamic stiffness method. The zeroes of the determinant gave the same results as the one shown in Table 9.1 based on the dynamic stiffness method and the Wittrick-Williams algorithm [23]. However, it was felt that further checks were necessary to validate the theory and the results. In order to achieve this objective, it has been decided to make use of Carrera Unified Formulation (CUF) for free vibration of beams, which has received wide attention in the literature [91]. In the context of the present research, CUF can capture the axial-bending coupling effect in the free vibration of beams as relevant to the theory of this chapter. Given the complexity of the problem, it was decided that the free-free (F-F) boundary condition of the example problem (channel section beam) given in section 9.4 would be much more convincing than other boundary conditions when validating the theory and results. This is because the F-F boundary condition will make use of all the dynamic stiffness terms unlike other boundary conditions for which some of the stiffness terms will not show up in the calculation as they will be constrained due to the support conditions.

Table 9.2: Natural frequencies of a channel section beam for free-free boundary conditions using present theory and CUF.

Frequency number (i)	Natural frequency f_i (Hz) for F-F boundary condition		
	Present theory	Carrera Unified Formulation	Percentage difference
1*	0	0	0
2*	0	0	0
3*	0	0	0
4	569.9	578.31	-1.48
5	1525.9	1449.8	4.98
6	2523.7	2542.4	-0.74
7	2886.4	2634.7	8.72

$*$Rigid-body mode. The percentage difference is relative to the present theory.

Table 9.2 shows the first seven natural frequencies (including the three zero natural frequencies corresponding to the rigid body modes) of the channel section beam with F-F boundary condition by using both the present theory and the CUF [91]. As can be seen in Table 9.2, the two sets of results agree very well with each other. Relative to the present theory, the percentage differences in the fourth, fifth, sixth and seventh natural frequencies (which represent the elastic modes) are -1.48%, 4.98%, -0.74% and 8.72%, respectively. Checks were also performed for other boundary conditions of the beam which showed similar percentage differences, but these results are not reported here for brevity.

9.5 Conclusions

Axial-bending coupled dynamic stiffness matrix for a beam with non-coincident centroid and shear centre has been developed by deriving the governing differential equations using Hamilton's principle, then solving the equations and finally imposing the boundary conditions. The resulting dynamic stiffness matrix is applied with particular reference to the Wittrick-Williams algorithm to solve the free vibration problems of an illustrative example with substantial coupling between the axial and bending deformation. The natural frequencies and mode shapes for different boundary conditions are compared and contrasted with those obtained from the classical beam theory. It has been shown that the classical beam theory may give unacceptably large errors when investigating the free vibration characteristics of axial-bending coupled beams. The theory and results are also validated using Carrera unified formulation (CUF). The developed dynamic stiffness matrix can be applied to complex structures, including frameworks.

Chapter 10

Principal conclusions and further work

10.1 Principal conclusions

10.1.1 Summary of principal conclusions from Section A

Section A focused on providing an improved understanding of the free vibration and flutter behaviour of both metallic and composite aircraft from an engineering perspective. Initially the theories behind the DSM and the programs used are discussed. Section A also used the dynamic stiffness method based on bending-torsion coupling of an aircraft wing to perform the free vibration and flutter analysis for eight aircraft of three different categories namely, sailplanes, light aircraft trainers and transport airliner. Essentially this section describes the method about estimation of stiffness properties for metallic and composite wings of both single and double cell configurations including the effect of bending torsion coupling parameter for the latter. Interesting case studies were carried out to understand the stiffness properties of metallic and composite wings better. Furthermore, parametric studies were carried out to understand the effect of stiffness properties, engine mass and its position and finally fuselage mass and its inertia on free vibration and flutter analysis. The dynamic stiffness method applied the Wittrick-Williams algorithm as a solution technique and various programs were developed to carry out the free vibration and flutter analysis. The theories behind these have been discussed in detail in Section A. Also during the course of investigation in Section A, analysis of aircraft wing and whole aircraft configuration are carried out to establish stiffness, free vibration and flutter characteristics.

Some interesting conclusions obtained from Section A are given below.

- One of the main contributions made in Section A is essentially in terms of the results computed for eight high aspect ratio aircraft from three different categories using dynamic stiffness method. Design curves have been generated and significant findings of the results showing trends to facilitate aircraft design in an aeroelastic context.

- Both metallic and composite wing has been analysed. Bending–torsional material coupling, which is not possible in metallic wing, can be varied on the composite wing to achieve desired aeroelastic effect. Also, by varying ply orientations and by using double cells improved results can be achieved.
- The geometric features such as cut-outs, sweep, taper ratio, flexible ribs in the 3D of the wing box have significant effect on the *GJ* results, especially taper along the wing planform contribute more to the torsional stiffness rather than the rest such as manholes, rigidity of ribs and sweep angle.
- It can be ascertained from the computed results that for sailplanes, the variation of *EI* does not affect the flutter speed to any appreciable extent while the flutter speed varies proportional to the change in *GJ*. For light aircraft trainers, the flutter speed varies proportional to both *EI* and *GJ*. For transport airliner, the flutter speed varies inversely proportional to change in *EI* and directly proportional to change in *GJ*. Overall *GJ* variation affects flutter speed more than *EI* variation.

10.1.2 Summary of principal conclusions from Section B

Section B focused on the development of the dynamic stiffness matrix for various engineering applications. This includes functionally graded beams, cracked beams, Rayleigh-Love bar and a Timoshenko beam and coupled axial-bending beam elements. In all these applications, governing differential equations were developed and dynamic stiffness matrix is formulated and the Wittrick-Williams algorithm was applied as a solution technique to extract the natural frequencies and the mode shapes. The derivations are given in detail for each of these engineering applications in the chapters of Section B. The results obtained by using the dynamic stiffness matrix were validated against published journals. However, when no previously published results were available, alternative methods and consistency checks on the reliability of results have been performed. The concept developed in Section B has a wide variety of practical usages and some examples are given. For instance, the theory developed for functionally graded beams can be applied to analyse high-rise building structures made of functionally graded materials which has advantageous mechanical properties of metal and virtuous fire-resistant characteristics of ceramic. The theory for cracked beams can be extended to frame works and other building structures, and within the context of structural health monitoring purposes, the developed theory is expected to be most useful. The subsequent theory developed for Rayleigh-Love and Timoshenko is particularly helpful when carrying out high frequency free vibration analysis of skeletal structures. Additionally, the developed dynamic stiffness matrix for axial-bending coupled beams can be applied to complex structures, including frameworks. Some interesting contributions made in Section B are given below.

- The literature on the free vibration of frameworks containing FGBs is virtually non-existent and chapter 6 addresses this by analysing a portal frame.
- The natural frequencies of intact beam for cantilever boundary condition was available in the existing literature and in chapter 7 natural frequencies of intact beam for simply supported, clamped-pinned and clamped-clamped boundary conditions have been obtained.
- A potential application of the research described in chapter 8 falls within the area of statistical energy analysis for which the knowledge of modal density distributions in the high frequency range is essential.
- It has been shown in chapter 9 that the classical beam theory may give unacceptably large errors when investigating the free vibration characteristics of axial-bending coupled beams.

10.2 Scope for further work

10.2.1 Scope for further work in Section A

- For the cross sectional model used in chapter 3, the stiffness properties evaluated based on 2-D wing box needs to be improved to include manhole and cut-out in the wing.
- There is a wide scope for aeroelastic optimisation studies using composite materials.
- Response to gust and turbulence can be included as an area of considerable research activity.
- The subject of aeroservoelasticity and actively controlled composite wing has wide application and consorted efforts will be needed when extending the present work.
- The results obtained can be verified using different unsteady aerodynamic theories particularly using ‘Doublet lattice’ theory.
- Only high aspect ratio aircraft wing has been considered in the analysis, this can be expanded to include low aspect ratio and delta wings.

10.2.2 Scope for further work in Section B

- Although the dynamic stiffness matrices for a wide range of elements has been developed, there are many more structural elements for which dynamic stiffness matrix has yet to be developed. These includes, rotating metallic and composite beams and other elements as well as micro and nano beam and plate elements.
- On the question of damping, serious and formidable challenges lies ahead.

Appendix A

Programs used in Section A

A.1 Single cell stiffness analysis (example data file)

For single cell box beam analysis of composite beams the program is based on BOXMXES.F. This program gives the stiffness properties such as bending stiffness (EI), torsional stiffness (GJ) and bending-torsion coupling stiffness (K).

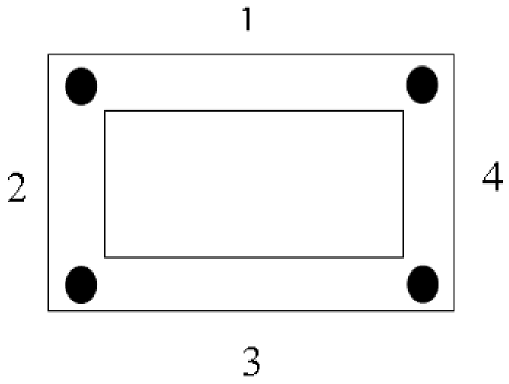

Figure A.1: Single cell box representation.

10 1 2 Line 1

- Number of laminate parts
- 1 – SI units
- 2– Circumferential asymmetric configuration

20 20 20 20 20 20 20 20 Line 2

- 20 – Number of Plies

1.48E11 1.03E10 0.270278 5.93E09 5.93E09 5.93E09 1580 Line 3

- E_1 E_2 V_{12} G_{12} G_{13} G_{23} density

45.0 0.0 -45.0 90.0 -45.0 -45.0 90.0 -45.0 0.0 45.0 Line 4

- Ply orientation

0.183E-3 0.183E-3 0.183E-3 0.183E-3 0.183E-3 Line 5

- Thickness of each ply

0.0 0.0047 0.0795 Line 6

- The x, y, z coordinates of each node

0.476599 0.159 10 Line 7

- Width, depth and total length of the box beam

1.0E6 0.0 5.0E4 0.0 0.0 0.0 Line 8

- In – plane force in X, Y, XY, moment about X, Y, torque applied

0.0173 0.0117 0.00622 0.0277 0.00902 Line 9

- Tensile and compressive strength in fibre direction (1), tensile and compressive strength in fibre direction (2), shear strength in 1-2 direction

A.2 Double cell stiffness analysis (example data file)

For double cell box beam analysis of composite beams the program is based on BOXMXES.F but it is further extended using general theory. This program gives the stiffness properties such as bending stiffness (EI), torsional stiffness (GJ) and bending-torsion coupling stiffness (K).

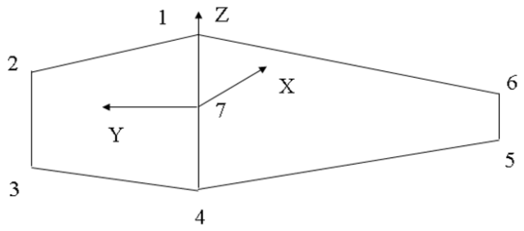

Figure A.2: Double cell box representation.

2 23 1 2 Line 1

- 2 – Double cell
- 23 – Number of laminates
- 1 – SI units
- 2 – Circumferential asymmetric configuration

42 42 42 42 42 42 42 Line 2

- 42 – Number of plies

1.48E11 1.03E10 0.270278 5.93E09 5.93E09 5.93E09 1580 Line 3

- E_1 E_2 V_{12} G_{12} G_{13} G_{23} density

45.0 0.0 45.0 90.0 0.0 0.0 90.0 45.0 0.0 45.0 Line 4

- Ply orientation

0.183E-3 0.183E-3 0.183E-3 0.183E-3 0.183E-3 Line 5

- Thickness of each ply

0.0 -0.7036 0.1457 Line 6

- The x, y, z coordinates of each node

1.976033 0.428196 10 Line 7

- Width, depth and total length of the box beam

1.0E6 0.0 5.0E4 0.0 0.0 0.0 Line 8

- In – plane force in X, Y, XY, moment about X, Y, torque applied

0.0173 0.0117 0.00622 0.0277 0.00902 Line 9

- Tensile and compressive strength in fibre direction (1), tensile and compressive strength in fibre direction (2), shear strength in 1-2 direction

1 18 Line 10

- The upper and lower node number connecting the mid - wall

A.3 COMPCAL input (example data file)

6 Line 1

- 6 – Number of modes to be used

1 2 3 4 5 6 Line 2

- Mode numbers

23.5 Line 3

- Sweep angle in degrees

13 Line 4

- Number of beam elements used to idealise the wing

13 1 Line 5

- 13 – Non – uniform wing, number of beam elements
- 1 – SI unit

1 1.69E+06 1.21E+06 0.001 39.97 2.53 0.53 1.25 Line 6

- Element number, bending stiffness (*EI*), torsional stiffness (*GJ*), coupling stiffness (*K*), mass per unit length, polar mass moment of inertia, projection of element length on X – axis and Y - axis

1 Line 7

- Number of nodes with lumped mass

10 3110.0 3076.22 21597.34 Line 8

- Node, lumped mass, rotatory inertia, torsional inertia

1 0.70 -0.070 Line 9

- Node number, semi – chord, elastic axis position

1 Line 10

- Modal analysis as well as flutter analysis

40.0 2.0 250.0 Line 11

- Starting frequency, increment, maximum frequency in rad/s

310.0 2.0 500.0 Line 12

- Starting air speed, increment, maximum air speed in m/s

1 1 Line 13

- 1 - Data group given in lines 11 and 12 are used in flutter analysis
- 1 – user specified accuracy needed for flutter speed only

0.5 0.5 Line 14

- Tolerance deviations for flutter frequency and flutter speed

2 Line 15

- Print flutter speed, flutter frequency, natural frequency, normal modes, real and imaginary parts of the flutter determinants

A.4 CALFUNB input (example data file)

6 Line 1

- 6 – Number of modes to be used

1 2 3 4 5 6 Line 2

- Mode numbers

23.5 Line 3

- Sweep angle in degrees

13 Line 4

- Number of beam elements used to idealise the wing

13 1 Line 5

- 13 – Non – uniform wing, number of beam elements
- 1 – SI unit

1 1.69E+06 1.21E+06 39.97 2.53 -0.08 0.53 1.25 Line 6

- Element number, bending stiffness (*EI*), torsional stiffness (*GJ*), mass per unit length, polar mass moment of inertia, distance between mass axis and elastic axis, projection of element length on X – axis and Y – axis

1 Line 7

- Number of nodes with lumped mass

10 3110.0 3076.22 21597.34 Line 8

- Node, lumped mass, rotatory inertia, torsional inertia

1 0.70 -0.070 Line 9

- Node number, semi – chord, elastic axis position

1 Line 10

- Modal analysis as well as flutter analysis

40.0 2.0 250.0 Line 11

- Starting frequency, increment, maximum frequency in rad/s

310.0 2.0 500.0 Line 12

- Starting air speed, increment, maximum air speed in m/s

1 1 Line 13

- 1 - Data group given in lines 11 and 12 are used in flutter analysis
- 1 – user specified accuracy needed for flutter speed only

0.5 0.5 Line 14

- Tolerance deviations for flutter frequency and flutter speed

2 Line 15

- Print flutter speed, flutter frequency, natural frequency, normal modes, real and imaginary parts of the flutter determinants

A.5 BIGCALFUN input (example data file)

1.00E+06 1.13E+00 15 14 11 6 48 0 0 0.00 0.33 1 1 0 -2 2 1 Line 1

- Convergence criteria, trail value of the frequency, nodes, elements, real numbers, modes, number of affected degrees of freedom, effect of shear, effect of rotational deformation, shape factor, Poisson's ratio, tail plane, lump mass lines, fin aerodynamics, metallic model and DSM, IPRS, whole analysis

-1 -2 -3 -4 -5 -6 Line 2

- Mode numbers

1 2 1 Line 3

- Connection list, showing the topology of the structure

2.36E07 5.44E08 7.29E+05 27.26 1.68 0.0001 1.0 0.0001 2.10E+06 0.04 Line 4

- EI_{ZZ}, AA, GJ, m/L, I_{alpha}, Z_{alpha}, K, X_{ref}, EI_{XX}, X_{alpha}

-8.15 15.21 0.00 Line 5

- Coordinates of nodes

10000 8654.14 107122.0 525692.0 6597435.0 -424 -290 -2028 -850 1000.0 10000.0 Line 6

- Real numbers

15 1 0 15 2 0 15 3 0 15 4 0 15 5 0 15 6 0 Line 7

- Degrees of freedom affected

11 3110.0 152.63 520.18 0.0 2.47 -0.06 0.91 Line 8

- Node, lumped mass, I_{XX}, I_{YY}, I_{ZZ}, offset$_x$, offset$_y$, offset$_z$

15 15 0 30 23.5 1.225 0.0 0 0 0 0 0 0 0 0 Line 9

- Node number, integration points, rigid body nodes disregarded, number of crossing points , sweep angle, density of air, structural damping, frequency to represents damping, number of undercarriages, IPRT

0 0 0 0 Line 10

- Tail data

0 0 0 0 Line 11

- Fin data

15.21 0.67 -0.001 6.283 -0.5 Line 12

- y coordinate, semi chord, elastic axis location, lift curve slope, distance between aerodynamic centre and mid-chord position in terms of semi chord

0 0 0 0 1 1 0 Line 13

- IFLAG, IFLAG2, IFLAG3, NZI, IDSL, NUNIT, NCM

1 2 2 1 0 Line 14

- IDWU, IQU2, IPOUT, IDVG, IQS

0.1 1.0 Line 15

- CRITW, CRITU

10.0 2.0 100.0 Line 16

- Initial frequency, increment, final frequency

10.0 2.0 100.0 Line 17

- Starting air speed, increment, maximum air speed in m/s

Appendix B

Laminate layup and stacking sequence

Table B.1: Laminate layup and stacking sequences for sections 1-19

SECTION		LAMINATE LAYUP
SECTIONS		
1-3	UPPER SKIN	[45/45/0/45/0/-45/90/-45/90/90]s
	LOWER SKIN	[45/45/0/-45/0/45/90/-45/90/90]s
	FRONT SPAR	[45/0/45/45/-45/0/-45/90/90/-45]s
	REAR SPAR	[45/45/0/45/0/-45/90/90-45/90]s
SECTIONS		
4-7	UPPER SKIN	[45/45/0/45/0/0/-45/-45/90/-45/90/90]s
	LOWER SKIN	[45/45/0/45/-45/0/45/0/90/45/90/90]s
	FRONT SPAR	[45/0/45/45/-45/0/0/-45/90/90/-45/90]s
	REAR SPAR	[45/45/0/45/0/-45/0/-45/90/90/-45/90]s
SECTIONS		
8-11	UPPER SKIN	[45/45/0/45/45/0/0/-45/-45/90/0/-45/90/90]s
	LOWER SKIN	[45/45/0/45/-45/0/45/0/0/90/-45/-45/90/90]s
	FRONT SPAR	[45/0/45/45/45/-45/0/0/-45/90/90/90/-45/90]s
	REAR SPAR	[45/45/0/45/45/0/-45/0/-45/90/90/90-45/90]s
SECTIONS		
12-15	UPPER SKIN	[45/45/0/45/45/0/0/-45/-45/90/0/-45/90/90/90/90/-45/90]s
	LOWER SKIN	[45/45/0/45/45/-45/0/45/0/0/90/-45/-45/90/90/90/-45]s
	FRONT SPAR	[45/0/45/45/45/-45/45/0/0/0/-45/90/90/90/-45/90]s
	REAR SPAR	[45/45/0/45/45/0/45/0/-45/0/-45/-45/90/90/90/-45/90]s
SECTIONS		
16-19	UPPER SKIN	[45/45/45/0/45/45/0/0/-45-45/90/0/-45/-45-90/90/90/-45/90/90/90/-45/90]s
	LOWER SKIN	[45/45/45/0/0/45/45/-45/0/45/0/0/90/-45/45/90/90/90-45]s
	FRONT SPAR	[45/0/45/45/45/-45/45/0/0/0/-45/90/-45/90/-45/90/90/-45/90]s
	REAR SPAR	[45/45/45/0/45/45/0/45/0/0/-45/0/-45/-45/90/90/90/-45/90]s

Table B.2: Laminate layup and stacking sequences for sections 20-26.

SECTION	LAMINATE LAYUP	
SECTIONS 20-22		UPPER SKIN
	1. FRONT BOX	[45/45/45/0/45/45/0/0/-45/-45/90/0/-45/0/-45/-45/90/90/90/-45/90]s
	2. REAR BOX	[45/45/45/0/45/45/0/0/-45/-45/90/0/-45/0/-45/-45/90/90/90/-45/90]s
		LOWER SKIN
	1. FRONT BOX	[45/45/45/0/0/45/45/-45/0/-45/45/0/0/90/-45/-45/90/90/90/90/-45]s
	2. REAR BOX	[45/45/45/0/0/45/45/-45/0/-45/45/0/0/90/-45/45/90/90/90/90/-45]s
	FRONT SPAR	[45/0/45/45/45/-45/45/45/0/0/0/0/-45/90/-45/90/-45/90/90/-45/90]s
	REAR SPAR	[45/45/45/45/0/0/45/45/0/0/-45/-45/0/-45/90/-45/90/-45/90/90/90/90/-45]s
	MIDWALL	[45/45/45/0/45/45/0/45/-45/0/0/0/-45/0/-45/-45/90/90/90/-45/90]s
SECTIONS 23-26		UPPER SKIN
	1. FRONT BOX	[45/45/45/45/0/45/45/0/0/0/-45/-45/90/0/-45/0/-45/-45/90/90/90/-45/90]s
	2. REAR BOX	[45/45/45/45/0/45/45/0/0/0/-45/-45/90/0/-45/0/-45/-45/90/90/90/-45/90]s
		LOWER SKIN
	1. FRONT BOX	[45/45/45/0/0/45/45/-45/0/-45/45/0/0/90/0/-45/-45/90/90/90/90/-45/-45]s
	2. REAR BOX	[45/45/45/0/0/45/45/-45/0/-45/45/0/0/90/0/-45/-45/90/90/90/90/-45/-45]s
	FRONT SPAR	[45/0/45/45/45/-45/45/45/0/45/0/0/0/0/-45/90/-45/90/-45/90/90/-45/90]s
	REAR SPAR	[45/45/45/45/0/0/45/45/0/0/-45/-45/0/-45/-45/90/-45/0/90/90/90/90/-45]s
	MIDWALL	[45/45/45/0/45/45/0/45/-45/0/0/0/-45/0/-45/-45/90/90/-45/90/-45/90/90]s

Appendix C

Geometric representation of parametric case studies

C.1 Case study of uniform wing box

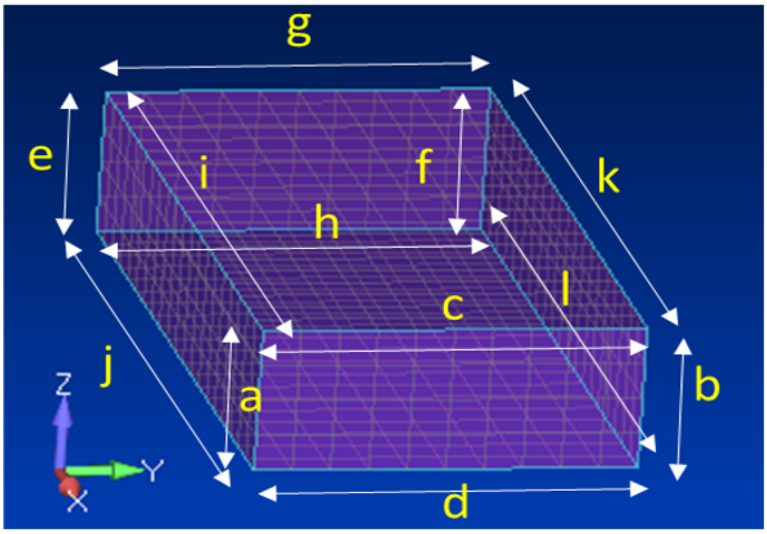

Figure C.1: Case study 1 showing principal dimension of the cross section.

C.2 Case study of uniform wing box – refined mesh

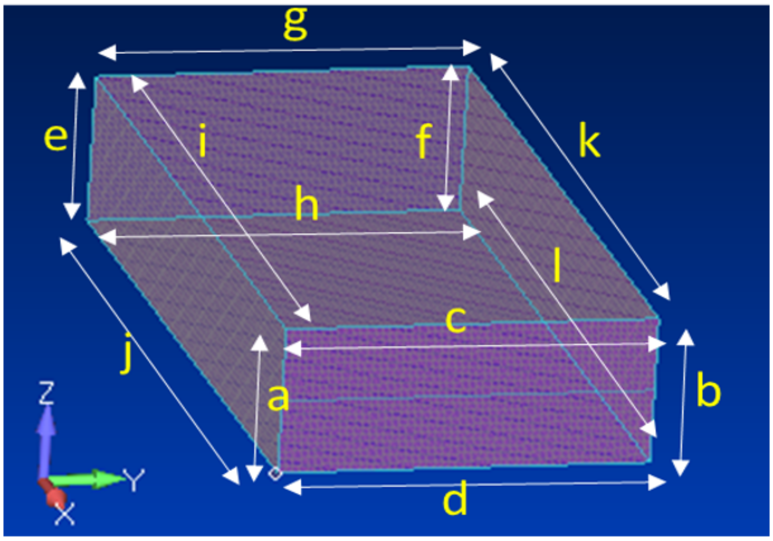

Figure C.2: Case study 2 showing principal dimension of the cross section.

C.3 Case study of non-uniform wing box – symmetry taper

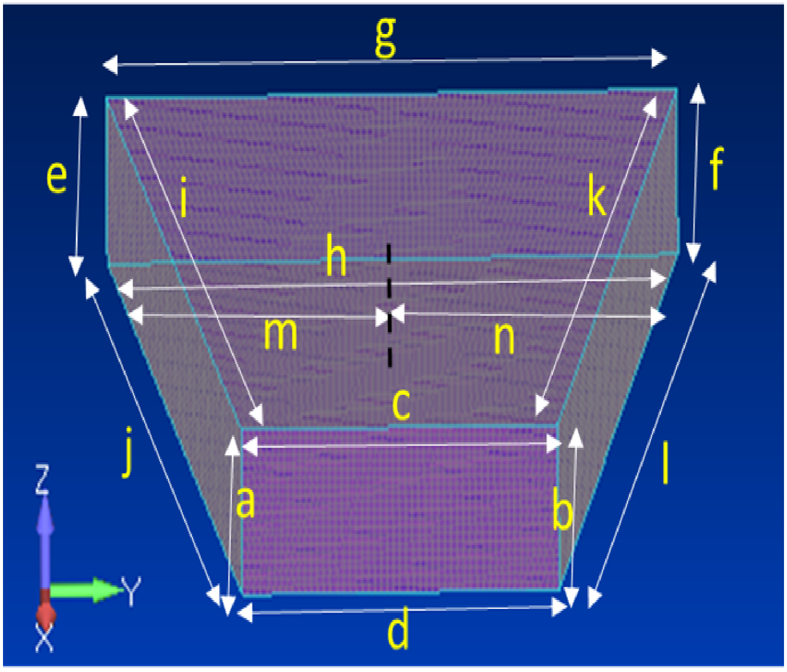

Figure C.3: Case study 3 showing principal dimension of the cross section.

C.4 Case study of non-uniform wing box with taper

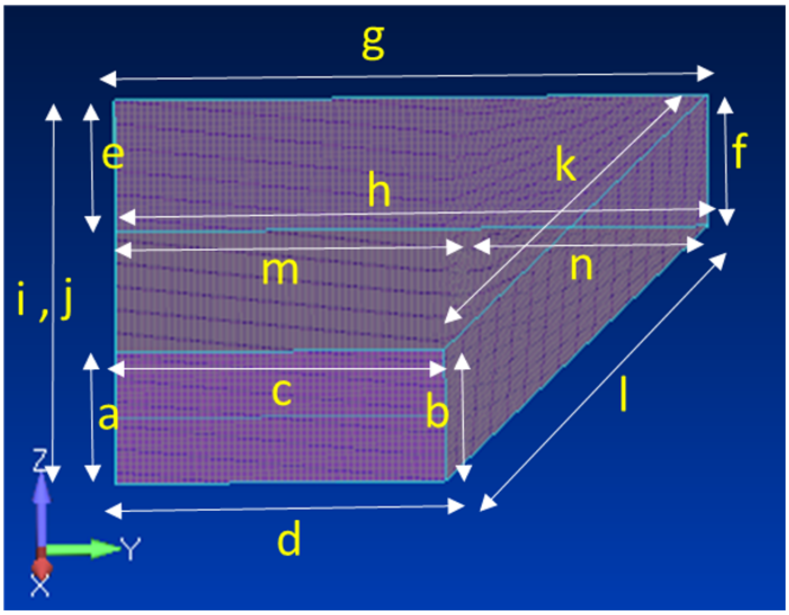

Figure C.4: Case study 4 showing principal dimension of the cross section.

C.5 Case study of trapezoidal wing box

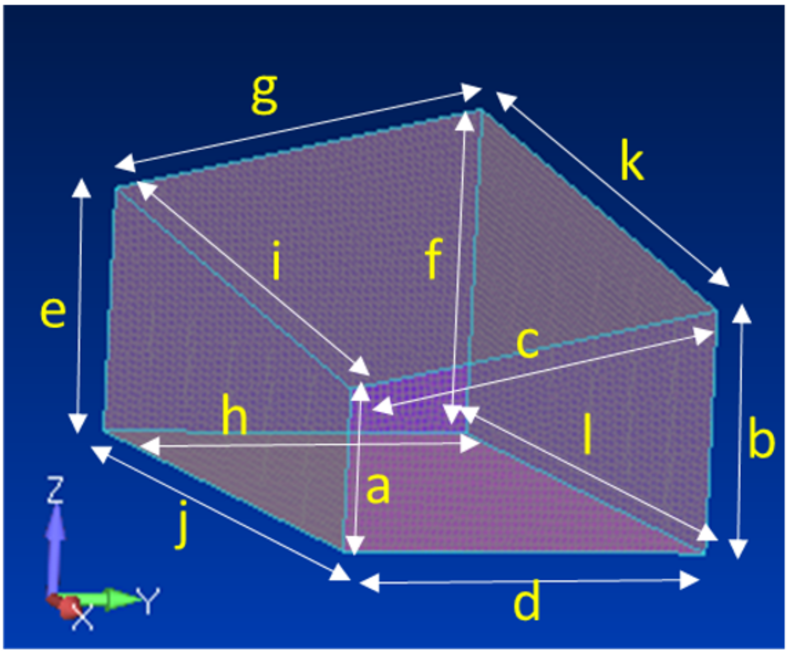

Figure C.5: Case study 5 showing principal dimension of the cross section.

C.6 Case study of trapezoidal wing box – symmetry taper

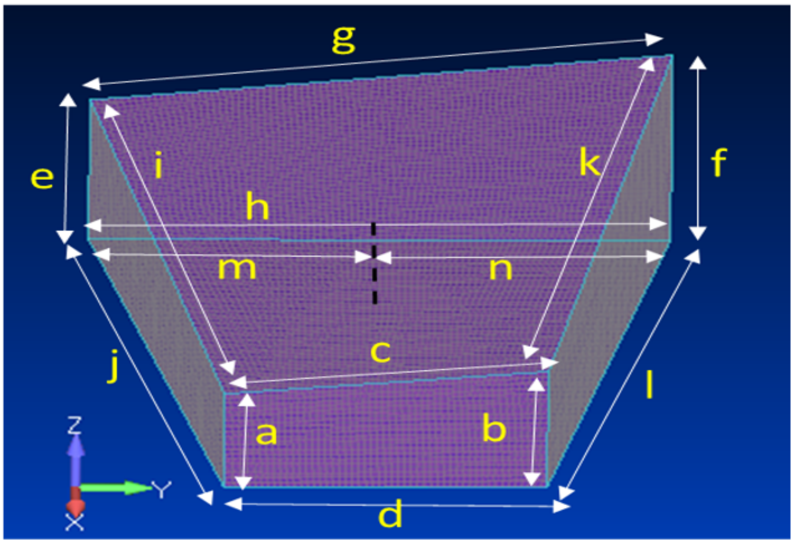

Figure C.6: Case study 6 showing principal dimension of the cross section.

C.7 Case study of trapezoidal wing box – leading edge tapered, trailing edge straight.

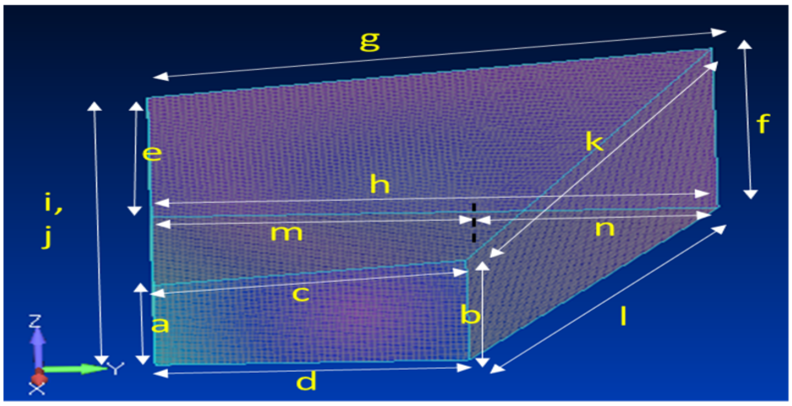

Figure C.7: Case study 7 showing principal dimension of the cross section.

C.8 Case study of wing box with taper

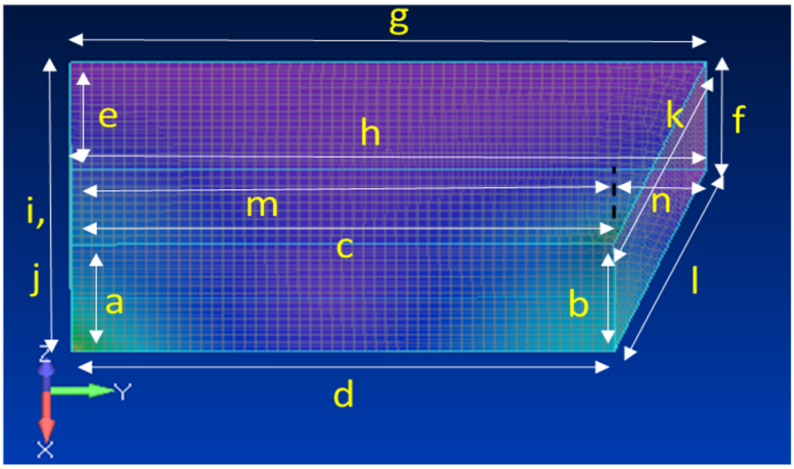

Figure C.8: Case study 8 showing principal dimension of the cross section.

C.9 Case study of wing box model with and without the manhole

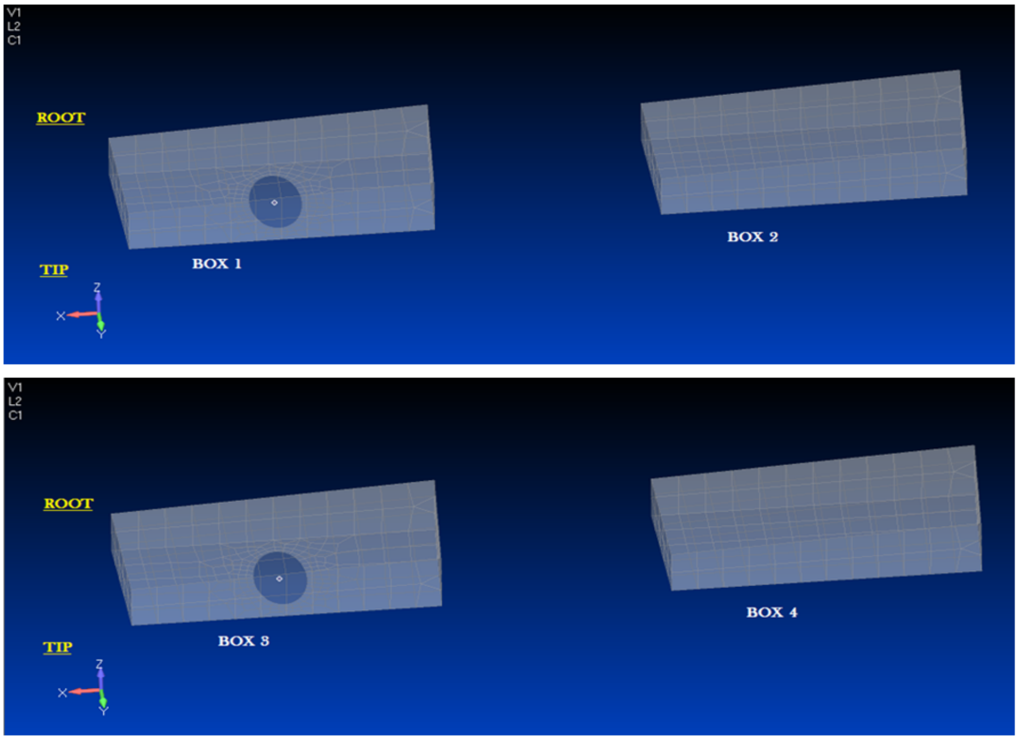

Figure C.9: Illustrations of case study 9a (Box 1), 9b (Box 2), 9c (Box 3), 9d (Box 4).

C.10 Case study of composite wing box showing section 16

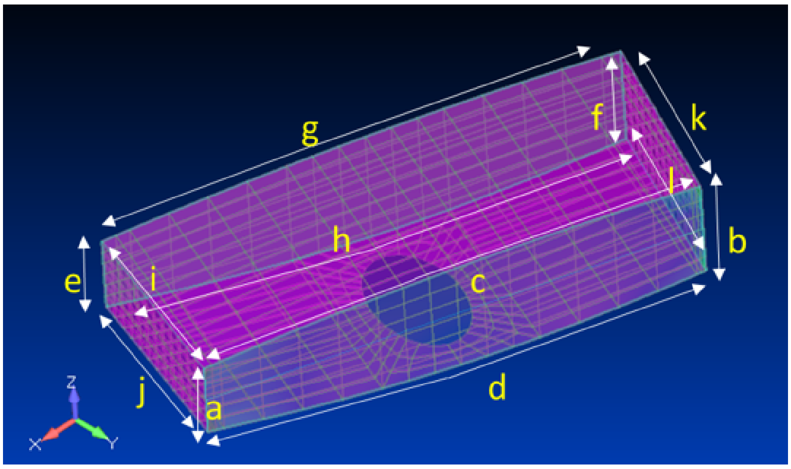

Figure C.10: Case study 10 showing principal dimension of the cross section.

Bibliography

References for Section A

[1] Raymond L Bisplinghoff, Holt Ashley, and Robert L Halfman. *Aeroelasticity*. Courier Corporation, 2013.

[2] Yuan Cheng Fung. *An introduction to the theory of aeroelasticity*. Courier Dover Publications, 2008.

[3] JR Banerjee. “Flutter characteristics of high aspect ratio tailless aircraft”. In: *Journal of Aircraft* 21.9 (1984), pp. 733–736.

[4] JR Banerjee. “Flutter modes of high aspect ratio tailless aircraft”. In: *Journal of Aircraft* 25.5 (1988), pp. 473–476.

[5] J Banerjee et al. “Free vibration and flutter sensitivity analyses of a large transport aircraft”. In: *7th AIAA/USAF/NASA/ISSMO Symposium on Multidisciplinary Analysis and Optimization*. 1998, p. 4765.

[6] V Kolousek. “Berechnung der schwingenden Stockwerkrahmen nach der Deformationsmethode”. In: *Der Stahlbau* 16.5 (1943).

[7] FW Williams and WH Wittrick. “An automatic computational procedure for calculating natural frequencies of skeletal structures”. In: *International Journal of Mechanical Sciences* 12.9 (1970), pp. 781–791.

[8] V Koloušek. “Anwendung des Gesetzes der virtuellen Verschiebungen und des Reziprozitätssatzes in der Stabwerksdynamik”. In: *Archive of Applied Mechanics* 12.6 (1941), pp. 363–370.

[9] WH Wittrick and FW Williams. “A general algorithm for computing natural frequencies of elastic structures”. In: *The Quarterly Journal of Mechanics and Applied Mathematics* 24.3 (1971), pp. 263–284.

[10] WH Wittrick and FW Williams. “An algorithm for computing critical buckling loads of elastic structures”. In: *Journal of Structural Mechanics* 1.4 (1973), pp. 497–518.

[11] JR Banerjee. “The dynamic stiffness method: theory, practice and promise”. In: *Computational Technology Reviews* 11.1 (2015), pp. 31–57.

[12] JR Banerjee. “Coupled bending–torsional dynamic stiffness matrix for beam elements”. In: *International journal for numerical methods in engineering* 28.6 (1989), pp. 1283–1298.

[13] JR Banerjee. “A FORTRAN routine for computation of coupled bending-torsional dynamic stiffness matrix of beam elements”. In: *Advances in Engineering Software and Workstations* 13.1 (1991), pp. 17–24.

[14] JR Banerjee. “Use and capability of Calfun—A program for calculation of flutter speed using normal modes”. In: *Proceedings of the International AMSE Conference on Modelling and Simulation, Athens, Greece*. 1984, pp. 121–131.

[15] JR Banerjee. “User’s guide to the computer program CALFUN (CALculation of Flutter speed Using Normal modes)”. In: *MEAD/AERO Report No. 164*. Department of Mechanical Engineering and Aeronautics, The City University London, 1989.

[16] JR Banerjee and FW Williams. “Free vibration of composite beams-an exact method using symbolic computation”. In: *Journal of Aircraft* 32.3 (1995), pp. 636–642.

[17] JR Bannerjee and FW Williams. “Exact dynamic stiffness matrix for composite Timoshenko beams with applications”. In: *Journal of sound and vibration* 194.4 (1996), pp. 573–585.

[18] Theodore Theodorsen. “General theory of aerodynamic instability and the mechanism of flutter”. In: (1979).

[19] Samuel J Loring. *Use of generalized coordinates in flutter analysis*. Tech. rep. SAE Technical Paper, 1944.

[20] Thomas Henry Gordon Megson. *Aircraft structures for engineering students*. Butterworth-Heinemann, 2016.

[21] Liviu Librescu and Ohseop Song. *Thin-walled composite beams: theory and application*. Vol. 131. Springer Science & Business Media, 2005.

[22] Frank L Matthews and Rees D Rawlings. *Composite materials: engineering and science*. CRC press, 1999.

[23] JR Banerjee, Huijuan Su, and C Jayatunga. “A dynamic stiffness element for free vibration analysis of composite beams and its application to aircraft wings”. In: *Computers & Structures* 86.6 (2008), pp. 573–579.

[24] GA Georghiades and JR Banerjee. “Flutter prediction for composite wings using parametric studies”. In: *AIAA journal* 35.4 (1997), pp. 746–748.

[25] JR Banerjee and FW Williams. “Free vibration of composite beams-an exact method using symbolic computation”. In: *Journal of Aircraft* 32.3 (1995), pp. 636–642.

[26] Terrence A Weisshaar and RJ Ryan. “Control of aeroelastic instabilities through stiffness cross-coupling”. In: *Journal of Aircraft* 23.2 (1986), pp. 148–155.

[27] Erian A Armanios and Ashraf M Badir. “Free vibration analysis of anisotropic thin-walled closed-section beams”. In: *AIAA journal* 33.10 (1995), pp. 1905–1910.

[28] Ashraf Badir. “Analysis of two-cell composite beams”. In: *36th Structures, Structural Dynamics and Materials Conference*. 1995, p. 1208.

[29] Marthinus C Van Schoor and Andreas H von Flotow. “Aeroelastic characteristics of a highly flexible aircraft”. In: *Journal of Aircraft* 27.10 (1990), pp. 901–908.

[30] Deman Tang and Earl H Dowell. “Experimental and theoretical study on aeroelastic response of high-aspect-ratio wings”. In: *AIAA journal* 39.8 (2001), pp. 1430–1441.

References for Section B

[1] Pentaras Demetris, Gentilini Cristina, et al. *Mechanics of functionally graded material structures*. World Scientific, 2015.

[2] Rasheedat Modupe Mahamood and Esther Titilayo Akinlabi. *Functionally graded materials*. Springer, 2017.

[3] Snehashish Chakraverty and Karan Kumar Pradhan. *Vibration of functionally graded beams and plates*. Academic Press, 2016.

[4] Zheng Zhong, Linzhi Wu, and Weiqiu Chen. *Mechanics of Functionally Graded Materials and Structures*. Nova Science Publishers, 2012.

[5] A-Y Tang et al. “Exact frequency equations of free vibration of exponentially non-uniform functionally graded Timoshenko beams”. In: *International Journal of Mechanical Sciences* 89 (2014), pp. 1–11.

[6] Trung-Kien Nguyen, Thuc P Vo, and Huu-Tai Thai. “Static and free vibration of axially loaded functionally graded beams based on the first-order shear deformation theory”. In: *Composites Part B: Engineering* 55 (2013), pp. 147–157.

[7] Mesut Şimşek. “Fundamental frequency analysis of functionally graded beams by using different higher-order beam theories”. In: *Nuclear Engineering and Design* 240.4 (2010), pp. 697–705.

[8] Bhavani V Sankar. “An elasticity solution for functionally graded beams”. In: *Composites Science and Technology* 61.5 (2001), pp. 689–696.

[9] Amal E Alshorbagy, MA Eltaher, and FF Mahmoud. “Free vibration characteristics of a functionally graded beam by finite element method”. In: *Applied Mathematical Modelling* 35.1 (2011), pp. 412–425.

[10] A Chakraborty, S Gopalakrishnan, and JN Reddy. “A new beam finite element for the analysis of functionally graded materials”. In: *International Journal of Mechanical Sciences* 45.3 (2003), pp. 519–539.

[11] KK Pradhan and S Chakraverty. “Free vibration of Euler and Timoshenko functionally graded beams by Rayleigh–Ritz method”. In: *Composites Part B: Engineering* 51 (2013), pp. 175–184.

[12] Li-long Jing et al. “Static and free vibration analysis of functionally graded beams by combination Timoshenko theory and finite volume method”. In: *Composite structures* 138 (2016), pp. 192–213.

[13] Jing-Feng Gong et al. “Thermoelastic analysis of three-dimensional functionally graded rotating disks based on finite volume method”. In: *Proceedings of the Institution of Mechanical Engineers, Part C: Journal of Mechanical Engineering Science* 228.4 (2014), pp. 583–598.

[14] Sundaramoorthy Rajasekaran. “Differential transformation and differential quadrature methods for centrifugally stiffened axially functionally graded tapered beams”. In: *International Journal of Mechanical Sciences* 74 (2013), pp. 15–31.

[15] S Rajasekaran. “Buckling and vibration of axially functionally graded nonuniform beams using differential transformation based dynamic stiffness approach”. In: *Meccanica* 48.5 (2013), pp. 1053–1070.

[16] Yousef S Al Rjoub and Azhar G Hamad. “Free vibration of functionally Euler-Bernoulli and Timoshenko graded porous beams using the transfer matrix method”. In: *KSCE Journal of Civil Engineering* 21.3 (2017), pp. 792–806.

[17] Jung Woo Lee and Jung Youn Lee. “Free vibration analysis of functionally graded Bernoulli-Euler beams using an exact transfer matrix expression”. In: *International Journal of Mechanical Sciences* 122 (2017), pp. 1–17.

[18] Huijuan Su and JR Banerjee. “Development of dynamic stiffness method for free vibration of functionally graded Timoshenko beams”. In: *Computers & Structures* 147 (2015), pp. 107–116.

[19] H Su, JR Banerjee, and CW Cheung. “Dynamic stiffness formulation and free vibration analysis of functionally graded beams”. In: *Composite Structures* 106 (2013), pp. 854–862.

[20] John Fitch. “Solving algebraic problems with REDUCE”. In: *Journal of Symbolic Computation* 1.2 (1985), pp. 211–227.

[21] Anthony C Hearn. *REDUCE user's manual. Version 3.2*. Rand Corporation, 1985.

[22] JR Banerjee et al. "Use of computer algebra in Hamiltonian calculations". In: *Advances in Engineering Software* 39.6 (2008), pp. 521–525.

[23] W_H Wittrick and FW Williams. "A general algorithm for computing natural frequencies of elastic structures". In: *The Quarterly Journal of Mechanics and Applied Mathematics* 24.3 (1971), pp. 263–284.

[24] Diana Virginia Bambill, Carlos Adolfo Rossit, and Daniel Horacio Felix. "Free vibrations of stepped axially functionally graded Timoshenko beams". In: *Meccanica* 50.4 (2015), pp. 1073–1087.

[25] Nuttawit Wattanasakulpong and Jarruwat Charoensuk. "Vibration characteristics of stepped beams made of FGM using differential transformation method". In: *Meccanica* 50.4 (2015), pp. 1089–1101.

[26] Metin Aydogdu and Vedat Taskin. "Free vibration analysis of functionally graded beams with simply supported edges". In: *Materials & design* 28.5 (2007), pp. 1651–1656.

[27] Zheng Zhong and Tao Yu. "Analytical solution of a cantilever functionally graded beam". In: *Composites Science and Technology* 67.3-4 (2007), pp. 481–488.

[28] SA Sina, HM Navazi, and H Haddadpour. "An analytical method for free vibration analysis of functionally graded beams". In: *Materials & Design* 30.3 (2009), pp. 741–747.

[29] Shi-rong Li, Ze-qing Wan, and Jing-hua Zhang. "Free vibration of functionally graded beams based on both classical and first-order shear deformation beam theories". In: *Applied Mathematics and Mechanics* 35.5 (2014), pp. 591–606.

[30] MA Eltaher, AE Alshorbagy, and FF Mahmoud. "Determination of neutral axis position and its effect on natural frequencies of functionally graded macro/nanobeams". In: *Composite Structures* 99 (2013), pp. 193–201.

[31] KS Al-Basyouni, Abdelouahed Tounsi, and SR Mahmoud. "Size dependent bending and vibration analysis of functionally graded micro beams based on modified couple stress theory and neutral surface position". In: *Composite Structures* 125 (2015), pp. 621–630.

[32] JR Banerjee. "Coupled bending–torsional dynamic stiffness matrix for beam elements". In: *International journal for numerical methods in engineering* 28.6 (1989), pp. 1283–1298.

[33] JR Banerjee. “Explicit analytical expressions for frequency equation and mode shapes of composite beams”. In: *International Journal of Solids and Structures* 38.14 (2001), pp. 2415–2426.

[34] Louis A Pipes and Lawrence R Harvill. *Applied mathematics for engineers and physicists*. Courier Corporation, 2014.

[35] CP Filipich and PAA Laura. “In-plane vibrations of portal frames with end supports elastically restrained against rotation and translation”. In: *Journal of Sound Vibration* 117 (1987), pp. 467–473.

[36] İlhan Tatar. “Vibration characteristics of portal frames”. MA thesis. Izmir Institute of Technology, 2013.

[37] Peter Gudmundson. “Eigenfrequency changes of structures due to cracks, notches or other geometrical changes”. In: *Journal of the Mechanics and Physics of Solids* 30.5 (1982), pp. 339–353.

[38] Fr D Ju and ME Mimovich. “Experimental diagnosis of fracture damage in structures by the modal frequency method”. In: *Journal of Vibration, Acoustics, Stress, and Reliability in Design* 110.4 (1988), pp. 456–463.

[39] Peter Gudmundson. “The dynamic behaviour of slender structures with cross-sectional cracks”. In: *Journal of the Mechanics and Physics of Solids* 31.4 (1983), pp. 329–345.

[40] TG Chondros, AD Dimarogonas, and J Yao. “A continuous cracked beam vibration theory”. In: *Journal of sound and vibration* 215.1 (1998), pp. 17–34.

[41] S Christides and ADS Barr. “One-dimensional theory of cracked Bernoulli-Euler beams”. In: *International Journal of Mechanical Sciences* 26.11-12 (1984), pp. 639–648.

[42] AD Dimarogonas and CA Papadopoulos. “Vibration of cracked shafts in bending”. In: *Journal of sound and vibration* 91.4 (1983), pp. 583–593.

[43] CA Papadopoulos and AD Dimarogonas. “Coupling of bending and torsional vibration of a cracked Timoshenko shaft”. In: *Ingenieur-Archiv* 57.4 (1987), pp. 257–266.

[44] CA Papadopoulos and AD Dimarogonas. “Coupled longitudinal and bending vibrations of a rotating shaft with an open crack”. In: *Journal of sound and vibration* 117.1 (1987), pp. 81–93.

[45] CA Papadopoulos and AD Dimarogonas. “Coupled longitudinal and bending vibrations of a cracked shaft”. In: *Journal of vibration, acoustics, stress, and reliability in design* 110.1 (1988), pp. 1–8.

[46] Thomas M Tharp. “A finite element for edge-cracked beam columns”. In: *International Journal for Numerical Methods in Engineering* 24.10 (1987), pp. 1941–1950.

[47] N Miyazaki. “Application of line-spring model to dynamic stress intensity factor analysis of pre-cracked bending specimen”. In: *Engineering fracture mechanics* 38.4-5 (1991), pp. 321–326.

[48] Robert Y Liang, Jialou Hu, and Fred Choy. “Theoretical study of crack-induced eigenfrequency changes on beam structures”. In: *Journal of Engineering Mechanics* 118.2 (1992), pp. 384–396.

[49] HP Lee and TY Ng. “Natural frequencies and modes for the flexural vibration of a cracked beam”. In: *Applied Acoustics* 42.2 (1994), pp. 151–163.

[50] G Bamnios and A Trochides. “Dynamic behaviour of a cracked cantilever beam”. In: *Applied Acoustics* 45.2 (1995), pp. 97–112.

[51] M Kisa, J Brandon, and M Topcu. “Free vibration analysis of cracked beams by a combination of finite elements and component mode synthesis methods”. In: *Computers & structures* 67.4 (1998), pp. 215–223.

[52] M Kisa and J Brandon. “The effects of closure of cracks on the dynamics of a cracked cantilever beam”. In: *Journal of sound and vibration* 238.1 (2000), pp. 1–18.

[53] Ding Yang Zheng and NJ Kessissoglou. “Free vibration analysis of a cracked beam by finite element method”. In: *Journal of Sound and vibration* 273.3 (2004), pp. 457–475.

[54] JA Loya, L Rubio, and J Fernández-Sáez. “Natural frequencies for bending vibrations of Timoshenko cracked beams”. In: *Journal of Sound and Vibration* 290.3-5 (2006), pp. 640–653.

[55] E Viola, P Ricci, and MH Aliabadi. “Free vibration analysis of axially loaded cracked Timoshenko beam structures using the dynamic stiffness method”. In: *Journal of Sound and Vibration* 304.1-2 (2007), pp. 124–153.

[56] AS Bouboulas and NK Anifantis. “Formulation of cracked beam element for analysis of fractured skeletal structures”. In: *Engineering Structures* 30.4 (2008), pp. 894–901.

[57] Hiroyuki Okamura, Katsuhiko Watanabe, and Tachio Takano. “Deformation and strength of cracked member under bending moment and axial force”. In: *Engineering Fracture Mechanics* 7.3 (1975), pp. 531–539.

[58] G Gounaris and A Dimarogonas. “A finite element of a cracked prismatic beam for structural analysis”. In: *Computers & Structures* 28.3 (1988), pp. 309–313.

[59] N Papaeconomou and A Dimarogonas. “Vibration of cracked beams”. In: *Computational Mechanics* 5.2-3 (1989), pp. 88–94.

[60] FW Williams and WP Howson. “Compact computation of natural frequencies and buckling loads for plane frames”. In: *International Journal for Numerical Methods in Engineering* 11.7 (1977), pp. 1067–1081.

[61] ML Kikidis and CA Papadopoulos. “Slenderness ratio effect on cracked beam”. In: *Journal of Sound and Vibration* 155.1 (1992), pp. 1–11.

[62] Andrew J Keane and WG Price. *Statistical energy analysis: an overview, with applications in structural dynamics*. Cambridge University Press, 1997.

[63] Richard H Lyon, Richard G DeJong, and Manfred Heckl. *Theory and application of statistical energy analysis*. 1995.

[64] JC Wohlever and RJ Bernhard. “Mechanical energy flow models of rods and beams”. In: *Journal of sound and vibration* 153.1 (1992), pp. 1–19.

[65] Y Lase, MN Ichchou, and L Jezequel. “Energy flow analysis of bars and beams: theoretical formulations”. In: *Journal of Sound and Vibration* 192.1 (1996), pp. 281–305.

[66] OM Bouthier and RJ Bernhard. “Simple models of energy flow in vibrating membranes”. In: *Journal of sound and vibration* 182.1 (1995), pp. 129–147.

[67] OM Bouthier and RJ Bernhard. “Simple models of the energetics of transversely vibrating plates”. In: *Journal of Sound and Vibration* 182.1 (1995), pp. 149–164.

[68] Bengt Å Åkesson. “PFVIBAT—a computer program for plane frame vibration analysis by an exact method”. In: *International Journal for Numerical Methods in Engineering* 10.6 (1976), pp. 1221–1231.

[69] WP Howson, JR Banerjee, and FW Williams. “Concise equations and program for exact eigensolutions of plane frames including member shear”. In: *Engineering Software III*. Springer, 1983, pp. 443–452.

[70] Ju-Bum Han et al. “Vibrational energy flow models for the Rayleigh–Love and Rayleigh–Bishop rods”. In: *Journal of Sound and Vibration* 333.2 (2014), pp. 520–540.

[71] Michael Shatalov et al. “Longitudinal vibration of isotropic solid rods: from classical to modern theories”. In: *Advances in Computer Science and Engineering, M. Schmidt, ed., InTech Open, Rijeka, Croatia* (2011), pp. 187–214.

[72] John William Strutt and Baron Rayleigh. *The theory of sound*. Dover, 1945.

[73] Augustus Edward Hough Love. *A treatise on the mathematical theory of elasticity*. Cambridge university press, 2013.

[74] VD Belov, SA Rybak, and BD Tartakovskii. “Propagation of vibrational energy in absorbing structures”. In: *Soviet Physics Acoustics-USSR* 23.2 (1977), pp. 115–119.

[75] DJ Nefske and SH Sung. “Power flow finite element analysis of dynamic systems: basic theory and application to beams”. In: *Journal of Vibration, Acoustics, Stress, and Reliability in Design* 111.1 (1989), pp. 94–100.

[76] Franklin Y Cheng. “Vibrations of Timoshenko beams and frameworks”. In: *Journal of the structural division* 96.3 (1970), pp. 551–571.

[77] TM Wang and TA Kinsman. “Vibrations of frame structures according to the Timoshenko theory”. In: *Journal of Sound and Vibration* 14.2 (1971), pp. 215–227.

[78] WP Howson and FW Williams. “Natural frequencies of frames with axially loaded Timoshenko members”. In: *Journal of Sound and Vibration* 26.4 (1973), pp. 503–515.

[79] Singiresu S Rao. *Vibration of continuous systems*. Vol. 464. Wiley Online Library, 2007.

[80] Mihai Valentin Predoi et al. “High frequency longitudinal damped vibrations of a cylindrical ultrasonic transducer”. In: *Shock and Vibration* 2014 (2014).

[81] Walter C Hurty and Moshe F Rubinstein. “Dynamics of structures”. In: *Prentice-Hall Series in Engineering of the Physical Sciences, Englewood Cliffs: Prentice-Hall, 1964* (1964).

[82] Igor Fedotov et al. “Analysis for an N-stepped Rayleigh bar with sections of complex geometry”. In: *Applied Mathematical Modelling* 32.1 (2008), pp. 1–11.

[83] AS Yigit and AP Christoforou. “Coupled axial and transverse vibrations of oilwell drillstrings”. In: *Journal of sound and vibration* 195.4 (1996), pp. 617–627.

[84] Seon Han and Haym Benaroya. “Coupled transverse and axial vibration of a compliant tower-Comparison of linear and nonlinear models”. In: *41st Structures, Structural Dynamics, and Materials Conference and Exhibit*. 2000, p. 1347.

[85] Marcelo A Trindade, Claudio Wolter, and Rubens Sampaio. “Karhunen–Loeve decomposition of coupled axial/bending vibrations of beams subject to impacts”. In: *Journal of sound and vibration* 279.3-5 (2005), pp. 1015–1036.

[86] Rubens Sampaio, Marcelo Tulio Piovan, and G Venero Lozano. “Coupled axial/torsional vibrations of drill-strings by means of non-linear model”. In: *Mechanics Research Communications* 34.5-6 (2007), pp. 497–502.

[87] Jerry H Ginsberg. “Coupling of axial and transverse displacement fields in a straight beam due to boundary conditions”. In: *The Journal of the Acoustical Society of America* 126.3 (2009), pp. 1120–1124.

[88] Stefano Lenci and Giuseppe Rega. “Axial–transversal coupling in the free nonlinear vibrations of Timoshenko beams with arbitrary slenderness and axial boundary conditions”. In: *Proceedings of the Royal Society A: Mathematical, Physical and Engineering Sciences* 472.2190 (2016), p. 20160057.

[89] Zhiyang Lei, Jinpeng Su, and Hongxing Hua. “Longitudinal and transverse coupling dynamic properties of a Timoshenko beam with mass eccentricity”. In: *International Journal of Structural Stability and Dynamics* 17.07 (2017), p. 1750077.

[90] Zhen Ni and Hongxing Hua. “Axial-bending coupled vibration analysis of an axially-loaded stepped multi-layered beam with arbitrary boundary conditions”. In: *International Journal of Mechanical Sciences* 138 (2018), pp. 187–198.

[91] Erasmo Carrera and Marco Petrolo. “On the effectiveness of higher-order terms in refined beam theories”. In: *Journal of Applied Mechanics* 78.2 (2011), p. 021013.

[92] Phill-Seung Lee and Ghyslaine McClure. “A general three-dimensional L-section beam finite element for elastoplastic large deformation analysis”. In: *Computers & structures* 84.3-4 (2006), pp. 215–229.

[93] JR Banerjee. “Modal analysis of sailplane and transport aircraft wings using the dynamic stiffness method”. In: *Journal of Physics: Conference Series*. Vol. 721. 1. IOP Publishing. 2016, p. 012005.

[94] R Butler and JR Banerjee. “Optimum design of bending-torsion coupled beams with frequency or aeroelastic constraints”. In: *Computers & structures* 60.5 (1996), pp. 715–724.

[95] JR Banerjee. “Free vibration of sandwich beams using the dynamic stiffness method”. In: *Computers & structures* 81.18-19 (2003), pp. 1915–1922.

[96] FS Tse, IE Morse, and RT Hinkle. “Mechanical Vibrations, Theory and Applications, Allyn and Becon”. In: *Inc.(Pearson Publishers)* (1978).

[97] JR Banerjee. “Free vibration analysis of a twisted beam using the dynamic stiffness method”. In: *International Journal of Solids and Structures* 38.38-39 (2001), pp. 6703–6722.

[98] RED Bishop, SM Cannon, and S Miao. “On coupled bending and torsional vibration of uniform beams”. In: *Journal of sound and vibration* 131.3 (1989), pp. 457–464.